

**NOVEL SYNTHESIS AND APPLICATIONS
OF FUNCTIONAL CARBON, TRANSITION
METAL OXIDES AND THEIR
NANOCOMPOSITES**

**A THESIS SUBMITTED TO THE
UNIVERSITY OF PUNE
FOR THE DEGREE OF DOCTOR OF PHILOSOPHY**

**IN
CHEMISTRY**

**BY
MANDAKINI BISWAL**

**DR. CHANDRASHEKHAR V. RODE
(RESEARCH GUIDE)**

**DR. SATISHCHANDRA B. OGALE
(RESEARCH CO-GUIDE)**

**CHEMICAL ENGINEERING & PROCESS DEVELOPMENT
DIVISION**

**PHYSICAL AND MATERIALS CHEMISTRY DIVISION
NATIONAL CHEMICAL LABORATORY**

**PUNE – 411 008
INDIA**

AUGUST 2013



सीएसआयआर-राष्ट्रीय रासायनिक प्रयोगशाला

(वैज्ञानिक तथा औद्योगिक अनुसंधान परिषद)

डॉ. होमी भाभा मार्ग, पुणे - 411 008. भारत

CSIR-NATIONAL CHEMICAL LABORATORY

(Council of Scientific & Industrial Research)

Dr. Homi Bhabha Road, Pune - 411008. India



CERTIFICATE

This is to certify that the work presented in the thesis entitled "NOVEL SYNTHESIS AND APPLICATIONS OF FUNCTIONAL CARBON, TRANSITION METAL OXIDES AND THEIR NANOCOMPOSITES" by MANDAKINI BISWAL, submitted for the degree **Doctor of Philosophy in Chemistry** was carried out under our supervision at the Chemical Engineering and Process Development Division and Physical and Materials Chemistry Division, National Chemical Laboratory, Pune, 411008, India. All the materials from other sources have been duly acknowledged in the thesis.

Dr. Chandrashekhar Rode

(Research Guide)

Dr. Satishchandra Ogale

(Research co-Guide)

Date: 20/8/2013

Place: Pune.

Communication
Channels

NCL Level DID : 2590
NCL Board No. : +91-20-25902000
EPABX : +91-20-25893300
: +91-20-25893400

FAX

Director's Office : +91-20-25902601
COA's Office : +91-20-25902660
COS&P's Office : +91-20-25902664

WEBSITE

www.ncl-india.org

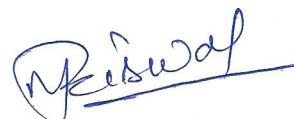
Declaration by the candidate

I hereby declare that the thesis entitled “NOVEL SYNTHESIS AND APPLICATIONS OF FUNCTIONAL CARBON, TRANSITION METAL OXIDES AND THEIR NANOCOMPOSITES” submitted for the degree Doctor of Philosophy in Chemistry to the University of Pune, has been carried out by me at the Chemical Engineering and Process Development Division, and Physical and Material Chemistry Division of National Chemical Laboratory, Pune under the joint supervision of Dr. Chandrashekhar V. Rode and Dr. Satishchandra B. Ogale. Such material as has been obtained by other sources has been duly acknowledged in this thesis. The work is original and has not been submitted in part or full by me for any other degree or diploma to other University.

Date: 26/08/2013

National Chemical Laboratory

Pune – 411 008



Mandakini Biswal

(Research Student)

*Dedicated
To
My
Beloved
Family*



Acknowledgements

First, I would like to thank Dr. Chandrashekar Rode, my Ph.D. supervisor, for giving me an opportunity to pursue Ph.D. with him. It has been a great privilege to work under his able guidance and valuable scientific advice over the past five years. I greatly appreciate the insights he provided in various studies, especially in the domain of catalysis.

I would also like to express my deepest gratitude to Dr. Satishchandra Ogale, my co-supervisor for giving me an opportunity to work in his dynamic laboratory environment. His innovative thinking and highly spirited attitude have inspired me to conduct and complete my doctoral research quite efficiently. He has not only grafted my scientific skills and knowledge but also moulded me into a better human being. His guidance always challenged me intellectually and provided a perfect ambience that I needed to grow as a material chemist.

I am really grateful to both Dr. Ogale and Dr. Rode for their critical comments and tremendous efforts in preparing this dissertation. I thank them for their endless support filled with patience and enthusiasm during my whole tenure of Ph.D.

I sincerely thank various funding agencies namely, the Council for Scientific and Industrial Research (CSIR), the Department of Science and Technology (DST), the Department of Information Technology (DIT), and last but not the least, the Govt. of India for the research fellowship and travel grants.

I express my sincere thanks to the Dr. S. Sivram, former Director of CSIR-NCL, Dr. Sourav Pal, Director, CSIR-NCL and Dr. Anil Kumar, HOD, Physical and Materials Chemistry Division, for providing the infrastructure and facilities for performing research at CSIR-NCL and for their whole-hearted help and constant support from the very first days in National Chemical Laboratory. Also I would like to thank Dr. (Mrs.) Jyoti P. Jog, Dr. Sreekumar, Dr. P.A. Joy, Dr. Rahul Banerjee, Dr. B.L.V. Prasad, Dr. Krishnamoorthy, and Dr. Manjusha Shelke for their timely advice and help. I also appreciate Dr. K. R. Patil, Mr. Gholap and Mr. A.B. Gaikwad, for their help in materials characterization. I also admire help of Dr. C. G. Suresh, Mr. Naveen Pavithran, Mr. Deepak Jori, Mr. Punekar, Mrs. Puranik and Mrs. Kolhe throughout this journey.

A special thanks to all collaborators, especially Dr. B. B. Kale, CMET, Pune and Dr. S. N. Kale, DIAT, Pune. I also take this opportunity to thank all our international collaborators Prof. Beatrice Hannoyer (Rouen, France), Prof. Wegdan Ramadan (Alexandria, Egypt), Prof. Madhavi Srinivasan and Prof. Subodh Mhaisalkar (NTU, Singapore). Indeed, Prof. Madhavi Srinivasan and Prof. Subodh Mhaisalkar gave me an opportunity to work at the Energy Research Institute @ NTU (ERI@N), Nanyang Technological University, for a period of two months.

I would like to thank my senior colleagues, Dr. Hrushikesh, Dr. Sneha Kulkarni, Dr. Kashinath Bogle, Dr. Rajesh Hyam, Dr. Sarfraj Mujawar, Dr. Anup Kale, Dr. Tushar Jagdale, Dr. Abhimanu Rana, Dr. Subas Muduli, Dr. Vivek, Dr. Prasad for their mentoring and care during my initial research days. A very special thanks to all my current labmates, Dr. Dattatryay Latte, Dr. Debanjan, Dr. Vivek Antad, Dr. Sarika Kelkar, Dr. Arif Sheikh, Dr. Parvez Shaikh, Dr. Meenakshi, Datta, Meenal, Shruti, Reshma, Lily, Onkar, Vishal, Anil, Satish, Abhik, Rohan, Umesh, Wahid, Yogesh, Deepti, Rounak, Pradeep, Pooja, Dhanya, Mukta, Shraddha, Satyawan, Aniruddh, Subhra, Aparna, Ketki, Rupali, Nilima, Dr. Sambhaji, Harish Sir, Ashish Sir, Upendra, Praverthana, Kirti, Sumit, Kush, Tanya, Divya, Jayaprakash Sir, Rasika, Ajay, Vivek Mate, Aparna, Narayan, Amol, Sumit, Sharda for all their support and creating interesting brainstorming sessions. I would also like to thank friends from other labs which include Dr. Aravindan (NTU, Singapore), Pradip, Sreekuttan, for their support in my research work.

A very special thank to my Oriya group members Debasis bhai, Gorkarna Bhai, Rosy apa, Manaswini apa, Ramakanta bhai, Pitamber bhai, Jeetu, Raju, Pushpanjali, Rudra, Manoj for their memorable, pleasant and perpetual refreshment and support in my difficult time during this journey. I would like to offer my special thank to my friend Chaka and my senior Debasis bhai for their friendly support and care throughout this period. The list of my friends who stood for me during the days of my need will be very long but I would like to name some of them who deserve a special place in my life Kuni, Mamuni, Pinky, Mami, Manisha, Purna, Sthita, Sunita, Jublee, Jhasa, Chandra, Sudhir, Saroj, Sabya, Pravati, Subhendu. I would also like to acknowledge Naresh bhai, Deepak bhai, who always encouraged me. I would also like to thank my roommates Sivaranjini and Praji for their friendly support and encouragement. I would like to thank everybody who was important for the successful realization of the thesis, and express my sincere apology to anyone if I have inadvertently missed him/her.

Finally I specially acknowledge Siba for his understanding, support, care and for being there with me at all times. I would like to have the opportunity to thank my family Baba, Bou, my brother Papu and Dipu, for their love, being caring and becoming.

I would like to thank all my teachers from primary school till my master's degree for imbibing good values and knowledge in me.

Last but by no means least I thank Lord Jagannath for making my life so special and for being with me always.

Mandakini Biswal.....

List of Abbreviations

QD	Quantum Dots
NIR	Near Infrared
0D	Zero- Dimensional
1D	One- Dimensional
2D	Two- Dimensional
3D	Three- Dimensional
CNT	Carbon Nanotube
SWNT	Single Wall Carbon Nanotube
MWNT	Multi Wall Carbon Nanotube
CVD	Chemical Vapour Deposition
CCVD	Catalytic Chemical Vapour Deposition
TNT	Trinitrotoluene
CMR	Colossal Magnetic Resistance
ESR	Equivalent Series Resistance
EDLC	Electric Double Layer Capacitors
EC	Ethylene carbonate
DMC	Dimethyl carbonate
CNF	Carbon Nanofiber
LTO	$\text{Li}_4\text{Ti}_5\text{O}_{12}$
PVC	Poly Vinyl Chloride
XRD	X-ray Diffraction
FWHM	Full Width at Half Maximum
TEM	Transmission Electron Microscopy

EDS	Energy-Dispersive X-ray Spectroscopy
HRTEM	High Resolution TEM
SAED	Selected Area Electron Diffraction
SEM	Scanning Electron Microscopy
SE	Secondary Electrons
BSE	Backscattered Electrons
AES	Auger electron spectroscopy
EDAX	Energy Dispersive analysis of X-rays
PL	Photoluminescence
CB	Conduction Band
VB	Valence Band
FTIR	Fourier Transform Infrared
UV-VIS	Ultraviolet-Visible
DRS	Diffuse Reflectance
QS	Quadrupole Splitting
XPS	X-ray Photoelectron Spectroscopy
ESCA	Electron Spectroscopy for Chemical Analysis
KE	Kinetic Energy
BE	Binding Energy
UHV	Ultra High Vacuum
BET	Brunauer–Emmett–Teller
SQUID	Superconducting Quantum Interferometry Device
VSM	Vibrating Sample Magnetometer
CV	Cyclic Voltammetry
PSD	Pore Size Distribution
DEC	Diethyl Carbonate
LIB	Li Ion Battery

OCV	Open Circuit Voltage
HEC	Hybrid Electrochemical Capacitor
NHE	Normal Hydrogen Electrode
RHE	Reversible hydrogen electrode
CQD	Carbon Quantum Dot
SEI	Solid Electrolyte Inter-phase Layer

Contents

Abstract	i-ii
1. Chapter 1	1-52
Introduction	
1.1. Preamble	2
1.2. Synthesis of nanomaterials	4
1.3. Property change from bulk to nano	6
1.3.1. Surface Properties	7
1.3.2. Optical Properties	9
1.3.3. Electronic Properties	9
1.3.4. Magnetic Properties	11
1.3.5. Mechanical Properties	12
1.4. Types of nanomaterials	13
1.4.1. Carbon based nanomaterials	14
1.4.2. Types of carbon based nanomaterials	15
1.4.3. Metal oxide based nanomaterials	21
1.4.4. Carbon - transition metal oxide nanocomposites	22
1.5. Applications Nanomaterials	23
1.5.1. Energy Storage	23
1.5.2. Water Splitting	37
1.5.3. Catalysis	40
1.6. Objectives and outline of the thesis	41
1.7. Reference	43

2. Chapter 2	53-83
Experimental Methods and Characterization Techniques	
Section I	54
2.I Synthesis Techniques	54
2.I.1 Co-Precipitation Methods	55
2.I.2 Sol Gel method	55
2.I.3 High temperature Pyrolysis	58
2.I.4 Pulsed Laser synthesis method	59
Section II	60
2.II Characterization Techniques	60
2.II.1 X-Ray Diffraction	60
2.II.2 Raman Spectroscopy	62
2.II.3 Transmission Electron Microscopy (TEM)	64
2.II.4 Scanning Electron Microscope (SEM)	66
2.II.5 Photoluminescence Spectroscopy	67
2.II.6 Fourier Transform IR Spectroscopy	69
2.II.7 UV-VIS Spectroscopy	71
2.II.8 Mössbauer Spectroscopy	73
2.II.9 X-Ray Photoelectron Spectroscopy	75
2.II.10 BET Surface Area Measurement	77
2.II.11 Superconducting Quantum Interferometry Device	78
2.II.12 Electrochemical Measurements	80
2.III References	82
3. Chapter 3	84-121
From Dead Leaves to High Energy Density Supercapacitor	

3.1. Introduction	85
3.2. Experimental	87
3.2.1. Materials	87
3.2.2. Synthesis of Functional Carbon	87
3.2.3. Electrochemical Measurements in 1M H ₂ SO ₄	89
3.2.4. Electrochemical Measurements with 1M LiPF ₆ in EC:DEC	89
3.2.5. Electrochemical Impedance Spectroscopy Measurements	89
3.2.6. Electrochemical measurements for battery type hybrid Supercapacitor	90
3.2.7. Characterization	90
3.3. Results and Discussions	90
3.4. Conclusion	115
3.5. References	116
4. Chapter 4	122-141
Water Electrolysis with a Conducting Carbon Cloth: Sub-Threshold Hydrogen Generation and Super-Threshold Carbon Quantum Dot Formation	
4.1. Introduction	123
4.2. Experimental	125
4.2.1. Materials	125
4.2.2. Functional Carbon Cloth Synthesis	125
4.2.3. Characterization of Carbon Cloth	125
4.2.4. Electrochemical Measurements of Water electrolysis process	126

4.2.5. Gas Analysis	126
4.2.6. Synthesis and Purification of Carbon Quantum dots	126
4.3. Results and Discussions	127
4.3.1. Sub-threshold hydrogen generation	129
4.3.2. Super-threshold Carbon quantum dots formation	135
4.4. Conclusion	138
4.5. References	139
5. Chapter 5	142-163
Pulsed Laser Synthesis of Mesoscopic Fe₃O₄ Spheres for Use as Anode	
Material in High Performance Li ion Battery	
5.1. Introduction	143
5.2. Experimental	145
5.2.1. Materials	145
5.2.2. Synthesis of Fe ₃ O ₄ particles from bulk α -Fe ₂ O ₃	145
5.2.3. Characterizations	146
5.2.4. Electrochemical Measurements	146
5.3. Results and Discussions	147
5.4. Conclusion	159
5.5. References	160
6. Chapter 6	164-185
Selectivity Tailoring in Liquid Phase Oxidation of <i>p</i>-cresol over	
MWNT-Mn₃O₄ Nanocomposite Catalysts	
6.1. Introduction	165
6.2. Experimental	166
6.2.1. Materials	166

6.2.2. Synthesis of Mn ₃ O ₄ and MWNT-Mn ₃ O ₄ nanocomposites	166
6.2.3. Characterizations	167
6.2.4. Catalytic Activity	167
6.3. Results and Discussions	168
6.4. Conclusion	182
6.5. References	183
7. Chapter 7	186-192
Summary and Future Scope	
7.1. Summary of the thesis	187
7.2. Scope for future work	189
8. Appendix	193-212
9. List of Publications and Patents	213

Abstract

A decade ago nanoscience was a curiosity-driven field focusing on diverse ways to synthesize nanoparticles and studies of their physical and chemical properties. With enhanced understanding and ability to manipulate and control nano-synthesis on a large scale, emphasis is now being laid upon novel applications of such systems emanating from their unique set of properties. Amongst the most investigated of nanosystems are semiconductor quantum dots, noble metals and functional metal oxides. The work on metal oxides has witnessed considerable upsurge during the past few years with fields such as solar energy conversion, water splitting, energy storage, catalysis, photocatalysis etc. acquiring centre-stage. Another major development of the past decade has been the progress in the field of functional carbon materials, in particular, the low dimensional carbon systems such as fullerenes, CNTs, and graphene. Here again the current work is focused on fundamental science as well as application development.

In this work we have attempted to bridge these two separately developing, interesting and key disciplines of science (metal oxide nanomaterials and functional carbon) to explore newer application domains in the field of energy and environment. This forms the brief introduction to the thesis and is presented in **Chapter 1**. A brief overview of the techniques used for the synthesis of functional carbon, various transition metal oxides and their nanocomposites is presented in **Chapter 2** along with a general outline of the instruments and methods used for the characterization of these nanomaterials.

Chapter 3 comprises of the synthesis of functional carbon from pyrolysis of natural waste such as plant dead leaves which is used as electrode material in both electric double layer supercapacitor and battery type hybrid supercapacitor. The functional carbon derived from dead leaves shows high performance in supercapacitor applications.

In the **Chapter 4** functional carbon cloth is synthesized from the pyrolysis of cellulose fabric which is used as electrode material in alkaline electrolysis process. The use of the carbon cloth as electrode (anode) leads to substantial hydrogen generation at sub-threshold potential ($< 1.23\text{V}$) and carbon quantum dots formation at super-threshold

potential ($> 1.23\text{V}$). The detail mechanism of the hydrogen generation and quantum dots formation is discussed in this chapter.

The **Chapter 5** discusses the pulsed laser synthesis of mesoscopic Fe_3O_4 spheres from bulk Fe_2O_3 powder. The high energy laser pulses ($h\nu = 5\text{ eV}$) created an extremely high local temperature of $\sim 12000^\circ\text{C}$ by transient laser heating of particles which allowed the particles to melt and evaporate forming a micro-bubble reaction zone. Dissipation of the energy occurred by micro-bubble collapsed through new bond formation and phase evolution. The presence of ammonia helped in the reduction of $\alpha\text{-Fe}_2\text{O}_3$ to Fe_3O_4 . The synthesized Fe_3O_4 is used as anode material in Li ion battery which shows high capacity with high rate performance and stability.

In the **Chapter 6**, nanocomposites Mn_3O_4 and multiwall carbon nanotube (MWNT) are synthesized by co-precipitation route, by varying the MWNT percentage which shows excellent activity for liquid phase oxidation of *p*-cresol. The detail mechanism of such high selectivity, the geometric and electronic effect of carbon nanotube on the conversion and selectivity is discussed in this chapter.

The **Chapter 7** summarizes the work described in this thesis by presenting the salient features of the work and also mentions the possible avenues for future investigations.

Chapter-1

Introduction

This chapter gives an overview of the field of nanomaterials and discusses their impact on science and technology. Here we have briefly discussed various approaches for nanomaterial synthesis. The primary focus is on carbon nanomaterials, transition metal oxide nanomaterials and nanocomposites of the two. Also in this chapter we have emphasized various practical applications of the above mentioned nanomaterials. Use of these materials in energy and environmental applications are addressed in greater details. Finally, the objectives and scope of have been discussed.

1.1 Preamble

Nanotechnology can be defined as the technology which allows not only the creation of nanomaterials by a controlled way but also their utilization for an intended purpose. It involves a combination of a variety of disciplines such as chemistry, physics and biology. Prof. Richard Feynman, Physics Nobel laureate and Professor of Californian Institute of technology first introduced (1959) the field of nano in his lecture called “There is plenty of room at the bottom” wherein he gave first insight into the possibility of creating nanosized materials by using atoms as the building blocks.^[1] However, the term “nanotechnology” was first defined by Norio Taniguchi in 1974 at the international conference on industrial production in Tokyo.^[2] Nanotechnology is shortened to Nanotech, which explains the study of manipulation of matter on an atomic and molecular scale.

In the early 1990s there were a number of important discoveries and inventions which gave an impetus to the further developments of nanotechnology as a field of science and technology. From 1980s most scientists had embarked on the synthesis of dispersible, stable nanoparticles of metals, sulfides and also binary oxides. However a real breakthrough came with the invention of Scanning Probe Microscope (SPM) which rendered an ability to probe and even manipulate atoms. After that Smalley and co-workers discovered C₆₀ fullerene (a spherical case of 60 carbon atoms football) during laser ablation of graphite and in 1986 Atomic Force Microscope (AFM) was discovered by Bining and his co-workers. The latter gave us the technological eyes to see nanomaterials and understand the corresponding assemblies. The discoveries of some fascinating properties of semiconductor quantum dots and a rolled version of single and multilayer graphitic carbon as represented by carbon nanotube gave an exciting new direction to the field of nanoscience and nanotechnology. The field has gone from strength to strength thereafter and vast research is still going on to reap the benefits of nanotechnology in the technological sector. There are still immense open opportunities to understand the behavior of these nanomaterials by understanding their physical and chemical properties.

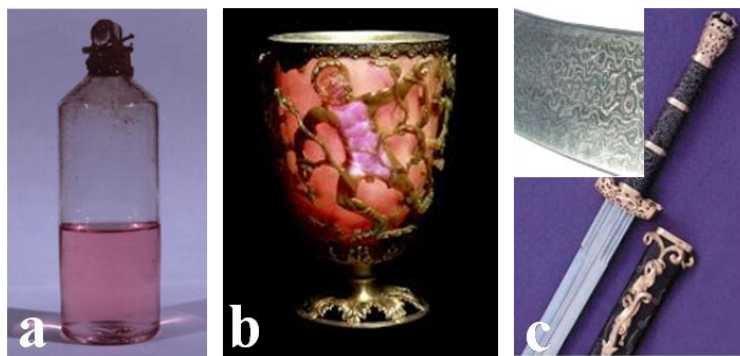


Figure 1.1: (A) Gold-colloids made by M. Faraday^[11b,c], (B) Lycurgus cup^[11a], (C) Damascus sword with inset showing the microscopy image revealing incorporated CNTs.^[11d,e]

In general nanomaterials are defined as materials with an average diameter less than 100 nm (1-100nm). The length of 1 nm = 10^{-9} m represents one billionth of one meter.^[3-10] Typically a single particle of smoke is of the order of 1000 nm and a human hair is of the order of 100,000 nanometers. The word ‘Nano’ for common people is just a very tiny little thing. Although the word nanotechnology was coined relatively recently, mankind has known and used the properties of such materials hundreds of years back without really knowing the origin of their fascinating properties. An attractive ancient bowl (Lycurgus bowl, created on 4th century AD) kept in the British museum, possesses some unusual optical properties.^[11a] It changes color with a change of the light source. The bowl is green in normal light and red in illuminated light. It is now realized that this unusual property of color change is due to colloidal gold particles present in the bowl. The famous chemist and physicist Michael Faraday had in fact prepared such gold nanoparticles 1957 to study their interactions with light and had named them as “divided states of the metals”.^[11b,c] Separately, a special kind of sword was made during the period of AD 900 to early AD 1800 called the ‘Damascus’ sword.^[11d, e] This sword was processed in a special way which led to incorporation of multiwall carbon nanotubes in the blade and hence it possessed remarkably high mechanical strength, flexibility, and acute sharpness. These are just a few outstanding examples of nanotechnology as shown in **Figure 1.1**. Even a range of traditional Indian medicines, such as for example gold bhasma, or kajal used for eyes had gold nanoparticles and fullerenes, respectively, as revealed by new research.

It is now known that if the size of a material is reduced to nanoscale level, the same material may behave very differently with totally new properties. We know the famous golden color of gold ornaments. However, nanoparticles of gold exhibit several size-dependent colors in the nanosize regime as shown in **Figure 1.2**. An overview of many materials with different dimensions ranging from macro to nano is shown in **Figure 1.3**. A question is thus raised as to why size should matter so much in the materials properties? Why nanomaterials are so different in their property features from their bulk counterparts? This is because in the nano-regime, classical physics is no longer applicable and quantum phenomena predominate due to confinement effects. Moreover, such materials also have a very high surface to volume ratio and as such the surface properties dominate in the overall properties.

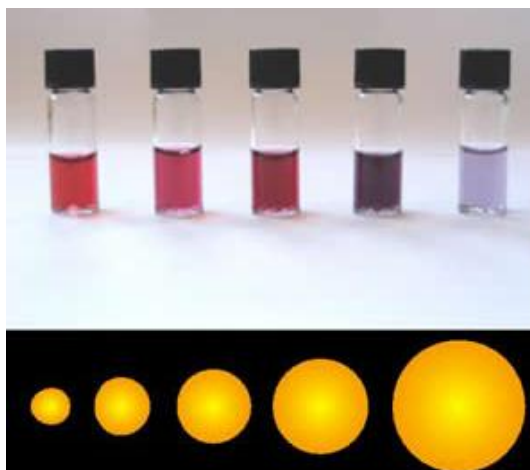


Figure 1.2: Gold colloidal solutions with different colors corresponding to different sizes of particles. (http://en.wikipedia.org/wiki/Colloidal_gold access on 9th July 2013)

1.2 Synthesis of nanomaterials

Controlled synthesis of nanomaterials is important for various applications because the properties of these materials depend on size, shape, morphology and also stoichiometry. There are mainly two broad approaches for the synthesis of nanomaterials i.e. top-down and bottom-up. Top down approach mainly involves physical processes such as lithography, cutting, etching, grinding etc. to break larger bulk materials into nanosized particles. ^[12] Ball milling is a typical example of top-down approach. The main advantage of this method is high scale production of

nanomaterials is possible. But the main disadvantage of the top-down approach is non-uniformity of shape, size and compositions.

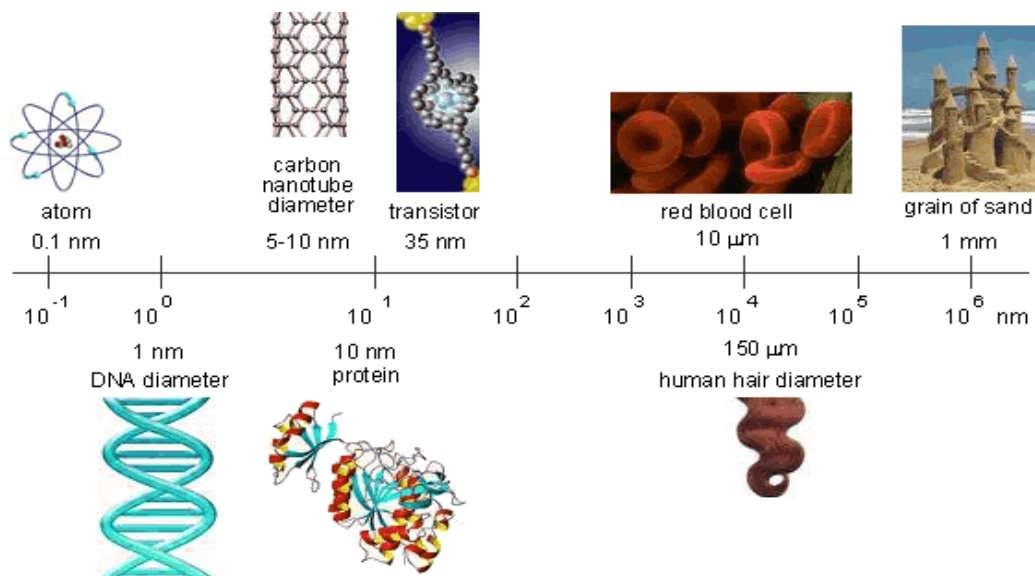


Figure 1.3: Materials on different length scales [<http://nanoscience.massey.ac.nz/> access on 9th July 2013]

Achievement of desired particle shape and size is difficult in this process. Hence, to overcome these disadvantages new approach of synthesis method was developed i.e. Bottom-up approach. In this method, nanomaterials are synthesized atom by atom, molecule by molecule or cluster approach. Chemical synthesis, laser assembly, self assembly and also colloidal aggregations are few examples of bottom up approaches.

Figures 1.4 and 1.5 show the schematics of Top-down and Bottom-up approaches of synthesis along with the corresponding examples. Overall in nanomaterial synthesis, not only small size matters but also uniformity of size, morphology and stoichiometry are important parameters defining the overall performance in practical applications. A detailed understanding of nanomaterial formation and synthesis mechanisms can help to engineer the nanoparticle growth. This can further help is attaining and controlling the desired properties in a reproducible manner for important application domains such as supercapacitor, battery, water splitting, catalysis etc.

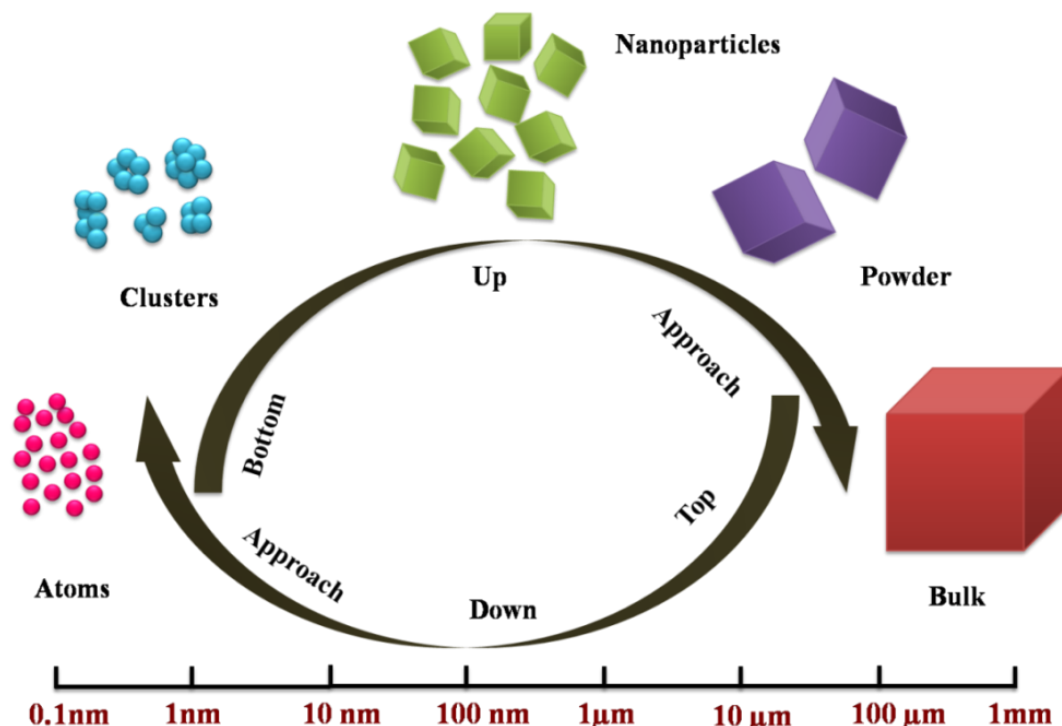


Figure 1.4: Schematic diagram representing Top-down and Bottom-up approaches for nanomaterial synthesis.

Bottom Up Approach	Top Down Approach
<ul style="list-style-type: none"> ▪ Chemical Synthesis (Nano crystals, Nanowires, etc.) ▪ Self Assembly (Ordered Nanostructures) ▪ Laser induced assembly ▪ Colloidal aggregation 	<ul style="list-style-type: none"> ▪ Lithographic techniques (UV, Electronic, ion beam) ▪ Laser beam process ▪ Film deposition and growing ▪ Mechanical techniques (grinding, milling, cutting, etching, polishing)

Figure 1.5: Examples of Top-down and Bottom-up approaches

1.3 Properties Change from Bulk to Nano

Nanomaterials are made up of clusters of atoms and molecules and not single atoms or molecules, hence they have an intermediate size between that of a single atom or molecule and the bulk material. In this typical size regime, nanomaterials show some exceptional properties which can be explained by quantum mechanics.

The size of nanomaterial being close to that of a single atom, quantum confinement effects play a major role in rendering some unusual properties to them. In case of nanomaterials, electrons can only attain discrete energy levels contributed by a few atoms whereas in bulk material, the energy bands are composed of closely packed energy levels emanating from several atoms or molecules. The band diagram evolution from single atom to nano to bulk is shown in **Figure 1.6**.

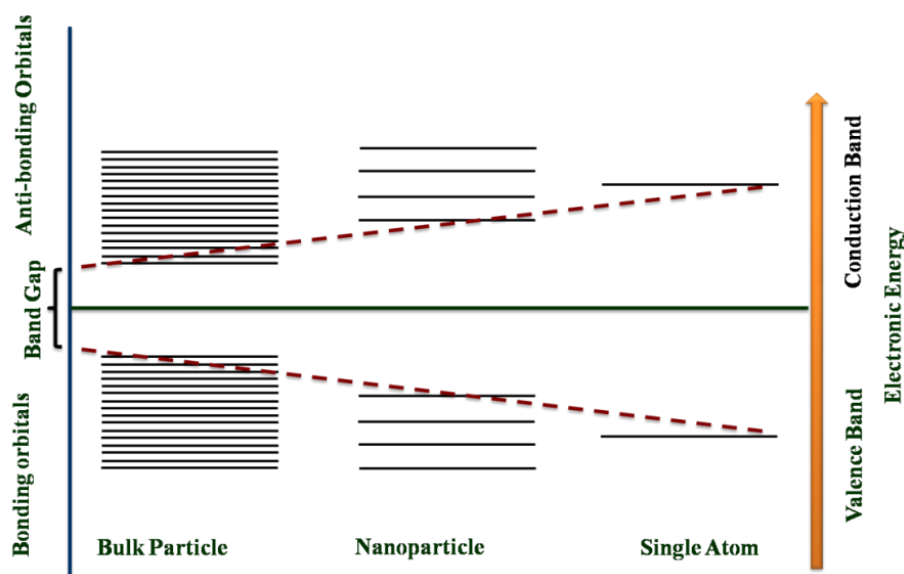


Figure 1.6: Electron energy states for a bulk particle, a nanoparticle and a single atom

1.3.1 Surface Properties

Other than quantum confinement, the second most important property of nanomaterials is that they have a very high surface to volume ratio. If a bulk material is divided into individual nano particles, total volume remains the same but the collective surface area increases dramatically, which is shown in **Figure 1.7** and **Table 1.1**. For surface chemistry, the chemical groups which are present at the interface of a material and its ambience are the decisive factors for the determination of the properties such as chemical reactivity, adhesion, gas storage, catalytic activity etc. In the case of nanomaterials, because of the exposure of large number of atoms, the surface is highly active and reactive than their bulk counterparts.

Consider a spherical particle of radius “r”,

$$\text{Surface area of the particle} = S = 4\pi r^2$$

$$\text{Volume of the particle} = V = (4/3) \pi r^3$$

So, the surface to volume ratio = $(S/V) = (3/r)$

From the above the surface to volume ratio is inversely proportional to 'r'.

Hence with decrease in the particle size the surface effects become more prominent.

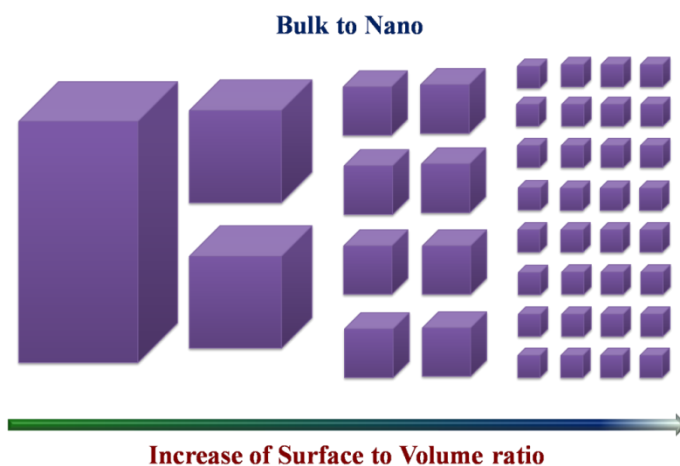


Figure 1.7: Bulk to nano showing high surface to volume ratio.

Size of cube side	Number of cubes	Collective surface area
1m	1	6 m ²
0.1m	1000	60 m ²
0.01m = 1cm	10 ⁶ = 1 million	600 m ²
0.001m = 1mm	10 ⁹ = 1 billion	6000 m ²
10 ⁻⁹ m = 1nm	10 ²⁷	6 × 10 ⁹ = 6000 km ²

Table 1.1: Increase in the surface area with decrease in size

Due to very high surface to volume ratio nanomaterials are generally unstable and adapt various methods to minimize their energy to attain a low energy state. Hence small nanoparticles have a tendency to form agglomeration producing larger particles in order to minimize their surface energies. The most common example of enhanced surface activity of nanoparticles is nano-catalyst. A very good example of nanocatalyst is gold. In the case of bulk form, gold is stable and hence used in jewellery, but when it comes to nanosize it is used as catalysts because of its high reactive nature. ^[13]

1.3.2 Optical properties

Like surface chemical properties, nanomaterial also shows very different optical properties than the bulk. The reason for this is the size modified absorption and scattering of light in nano regime. When an object interacts with light it absorbs, reflects and also possibly re-radiates certain wavelengths yielding a certain color. Apart from absorption, reflection and transmission, scattering also plays an important role. This phenomenon depends on the particle's properties, shape and size. Multiple scattering is also possible. Hence color in nanoparticle dispersion can be due to interference, scattering, surface plasmons, quantum fluorescence etc. The change in the color with the particle size of cadmium selenium Quantum Dots (QDs) is shown in **Figure 1.8**.

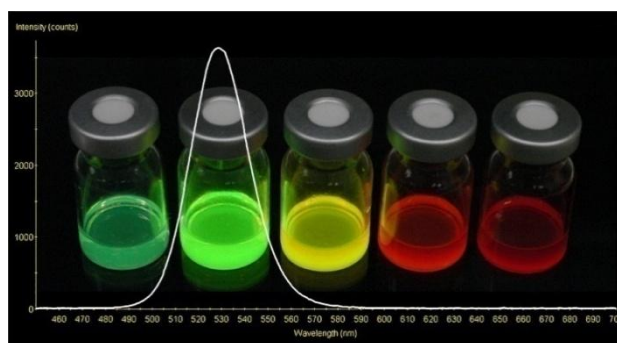


Figure 1.8: Cadmium selenium quantum dots of different sizes showing different colors. (<http://www.greenfudge.org/2010/03/11/nanotech-lighting-are-quantum-dots-the-future-of-lighting/> access on 9th July 2013)

Generally, metal nanoparticles show variable optical properties than their bulk counterparts.^[14a] These properties depend upon size, shape, composition and surroundings.^[14b,14c] This effect appears due to interaction of electromagnetic radiation with the electron cloud present on the surface of metal nanoparticles leading to surface plasmon excitation. Gold, silver and copper nanoparticles are known to exhibit exceptional optical properties in visible and in NIR region within certain size limit of particles.^[14a]

1.3.3 Electronic Properties

Some nanomaterials exhibit exceptional electrical properties as well. At extremely small dimensions the energy levels are quantized, the band overlaps present

in the bulk materials disappear and a band gap is enhanced or created. Hence a few metals can behave as semiconductors and semiconductors can behave as insulators when their size is decreased. At a given temperature size dependant properties vary significantly in semiconductors than in metals, insulators, Van-der-Waal's crystals or molecular crystals. In each case the density of the states is discrete at the band edges. As a function of increasing size, the center of a band develops first and the edges develop last. In the case of Van-der-Waals or molecular crystals, the nearest-neighbor interactions are weak and the bands in the solid are very narrow. As a consequence not much size variation in optical or electrical properties is expected or observed in the nanocrystal regime.

These changes in the properties arise because of the systematic transformations in the density of electronic energy levels as a function of the size of the interior which is known as quantum size effects. Nanocrystal lies in between the atomic and molecular limit of discrete density of electronic states and the extended crystalline limit of continuous bands. **Figure 1.9a** shows the band structure of metals in bulk form, nano form and as atoms and **Figure 1.9b** shows the density of states in semiconductor nanocrystals. In metals the band gap is zero (valence and conduction bands overlap) and Fermi level coincides with the top of the filled band. The energy level spacings being negligible, at temperatures above a few Kelvin the electrical and optical properties more closely resemble those of a continuum, even in relatively small sizes (tens or hundreds of atoms).^[15a] In semiconductors, however, the Fermi level lies between two bands, therefore the edges of the bands dominate the low-energy optical and electrical behavior. The band gap of semiconductors increases with decreasing size, because a) reduction in the band width in the nano-regime, b) decreased number of atoms, and weakening of nearest neighbor interactions. This is the major effect in the semiconductor nanocrystals that leads to significant changes in optical properties as a function of the size.^[15 b-d] As the size of metal nanocrystals is reduced, they can show insulating behaviour due to the changes in the electronic structure. This transition is called the size-induced metal–insulator transition.

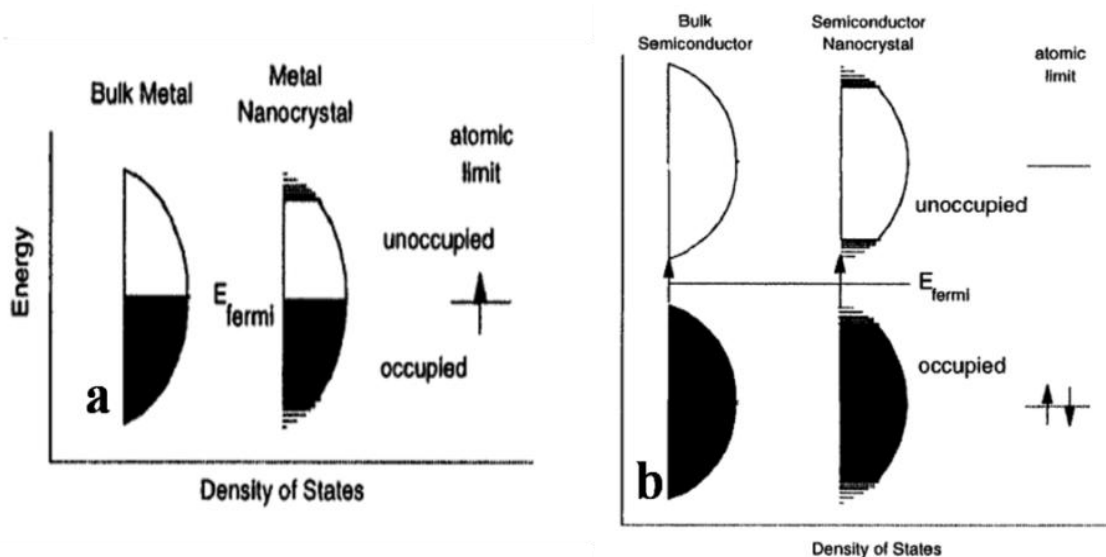


Figure 1.9: Density of states in (a) bulk metal, metal nanocrystals and atom and (b) semiconductor ^[15e]

1.3.4 Magnetic properties

Nanomaterials also show different magnetic properties than their corresponding bulk materials. ^[16a-c] When the size is reduced from bulk to nano, below a certain critical size, the magnetic particle can exist as a single magnetic domain with all the spins coupled in the same directions. Hence the particle behaves as a single magnetic dipole as shown in **Figure 1.10**. At extremely small size the magneto hysteresis vanishes and coercive field reduces. In this case, quantum tunneling of the magnetic moment becomes possible. If the particle size is smaller than the single magnetic domain, the thermal energy $k_B T$ is enough to overcome the anisotropy barrier kV . This results in the rotation of the magnetization spontaneously giving an average zero magnetization when no external field is applied. This phenomenon is called super paramagnetism. ^[16d] It occurs below a specific temperature called blocking temperature. This can be understood from the equation $kV = 25 k_B T_B$ where, V , k_B and T_B are the volume of a single particle, Boltzmann constant and blocking temperature, respectively. ^[16e]

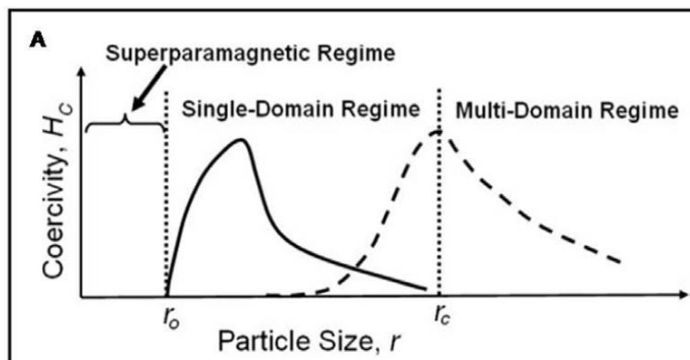


Figure 1.10: Change in the coercivity of a ferromagnetic particle with the diameter in the super paramagnetic, single-domain and multi-domain regions. ^[16f]

From this equation, it is clear that as the particle size decreases, the magnetic anisotropy energy KV (the energy difference involved in changing the magnetization direction from a low-energy direction or easy axis to a high energy direction or hard axis) also decreases. For a given particle, k , V and k_B would be constant and the thermal energy would be a function of the blocking temperature. Above the blocking temperature, the thermal energy is sufficient to flip the spins in the magnetic material; hence the material does not show any hysteresis loop. Consequently, for superparamagnetic materials, a hysteresis loop is obtained only below its blocking temperature. In case of super paramagnetic materials, a plot of magnetization (M) and the ratio of magnetic field and the temperature (H/T) produce an universal curve for all temperature above blocking temperature T_B . Super paramagnetism is also related to the relaxation rate and is therefore sensitive to the characteristic measurement time scale.

1.3.5 Mechanical Properties

Nanostructured materials sometimes show unusual mechanical properties such as extremely high strength. Even the temperatures at which phase transitions such as melting occurs also change. These properties show drastic changes at the nanoscale. For example, single wall and multiwall carbon nanotubes are extremely small in size but 100 times stronger than steel and also have lighter weight. These carbon nanotubes have honeycomb lattice structure of graphite. Generally in addition to the basic features of bonding the mechanical properties of a materials also depend on several parameters such as impurities, imperfections etc. The presence of defects or

imperfections decreases the strength of the materials. Hence because of small cross section and less numbers of imperfections nanomaterials such as nanorods, nanowires etc. show high mechanical strength.^[17] As imperfections are thermodynamically energy intensive, small size nanomaterials try to eliminate the imperfections to acquire higher mechanical strength.

Apart from strength, melting points of materials also decrease with decrease in the size. Generally, melting point can be defined as the temperature at which lattice vibrations tend to partly overcome fraction of the intermolecular force strength that holds them in a fixed position in a solid. In a material the atoms present at the surface are surrounded by less number of atoms whereas atoms present inside the bulk are surrounded by a large numbers of atoms. Since with decrease in size more atoms are present at the surface than in the bulk the change in the size to nano level decreases the melting point of the material.^[18]

1.4 Types of Nanomaterials

Nanomaterials can be classified in various ways. Based on dimensions they can be classified as zero dimension nanomaterials (0D), 1D nanomaterials (1D), 2D nanomaterials (2D) and three dimension nanomaterials (3D). In zero dimensional materials all the dimensions measure within the nanoscale. Examples 0D materials are quantum dots, spherical or faceted nanoparticles, atomic clusters etc. In one-dimensional nanomaterials only one of the dimensions is outside the nanoscale which includes examples such as nanorods, nanotubes, nanowires etc. Similarly two-dimensional materials exhibit plate-like morphology where two of the dimensions are not confined to the nanoscale. Nanofilms or nanosheets such as graphene etc are examples of 2D nanomaterials. Finally, the materials which are not confined to the nanoscale in any directions are known as 3D materials. Examples are graphite, diamonds, nano-assemblies etc. **Figure 1.11** represents the 0D to 3D materials with various examples.

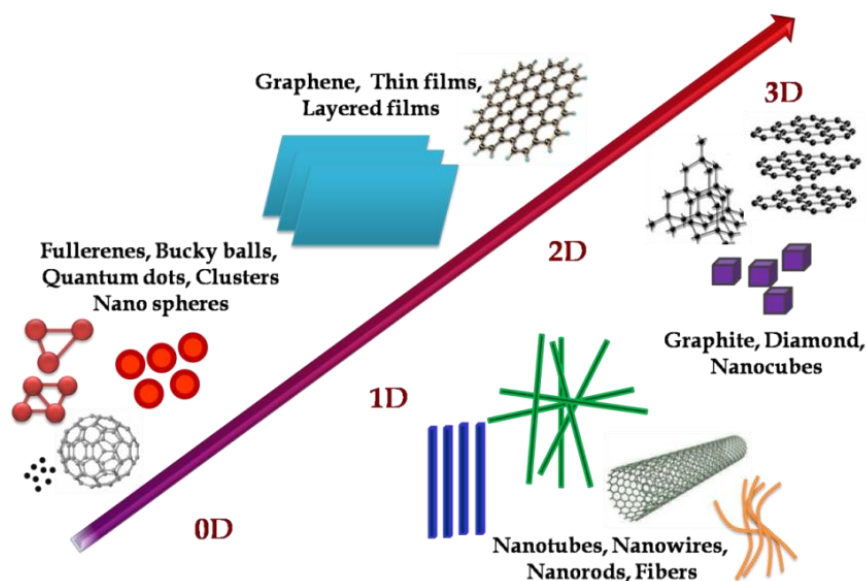


Figure 1.11: Various examples of 0D, 1D, 2D and 3D nanomaterials

Apart from this classification another important and current classification of nanomaterials is based on their properties: i) carbon based nanomaterials, ii) metal and metal oxides based nanomaterials, iii) dendrimers, and iv) nanocomposites. Among all these, the present thesis focuses on carbon materials, metal oxides and their nanocomposites.

1.4.1 Carbon based Nanomaterials

Carbon is the sixth most abundant chemical element in the universe. In 1772 Antoine Lavoisier showed that diamonds are a pure form of carbon. ^[19a] Prior to that in 1594 D.L.G. Harsten and A.G. Werner named the substance graphite that was used in pencil for writing. In 1779 Carl Wilhelm Scheele showed that graphite is also another pure form of carbon. ^[19b] A new form of carbon was discovered in 1985 by Harold Kroto (Sussex University), Robert Curl, Jr. (Rice University), and Richard Smalley (Rice University) which was called "buckminsterfullerene" because its molecular structure resembles the geodesic domes designed by architect Buckminster Fuller for the 1967 World's fair. ^[19c] These "Buckyballs" or fullerenes are being considered as attractive elements for the design of next-generation lubricants, drug delivery systems, industrial catalysts, and nanoscale machinery. ^[19d,e]

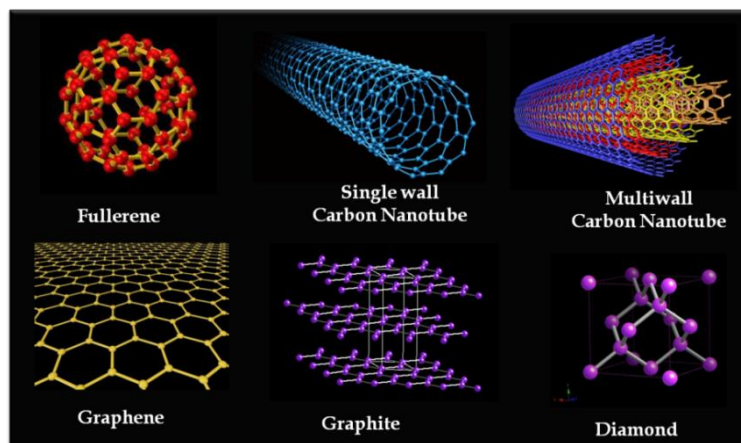


Figure 1.12: Various forms of carbon

Carbon is the building material for organic life and hence is the basic element of organic chemistry. Apart from this, carbon can exist in various allotropic forms such as diamond, graphite and also as amorphous carbon. These are the most common and important forms of carbon. These allotropic forms of carbon possess different physical and chemical properties and are known by their unique characteristics. ^[19, 20-23a-f] Diamond is highly transparent and is known to be the hardest material in the nature. The nanoforms of carbon include carbon nanotubes, graphene, porous carbon, nanodiamonds, carbon quantum dots, fullerenes, nanofibers etc. These are shown in **Figure 1.12.** ^[19c,23a-f] On the nanoscale dimensions, the properties of various carbon materials strongly depend on their form, constitution and atomic structure. For example, graphitic (3 dimensional) sp^2 carbon can be found in all reduced dimensions such as graphene in 2D, carbon nanotubes as 1D, quantum dots and fullerenes as 0D. All these materials have different chemical and physical properties based on their structural arrangements. Some important carbon nanomaterials, their properties and applications are discussed below.

1.4.2 Types of Carbon Nanomaterials

1.4.2.1 Carbon Nanotubes

Carbon nanotubes had been unknowingly used in Damascus sword many centuries back but their true form and importance was not realized until recently. In 1991 after the discovery of fullerenes Samio Iijima observed multi-walled carbon nanotubes formed in a carbon arc discharge. Two years later in 1993, single wall carbon nanotube formation was also observed by Iijima and Bethune. These

nanotubes have been used in a variety of applications because of their unique properties. Multiwalled carbon nanotubes have already been used in tennis racket which is much stronger than steel and is lightweight. These are also used in sunscreen, skin care products, UV protecting clothing etc. Carbon nanotubes can be broadly classified into single wall and multi-wall carbon nanotubes (SWNTs and MWNTs respectively). Carbon nanotube has very high aspect ratio (length to diameter ratio) than any other materials. Single-walled carbon nanotubes have a diameter of close to 1 nanometer, with a tube length that can be longer up to few centimeters. ^[24a]The structure of SWNT can be described by wrapping a single atom thick graphite or graphene into cylinder. Single wall carbon nanotube exhibits important electric properties which are not shown by multiwall carbon nanotubes. MWNTs are composed of multiple layers of graphite rolled to form cylindrical tubes with an interlayer spacing of 3.4Å. The outer diameter of MWNT may range from 1 to 50 nm while, the inner diameter is usually of few nanometers. Generally, two models are used to describe the structure of multi-wall carbon nanotube. One is the Russian Doll model which describes the sheets of graphite arranged in concentric cylinders and another is the Parchment model which describes the single sheet of graphite rolled in around itself, resembling a rolled up newspaper or scroll of parchment. ^[24b-d]

CNTs are generally synthesized by several techniques such as carbon arc discharge, chemical vapour deposition (CVD), laser ablation etc. These nanotubes can be metallic, conducting and also semiconducting. ^[24e]In carbon nanotubes, ballistic electronic transport occurs over its long length because of its one dimensional structure. This results in carrying high current with very negligible heating and it has also been reported that MWNTs can carry high current densities up to 10^9 to 10^{10} A/cm² without any change in their resistance for a long time. ^[24f] The electric conductivity of these carbon nanotubes can be highly affected by the presence of defects such as bending, twisting etc. The strength of the carbon nanotube is also affected by temperature. At low temperature these are brittle. The strong bonding between the carbon atoms provides a very high Young's modulus and tensile strength. The structural properties with strong bonds between the carbon atoms give nanotubes a very high Young's modulus and tensile strength.

Carbon nanotubes have been used for several applications because of their unique properties such as high electric conductivity, high thermal conductivity, high mechanical strength, actuation properties at low voltages and field emission properties.^[24g-i] The specific heat and thermal properties of CNTs are dominated by phonons because of the negligible electronic contribution due to low density of free charge carriers. Introduction of defects into carbon nanotubes can result in various structural changes with interesting property changes. Under certain circumstances, defects can be introduced in carbon nanotubes in a controlled manner to get a desired property. Because of these aspects, carbon nanotubes have been used in space elevator, faster computer chips, better solar cells, cancer treatments, better and thinner TVs, energy applications, flexible displays, bone healing, sensors and also in faster fly wheels etc.^[25a-g]

1.4.2.2 Graphene

Graphene is another allotrope of carbon which was discovered in 2004 and has gained much interest in several fields. The term graphene was first coined by Hanns Peter-Boehm in 1962 for describing single-layer carbon foils, a combination of prefix from word graphite and the suffix –ene.^[26a-b] Graphene is one atom thick sheet of carbon arranged in two-dimensions which was a surprise observation because of the fact that a perfect crystal cannot exist in two dimensional space.^[27a] The existence of graphene has been explained by the idea that it has intrinsic roughness. This rippling makes graphene as a nearly perfect two dimensional crystal in 3D space which is not forbidden.^[27b-c] Graphene is composed of hexagonal arrangements of sp^2 bonded carbon atoms which are densely packed in a Honeycomb lattice. It is the basic structural unit of many other forms of carbon such as fullerene, carbon nanotubes and also graphite because it can be wrapped into 0 D bucky balls, rolled into 1D carbon nanotubes and stacked to form 3D graphite.^[28] Graphene can be synthesized by chemical vapour deposition, mechanical exfoliation, chemical exfoliation, thermal decomposition of SiC, chemical synthesis etc. Because of 2D structure, properties of graphene differ from most 3D materials. It exhibits properties like mechanical stiffness, strength, elasticity, high electrical and thermal conductivity etc which are superior to many other materials.^[29a-c] Hence, graphene can replace any other material in several existing applications. From experiments it has been observed that some

properties of graphene are closer to their theoretical values such as electron mobility of $2.5 \times 10^5 \text{ cm}^2 \text{ V}^{-1} \text{ S}^{-1}$, Young's modulus of 1TPa, high thermal conductivity (above 3000 WmK^{-1}), optical absorption of exactly 2.3%, high surface area etc. Electron moving in graphene behaves like mass less Dirac Fermions, which results in very high electron mobility at room temperature.^[26b,30-32] The theoretical resistivity of graphene is expected to be $10^{-6} \Omega\text{-cm}$, which is less than silver.

Apart from electronic properties, graphene also is observed to possess some exceptional optical properties. Monolayer and bilayer graphenes are zero band gap semiconductor materials. They have optical absorption of 2.3% and hence can be used as transparent conducting coatings.^[33] Graphene has no intrinsic band gap but by applying external electric field the band gap can be tuned from 0-0.25eV. Because of all these superior properties, graphene has been widely used in transistors, spin devices, semiconductor memory devices, transparent electrodes, sensors, hydrogen storage, charge storage, drug delivery etc.^[34a-g]

1.4.2.3 Fullerenes

Fullerenes or Buckminsterfullerenes are another form of carbon which exists in the form of hollow spheres, ellipsoids, tubes or rings. This molecule was named for Richard Buckminster Fuller a noted architect who created the geodesic dome of the same form. These have a structure like graphite but do not have hexagonal layers. These contain pentagonal and heptagonal rings along with hexagons which prevent them from being planar. They are also called as bucky-balls or bucky tubes depending upon the shape. The smallest fullerene is C_{60} in which no pentagons share an edge. C_{60} is the most common fullerene which contains 12 pentagones and 20 hexagones.^[7] It was discovered by Harold Kroto (from the University of Sussex), James Heath, Sean O'Brien, Robert Curl and Richard Smalley (from Rice University). The structure of C_{60} is that of truncated icosahedrons, which resembles a football made up of hexagons and pentagons. According to rules for making icosahedra an infinite numbers of fullerenes can exists.

In fullerene, each carbon atom is sp^2 hybridized and bonded to three other carbon atoms. C_{60} molecule has two types of bond lengths i.e. the 6:6 ring bonds (between two hexagons) which are also termed as double bonds and are shorter than

the 6:5 bonds (between pentagons and hexagons). The average bond length in fullerene is 0.14 nm. Due to poor delocalization of electron in fullerene these behaves like an electron deficient alkene and react readily with electron rich species. Hence, C₆₀ is much reactive than expected. It is the only one structure in fullerene family which avoids having double bonds in pentagonal rings. The need to avoid double bonds in the pentagonal rings largely governs the stability of fullerene derivatives and hence also controls the overall chemistry of fullerenes.

Hence, the properties of fullerenes largely depend on their structures. Mostly fullerenes are considered to be stable molecules but not fully unreactive. Fullerenes take part in several chemical reactions due to the easy breakage of one of the double bonds.^[19d, 35a-b] They also serve as strong electron acceptors in the presence of strong inorganic donors. These are mainly used in medicines, superconductors, solar cells, cosmetics, organic magnets etc.

1.4.2.4 Carbon Nanofibers

Carbon nanofibers are cylindrical nanostructures with stacked graphene layers arranged into cone, cups or plates. Hughes and Chambers patented the synthesis of filamentous carbon in 1889, which was the first technical records regarding carbon nanofibers.^[36a,b] They used methanol/ hydrogen gaseous mixture and grew carbon filaments through gas pyrolysis and subsequent carbon deposition and filament growth. Later the structure was analyzed by electron microscope. Catalytic chemical vapour deposition (CCVD) and chemical vapour deposition techniques have also been used for the synthesis of carbon nanofibers.^[36c] In early 1950s Soviet scientists Radushkevich and Lukyanovich showed hollow graphitic carbon fiber of 50 nm diameter by electron microscope.^[36d] In recent decades electro-spinning has been widely used for the synthesis of carbon nanofibers. These are extensively used in electrode materials, field electron emission sources, platform for gene delivery, scanning probe microscopy tips etc.

1.4.2.5 Porous Carbons

Another form of carbon which has attracted considerable research interest is porous carbon. Porous carbon can be divided into two categories: Carbon foams with desired architecture of pores which are used as template for making ceramics and

activated carbon that can be defined as porous carbon with added active surface chemical groups. These are the groups of materials with highly developed internal surface area and porosity, and hence a large capacity for adsorbing chemicals from gases and liquids. In industries, these activated carbons have been widely used for several years for water purification and gas storage applications. Because of their porous nature these possess very high surface area (more than $2000 \text{ m}^2\text{g}^{-1}$) and have potential applications for gas storage and energy areas. Generally activated carbons are manufactured by the pyrolysis of carbonaceous materials of natural products such as peat, wood, coal, fruit stones, and shells and also from polymers such as polyacrylonitrile viscose rayon etc. [37a-g] These can be synthesized on a large scale and are commonly activated by external activating agents by chemical or physical activations to introduce pores into carbon matrix. Chemical activation includes activation by using KOH, ZnCl_2 , NaOH etc. and physical activation is usually done with steam, CO_2 etc. [37, 38]

Sometimes due to the presence of internal activating agents external activation is not necessary for the creation of pores. The internal activating agents help in the creation of appropriate pores during the pyrolysis process. Porous carbon materials have been widely used as electrode materials, water purification, gas storage, as catalyst support etc. Research is still going on to improve pore size distribution and structure to achieve maximum performance of the materials. Few images of porous carbon are shown in **Figure 1.13**.

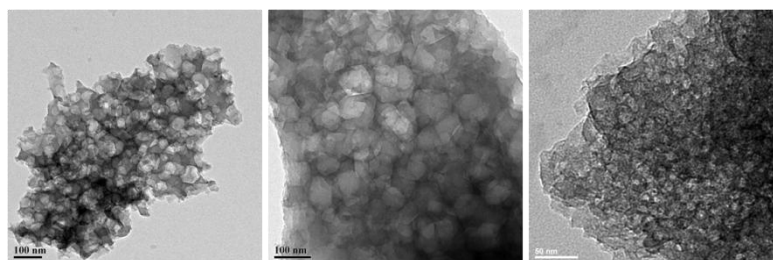


Figure 1.13: Images of porous carbon derived from various sources

1.4.2.6 Nanodiamonds

Nanodiamonds are generally referred to as the nanosized diamonds having dimension of less than 100 nm. A nanodiamond is made up of diamond core (size 1-10 nm) containing carbon atoms in the sp^3 hybrid state shielded by a carbon onion

cover containing carbon atoms in the sp^2 hybrid state. A hybrid layer occurs between the core and the cover that may contain carbon atoms in both sp^2 and sp^3 hybrid states. Among few methods for the synthesis of nanodiamonds detonation method is the most famous method. ^[39, 40] In this method, a mixture of trinitrotoluene (TNT) and hexogen are detonated to form nanodiamonds with a size of around 5 nm. Detonation nanodiamonds were first synthesized in 1962 by a group of Soviet scientists Yevgeny Zababakhin, including K. V. Volkov, Vyacheslav Danilenko and V. I. Elina. The detonation nanodiamond grains mostly have diamond cubic lattice and are structurally imperfect. ^[39, 40, 41] These have a round shape with an active surface area and diamond-like hardness. These properties make them useful for a number of applications. Nanodiamonds also have wear resistance and lubricating power like oil. These have already been used in some commercial products such as lapping, polishing etc. Nanodiamonds have also found use in some medical applications such as administering insulin which acts as a growth hormone into the body. ^[42]

1.4.3 Metal Oxide Based Nanomaterials

Metal oxides are the most interesting materials which exhibit a variety of structures and wide range of properties hence they have important role in various areas such as physics, chemistry and also in materials science. ^[43] Amongst the broad classes of metal oxides, transition metal oxides have attracted most of the research interest because of their high impact on the technology sector. Transition metal oxides are the compounds composed of transition metals and oxygen atoms. Transition metal oxides have fascinating properties such as semiconducting, magnetic, dielectric, piezoelectric as well as physical, chemical, thermal, optical, mechanical, electrochemical and catalytic properties. ^[44] They can exhibit metal semiconductor insulator transitions, superconductivity, colossal magnetic resistance (CMR), dielectric, piezo, pyro, ferroelectricity, magnetism such as ferromagnetism, paramagnetism, antiferromagnetism, and multiferroicity. Because of such wide range of properties, immense research is going on to manipulate their properties for a variety of applications. Metal oxides are expected to play a vital role in meeting the increasing demands of present and future technologies which other materials are not able to accomplish. Hence the research effort is towards the fabrication of engineered

nanomaterials to improve their properties in order to get enhanced or multiple functionalities than the existing technologies.

The usual properties of these metal oxides are due to the outer d electrons. A single transition metal can exhibit a variety of oxides such as monoxide, dioxide, trioxide etc. because of a variety of possible oxidation states.^[45] Hence these oxides can be metallic at one end and insulator at the other end. They have also interesting electronic as well as magnetic properties.

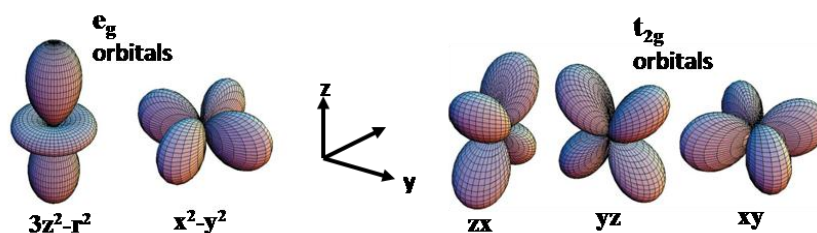


Figure 1.14: Five 'd' orbitals. In the cubic crystal field, this fivefold degeneracy is lifted to two e_g [$(3z^2-r^2)$, (x^2-y^2)] and three t_{2g} [zx , yz , xy] orbitals

Figure 1.14 shown above represents 5d orbitals which play an important role in various applications of transition metal oxides.^[46] For example, transition metal oxides have been used in memory devices, optoelectronics, catalysis, environmental, industrial and also in biomedical applications. They are mostly used as dielectrics, semiconductors and metals, and as materials for magnetic and optical uses.

In this work, we have synthesized several transition metal oxide nanoparticles such as Mn_3O_4 , Fe_2O_3 , Fe_3O_4 , TiO_2 etc. and studied their properties for applications such as catalysis, electrode material for Li ion battery, supercapacitors, environmental applications etc.

1.4.4 Carbon –transition metal oxide nanocomposites

Nanocomposites are materials that incorporate nanosize particles into a matrix of standard materials. The result of the addition of nanoparticles improves some of the properties such as mechanical strength, toughness, electrical or thermal conductivity etc. In carbon transition metal oxide nanocomposites carbon usually serves a matrix in which metal oxide nanoparticles are embedded. Nanocomposite materials have lot of research interest because of the advantage over bare carbon or bare metal oxides. In various types of nanocomposites carbon metal oxides nanocomposite is the most

popular research area because of the interesting properties of carbon materials. Incorporation of carbon in to the nanocomposite can enhance stability, mechanical strength, electrical and thermal conductivity etc. Generally, carbon materials such as graphene, carbon nanotubes, porous carbon etc. have been commonly used as matrix for metal oxides such as TiO_2 , ZnO , Fe_3O_4 , Mn_3O_4 , MnO_2 , SnO_2 , NiO etc. in the nanocomposite formations. Transition metal oxide carbon nanocomposites have gained research interest in the fields of energy storage, solar cells, H_2 generation, and catalysis. Various nanocomposites have already been employed in different technology sectors such as solid polymer electrolytes for batteries, thin films capacitor for computer chips, automotive engine parts, fuel cells, food packaging etc.

1.5 Applications of Nanomaterials

A basic and general overview of various carbon materials and their nanocomposites was presented in the previous sections. In the current research work carbon materials such as carbon nanotubes, porous carbons, carbon cloth; metal oxides such as Mn_3O_4 , Fe_3O_4 , TiO_2 ; and several nanocomposites of the two have been synthesized and tested. These materials have been studied for various applications such as supercapacitor, Li ion battery, catalysis, H_2 generation, photocatalysis and also for environmental application such as water purification. In the following sections we have mainly discussed the following applications: Supercapacitor, Li ion battery, catalysis, H_2 generation, photocatalysis and water purification.

1.5.1 Energy Storage

Electric energy is the dominant form of energy used in many developed and developing countries and hence the demand for the electric energy is increasing much faster.^[47] Since energy generation and usage requirements need not be concurrent the most logical approach is to store energy efficiently for later use when required. Growing interest in portable electronic devices and electric vehicles has increased the demand for clean and high performance energy storage devices. The groups of devices that can store energy are batteries, capacitors or supercapacitors.^[48] Supercapacitors store electrical energy directly in the form of electrical charges. These are highly efficient (high power density), but have low energy density.^[49] Batteries can store energy chemically and can release it reversibly according to the demand. Batteries have high energy density but with a limited cyclic capability.^[50]

Overall most existing technologies are not able to meet the current economic requirements. Hence enormous research is ongoing for low cost, safe, small size and light weight energy storage devices with high cyclability and durability to meet the energy sector demands.

Energy storage devices are characterized by their energy density (energy stored per unit volume) and power density (how fast that energy can be delivered from the device). Batteries have been always the preferred storage device for most of the applications because of their superior energy storage capability (high energy density). Despite high energy storage however, these have limitations of low power density and lack of stability and durability. Hence batteries do not fulfill the requirement of high power. Because of these limitations battery and conventional capacitor industries are not able to fulfill today's energy storage need. However supercapacitor with the capability of high energy density and power density can be used more efficiently to meet the energy demand, and hence has advantage over both capacitors and batteries. Novel designs of hybrid battery-supercapacitor systems are also being intensely researched.

1.5.1.1 Supercapacitor

Supercapacitor is the electrochemical capacitor that has high capacitance and high energy density as compared to a conventional capacitor and high power density as compared to a battery. In addition they also possess high stability and durability as compared to batteries.

Conventional capacitors consist of two conducting electrodes which are separated by an insulator or a dielectric material. When external voltage is applied to a capacitor opposite charges accumulate on the surface of each electrode. The dielectric present separates the charges and produces internal electric field that allows the capacitor to store charges. The schematic diagram of a conventional capacitor is shown in **Figure 1.15**.

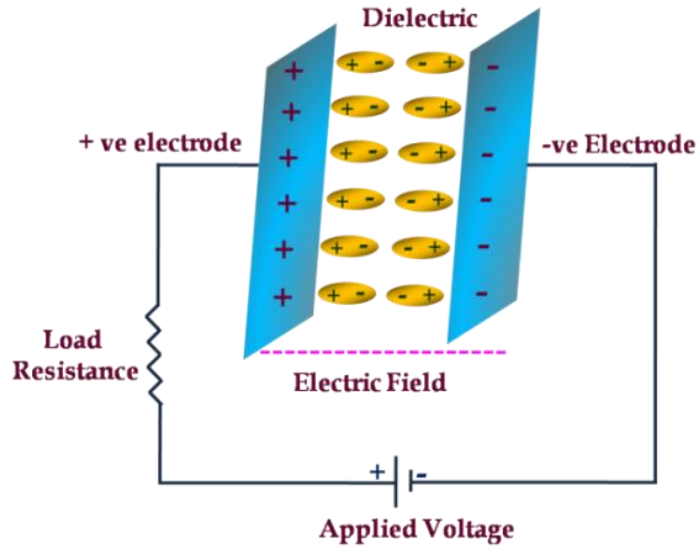


Figure 1.15: Schematic of a conventional Capacitor

Capacitance C_s for a capacitor can be represented by the formula.

$$C_s = Q/V \quad 1.1$$

Where Q is the charge stored and V is the applied voltage. For a conventional capacitor C_s is directly proportional to the surface area A of each electrode and inversely proportional to the distance D between the electrodes.

$$C_s = (\epsilon_0 \epsilon_r A)/D \quad 1.2$$

Where ϵ_0 and ϵ_r are constants and represent the dielectric constant (permittivity) of free space and of the insulating material between the electrodes, respectively.

Energy density (S_E) of a capacitor can be represented by the following equation,

$$S_E = C(\Delta V)^2/2 \quad 1.3$$

To determine the power density of a capacitor, it can be considered as a circuit in series with an external load resistance R as shown in **Figure 1.15**. The internal components of the capacitor such as electrode, dielectric material, and current collector also contribute to the internal resistance and hence can be represented by

equivalent series resistance (ESR). Hence the maximum power P_{\max} of a capacitor can be represented by the following equation below. ^[51]

$$P_{\max} = V^2 / 4 \times \text{ESR} \quad 1.4$$

Hence for max power ESR has to be minimized. Conventional capacitor has relatively high power density but also has low energy density when compared to batteries and fuel cells. As stated earlier, a battery has a high energy density but it delivers the energy slowly.

A supercapacitor basically works on a similar principle as a capacitor. However its design is characteristically different with very high surface area electrodes and with much thinner auto-formed dielectric layer that leads to nanometer scale distance between the electrodes. From the above equations it is clear that both increasing surface area and decreasing distance between the electrodes increases the capacitance dramatically. Hence a supercapacitor has a high specific capacitance, energy density as well as power density than conventional capacitors. **Figure 1.16** shows charging and discharging cycles of a supercapacitor. The advantages and disadvantages of supercapacitor have been listed below.

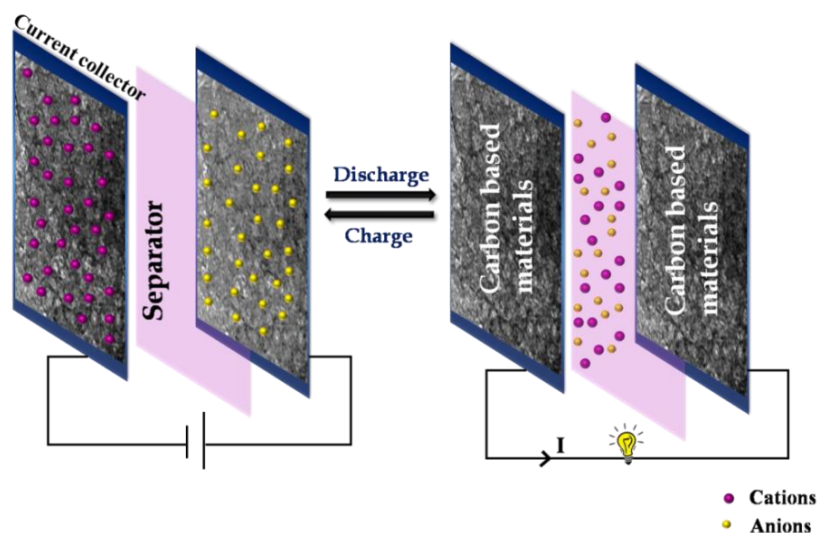


Figure 1.16: Charging and discharging state of supercapacitor

Advantages of supercapacitor

- ✓ Long life time
- ✓ High power density (Rapid charging and discharging)
- ✓ Absence of chemical reaction
- ✓ Recycle ability
- ✓ Cost-effective energy storage
- ✓ Extended operation temperature range
- ✓ Meets environmental standards
- ✓ Improved safety (Supercapacitors do not explode even if overcharged)
- ✓ Light weight

Disadvantages of supercapacitor

- ✓ Low energy density (Typically holds one-fifth to one-tenth)
- ✓ Low voltage (Serial connections are needed to obtain higher voltages)
- ✓ Linear discharge
- ✓ Higher self-discharge than that of an electrochemical battery

The performance of a supercapacitor and battery is represented by Ragone plot which represents the plot of energy density vs. power density.^[52] **Figure 1.17** shows the Ragone plot for battery, supercapacitors, conventional capacitors and fuel cells. From this figure it can be clearly seen that the supercapacitor has the performance between battery and conventional capacitors.^[53] Although it has high power density it has to still improve the energy density like high end batteries and fuel cells. Based on the current research trend supercapacitors can be classified into electric double layer capacitors (EDLC), pseudocapacitors and hybrid capacitors based upon the mechanism involved in the charge storage. In EDLC type capacitor there is no involvement of Faradic reactions (oxidation or reduction) and charge storage takes by surface adsorption with the formation of double layer formation.^[51,54]

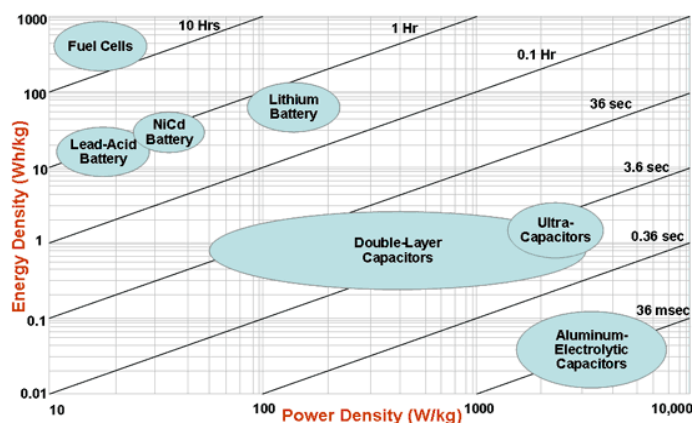


Figure 1.17: Ragone plot for energy storage devices

[<http://www.mpoweruk.com/performance.htm>]

In the case of pseudocapacitors the oxidation and reduction reactions take place at the interface and hence faradic charge storage phenomenon occurs via the transfer of charges between electrode and electrolytes. ^[55] A hybrid capacitor stores charges by the combination of both Faradic and non-Faradic type mechanisms. ^[56]

1.5.1.2 Electrochemical Double Layer Capacitors (EDLC)

These are the most commonly used and commercialized supercapacitors. EDLC type supercapacitor involves two similar carbon based electrodes, an electrolyte (aqueous/organic) and a separator (that provides electric insulation but allows transfer of ions). The mechanism of charge storage in EDLC type supercapacitor is shown in **Figure 1.18**. When an external voltage is applied through the electrodes the +ve and -ve charges separate and migrate towards opposite electrodes and the separator acts as a barrier for the recombination of ions. Hence charges are accumulated at the electrode / electrolyte interface and form a double layer. The double layer formation occurs between a conductive solid and liquid interface, and forms two charged layers with a separation of several angstroms only. Hence it stores the charges more efficiently. In EDLC type supercapacitors completely non-Faradic type charge storage occurs and there is no involvement of any oxidation and reduction reactions. As no transfer of charge is involved EDLC type capacitors they operate are highly reversibly and allow very high cyclic stability. Sometimes these show the stability up to 10^6 cycles whereas cyclic stability of battery is limited only to 10^3 cycles.

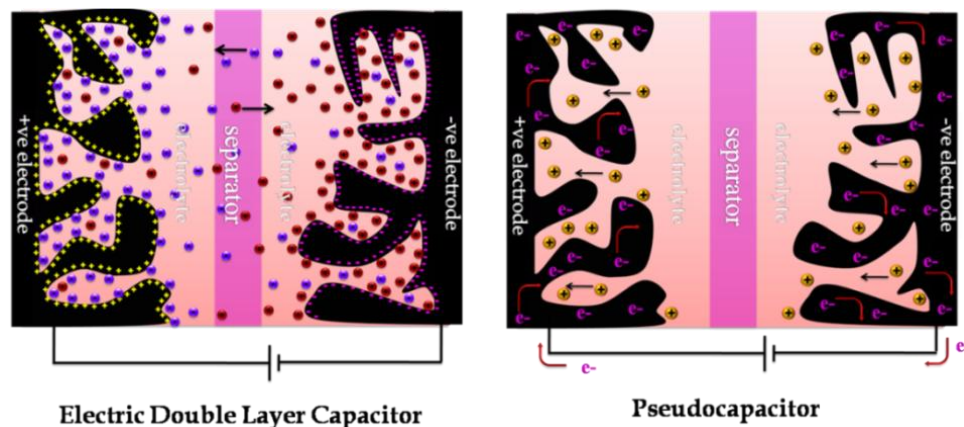


Figure 1.18: Mechanism of charge storage in electric double layer capacitor and pseudocapacitor

The performance of EDLC largely depends upon electrolyte and electrode materials. The electrolyte used in EDLC is either aqueous (H_2SO_4 , KOH , Na_2SO_4 etc.) or organic electrolytes (e.g. LiPF_6 in ethylene carbonate, diethyl carbonate and dimethyl carbonate). Aqueous electrolyte can operate only up to 1V because of the limitation of water splitting but it has low ESR value as compared to the organic electrolyte. On the other hand, organic electrolyte can be operated up to a much higher voltage (3-4 V). Hence increase in the potential window increases the energy density but simultaneously compromises the capacitance value because of high internal resistance in the case of organic electrolytes.

In the case of an aqueous electrolyte, as the size of the electrolyte ions is small it can easily penetrate deep inside through the porous network and can access maximum surface area which results in high capacitance. However in the case of organic (non-aqueous) electrolytes due to relatively larger ionic sizes of the electrolyte ions, they are unable to penetrate through smaller pores and hence cannot access all the surfaces, resulting lowering of capacitance. Hence the choice of electrolyte often depends upon the intended applications.

The nature of electrode materials also is a matter of concern in supercapacitor performance. Usually the electrode materials used in EDLC are high surface area carbon materials. Carbon materials are low cost materials and can be synthesized easily on a large scale, hence reduce the cost of overall fabrication. A variety of

carbon materials have been studied for EDLC type supercapacitors such as activated carbon, carbon aerogels, carbon nanotubes, graphene etc.

Among all the carbon based materials activated carbon is the most commonly used and commercialized carbon in EDLC. These are low cost materials with very high surface area ($> 2000 \text{ m}^2/\text{g}$) and are having porous structures including micropores ($< 2 \text{ nm}$), mesopores (2-50 nm) and macropores ($> 50 \text{ nm}$). These materials are synthesized from carbonaceous materials such as coal, peat, coconut shells, plant waste etc. ^[37a-e] The carbon derived from these materials are usually activated to introduce pores into the carbon surface by external activating agents. Carbon electrode materials usually have higher surface area, low cost, and well established fabrication techniques than other materials, such as conducting polymers and metal oxides. ^[51, 57] Although capacitance is directly proportional to surface area not all high surface area carbons give high capacitance. ^[57, 58a-b] The important factor for high capacitance is the comparative size of the electrolyte ions with the pore size of the electrode materials. If the electrolyte ions are too large in size then they cannot diffuse into smaller micropores and hence the entire electrode surface cannot be accessed by the electrolyte ions. Similarly if the pores are too big such as macropores then there is a loss of surface because of the larger pores. ^[58b, 59] Hence the pore size should be optimized according to the electrolyte ions. There should be a narrow distribution of pores with which maximum electrode surfaces can be accessible to electrolyte ions results in high capacitance. Hence immense research is currently ongoing to improve the pore structure and to control the pore size of the carbon materials to get the highest capacitance with high energy density and power density. Apart from activated carbon, carbon aerogels, carbon nanotubes, graphene have been widely used as electrode materials in supercapacitors. ^[58a-b,60]

1.5.1.3 Pseudocapacitors

In contrast with EDLC, pseudocapacitors store charge by Faradic reactions through the transfer of charges between the electrode and electrolyte. This basically involves oxidation reduction reactions electrosorption and intercalation processes. ^[55,51a,61] Because of charge transfer through Faradic reactions these can store a high amount of charge and hence high capacitance is achieved. ^[62a-b] Simultaneously due to

the lack of reversibility it has to compromise with the stability. The basic charge storage mechanism of pseudocapacitors has been shown in **Figure 1.18**. In this type of capacitors the electrode materials used are metal oxides and/or conducting polymers.

Because of their high conductivity some specific metal oxides have been used as electrode materials in pseudocapacitors.^[62a, 63] For instance, Ruthenium oxide has been widely used as electrode material. In aqueous medium the capacitance of Ruthenium oxide is too high than an EDLC type capacitor. RuO₂ also has low ESR and hence it has high energy density as well as power density. But the use of RuO₂ has been limited because of the high cost. Hence a major area of research has been focusing on the use of low cost metal oxides for supercapacitor. Transition metal oxides such as MnO₂, Co₃O₄, NiO, etc. have already been tested for the pseudocapacitor. Apart from metal oxides conductive polymers also have relatively high capacitance and conductivity with low ESR. Commonly n-type and p-type conductive polymers are used as the electrode materials and have high capacity with high energy and power density; but the lack of suitable n-type conducting polymers limits the use of conducting polymers in supercapacitors. Also the mechanical stress on the conducting polymers during Faradic reactions affects the stability of these materials.^[58a, 64] This lack of durability and stability limits the use of these materials in supercapacitor in the technology sectors.

1.5.1.4 Hybrid Supercapacitor

As discussed above there are some advantages and disadvantages of batteries and supercapacitors, in charge storage applications. The most crucial matter in these devices is the improvement in the energy density in case of EDLC type supercapacitor, and power density, durability in case of battery. There are three ways to overcome these limitations. One way is to change the electrode materials to a higher capacity material, second is to replace the electrolyte with an ionic liquid which can be operated at a higher potential, and the third and possibly most interesting is to use a hybrid type configuration. Many studies are now being performed on an effective hybrid type battery configuration. Hybrid systems combine both Faradic and non-Faradic processes to store charge. These have superior energy

and power density than either case without compromising the cycling stability and affordability. Generally Hybrid capacitor can be broadly classified on the basis of electrode configuration such as a composite, asymmetric and battery type.

1.5.1.5 Composite Type

In these types of hybrid systems composite materials of carbon with metal oxides or conducting polymers are used as electrode materials. Because of carbon materials double layer charge storage phenomenon occurs along with the Faradic type charge storage attributed to metal oxides or conducting polymers. Carbon materials provide a high surface area, stability as well as double layer charge storage whereas metal oxides and conducting polymers increase the capacitance by the Faradic reactions. ^[64, 65] To get better performance the amount of carbon and that of the pseudo-capacitive material in the composite have to be optimized. Hence use of composite materials in supercapacitors can overcome the individual limitations of bare materials.

1.5.1.6 Asymmetric

Asymmetric supercapacitor combines Faradic and non-Faradic processes by combining EDLC type electrode with pseudocapacitor type. Among the two carbon electrodes in the EDLC type one is replaced by pseudocapacitor type material such as a metal oxide or a conducting polymer ^[66]. These are of great current interest because of their projected high performance. The problem of stability, irreversibility and durability can also be improved by using asymmetric electrode configurations. Also the limitation of suitable n-type conducting polymer can be overcome by replacing this with activated carbon. This asymmetric configuration of conducting polymer (Faradic) and activated carbon (non-faradic) can achieve high capacitance as well as high stability because of the use of activated carbon. ^[66]

1.5.1.7 Battery Type

Similar to the asymmetric-type configuration, the battery-type hybrid capacitor couples one supercapacitor electrode with a battery electrode. This configuration combines high energy of a battery and high power of a supercapacitor to make an efficient device. Generally in a battery-supercapacitor hybrid type one

electrode is activated carbon and another one is composed of materials such as $\text{Li}_4\text{Ti}_5\text{O}_{12}$ (LTO) with electrolyte 1 M LiPF_6 (EC/DMC). Li^+ intercalates into the carbon electrode during charging of the cell. ^[67] This approach can overcome the energy density limitation of supercapacitors and also improves the stability. Recently a group of researcher developed a novel hybrid system that has achieved high energy density, high stability and high safety. ^[68] A new lithium-ion based hybrid capacitor which uses lithium titanate ($\text{Li}_4\text{Ti}_5\text{O}_{12}$) or LTO as negative intercalation electrode that can operate at unusually high current densities has also been developed. This $\text{Li}_4\text{Ti}_5\text{O}_{12}$ negative electrode, which performs at a high rate has a unique nanostructure consisting of unusually small nanocrystalline $\text{Li}_4\text{Ti}_5\text{O}_{12}$, nucleated and grafted onto carbon nanofiber anchors (nc- $\text{Li}_4\text{Ti}_5\text{O}_{12}$ /CNF). This type is most popularly called as “nanohybrid capacitors”. It has been proved that $\text{Li}_4\text{Ti}_5\text{O}_{12}$ is a stable and safe electrode material which operates at a potential of 1.55V (vs Li/Li^+) which is outside the potential range that electrolyte decomposes. ^[68] There are certain advantages associated with the use of LTO which are a) high coulombic efficiency ~100% during charge and discharge, b) safe charge and discharge at a constant potential of 1.55 V vs Li/Li^+ , c) high theoretical capacitance (172 mAhg^{-1}) that is 4 times higher than activated carbon, d) inexpensive raw material. Hence such a nanohybrid supercapacitor renders a much superior performance than the other cases.

Hybrid supercapacitor systems represent a potentially strong approach to meet the goal of an effective increase in the energy density, stability and durability. This type of capacitors can be used for both high energy and high power applications. Hence these can be considered as the future energy storage devices for many potential technologies.

From the above discussion it is clear that carbon materials are the most common electrode materials for supercapacitor. The main challenge in the use of carbon materials is to obtain high surface area with optimum porosity and high conductivity. All three properties are important parameters for the supercapacitor application. Generally carbon materials are synthesized by chemical synthesis, by pyrolysis of natural waste, polymers, chemical vapour deposition (CVD) etc. Among all these techniques pyrolysis of natural waste is the most efficient, cost effective and large scale technique. The carbon synthesized by pyrolysis needs activation by

activating agents such as KOH, NaOH, CaCl₂ etc to introduce pores to achieve high surface area. In our work we have synthesized high surface area functional carbon from natural waste materials such as dead Neem leaves by pyrolyzing in inert atmosphere without any external activation. This carbon derived from Neem (*Azadirachta indica*) dead leaves showed high specific capacitance in EDLC and hybrid type supercapacitors. To verify the generic nature of dead leaves another type of dead leaves such as Ashoka (*Saraca asoca*) was also examined. It was observed that the constituents of dead leaves affect the supercapacitor performance of the carbon formed.

1.5.1.8 Battery

Battery is another most common energy storage device. It most commonly called as electrochemical cell. In battery electrical energy is generated by the conversion of chemical energy by redox reactions at anode and cathode. Reactions at anode usually take place at lower electrode potential than that of cathode and these termed as -ve and +ve electrode, respectively. As compared to a supercapacitor the battery currently holds a higher position in the technology sector. Batteries are devices that store chemical energy and can convert this on demand to electrical energy to power several applications. Batteries are generally 3 types: primary battery which can be discharged once and then discarded, secondary battery or rechargeable battery that can be charged several cycles and can be reused, and the third specially designed type used for military and medical purposes.^[48] These have high energy storage capacity than supercapacitor but deliver power slowly (low power density). Battery can operate over a wide range of temperatures and at high voltage. The overall applicability and performance of battery for commercialization depends upon several factors such as cost, performances, reliability etc.

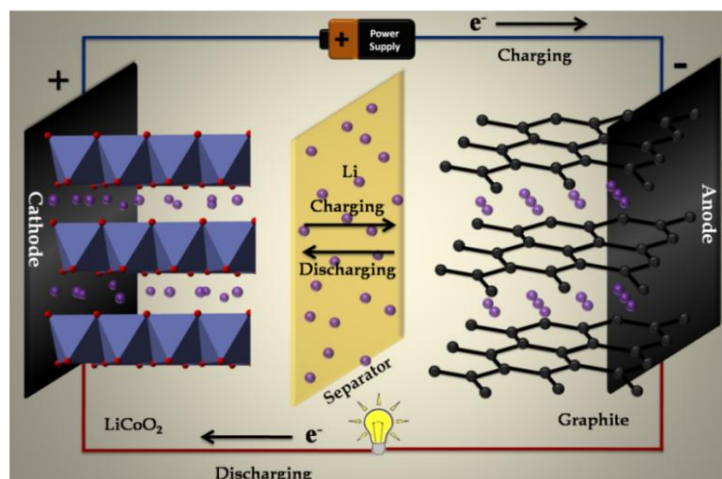
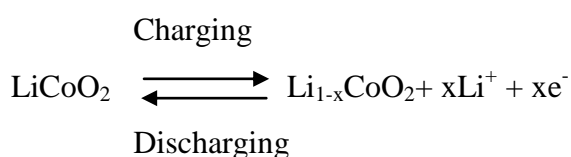


Figure 1.19: Charging and discharging cycles of a lithium ion battery

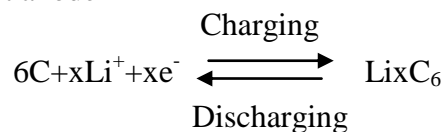
Among all the battery types, rechargeable batteries are the most popular and commonly used batteries. There are many rechargeable batteries such as lead acid battery, nickel cadmium battery and Li ion battery. ^[69] Among all these types, Li ion battery with high energy density and lighter weight has replaced most of the other batteries. Since in this work we have studied Li ion battery aspects, the focus of the ongoing discussion is on Li ion battery. ^[70] Several materials have been tested as anodes and cathodes in Li ion batteries. ^[71] The most common Li ion cell consists of a carbon anode and lithium cobalt oxide (LiCoO₂) as cathode along with an electrolyte lithium hexafluoro phosphate (LiPF₆) salt with Ethylene carbonate organic solvent mixture. ^[70,71]

The mechanism of Li ion cell is shown in **Figure 1.19** which involves insertion type mechanism. Li ions are inserted and reinserted in the respective charge and discharge cycles. In charging, the Li⁺ ions are derived from the cathode and inserted in between the layers of graphite and form LiC₆ and. In the discharge cycle they are drawn out from the anode (commonly graphite) and go back to the cathode. The reactions involved in charging and discharging cycles are as follows:

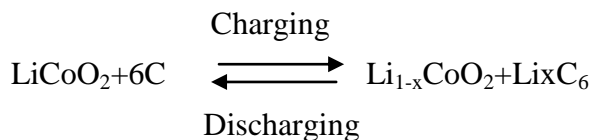
At cathode



At anode



Net reaction



The performance of Li ion battery largely depends upon the anode and cathode materials. Generally the cathode materials are Li containing materials which must be capable of providing Li. Suitable candidate for cathode materials are LiCoO₂ (Lithium Cobaltate), LiNiO₂ (Lithium Nickelate) and LiMn₂O₄ (Lithium Manganate). Among all these materials LiCoO₂ is the most commonly used cathode material because of its reversibility, discharge capacity and charge-discharge efficiency. For anodes the material should have high Li storage capacity.^[70,71] Mostly carbon materials have been used extensively as anodes in Li ion battery. Three types of carbon materials have been widely studied as anode materials such as graphite, graphitizable carbon (soft carbon), and non-graphitizable carbon (hard carbon).^[72] Anode and cathode materials are the main focus of research in Li ion battery to achieve a high performance. Li ion battery has many advantages over other types of batteries such as high energy density, low self discharge, low maintenance, ability to operate over a wide range of temperatures and at high voltage such as 3.6-3.8 V. The high energy density of Li ion batteries makes them useful for several applications. Along with these advantages there are some disadvantages of batteries which limit their use such as high cost, ageing, protection requirements etc. Despite some such limitations there has always been a high demand for rechargeable Li ion batteries after Sony released the rechargeable battery in 1991 for the first time. In addition to a high energy density, this battery offered excellent low-temperature characteristics, load characteristics and cycle stability. As a result, it became an essential source of power for audio and video equipment, personal computers, portable telephones, and other portable equipment very quickly. Thereafter Sony has been putting in significant efforts for the next generation batteries with improved performance. Light-weight and

more compactness have now become necessary criteria for portable electronics. In these circumstances the Li ion batteries which charge them play quite a key role. Hence along with light-weight and compactness the performance has to be improved to match the increasing technology demands.

Various metal oxides are known to be very promising electrode materials for Li ion battery. Mainly three types of materials are used as electrode materials for Li ion battery which are insertion type, conversion type and alloying type. Graphite, Nb_2O_5 , $\text{Li}_4\text{Ti}_5\text{O}_{12}$ etc are known as insertion type materials whereas Fe_2O_3 , CoO , Co_3O_4 , NiO , Fe_3O_4 etc are used as conversion electrode materials.^[73] Alloying materials includes materials such as Si, Ge and Sn etc which generally form an alloy during interaction with Li.^[74] Insertion type of materials have higher operating potential with low discharge capacity whereas alloying type electrode materials have problems of agglomeration growth of passivation layers which restrict the full utilization of reversible insertion/de-insertion process. Hence among all these types of electrode materials, conversion type electrode materials possess high capacity and operate up to high potentials. But in conversion type of electrodes cyclability is a major issue. Among different types of electrode materials Fe_2O_3 and Fe_3O_4 materials are known to possess high capacity in Li ion battery. However degradation of capacity is often observed in these types of materials because of conversion type reactions.^[73] In this work have synthesized Fe_3O_4 particles by novel synthesis methods and studied their electrode properties as anode materials in Li ion battery. This material shows a high capacity of 1000 mAhg^{-1} with very high cyclic stability. The mechanism of formation of Fe_3O_4 particles and the behavior of this material as an electrode material in battery has been studied in details.

1.5.2 Water Splitting

Water splitting is a common term for a chemical reaction in which water is split into oxygen and hydrogen. For a viable and sustainable hydrogen economy, efficient and economical water splitting is the key factor. Hydrogen is a potential fuel for motive power and portable electronics.^[75] Free hydrogen does not occur naturally in quantity and hence has to be generated by various processes such as steam reformation of hydrocarbons, water electrolysis, biomass, natural gas, or (after gasification) coal etc.^[76] Coal gasification can produce large amount of hydrogen and

electricity, however the energy required for the necessary sequestration increases the rate at which coal reserves are depleted. Similarly although biomass is a sustainable energy resource, it cannot supply the required amount of hydrogen. With all these drawbacks of the above mentioned methods we cannot just use whatever resources are available to us for the H_2 generation. The production of hydrogen in efficient ways employing low cost methods is absolutely necessary to fulfill the energy demands. [77]

Among all the methods electrolysis of water is the most important method whereby water can be split into hydrogen and oxygen by applying direct electricity. [78] As compared to other methods such as fossil fuels and biomass production, in the water electrolysis process hydrogen generated is 99.999% pure which is the main advantage of this method. From the technological point of view at present an advanced alkaline electrolyzer produces significant amount of H_2 but to meet the energy demand the production rate has to be significantly higher than the current rate. Hence further research is necessary to look for a high rate, low cost H_2 generation process.

In water electrolysis process, a direct current is circulated through the water to split the water molecule into hydrogen and oxygen. The current flows between the two electrodes which are immersed in the electrolyte to raise the ionic conductivity. The electrolysis process always requires a separator to avoid the recombination of hydrogen and oxygen generated at the electrode. The separator should have high ionic conductivity, high physical and chemical stability. The schematic diagram of water electrolysis process is shown in **Figure 1.20**.

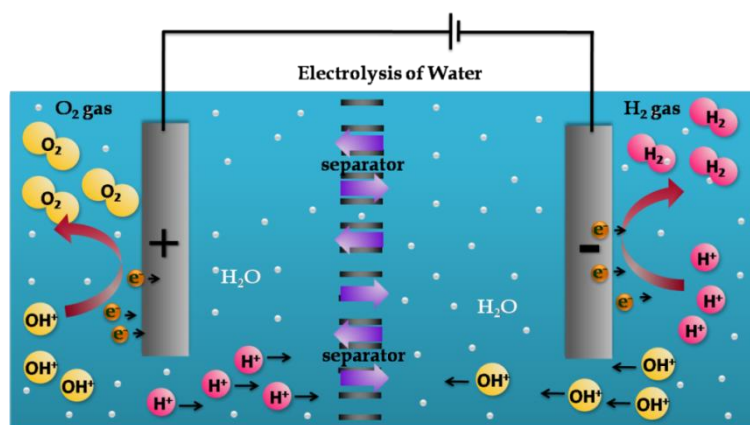
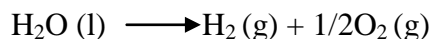
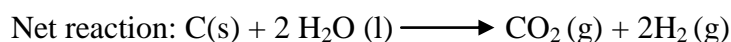
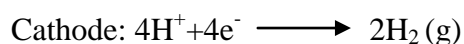
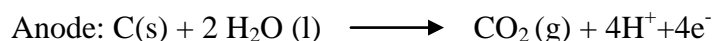


Figure 1.20: Schematic Diagram of water electrolysis process with two electrodes

The reaction for the electrolysis of water can be written as



In this process the electrons are taken or released by the ions at the electrodes surface. The reduction half-cell reaction takes place at the cathode and the oxidation reaction takes place at the anode. In this process the electric energy and thermal energy are converted into chemical energy and stored in hydrogen and oxygen. For an ideal electrolysis process the voltage required is 1.23V, but in a real electrolysis process voltage is higher, ~1.48 V, because of the thermodynamic irreversibility. To carry out the electrolysis process in a much more efficient and cost effective way researchers have used carbon as a part of the energy source. Coughlin and Farooque in 1979 reported hydrogen generation based on the use of sacrificial coal slurry as a carbon source in an electrolysis cell.^[79] The main key point in this process is that the electrical energy demand for hydrogen generation is minimized because part of the energy is supplied by the carbon oxidation at the anode as it gets consumed in the electrolysis process. According to Farooque and Coughlin the possible reaction at the anode and cathode are as follows



From the above reaction ΔG is calculated to be $9.6 \text{ kcal mol}^{-1}$ of H_2O . This lower value of free energy reduces the required voltage for the electrolysis. The calculated voltage from this reaction is as low as 0.21V which is a factor of 6 lower than the case of an ordinary electrolysis process. This greatly reduces the electrical energy requirement due to the consumption of carbon during the electrolysis process which supplies additional electrons during the process. The rate of production of hydrogen depends upon several factors such as surface area of the carbon used, catalysts types, temperature, electrolyte types etc. During the past few years the effect of these parameters on the hydrogen production rate has been studied in details.^[80]

In this context, we have synthesized specially processed carbon materials to act as electrodes for water electrolysis. These have not only exhibited superior

performance than the existing materials but have brought out some interesting new science. For the electrolysis of water we have used conducting a carbon cloth which was synthesized by controlled pyrolysis of a cotton cloth. This electrode was used as an anode material in the electrolysis process offering interesting advantages over using coal slurry for H₂ generation. The high surface area and porous nature of carbon cloth generate hydrogen much more efficiently at low voltage in an alkali medium. The efficiency of H₂ generation was observed to be much superior in the case of carbon cloth than other anode types such as stainless steel and Pt electrodes. The mechanism of H₂ generation in the case of carbon cloth was studied in detail. Interestingly we also found that controlled electrolysis at higher voltages yields carbon quantum dots by this novel process.

1.5.3 Catalysis

As discussed in the above sections, nanomaterials materials have proved their importance in several fields. Catalysis is another important area wherein nanomaterials have been used extensively and successfully. In past several years immense research has been conducted for the use of nanomaterials as catalysts and catalyst supports.^[81] The extremely small size of a nanoparticle enhances the surface area and hence exposes more active sites for the reactants to adsorb, which enhances the rates of reactions. The advances in nanotechnology allow the ability to design, synthesize and tune nanomaterial properties for certain applications. Interestingly, the exposure of certain planes leads to high selectivity in case of nanocatalyst which is difficult to realize in their bulk counterparts.

In catalysis, three different major directions have been developed which include homogeneous catalysis, heterogeneous catalysis and enzymatic catalysis. In homogeneous catalysis, high activity and high selectivity have been generally observed but suffer from a major drawback of separation and recyclability. This can be overcome using heterogeneous catalysts sometimes compromising on activity. Nanocatalysts act like a bridge between homogeneous and heterogeneous catalysts offering unique solutions to challenging problems. Nanocatalysts show not only high activity and selectivity but are easy to recover through suitable material engineering. Nanomaterials such as metal oxides, metals, carbon materials and their composites have already been studied in great details as nanocatalysts. The properties of these

catalysts can be tuned by varying different morphologies, sizes, facets etc. for achieving the specific objectives. Metal oxides such as MnO_2 , Mn_3O_4 , TiO_2 , CuO , Cu_2O , Fe_2O_3 , Fe_3O_4 , zeolites and metals such as Fe, Cu, Co, noble metals etc. have been widely used as nanocatalysts in various applications.^[82] The surface areas of metal oxides can be further enhanced by embedd in high surface area matrix such as

Carbon nanotubes, porous carbon, graphene, and carbon nanofibers provide high surface area and high mechanical strength to the catalysts.^[83] Some of the conducting support also tunes the electronic properties of the catalysts. Because of nanocomposite formation sometimes due to the exposure of certain planes of catalysts the selectivity to a particular product can be enhanced. Hence both geometric as well as electronic effect plays important roles in the case of nanocomposite catalysts.

Several industrial applications of these nanomaterials as catalyst includes fuel cells, exhaust catalysts, photo-catalysts, enantioselective catalysts etc. Vast research is being conducted to improve the performance of these catalysts to get better output. Hence the main objective of nanocatalysis research is to improve activity and selectivity, realize low energy consumption, and achieve a long life time of the catalysts. This goal can be achieved by controlling the size, shape, thermal and chemical stability of the individual nanoscale components of a nanocatalyst.

In our work we have synthesized various nanocomposites of Mn_3O_4 and multiwall carbon nanotubes (MWNT) and tested their properties for catalytic oxidation of p-cresol and also as an electrode material for supercapacitor and battery applications. These nanocomposites with different ratios of Mn_3O_4 and MWNT have shown very promising results. Mn_3O_4 is a versatile oxide having wide range applications in ion exchange, magnetic storage media, electrode material, solar energy transformation, molecular adsorption, oxygen reduction reaction etc.^[84] Mn_3O_4 nanoparticles have been well reported for catalyzing s oxidation of methane and carbon monoxide and the selective reduction of nitrobenzene. They have also been extensively used as electrode materials in Li ion battery and supercapacitors.

1.6 Objectives and outline of Thesis

We have discussed the history of nanomaterials and its impact on modern research. Various applications of these nanomaterials have been discussed at length in

this chapter. From these discussions it is clear that intense research is still needed to further improve the properties of various carbon materials, metal oxides and their nanocomposites to fulfill the desired property requirements. The objective of the thesis has been to synthesize carbon based materials, transition metal oxides and their nanocomposites by employing novel routes for energy and environmental applications such as Li-ion battery, supercapacitors, H₂ generation and catalysis. The detailed synthesis mechanisms and the structure-constitution-morphology-property relationships have been examined and pursued in more details.

Keeping these objectives in mind, outline of my thesis includes the following chapters.

The important concepts in nanoscience with brief history and a literature survey of the properties and applications of nanomaterials have been discussed in **Chapter 1**.

In the **Chapter 2**, a brief overview of the techniques used for the synthesis of functional carbon, various transition metal oxides and their nanocomposites functionalized is presented. Furthermore, a general outline of the instruments and methods used for the characterization of these nanomaterials is also presented.

The **Chapter 3** discusses the synthesis of functional carbon from pyrolysis of natural waste such as plant dead leaves which is used as electrode material in both Electric double layer supercapacitor and battery type hybrid supercapacitor. It is shown that this functional carbon shows high performance in supercapacitor applications.

In the **Chapter 4** functional carbon cloth is synthesized from the pyrolysis of cellulose fabric which is used as electrode material in alkaline electrolysis process. The use of the carbon cloth as electrode (anode) leads to substantial hydrogen generation at sub-threshold potential (< 1.23V) and carbon quantum dots formation at super-threshold potential (> 1.23V). The detail mechanism of the hydrogen generation and quantum dots formation is discussed in this chapter.

The **Chapter 5** discusses the pulsed laser synthesis of mesoscopic Fe₃O₄ spheres from bulk Fe₂O₃ powder. The high energy laser pulses ($h\nu = 5\text{ eV}$) created an extremely

high local temperature of $\sim 12000^{\circ}\text{C}$ by transient laser heating of particles which allowed the particles to melt and evaporate forming a micro-bubble reaction zone. Dissipation of the energy occurred by micro-bubble collapsed through new bond formation and phase evolution. The presence of ammonia helped in the reduction of $\alpha\text{-Fe}_2\text{O}_3$ to Fe_3O_4 . The synthesized Fe_3O_4 is used as anode material in Li ion battery which shows high capacity with high rate performance and stability.

In the **Chapter 6**, nanocomposites Mn_3O_4 and multiwall carbon nanotube (MWNT) are synthesized by co-precipitation route, by varying the MWNT percentage which shows excellent activity for liquid phase oxidation of *p*-cresol. The detail mechanism of such high selectivity, the geometric and electronic effect of carbon nanotube on the conversion and selectivity is discussed in this chapter.

The **Chapter 7** summarizes the work described in this thesis by presenting the salient features of the work and also mentions the possible avenues for future investigations.

1.7 References

1. R. P. Feynman, *Engineering and Science magazine*, **February 1960**, vol. XXIII, no. 5.
2. (a) H. Sundeep, H. Yo, J. Huang, *Int. J. Nanoscience*, **2010**, 9, 225; (b) A. Ravikrishna, *Engineering Chemistry*, Sri Krishna Hi-Tech Publishing Company, 10th Edition, Chennai, **July 2009**; (c) K. Arivalagan, R. Karthikeyan, *Engineering Chemistry*, Shiv Publications, Chennai, **July 2007**.
3. (a) R. E. Hummel, *Understanding of Materials Science*, 2nd Edition, Springer, **June 2004**. (b) K. J. Klabunde, *Nanoscale Materials in Chemistry*, A John Wiley and Sons Inc., Publication, **2001**. (c) M. Ratner, D. Ratner, *Nanotechnology*, Prentice Hall, **2002**.
4. (a) A. P. Alivisatos, *J. Phys. Chem.* **1996**, 100, 13226; (b) A. P. Alivisatos, *Science* **1996**, 271, 933; (c) A. P. Alivisatos, *ACS Nano*, **2008**, 2, 1514 (d) G. Hodes, *Adv. Mater.* **2007**, 19, 639; (e) S. Eustis, M. A. El-Sayed, *Chem. Soc. Rev.* **2006**, 35, 209. (f) T. Pradeep, A Book, *Nano: The Essentials*, **2004**, Publisher.
5. R. Rossetti, S. Nakahara, L. E. Brus, *J. Chem. Phys.* **1983**, 79, 1086.

6. G. Binning, H. Rohrer, Ch. Gerber, E. Weibel, *Phys. Rev. Lett.*, **1982**, 49, 57.
7. H. W. Kroto, J. R. Heath, S. C. O’Brion, R.C. Curl, R.E. Smalley, *Nature*, **1985**, 318, 162.
8. G. Binning, C. F. Quate, Ch. Gerber; *Phys. Rev. Lett.*, **1986**, 56, 930.
9. (a) D. M. Eigler, E.K. Schweizer, *Nature*, **1990**, 344, 524; (b) H. C. Manoharan, C. P. Lutz, D. M. Eigler, *Nature* **2000**, 403, 512; (c) S. Seal, M. Baraton, *MRS Bulletin*, **2004**, 9.
10. C. Gerber, H. P. Lang, *Nat. Nanotechnol.*, **2006**, 1, 3.
11. (a) D. Thompson, *Gold Bulletin* **2007**, 40/4, 268; (b) M. Faraday, *Phil. Trans.* **1857**, 147, 145. (c) I. Freestone et. al., *Gold Bulletin* **2007**, 40/4, 270. (d) C. Srinivasan, *Current Science*, **2007**, 92, 1338; (e) J. D. Verhoeven, A. H. Pendray, *Muse*, **1998**, 2, 35.
12. G. Cao, A Book: *Nanostructures and Nanomaterials*, **2004**, Imperial College Press.
13. (a) G. Schmid and B. Corain, *Eur. J. Inorg. Chem.* **2003**, 3081; (b) K. Akamatsu, J. Hasegawa, H. Nawafune, H. Katayama, F. Ozawa, *J. Mater. Chem.* **2002**, 12, 2862.
14. (a) A. Henglein, *J. Phys. Chem.*, **1993**, 97, 5457-5471; (b) C. Burda, X. Chen, R. Narayanan and M. A. El-Sayed, *Chem. Rev.*, **2005**, 105, 1025; (c) K.L. Kelly, E. Coronado, L.L. Zhao, G.C. Schatz, *J. Phys. Chem. B*, **2003**, 107, 668.
15. (a) C. Ellert, M. Schmidt, C. Schmitt, T. Reiners, H. Haberland, *Phys. Rev. Lett.* **1995**, 75, 1731; (b) W. P. Halperin, *Rev. Mod. Phys.* **1986**, 58, 533; (c) U. Simon, *Adv. Mater.* **1998**, 10, 1487; (d) A. P. Alivisatos, *ACS Nano*, 2008; (e) A. P. Alivisatos, *J. Phys. Chem.* **1996**, 100, 13226.
16. (a). B. Darling, S. D. Bader, *J. Mater. Chem.*, **2005**, 15, 4189; (b) Y. W. Jun, J. W. Seo, A. Cheon, *Acc. Chem. Res.*, **2008**, 41, 179; (c) K. M. Krishnan, A. B. Pakhomov, Y. Bao, P. Blomqvist, Y. Chun, M. Gonzales, K. Griffin, X. Ji, B. K. Roberts, *J. Mater. Sci.*, **2006**, 41, 793; (d) C. P. Bean, Livingston, J. D. *J. Appl. Phys.*, **1959**, 30, S120; (e) D. L. LesliePelecky, R. D. Rieke, *Chem. Mater.* **1996**, 8, 1770; (f) U. Jeong, X. Teng, Y. Wang, H. Yang, Y. Xia, *Adv. Mater.* **2007**, 19, 33.

17. J. R. Weertman, R. S. Averback, "Nanomaterials: synthesis, properties, and applications" eds. Edelstein, A.S. Cammarata, R.C. *London institute of Phys. Publ.*, **1996**, chapter 13, 323.
18. T. Castro, R. Reifengerger, E. Choi, R. P. Andres, *Phys. rev., B, Condens. matter*, **1990**, 13, 8548.
19. (a) Antoine Lavoisier's original table of elements, taken from the *Traité Élémentaire de Chimie*, 1789, as quoted in J. R. Partington's *A Short History of Chemistry* (Dover, **1989**, ISBN 0486659771); (b) *Chemical Observations and Experiments on Air and Fire*. Uppsala & Leipzig, **1780**; (c) H. W. Kroto, J. R. Heath, S. C. O'Brien, R. F. Curl, R. E. Smalley *Nature*, **1985**, 318, 162. (d) R. Taylor, D. R. M. Walton, *Nature*, 1993, 363, 685; (e) R. Bakry, R. M. Vallant, M. Najam-ul-Haq, M. Rainer, Z. Szabo, C. W Huck and G. K Bonn, *Int J. Nanomedicine*, **2007**, 2, 639.
20. A. T. Collins, *Philosophical Transactions of the Royal Society A*, **1993**, 342, 233.
21. N. Deprez, D. S. McLachlan, *J. Phys. D: Appl. Phys.* **1988**, 21, 101.
22. R. Sengupta, M. Bhattacharya, S. Bandyopadhyay, A. K. Bhowmick, *Progress in Polymer Science*, **2011**, 36, 638.
23. (a) S. Iijima, *Nature* **1991**, 354, 56; (b) C. Frondel, U. B. Marvin, *Nature*, **1967**, 214, 587; (c) G. Tibbetts, *J. Cryst. Growth*, **1985**, 73, 431; (d) A. Geim, K. Novoselov, *Nat. Mater.*, **2007**, 6, 183; (e) R. Bacon, *J Appl Phys.* **1960**, 31, 283; (f) L. Viculis, J. Mack, R. Kaner, *Science*, **2003**, 299, 1361.
24. (a) X. Wang, Q. Li, J. Xie, Z. Jin, J. Wang, Y. Li, K. Jiang, S. Fan, *Nano Lett.* **2009**, 9, 3137; (b) W. Rulanda, A. K. Schaperb, H. Houa, A. Greinera, *Carbon*, **2003**, 41, 423; (c) O. Zhou, R. M. Fleming, D. W. Murphy, C. H. Chen, R. C. Haddon, A. P Ramirez, *Science*, **1994**, 263, 1744; (d) G. Xu, Z. Feng, Z. Popovic, J. Lin, J. J. Vittal, *Adv Mater.*, **2001**, 13, 264; (e) X. Lu, Z. Chen, *Chem. Rev.*, **2010**, 105, 3643; (f) S. Hong, S. Myung, *Nat. Nanotechnol.*, **2007**, 2, 207; (g) P. G. Collins, *Sci. Am.*, **2000**, 5, 67; (h) B. Peng, M. Locascio, P. Zapol, S. Li, S. L. Mielke, G. C. Schatz, H. D. Espinosa, *Nat. Nanotechnol.*, **2008**, 3, 626; (i) T. Filleter, R. Bernal, S. Li, H. D. Espinosa, *Adv Mater*, **2011**, 23, 2855.

25. (a) L. Lacerda, A. Bianco, M. Prato, K. Kostarelos, *Adv. Drug Delivery Rev.*, **2006**, 58,1460; (b) G. Centi and S. Perathoner, *ChemSusChem* **2011**, 4, 913; (c) M. F. L. De Volder, S. H. Tawfick, Ray H. Baughman, A. John Hart, *Science*, **2013**, 339, 535; (d) D. Tasis, N. Tagmatarchis, A. Bianco and M. Prato, *Chem. Rev.* **2006**, 106, 1105; (e) J. M. Schnorr and T. M. Swager, *Chem. Mater.* **2011**, 23, 646; (f) A. Star, V. Joshi, S. Skarupo, D. Thomas, and J. P. Gabriel, *J. Phys. Chem. B*, **2006**, 110, 21014; (g) Y. Sun, K. Fu, Y. Lin and W. Huang, *Acc. Chem. Res.* **2002**, 35, 1096.
26. (a) H. P. Boehm, R. Setton, E. Stumpp, *Pure and Applied Chemistry*, **1994**, 66, 1893; (b) H. P. Boehm, A. Clauss, G. O. Fischer, U. Hofmann, *Zeitschrift für anorganische und allgemeine Chemie*, **1962**, 316, 119.
27. (a) N. D. Mermin, *Physical Review*, **1968**, 176, 250; (b) A. Fasolino, J.H. Los and M.I. Katsnelson, *Nat. Mater.*, **2007**, 6, 858; (c) J. C. Meyer, A. K. Geim, M. I. Katsnelson, K. S. Novoselov, T. J. Booth and S. Roth, *Nature*, **2007**, 446, 60.
28. A.K. Geim and K.S. Novoselov, *Nat. Mater.*, **2007** 6, 183.
29. (a) A. K. Geim & K. S. Novoselov, *Nat. Mater.*, **2007**, 6, 183; (b) Y. Zhu , S. Murali, W. Cai, X. Li, J. W. Suk, J. R. Potts and R. S. Ruoff, *Adv. Mater.* **2010**, 22, 3906; (c) A. K. Geim, *Science*, **2009**, 324, 1530; (d) S. D. Sarma, S. Adam, E. H. Hwang, E. Rossi, *Rev. Mod. Phys.*, **2011**, 83, 407; (e) P. Avouris, *Nano Lett.* **2010**, 10, 4285.
30. J. C. Charlier, P. C. Eklund, J. Zhu, A. C. Ferrari, *Advanced Topics in the Synthesis, Structure, Properties and Applications*, ed. A. Jorio, G. Dresselhaus, M. S. Dresselhaus. Berlin/Heidelberg: Springer-Verlag, **2008**.
31. S. V. Morozov, *Phys. Rev. Lett.* **2008**, 100, 016602.
32. J. H. Chen, *Nat. Nanotechnol.*, **2008**, 3, 206.
33. A. B. Kuzmenko, E. V. Heumen, F. Carbone, D. V. Marel, *Phys Rev Lett.* **2008**, 100, 117401.
34. (a) Frank schwierz, *Nat. Nanotechnol.*, **2010**, 5, 487; (b) F. Bonaccorso, Z. Sun, T. Hasan and A. C. Ferrari, *Nat. Photonics*, **2010**, 4, 611; (c) D. A.C. Brownson, D. K. Kampouris, C. E. Banks, *J. Power Sources*, **2011**, 196, 4873; (d) K. S. Subrahmanyam, P. Kumara, U. Maitra, A. Govindaraja, K. P. S. S. Hembram, U. V. Waghmare, and C. N. R. Rao, *Proceedings of the National*

- Academy of Sciences*, **2011**, 108, 2674; (e) Y. Sun, Q. Wu and G. Shi, *Energy Environ. Sci.*, **2011**, 4, 1113; (f) M. Pumera, *Energy Environ. Sci.*, **2011**, 4, 668; (g) K. Ratinac, W. Yang, S. Ringer, and F. Braet, *Environ. Sci. Technol.* **2010**, 44, 1167.
35. (a) M. P. Johansson, J. Jusélius, D. Sundholm, *Angew. Chem. Int. Ed.*, **2005**, 44, 1843; (b) C.M. Lieber, C. Chen, *Solid state physics*, 1986, 48, 109.
36. (a) T. V. Hughes, C. R. Chambers, *Manufacture of Carbon Filaments*, *US Patent No. 405*, **1889**, 480; (b) P. Morgan, *Carbon Fibers and Their Composites*, *Taylor & Francis Group*, CRC Press, Boca Raton, FL, **2005**; (c) K. P. De Jong and J. W. Geus, *Catal. Rev.-Sci. Eng.*, **2000**, 42, 481; (d) L. V. Radushkevich, V. M. Lukyanovich, *Zh. Fiz. Khim.* **1952**, 26, 88.
37. (a) J. Laine and A. Calafat, *Carbon*, **1991**, 29, 949; (b) F. Caturla, M. Molina-Sabio, And F. Rodriguez-Reinoso, *Carbon*, **1991**, 29, 999; (c) A. Ahmadpour and D. D. Do, *Carbon*, **1997**, 35, 1723; (d) C. Moreno-Castilla, F. Carrasco-Marín, M. V. López-Ramón, M. A. Alvarez-Merino, *Carbon*, **2001**, 39, 1415; (e) J. Matos, C. Nahas, L. Rojas, M. Rosales, *J. Hazard. Mater.*, **2011**, 196, 360; (f) K. László, A. Bóta, L. György Nagy, I. Cabasso, *Colloids and Surfaces A: Physicochemical and Engineering Aspects*, **1999**, 151, 311(g) N. Cohen, M. S. Silverstein, *Polymer*, **2011**, 52, 282.
38. (a) J. A. Maciá-Agulló, B.C. Moore, D. Cazorla-Amorós, A. Linares-Solano, *Carbon*, **2004**, 42, 1367; (b) M. A. Lillo-Ródenas, D. Cazorla-Amorós, A. Linares-Solano, *Carbon*, **2003**, 41, 267.
39. K. Iakoubovskii, K. Mitsuishi and K. Furuya, *Nanotechnology*, **2008**, 19, 155705.
40. K. Iakoubovskii, M.V. Baidakova, B. H. Wouters, A. Stesmans, G.J. Adriaenssens, A.Ya. Vul', P.J. Grobet, *Diamond and Related Materials*, **2000**, 9, 861.
41. (a) S. Ji, T. Jiangb, K. Xub, S. Li, *Appl. Surf. Sci.* **1998**, 133, 231; (b) E. M. Galimov, A. M. Kudin, V. N. Skorobogatskii, V. G. Plotnichenko, O. L. Bondarev, B. G. Zarubin, V. V. Strazdovskii, A. S. Aronin, A. V. Fisenko, I. V. Bykov, A. Y. Barinov, *Doklady Physics*, **2004**, 49, 150.
42. (a) E. Osawa, D. Ho, *J. Med Allied Sci*, **2012**, 2, 31; (b) A.P. Puzyr, A.V. Baron, K.V. Purtov, E.V. Bortnikov, N. N. Skobelev, O. A. Mogilnaya, V.S.

- Bondar, *Diamond & Related Materials*, **2007**, 16, 2124; (c) I. P. Chang, K. Chu Hwang, and C. Chiang, *J. Am. Chem. Soc.* **2008**, 130, 15476; (d) V.N. Mochalin, O. Shenderova, D. Ho, Y. Gogotsi, *Nat. Nanotechnol.*, **2012**, 7, 11.
43. (a) C. Noguera, *Physics and Chemistry at Oxide Surfaces*; Cambridge University Press: Cambridge, UK, **1996**; (b) H. H. Kung, *Transition Metal Oxides: Surface Chemistry and Catalysis*; Elsevier: Amsterdam, **1989**; (c) V. E. Henrich, P. A. Cox, *The Surface Chemistry of Metal Oxides*; Cambridge University Press: Cambridge, UK, **1994**; (d) A. F. Wells, *Structural Inorganic Chemistry*, 6th ed.; Oxford University Press: New York, **1987**; (e) W. A. Harrison, *Electronic Structure and the Properties of Solids*; Dover: New York, **1989**.
44. (a) H. H. Kung, *Transition Metal Oxides: Surface Chemistry and Catalysis*, 1st ed.; Elsevier science publisher: New York, **1989**; (b) P. Poizot, S. Laruelle, S. Grugeon, L. Dupont & J-M. Tarascon, *Nature*, **2000**, 407, 496; (c) T. Gershon, *Materials Science and Technology*, **2011**, 27, 1357.
45. R. W. G. Wyckoff, *Crystal Structures*, 2nd ed.; Wiley: New York, **1964**.
46. (a) K. W. Powers, M. Palazualos, B. M. Moudgil, S. M. Roberts, *Nanotoxicology*, **2007**, 1, 42. (b) S. T. Stern, S. E. McNeil, *Toxicological Sciences* **2008**, 101, 4. (c) W. Hannah, P. B. Thompson, *J. Environ. Monit.*, **2008**, 10, 291. (d) A. S. Barnard, *Nat. Mater.*, **2006**, 5, 245. (e) A. Nel, T. Xia, L. Mädler, N. Li, *Science*, **2006**, 311, 622.
47. M. J. Hudson, J. W. Peckett, C. S. Sibley, P. J. F. Harris, *Ind. Eng. Chem. Res.*, **2008**, 47, 2605.
48. M. Winter, R. J. Brodd, *Chem. Rev.* **2004**, 104, 4245.
49. M. Jayalakshmi, K. Balasubramanian, *Int. J. Electrochem. Sci.*, **2008**, 3, 1196.
50. Bruno Scrosati, Jürgen Garche, *J. Power Sources*, **2010**, 195, 2419.
51. (a) B. E. Conway, *Electrochemical Supercapacitors: Scientific Fundamentals and Technological Applications*. New York, Kluwer-Plenum, **1999**; (b) A. Burke, *J. Power Sources*, **2000**, 91, 37; (c) A. Chu and P. Braatz, *J. Power Sources*, **2002**, 112, 236.
52. Thomas Christen, Martin W. Carlen, *J. Power Sources*, **2000**, 91, 210.
53. R. Kotz and M. Carlen, *Electrochim. Acta*, **2000**, 45, 2483.
54. P. Sharma, T.S. Bhatti, *Energy Convers. Manage.*, **2010**, 51, 2901.

55. G. Wang, L. Zhang and J. Zhang, *Chem. Soc. Rev.*, **2012**, 41, 797.
56. D. Cericola, R. Kötz, *Electrochim. Acta*, **2012**, 72, 1.
57. E. Frackowiak, and F. Beguin, *Carbon*, **2001**, 39, 937.
58. (a) C. Arbizzani, M. Mastragostino, F. Soavi, *J. Power Sources*, **2001**, 100, 164-170; (b) D. Y. Qu, and H. Shi, *J. Power Sources*, **1998**, 74, 99.
59. (a) J. Gamby, P. L. Taberna, P. Simon, J.F. Fauvarque, M.Chesneau, *J. Power Sources*, **2001**, 101, 109-116; (b) H. Shi, *Electrochim. Acta*, **1996**, 41, 1633.
60. (a) J. Wang, S. Q. Zhang, Y. Z. Guo, J. Shen, S. M. Attia, B. Zhou, G. Z. Zheng, and Y. S. Gui, *J. Electrochem. Soc.*, **2001**, 148, D75; (b) K. Hyeok An, K. K. Jeon, J. K. Heo, S. C. Lim, D. J. Bae, and Y. H. Lee, *J. Electrochem. Soc.*, **2002**, 149, A1058; (c) E. Frackowiak and F. Beguin, *Carbon*, **2002**, 40, 1775; (d) F. Pico, J. M. Rojo, M. L. Sanjuán, A. Ansón, A. M. Benito, M. A. Callejas, W. K. Maser, and M. T. Martínez, *J. Electrochem. Soc.*, **2004**, 151, A831; (e) C. Du, J. Yeh and N. Pan, *Nanotechnology*, **2005**, 16, 350; (f) C. Niu, E. K. Sichel, R. Hoch, D. Moy, and H. Tennent, *Appl. Phys. Lett.*, **1997**, 70, 1480.
61. (a) B. E. Conway, *J. Electrochem. Soc.*, **1991**, 138, 1539- 1548; (b) B.E. Conway, V. Birss, J. Wojtowicz, *J. Power Sources*, **1997**, 66, 1.
62. (a) I. H. Kim, and K. B. Kim, *Electrochemical and Solid State Letters*, **2001**, 4, A62; (b) M. Mastragostino, C. Arbizzani, F. Soavi, *J. Power Sources*, **2001**, 97-8, 812. (c) K. S. Ryu, K. M. Kim, N.Park, Y. J. Park, S.H. Chang, *J. Power Sources*, **2002**, 103, 305.
63. (a) J. P. Zheng, and T. R. Jow, *J. Electrochem. Soc.*, **1995**, 142, L6-L8; (b) J. P. Zheng, P. J. Cygan, and T. R. Jow, *J. Electrochem. Soc.*, **1995**, 142, 2699.
64. E. Frackowiaka, V. Khomenko, K. Jurewicz, K. Lota, F. Beguin, *J. Power Sources*, **2006**, 153, 413.
65. K. Jurewicz, S. Delpoux, V. Bertagna, F. Béguin, E. Frackowiak, *Chemical Physics Letters*, *Chem. Phys. Lett.*, **2001**, 347, 360.
66. (a) A. Laforgue, P. Simon, J. F. Fauvarque, M. Mastragostino, F. Soavi, J. F. Sarrau, P. Lailier, M. Conte, E. Rossi, and S. Saguatti, *J. Electrochem. Soc.*, **2003**, 150, A645; (b) M. Mastragostino, C. Arbizzani, F. Soavi, *Solid State Ionics*, **2002**, 148, 493.

67. (a) X. Wang and J. P. Zheng, *J. Electrochem. Soc.*, **2004**, 151, A1683; (b) A. D. Pasquier, I. Plitz, S. Menocal, G. Amatucci, *J. Power Sources*, **2003**, 115, 171; (c) W. G. Pell, and B. E. Conway, *J. Power Sources*, **2004**, 136, 334; (d) G. G. Amatucci, F. Badway, A. D. Pasquier, and T. Zheng, *J. Electrochem. Soc.*, **2001**, 148, A930.
68. (a) M. M. Thackeray, *J. Electrochem. Soc.* **1995**, 142, 2558; (b) S. Scharner, W. Weppner, P. Schmind-Beurmann, *J. Electrochem. Soc.* **1999**, 146, 857; (c) K. Naoi, *Fuel Cells*, **2010**, 10, 825.
69. M. Rosa Palaci'n, *Chem. Soc. Rev.*, **2009**, 38, 2565.
70. (a) B. Scrosati, J. Hassounab and Y. Sun, *Energy Environ. Sci.*, **2011**, 4, 3287; (b) B. Scrosati, J. Garche, *J. Power Sources*, **2010**, 195, 2419.
71. (a) F. Cheng, J. Liang, Z. Tao, and J. Chen, *Adv. Mater.* **2011**, 23, 1695; (b) H. Song, K. T. Lee, M. G. Kim, L. F. Nazar, and J. Cho, *Adv. Funct. Mater.*, **2010**, 20, 3818; (c) L. Ji, Z. Lin, M. Alcoutlabi and X. Zhang, *Energy Environ. Sci.*, **2011**, 4, 2682; (d) G. Jeong, Y. Kim, H. Kim, Y. Kimd and H. Sohn, *Energy Environ. Sci.*, **2011**, 4, 1986; (e) H. Li, Z. Wang, L. Chen, and X. Huang, *Adv. Mater.*, **2009**, 21, 4593.
72. (a) D. S. Su, and R. Schlögl, *ChemSusChem*, **2010**, 3, 136; (b) S. Flandrois, B. Simon, *Carbon*, **1999**, 37,165; (c) M. Endo, C. Kim, K. Nishimura, T. Fujino, K. Miyashita, *Carbon*, **2000**, 38, 183; (c) Y.P. Wu, E. Rahm, R. Holze, *J. Power Sources*, **2003**, 114, 228; (d) N. A. Kaskhedikar and J. Maier, *Adv. Mater.*, **2009**, 21, 2664.
73. (a) M. V. Reddy, T. Yu, C. Sow, Z. X. Shen, C. T. Lim, G. V. Subba Rao, and B. V. R. Chowdari, *Adv. Funct. Mater.*, **2007**, 17, 2792; (b) C. He, S. Wu, N. Zhao, C. Shi, E. Liu, and J. Li, *ACS Nano*, **2013**, 7, 4459; (c) Xiong Wen Lou, Da Deng, Jim Yang Lee, Ji Feng, and Lynden A. Archer, *Adv. Mater.* **2008**, 20, 258; (d) B. Varghese, M. V. Reddy, Z. Yanwu, C. S. Lit, T. C. Hoong, G. V. Subba Rao, B. V. R. Chowdari, A. T. Shen Wee, C. T. Lim, and C. Sow, *Chem. Mater.*, **2008**, 20, 3360; (d) X. Wang, X. Li, X. Sun, F. Li, Q. Liu, Q. Wang and D. He, *J. Mater. Chem.*, **2011**, 21, 3571; (e) X. Xu, R. Cao, S. Jeong, and J. Cho, *Nano Lett.*, **2012**, 12, 4988.
74. (a) M. Yoshio, H. Wang, K. Fukuda, T. Umeno, N. Dimov and Z. Ogumi, *J. Electrochem. Soc.*, **2002**, 149, A1598; (b) C. K. Chan, H. Peng, G. Liu, K.

- McIlwrath, X. F. Zhang, R. A. Huggins & Y. Cui, *Nat. Nanotechnol.*, **2008**, 3, 31; (c) C. K. Chan, X. F. Zhang, and Y. Cui, *Nano Lett.*, **2008**, 8, 307; (d) Y. Idota, T. Kubota, A. Matsufuji, Y. Maekawa, T. Miyasaka, *Science*, **1997**, 276, 1395; (e) G. Derrien, J. Hassoun, S. Panero, B. Scrosati, *Adv. Mater.* **2007**, 19, 2336.
75. (a) W. Lubitz, B. Tumas, *Chem. Rev.*, **2007**, 107, 3900; (b) J.O'M. Bockris, *Int. J. Hydrogen Energy*, **2002**, 27, 731.
76. (a) R. M. Navarro, M. A. Peña, and J. L. G. Fierro, *Chem. Rev.*, **2007**, 107, 3952; (b) M. Balat, *Int. J. Hydrogen Energy*, **2008**, 33, 4013; (c) P. A. Pilavachi, A. I. Chatzipanagi, and A. I. Spyropoulou, *Int. J. Hydrogen Energy*, **2009**, 34, 5294.
77. (a) J. A. Turner, *Science*, **2004**, 305, 972; (b) C. J. Winter, *Int. J. Hydrogen Energy*, **2009**, 34, S1; (c) F. A. Felder and A. Hajos, *Proc. IEEE*, **2006**, 94, 1864; (d) J. Rifkin, *The Hydrogen Economy*, New York: Tarcher & Penguin, **2002**.
78. R. de Levie, *J. Electroanal. Chem.*, **1999**, 476, 92.
79. R. W. Coughlin and M. Farooque, *Nature* (London), **1979**, 279, 301.
80. H. Wendt, G. Imarisio, *J. Appl. Electrochem.*, **1988**, 18, 1.
81. (a) D. Astruc, F. Lu, J. Ruiz Aranzaes, *Angew. Chem. Int. Ed.* **2005**, 44, 7852; (b) J. G. De Vries, *Dalton Trans.* 2006, 421; (c) D. Astruc, *Inorg. Chem.*, **2007**, 46, 1884.
82. (a) D. M. Robinson, Y. B. Go, M. Greenblatt, and G. C. Dismukes, *J. Am. Chem. Soc.*, **2010**, 132, 11467; (b) L. Espinal, S. L. Suib, and J. F. Rusling, *J. Am. Chem. Soc.*, **2004**, 126, 7676; (c) M. Liao, J. Feng, W. Luo, Z. Wang, J. Zhang, Z. Li, T. Yu, and Z. Zou, *Adv. Funct. Mater.* **2012**, 22, 3066; (d) Q. Yan, X. Li, Q. Zhao, G. Chen, *J. Hazard. Mater.*, **2012**, 209-210, 385; (e) K. Sivula, F. L. Formal, and M. Grätzel, *ChemSusChem*, **2011**, 4, 432; (f) C. Wang, H. Daimon, and S. Sun, *Nano Lett.*, **2009**, 9, 1493; (g) M. Stratakis, and H. Garcia, *Chem. Rev.* **2012**, 112, 4469.
83. (a) A. Marinkas, F. Arena, J. Mitzel, G. M. Prinz, A. Heinzl, V. Peinecke, H. Natter, *Carbon*, **2013**, 58, 139; (b) D. J. M. de Vlieger, D. B. Thakur, L. Lefferts, and K. Seshan, *ChemCatChem*, **2012**, 4, 2068; (c) B. F. Machado and P. Serp, *Catal. Sci. Technol.*, **2012**, 2, 54; (d) Jeffrey Pyun,

- Angew. Chem. Int. Ed.* **2011**, 50, 46; (e) H. Jüntgen, *Fuel*, **1986**, 65, 1436; (f) N. M. Rodriguez, M. Kim, and R. T. K. Baker, *J. Phys. Chem.* **1994**, 98, 13108.
84. (a) T. Zhou, S. Mo, S. Zhou, W. Zou, Y. Liu, D. Yuan, *J. Mater. Sci.* **2011**, 46, 3337; (b) Y. Li, H. Tan, X. Yang, B. Goris, J. Verbeeck, S. Bals, P. Colson, R. Cloots, G. V. Tendeloo, and B. Su, *Small*, **2011**, 7, 475; (c) H. Wang, L. Cui, Y. Yang, H. S. Casalongue, J. T. Robinson, Y. Liang, Y. Cui, and H. Dai, *J. Am. Chem. Soc.*, **2010**, 132, 13978; (d) C. H. Choi, S. H. Park and S. I. Woo, *Phys. Chem. Chem. Phys.*, **2012**, 14, 6842.

Chapter-2

Experimental Methods and Characterization Techniques

This chapter presents a brief description of the nanomaterials synthesis methods used in the research work, such as, sol-gel and co-precipitation, carbonization by pyrolysis, laser synthesis. This follows with the discussion on various experimental tools employed to characterize the structural, optical and electrical properties of the synthesized nanomaterials.

Section -I

2.I Synthesis Techniques

Over the past decades researchers have developed various techniques for synthesis and characterization of nanomaterials. Synthesis of nanomaterials is the most crucial and challenging step for the efficient use of these nanomaterials for several potential applications. The morphologies and properties of nanosystems and composites mainly depend upon their synthesis methods and protocols.

The first discovered nanomaterial was synthesized by vacuum evaporation of iron in inert gas and condensed on cooled substrate.^[1] After that a number of methods had been developed for the fabrication of nanoparticles including inorganic ceramics and organic compound, i.e. arc plasma torch to produce metallic powder,^[2,3] laser induced chemical vapor deposition method (CVD) to produce individual compounds,^[4] and microwave plasma enhanced CVD to produce hard and brittle nanomaterials.

Discovery and identification of newer properties of nanomaterials always lead to novel developments of synthesis, modification, and characterization techniques. Hence nanoscience has been largely associated with various discovery phases where new nanomaterials with novel properties and applications are born. The nature of engineered nanomaterials and their proposed uses provide strong reasons for the implementation of new chemistry in the development of the novel materials and applications.

The synthesis of multi-functional metal oxides and carbon based nanomaterials under desirable low temperature and mild conditions, with controlled size, shape and pure phase still remains a major task for scientists. Soft chemistry routes represent the most attractive alternative, because they allow good control from the molecular precursors to the final product at low processing temperatures, resulting in the formation of nanomaterials with high purity and compositional homogeneity. The advantages of such approaches include: (i) wet chemical control on oxidation states, (ii) ability to template various nanostructures, (iii) relatively low process cost, (iv) ability to form nano, meso and micron sized particles and thin films. The present research work is mainly focused on the synthesis and characterization of layered

ultrathin graphitic (conducting) forms of carbon, transition metal oxides based nanomaterials and their nanocomposites.

2.I.1 Co-precipitation Methods

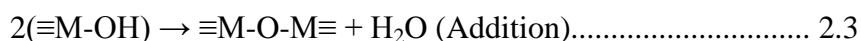
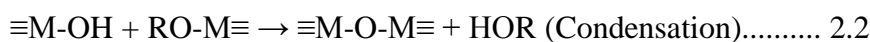
Precipitation and co-precipitation are important and highly successful wet chemical methods for the synthesis of various nanoparticles. Basically, solutions of different ions are mixed in well-defined proportions and under controlled conditions of heat, temperature, and pressure to promote the formation of insoluble compounds which precipitate out of solution. These precipitates are then collected through filtering and/or spray drying to produce a dry powder. The advantages of these wet chemical processes are that a large variety of compounds can be fabricated, including inorganic, organic, and also some metals, in inexpensive equipment and in significantly large quantities. Another important factor is the ability to control particle size and produce highly monodisperse materials. It is essential to control the factors that determine the precipitation process, such as the pH, temperature, concentration of the reactants and ions. Organic molecules are used to control the release of the reagents and ions in the solution during the precipitation process. The particle size and morphology are significantly influenced by the reactant concentration, pH, and temperature.

2.I.2 Sol Gel method

The sol-gel technique is one of the most widely used soft chemical methods and is mainly applied for the synthesis of metal and semimetal oxides. In sol-gel process, starting from molecular precursors an oxide network is obtained via inorganic polymerization reactions leading to the final nano-powder product. First silica sol-gel was prepared by Eblemen in 1856 and first homogenous mixed oxide gel was prepared by Rustom Roy in 1956. There are two ways of implementing the sol-gel process: aqueous and non-aqueous routes. In most cases, the precursor or starting compound is either an inorganic metal salts (acetate, chloride, nitrate, sulphate etc.) or a metal organic species such as metal alkoxide. Transition metal alkoxides are very reactive towards the nucleophilic reagents such as water. This is because of the electrophilic nature of transition metal ions due to lower electro-negativity and their ability to exhibit several co-ordinations where full coordination is usually not satisfied

in the molecular precursors, thus allowing coordination expansion. Due to this high reactivity, they must be handled with great care, in dry environment and are often stabilized via chemical modification.

The main principle of the classical sol-gel process is the controlled hydrolysis of metallo-organic compounds (alkoxides) in an organic solvent. The sol-gel process involves ololation (formation of hydroxyl bridges) and oxolation (formation of oxygen bridges) reactions during hydrolysis (reactions 2.1-2.3).^[5] The oxolation condensation reaction is responsible for the formation of colloidal agglomerates, and the ololation addition reaction is responsible for their aggregation into a polymeric gel.



Where R is alkyl group and M is metal or semimetal.

The gel formation depends on different parameters including the nature of starting Material (s) (precursor[s]), kind of solvent, precursor concentration in the solvent, alkoxy to water ratio, temperature of the reaction, pH, kind of catalyst, stirring and aging time.

Sol-gel and aero gel processes are the most widely used routes and involve a colloidal sol which is converted into a gel during aging.^[6,7] Metal alkoxides serve as starting materials and can be hydrolyzed by water. The alkoxides have been extensively used for the production of oxides and glasses. During hydrolysis, alkoxy groups are replaced by strong OH nucleophiles, and the following condensation and addition steps lead to the formation of oxide chains. The sol-gel synthesis goes through the formation of a sol of colloidal particles or units in a solution, gelation of the sol by the agglomeration of these particles or sub-units into a big gel network structure, removing of the solvent, and heat treatment to transfer gel into solid.

Depending on reaction conditions, the sol particles may grow further or form gel. The sol-gel process can be used for the preparation of a variety of materials (**Figure 2.1**). [8]

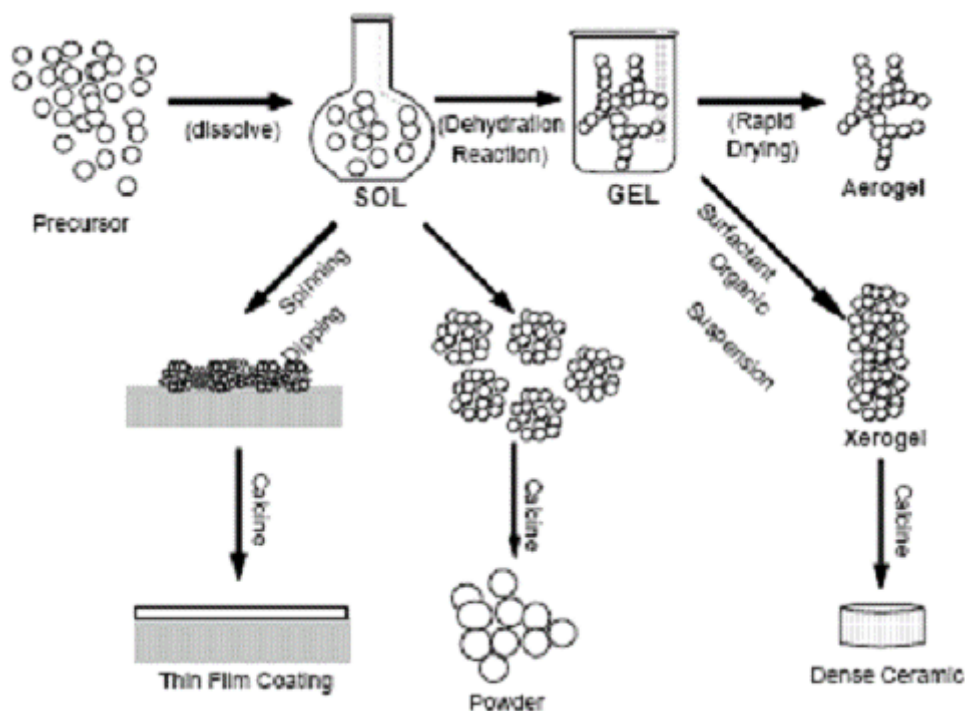


Figure 2.1: Sol-Gel processing options

(<http://www.gitam.edu/eresource/nano/nanotechnology/bottamup%20app.htm>)

The drying of the sol gives powders. The application of dip-coating or spin-coating leads to the preparation of the thin films. The removal of the solvent by drying causes the shrinking of the gel and significant reduction in the volume due to increasing capillary forces. The high capillary pressure in the pores causes the collapse of the gel network structure and the production of less porous powder (xerogel). In contrast, the supercritical extraction when the solvent is removed above its critical temperature preserves the structure of the gel network and yields a highly porous material (aerogel). Dense ceramic material or glass can be produced by sintering the xerogel or aerogel.

2.1.3 High temperature Pyrolysis

Pyrolysis is a thermo-chemical decomposition of organic material at elevated temperatures in the absence of oxygen (or any halogen). It involves the simultaneous change of chemical composition and physical phase, and is irreversible process. The word is coined from the Greek-derived elements pyro "fire" and lysis "separating". The process is used heavily in the chemical industry, for example, to produce charcoal, activated carbon, methanol, and other chemicals from wood, to convert ethylene dichloride into vinyl chloride to make Poly Vinyl Chloride (PVC), to produce coke from coal, to convert biomass into syngas and biochar, to turn waste into safely disposable substances, and for transforming medium-weight hydrocarbons from oil into lighter ones like gasoline.



Figure 2.2 Photo of split-tube furnace

This is the most common method for the synthesis of carbon nanomaterials. [9-¹¹] Past few decades this synthesis method has been widely used for the synthesis of activated carbon and porous materials from natural or manmade by-products. [12] In this process usually the samples are allowed to heat to very high temperature (~1000°C) for certain time in a split tube furnace (**Figure 2.2**) under continuous argon flow. At high temperature the materials burn and form carbonized products with some degree of graphitization. This method is mostly used to synthesize valuable products from waste materials, organic molecules etc.

2.I.4 Pulsed Laser synthesis method

Laser irradiation is a unique technique to control the shape and size of particles. In this method high energy laser pulses are allowed to interact with the precursor samples present either in solid or liquid medium for certain time period. It is a very unique method for the synthesis of nanoparticles because of high local heating (up to several thousand to tens of thousand degrees depending on the parameters) by laser pulses bringing out reformulating chemical changes in the molecules. Several transient reactions can be manipulated with the laser irradiation by adding some external reagents which can construct totally new compounds after the photo-thermal melting and vaporization. After the short time melting, evaporation and recondensation either photo-fusion or photo-fragmentation of the particles has been observed leading to bigger particles or smaller particles, respectively.^[13-14]

Section -II

2.II Characterization Techniques

A detail analysis of properties of the nanoparticles is very crucial in order to employ them for any application. When material's dimensions are reduced to nanoscale they have different properties from their bulk counterparts. Their structural, electronic and optical properties drastically change when the size is reduced. Such changes in the properties can make the analysis complicated at times. Therefore it is very important to select the appropriate characterization technique that will give precise and clear information about the nanomaterials under study. Following sections present the discussion on the various characterization techniques used for the present doctoral work.

2.II.1 X-Ray Diffraction

X-ray crystallography is the most crucial tool for studying structural properties of metal oxides.^[15] X-ray diffraction (XRD) is a fast, non destructive, analytical technique primarily used for phase identification of a crystalline material and can also provide information on unit cell dimensions. XRD patterns are generated from the interference pattern of elastically dispersed X-ray beams by atom cores (**Figure 2.3**). For materials with moderate/long range order information about atomic structure and particle characteristics such as size, strain, defects etc. can also be obtained via XRD patterns.^[13]

This technique is suitable for thin films, bulk and nanomaterials. In case of nanostructures, the change in lattice parameter with respect to bulk gives idea of nature of strain present in the film. In the XRD instrument, a collimated monochromatic beam of X-rays is incident on the sample. A constructive interference occurs only for certain θ 's correlating to those (hkl) plane, where path difference is an integral multiple (n) of wavelength. Based on this, the Bragg's condition is given by

$$2d\sin\theta = n\lambda \quad 2.4$$

Where, λ is the wavelength of the incident X-ray, d is the interplaner distance, ' θ ' is the scattering angle and n is an integer-called order of diffraction. In nanostructures, X-rays are diffracted by the oriented crystallites at a particular angle to satisfy the Bragg's condition. Since the value of θ and λ is known, one can

calculate the interplaner spacing. The XRD can be taken in different modes such as θ - 2θ scan mode, θ - 2θ rocking curve, and ϕ scan. In the θ - 2θ scan mode, a monochromatic beam of X-ray is incident on the sample at an angle of θ with the sample surface. The detector motion is coupled with the X-ray source in such a way that it always makes an angle 2θ with the incident direction of the X-ray beam (**Figure 2.3**). The resulting spectrum is a plot between the intensity recorded by the detector versus 2θ . Schematic view of XRD is shown in **Figure 2.3**.

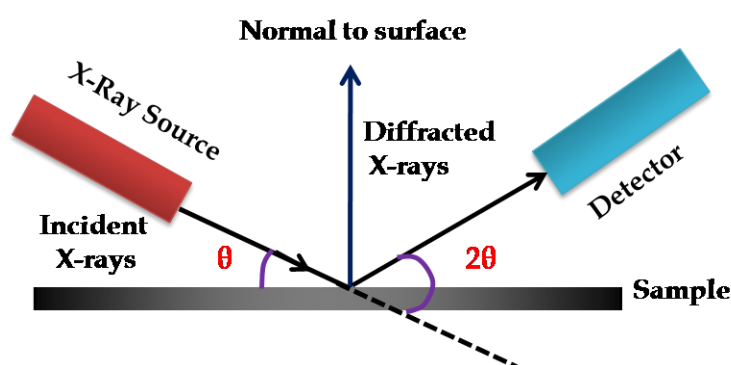


Figure 2.3: Representation of X-ray Diffraction. The θ - 2θ scan maintains these angles with the sample, detector and X-ray source. Only planes of atoms that share this normal will be seen in the θ - 2θ scan.

The incident X-rays may reflect in many directions but will only be measured at one location so we will require:

$$\text{Angle of Incidence } (\theta_i) = \text{Angle of Reflectance } (\theta_r) \quad 2.5$$

This is done by moving the detector twice as fast in (θ) as the source. So, only where $\theta_i = \theta_r$, will be the intensity of the reflected X-rays to be measured.

Nanomaterials have smaller sized crystallites and significant strains due to surface effects, causing considerable peak broadening and shifts in the peak positions w.r.t standard data. From the shifts in the peak positions, one can calculate the change in the d-spacing, which is the result of change of lattice constants under strain. The crystallite size (D) is calculated using Scherrer's formula:

$$D = k \lambda / \beta \cos\theta \quad 2.6$$

Where, k = Scherrer's Constant ≈ 0.9 , β = Full Width at Half Maximum (FWHM),

Only disadvantage of XRD is its less sensitivity towards low-Z materials, thus usually high-Z materials are used. In such cases, electron or neutron diffraction is employed to overcome the low intensity of diffracted X-rays.

2.II.2 Raman Spectroscopy

Raman spectroscopy is a powerful tool to analyze structural/morphological properties of solid oxides at a local or near surface level due to the strong sensitivity of the phonon characteristics to the crystalline nature of the materials. ^[16]

In Raman spectrometer, when a beam of visible light is passed through the sample a small amount of the radiation energy is scattered, the scattering persisting even if all other extraneous matter are rigorously excluded from the substance. If a monochromatic radiation is used and if the scattered energy is almost same as the incident frequency then it is called as Rayleigh scattering, however in addition, if some discrete frequencies above and below that of the incident beam are observed to scatter, it is referred to as Raman scattering. ^[17]

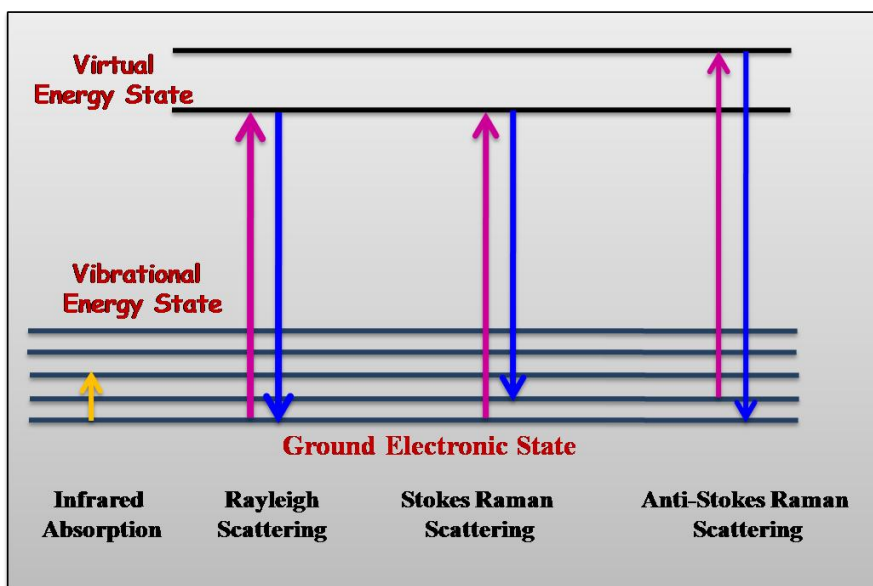


Figure 2.4 Energy level diagram for Raman scattering; (a) Stokes Raman scattering (b) Energy level diagram for Raman scattering; (a) Stokes Raman scattering (b) anti-Stokes Raman scattering ^[17]

The energy level diagrams for Raman scattering with Stokes, Anti Stokes and Rayleigh Scattering has been shown in **Figure 2.4**. According to quantum theory of

radiation, when photons having energy ' $h\nu$ ' undergo collisions with molecules, if the collision is perfectly elastic, they will be deflected unchanged. A detector placed to collect energy at right angles to an incident beam will thus receive photons of energy ' $h\nu$ ', i.e. radiation of frequency ' ν '. However, it may happen that energy is exchanged between photon and a molecule during the collision (such collisions are called inelastic). The molecule can gain or lose amounts of energy only in accordance with the quantum laws; i.e. its energy change, ΔE (joules) must be the difference in energy between two of its allowed states and it must represent a change in the vibrational and/or rotational energy of the molecule. If the molecule gains energy ΔE , the photon will be scattered with the energy $h\nu - \Delta E$ and the equivalent radiation will have a frequency $\nu - \Delta E/h$. Conversely, if the molecule loses energy ΔE , the scattered frequency will be $\nu + \Delta E/h$. Radiations scattered with a frequency lower than that of the incident beam is referred to as Stokes' radiation, while that at higher frequency is called anti-stokes' radiation. Stokes' radiation is accompanied by an increase in molecular energy, which is very common (subject to certain selection rules) while anti-stokes' radiation involves a decrease in molecular energy (which can only occur when the molecule is originally in an excited vibrational/rotational state), Stokes' radiation is generally more intense than anti-Stokes' radiation.

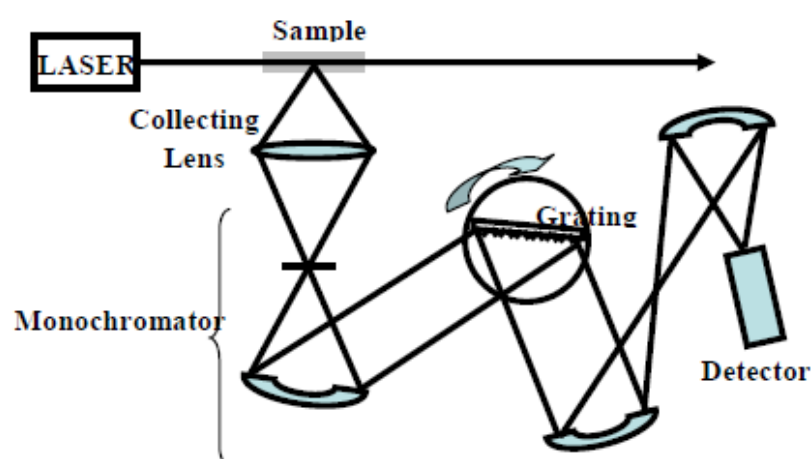


Figure 2.5: Schematic diagram of Raman Spectrometer

[http://www.isu.edu/chem/instr_Raman.shtml]

Figure 2.5 shows the schematic of Raman spectrometer. Raman Spectrometer consists of Laser beam (very narrow, monochromatic, coherent and powerful) which

when passed through the cell, usually a narrow glass or quartz tube filled with the sample, light get scattered sideways from the sample, which is collected by a lens and passed into a grating monochromator. The signal is measured by a sensitive PMT and after amplification; it is usually processed by a computer which plots the Raman spectrum.

2.II.3 Transmission Electron Microscopy (TEM)

Transmission electron microscopy (TEM) , due to its unique characteristics allow one to achieve atomic resolution of crystal lattices, hence is one of the most powerful and versatile techniques for the characterization of nanostructured systems. It can also be used to obtain chemical and electronic information at the sub-nanometer scale (with the assistance of energy-dispersive X-ray spectroscopy (EDS) complementary techniques). The line diagram of a typical TEM column is shown in **Figure 2.6**. In TEM, a thin specimen is illuminated with uniform and high intensity electrons. The interaction of an electron beam with a solid specimen results in a number of elastic or inelastic scattering phenomena (backscattering or reflection, emission of secondary electrons, X-rays or optical photons, and transmission of the undeviated beam along with beams deviated as a consequence of elastic – single atom scattering, diffraction - or inelastic phenomena). The TEM technique is dedicated to the analysis of the transmitted or forward-scattered beam. The beam is passed through a series of lenses to obtain the magnified image. The Objective lens mainly determines the final image resolution. In low resolution TEM, the objective aperture is adjusted for selection of the central beam (containing the less-scattered electrons) or of a particular diffracted (or scattered in any form) beam to form the bright-field or dark-field image, respectively. In high resolution TEM (HRTEM) is usually performed in bright-field mode where the image is formed by collecting a few diffracted beams in addition to the central one.

Angular distribution of scattering can be viewed in the form of diffraction patterns, commonly referred to as selected area electron diffraction (SAED). Spatial distribution of scattering can be observed as contrast in images of the specimen. This arrangement allows direct viewing of the area from which the diffraction pattern arises. Moreover, Kikuchi patterns obtained by inelastic scattering of electrons is also

very useful for understanding the crystallographic orientation as these are rigidly attached to a crystal plane and therefore move in the diffraction pattern when the crystal is tilted.

Many materials require extensive sample preparation and thinning procedures to produce a sample thin enough to be electron transparent, and this process may cause some changes in the sample. Therefore sample preparation method should be selected carefully. The field of view in TEM is relatively small, which can raise the possibility that the region analyzed may not be representative of the whole sample. There is also a possibility of the sample getting damaged by the electron beam, particularly in the case of biological materials. Despite these limitations, TEM has been the technique of choice due to the atomic-level resolution leading direct visual information of size, shape, dispersion and structure. Further, when coupled with SAED, the technique can provide important information on the crystallographic directions in the structures, helpful to understand the growth kinetics. ^[18,19]

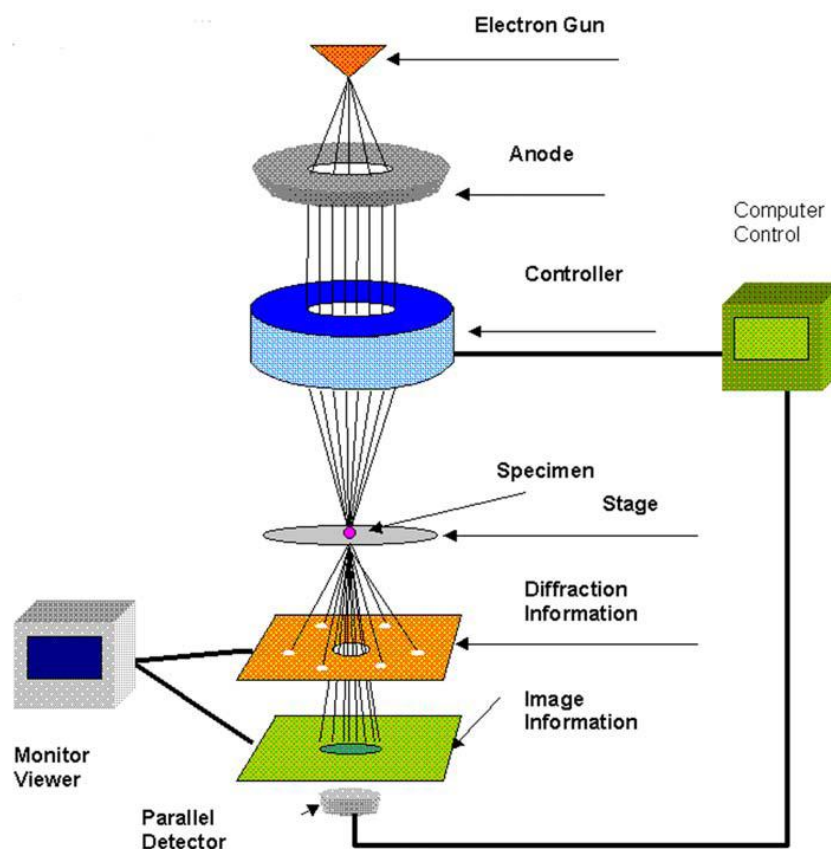


Figure 2.6 Schematic diagram of the Transmission Electron Microscope.

[<http://www.rpi.edu/dept/materials/COURSES/NANO/shaw/Page5.html>]

2.II.4 Scanning Electron Microscope (SEM)

Scanning Electron Microscopy allows direct observations of topography and morphological features with high resolution and depth of field than optical microscope. A typical schematic of a SEM is shown in **Figure 2.7**. The two major components of SEM are the electron column and control console.^[20] The electron column consists of an electron gun and two or more electron lenses, which influence the path of electrons travelling down an evacuated tube. The control console consists of a cathode ray tube viewing screen and computer to control the electron beam. The purpose of electron gun is to provide a stable beam of electrons. Generally, tungsten or Lanthanum hexaboride (LaB₆) thermionic emitters are used as electron gun. The spot size from a tungsten gun is too large and requires electron lenses to demagnify it to place a much smaller focused electron spot on the specimen.

When the electron beam impinges on the specimen, many types of signals are generated and any of these can be displayed as an image. The two signals most often used to produce SEM images are secondary electrons (SE) and backscattered electrons (BSE). Most of the electrons are scattered at large angles (from 0° to 180°) when they interact with the positively charged nucleus. These elastically scattered electrons usually called 'backscattered electrons' (BSE) are used for SEM imaging. Some electrons scatter inelastically due to the loss in kinetic energy upon their interaction with orbital shell electrons.

Incident electrons may knock off loosely bound conduction electrons out of the sample. These are secondary electrons (SE) and are used for SEM topographical imaging. Both secondary and back scattered electrons (BSE) are collected when a positive voltage is applied to the collector screen in front of detector. When a negative voltage is applied on the collector screen only BSE signal is captured because the low energy SEs is repelled. Electrons captured by the scintillator/ photomultiplier are then amplified and used to form an image in the SEM. If the electron beam knocks off an inner shell electron, the atom rearranges by dropping an outer shell electron to an inner one. This excited or ionized atom emits an electron commonly known as the Auger electron. Recently Auger electron spectroscopy (AES) has also been useful to

provide compositional information. Here instead of excited atom releasing Auger electron, it can release a photon of electromagnetic radiation. If the amount of energy released is high, the photon will be an X-ray photon. These electrons are characteristic of the sample and can be used for analysis. This type of analysis is known as Energy Dispersive analysis of X-rays (EDAX).

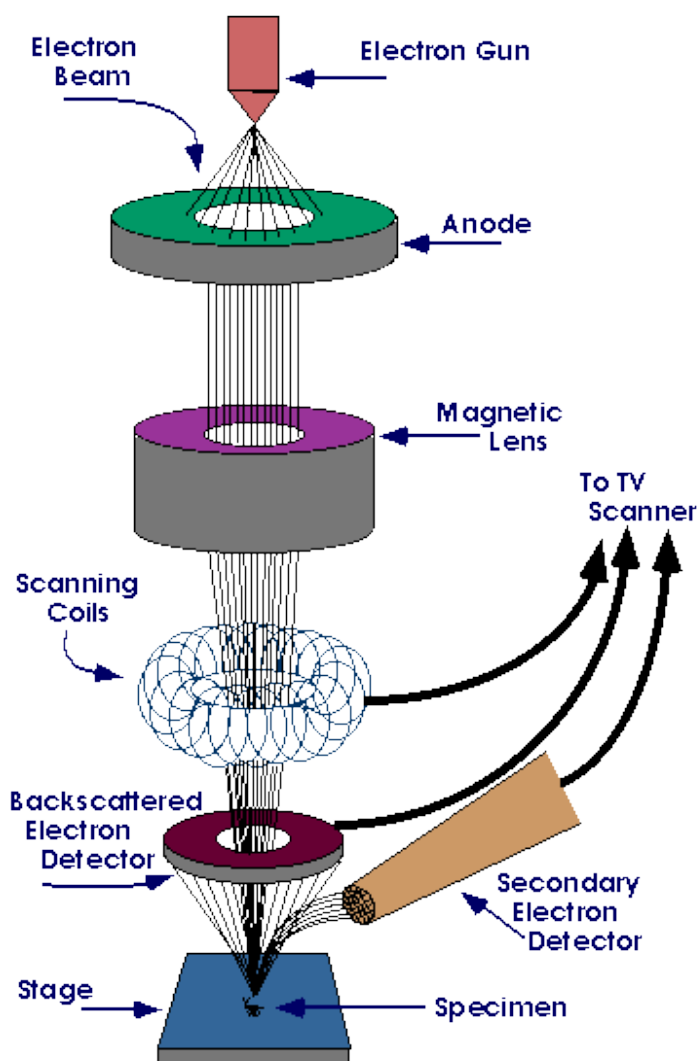


Figure 2.7: Schematic diagram of the Scanning Electron Microscope.

[<http://www.purdue.edu/rem/rs/sem.htm>]

2.II.5 Photoluminescence Spectroscopy

Photoluminescence (PL) is the spontaneous emission of light when a material is optically excited. The appropriate excitation energy and intensity is required to be

scanned properly to probe the sample's discrete electronic states accurately. When a light of sufficient energy is incident on a material, photons are absorbed causing electronic transitions within the allowable energy states of the material. Eventually, these excitations relax and the electrons return to the ground state. If radiative relaxation occurs, the emitted light is called PL. This light can be collected and analyzed to yield a wealth of information about the photo-excited material. The PL spectrum provides the transition energies, which can be used to determine electronic energy levels, defects and impurity states in the sample. The PL intensity gives a measure of the relative rates of radiative and non-radiative recombination.

PL is divided into two categories, fluorescence and phosphorescence, depending upon the electronic configuration of the excited state and the emission pathway. Fluorescence is the property of some atoms and molecules to absorb light at a particular wavelength and to subsequently emit light of longer wavelength after a brief interval, which is characterized as the fluorescence lifetime. The process of phosphorescence occurs in a manner similar to fluorescence, but with a much longer excited state lifetime.

PL is a simple, versatile, and nondestructive measurement technique. The PL signal is characterized by two essential features: peak energy and intensity. The excitation energy and optical intensity can be chosen properly in order to yield more accurate information on the energy levels available to electrons in the material. The PL signal often depends on the density of photo-excited electrons and the intensity of the incident beam. The intensity of the PL signal depends on the rate of radiative and nonradiative events, which depends in turn on the density of nonradiative interface. **Figure 2.8** represents the conduction band valence band direct transition along with donor states to valence and, conduction band to acceptor and then non radiative recombination via intermediate states. The bottom picture of **Figure 2.8** shows the schematic layout of photoluminescence set-up. Usually, defects and impurities break the periodicity of the lattice and perturb the band structure locally. This perturbation is attributed to the discrete energy levels lying within the band gap. Depending on the defect or impurity, the state acts as a donor or acceptor of electrons in the lattice.

Surfaces and interfaces contain a high concentration of impurity or defect states. Dangling bonds at a semiconductor surface or defects give rise to electronic states within the bandgap. These mid-gap states fill up to the Fermi level with electrons that originate in the bulk of the material. The fundamental limitation of PL analysis is its reliance on radiative events. Materials with poor radiative efficiency, such as low-quality indirect bandgap semiconductors, are difficult to study via ordinary PL.

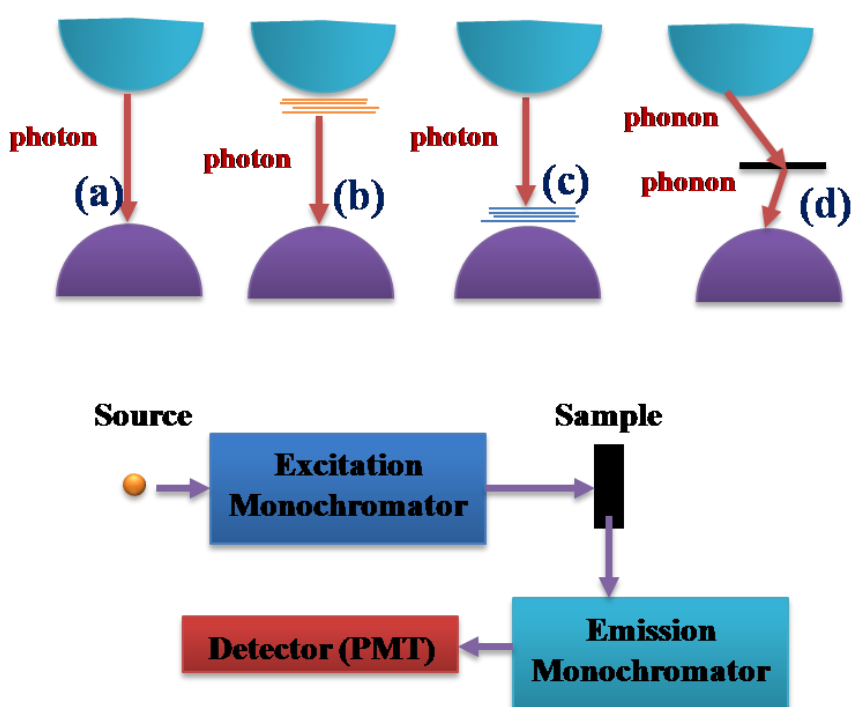


Figure 2.8: (a) CB to VB direct transition, (b) Donor states to VB, (c) CB to acceptor states, (d) Non-radiative recombination via intermediate states and Figure. at down shows: Schematic Layout of PL Set-up

2.II.6 Fourier Transform IR Spectroscopy

FTIR (Fourier Transform Infrared) Spectroscopy provides information about the chemical bonding or molecular structure of organic or inorganic materials. For this measurement, the sample is illuminated with infrared radiation which excites the vibrational modes in the chemically bonded functional groups. This spectrum appears only when the vibrations amongst bonded atoms produces a change in the permanent electric dipole moment of the molecule or solid. Usually it is considered that for a

more polar bond, the IR signal arising from the corresponding bond is more intense.^[21,22]

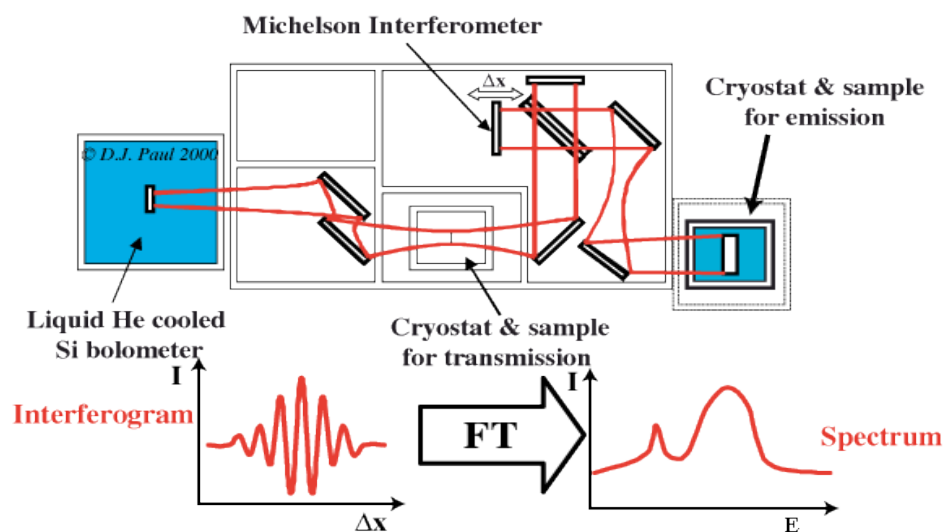


Figure 2.9: Schematic diagram of Fourier Transform Infra Red Spectroscopy (<http://www.sp.phy.cam.ac.uk/~SiGe/FTIR.html>)

The schematic diagram of a Fourier Transform Infra Red Spectrometer is shown in **Figure 2.9**. The spectrophotometer consists of mainly source, monochromator and detector. The source is in some form of filament (e.g. Nernst Filament, made of a spindle of rare earth oxides or globar filament, made of carborundum rod) which is maintained at red- or white-heat by an electric current. The monochromator guides IR beam and focuses to the sample. The detectors are based on either temperature (bolometer/thermometer) or conductivity rise at given frequency (PbS).

The advantage of using FTIR is that the whole spectrum is obtained across the entire frequency range at once with the same resolving power over the entire range. The technique works on the fact that bonds and groups of bonds vibrate at certain characteristic frequencies. A molecule that is exposed to infrared rays absorbs infrared energy at frequencies which are characteristic to that molecule. During FTIR analysis, a spot on the specimen is subjected to a modulated IR beam. The specimen's transmittance and reflectance of the infrared rays at different frequencies is translated into an IR absorption plot consisting of reverse peaks. The resulting FTIR spectral pattern is then analyzed and matched with known signatures of identified materials in

the FTIR library. For sample preparation, well-dispersed nanoparticles are drop-coated onto Si (111) wafers and air-dried while powdered samples are mixed with standard KBr powder. The FTIR measurements of these samples are carried out on a Perkin Elmer Spectrum One FTIR spectrometer operated in the diffuse reflectance mode at a resolution of 4 cm^{-1} .

2.II.7 UV-VIS Spectroscopy

UV-VIS Spectrometer presents information about the spectroscopic absorption of light by the material of interest due to electronic transitions. In semiconductors, when the incident photon energy exceeds the band gap energy of the materials, transition of electrons take place and signal is recorded by the spectrometer whereas in metals when the surface free electrons vibrate coherently with the incident frequency then resonant absorption takes place. This spectrometer can operate in two modes (i) transmission and (ii) reflection mode. For thin films and colloidal nanoparticles well-dispersed in solvent transmission mode is used. For opaque samples diffuse reflectance (DRS) mode is used.

Instrument: The light from the source is alternatively split into one of two beams by a chopper; one beam is passed through the sample and the other through the reference. The detector, which is often a photodiode, alternates between measuring the sample beam and the reference beam. Some double beam instruments have two detectors, and the sample and reference beam are measured at the same time. In other instruments, the two beams pass through a beam chopper which blocks one beam at a time. The schematic of UV-VIS Spectrophotometer in transmission mode has been shown in **Figure 2.10**.

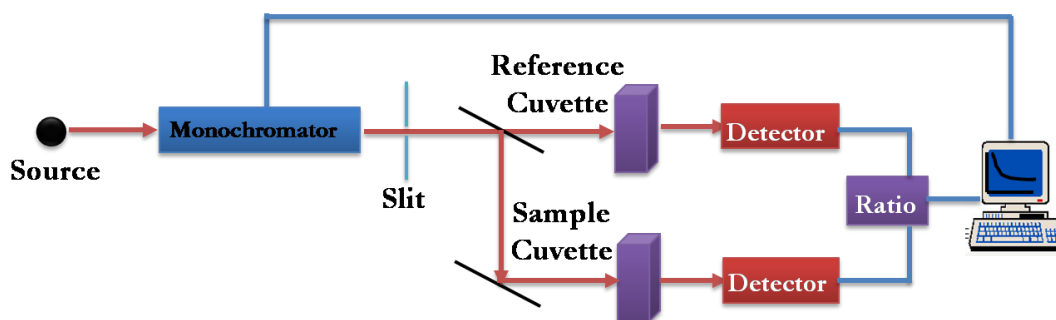


Figure 2.10: Schematics of UV-VIS Spectrophotometer in Transmission Mode

Broadening of spectral transitions: The possible sources for the signal broadening:

(a) Doppler Broadening: Random motion of nanoparticles in the liquids and gaseous samples causes their absorption and emission frequencies to show a Doppler shift and hence the spectrum lines are broadened. This effect is more pronounced in liquids than gaseous samples due to significant collisions in solutions. In the case of solids, the motions of the particles are more limited in extent and less random in direction, so that solid phase spectra are often sharp but show evidence of interactions by the splitting of the lines into two or more components. (b) Heisenberg's Uncertainty Principle: If a system exists in an energy state for a limited time ' δt ' seconds, then the energy of that state will be uncertain (fuzzy) to an extent ' δE ' and is given by $\delta E \times \delta t \approx h/2\pi \approx 10^{-34}$ J.s, where h = Planck's Constant.

Usually life time of excited state is 10^{-8} sec, i.e. 10^8 Hz uncertainty in the radiation frequency which is, in fact, small as compared to UV-Vis frequency regime (10^{14} – 10^{16} Hz).

Intensity of Spectral lines: There are three main factors that decide the intensity of spectral lines: (i) *Transition probability:* The likelihood of a system in one state changing to another state which is usually governed by quantum mechanical selection rules. (ii) *Population of states:* The number of atoms/molecules initially in the state from which the transition occurs. It is governed by the equation: $N_{\text{upper}}/N_{\text{lower}} = \exp(-\Delta E/kT)$; Where, $\Delta E = E_{\text{upper}} - E_{\text{lower}}$, T = temperature (K), k = Boltzman's Constant = 1.38×10^{-23} J/K. (iii) *Concentration and path length:* Clearly since sample is absorbing energy from a beam of radiation, the more sample the more beam traverses, the more energy will be absorbed from it. Besides the amount of the sample, the concentration of the sample is also deciding factor for the energy absorption. Based on this, Beer-Lambert law, which is often written as:

$$I / I_0 = \exp(-\kappa cl) \quad \text{or} \quad I / I_0 = 10^{-\epsilon cl} = T \quad 2.7$$

Where, κ = constant, for particular spectroscopic transition under consideration.

Where T = transmittance = I / I_0 , ϵ = molar absorption coefficient.

Inverting above equation and taking logarithms,

$$I_0 / I = 10^{\epsilon cl} \quad 2.8$$

$$\log(I_0 / I) = \epsilon cl = A, \quad 2.9$$

Where A = absorbance / optical density

Thus, absorbance is directly proportional to the concentration, where the path length and molar extinction coefficient is suppose to be constant for the particular measurement. The source used for the UV and visible light are deuterium and tungsten lamps respectively and the detector used is usually PMT.

2.II.8 Mössbauer Spectroscopy

Mössbauer spectroscopy is a versatile technique that can provide information about the chemical, structural and magnetic properties of a material. ^[23] The key to this technique is the discovery of recoilless γ -ray emission and absorption, referred to as the “Mössbauer Effect”. Certain nuclei embedded in a solid matrix can emit or absorb γ -rays with no recoil, giving rise to resonant nuclear γ -ray absorption. Nuclei in atoms undergo a variety of energy level transitions, often associated with the emission or absorption of γ -rays. These energy levels are influenced by their surrounding environment, both electronic and magnetic, which can change or split these energy levels (**Figure 2.11**). These changes in energy levels can be probed using Mössbauer spectroscopy as the sensitivity of this technique is 1 eV in 10^{13} eV.

When the source and absorber atoms are in different local environments, their nuclear energy levels are different (**Figure 2.11**). At its simplest (blue), this appears in the transmission spectrum as a shift of the minimum away from zero velocity; termed as isomer shift (IS or δ). The 1/2 and 3/2 labels represent the nuclear spin, or intrinsic angular momentum, quantum numbers, ‘I’. Interaction of the nuclear quadrupole moment with the electric field gradient leads to splitting of the nuclear energy levels (red). For ⁵⁷Fe, this causes individual peaks in the transmission spectrum to split into doublets (red) having a quadrupole splitting (QS or Δ). When a magnetic field is present at the nucleus, Zeeman splitting takes place, yielding a sextet pattern (green) and the internal magnetic field B_{hf} ; in the simplest case, the areas of the lines vary in the ratio of 3:2:1:1:2:3.

Therefore Mössbauer spectra are described using three parameters: isomer shift (δ), which arises from the difference in s electron density between the source and the absorber, quadrupole splitting (Δ which is a shift in nuclear energy levels that is induced by an electric field gradient caused by nearby electrons, and hyperfine splitting (for magnetic materials only). Graphically, quadrupole splitting is the separation between the two component peaks of a doublet, and isomer shift is the difference between the midpoint of the doublet and zero on the velocity scale (**Figure 2.11**). So, these changes in the energy levels can provide information about the atom's local environment within a system. Mössbauer spectroscopy can only be applied to a relatively small group of atoms ^{57}Fe is by far the most common element studied using the technique. The experiment was performed in transmission mode with a $^{57}\text{Co}(\text{Rh})$ source in a Wissel spectrometer. The solid sample is exposed to the beam of γ radiation, and a detector measures the intensity of the beam that is transmitted through the sample. The γ -ray energy is varied by accelerating the gamma-ray source through a range of velocities with a linear motor. The relative motion between the source and sample results in an energy shift due to the Doppler effect (change in the apparent frequency of a wave as observer and source move toward or away from each other).

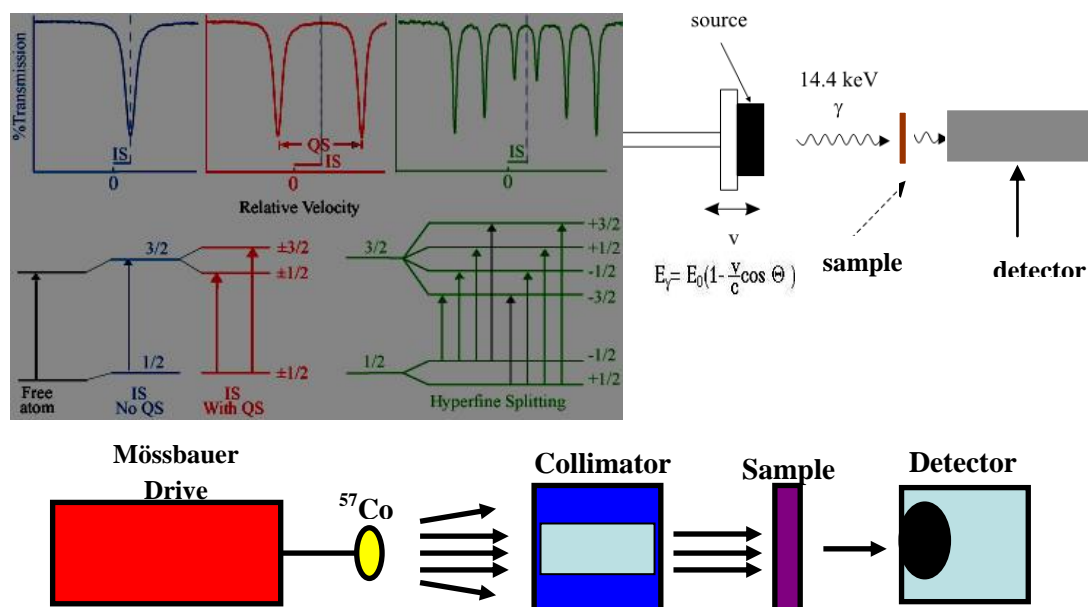


Figure 2.11: Schematics of Mossbauer spectrometer and nuclear energy level splitting

In the resulting spectra, gamma-ray intensity is plotted as a function of the source velocity. The source velocity is calibrated by means of a reference sample, metallic iron ($B_{hf} = 33T$). At velocities corresponding to the resonant energy levels of the sample, some of the gamma-rays are absorbed, resulting in a drop in the measured intensity and a corresponding dip in the spectrum. The number, positions, and intensities of the peaks provide information about the chemical environment of the absorbing nuclei and can be used to characterize the sample. The spectra are then computer-fitted assuming a Lorentzian line shape and isomer shifts are given relative to metallic iron. Mössbauer parameters are temperature-sensitive, and this characteristic is exploited by using lower temperatures to improve peak resolution and induce interesting magnetic phenomena.

2.II.9 X-Ray Photoelectron Spectroscopy

X-ray photoelectron Spectroscopy (XPS) probes the binding energies of core electrons in an atom. Although such electrons play little part in chemical bonding, different chemical environments can induce small changes in their binding energies; this is because the formation of bonds changes the distribution of electrons in the system and hence by modifying the nuclear shielding, produces changes in the effective nuclear charge of the bound atoms ^[24]. XPS is also rarely called as electron spectroscopy for chemical analysis (ESCA). Since only the photoelectrons from the atoms near the surface escape the information obtained is typically from the surface layer of 2-5 nm with a typical sampling area of 1 cm². The actual depth varies with the materials and electron energy. This technique mainly gives information about the elemental composition of the surface of the materials and the information about the chemical state of elements. Usually Al and Mg source is used for producing X-rays to excite photoelectrons from the core levels of atoms in a specimen.

Figure 2.11 shows the schematic for principle of photo-electron spectroscopy as well as Schematic of XPS instrument. When an atom or molecule is subjected to higher energy radiations, photons in the radiations collide with and eject electrons from atoms, leaving behind ions. Ejected electrons depart with different velocities and photoelectron spectroscopy measures the velocity distribution of the released

electrons. Each electron is held in place by nucleus with a characteristic binding energy.

The energy of the photon is imparted to the electron and, if this energy is greater than the B.E., the electron will leave the atom and carry with it an excess energy – thus it will have certain K.E. (and velocity). Clearly the total energy must conserve:

$$h\nu = \text{binding energy} + \text{Work Function} + \text{kinetic energy}$$

$$\text{Binding Energy} = h\nu - \text{Kinetic Energy}$$

Since the excitation energy is known and the kinetic energy is measured, the binding energies of electrons in the atom under examination can be determined. Main components of XPS are (i) X-ray source, (ii) Sample holder, (iii) electron energy analyzer. The (ii) and (iii) component must be in UHV. The X-ray source is a simple X-ray tube with double anodes (typically Al and Mg) incident radiation energy can be switched from one to the other. In both, XPS, the kinetic energy of the ejected electrons is measured using a hemispherical analyzer.

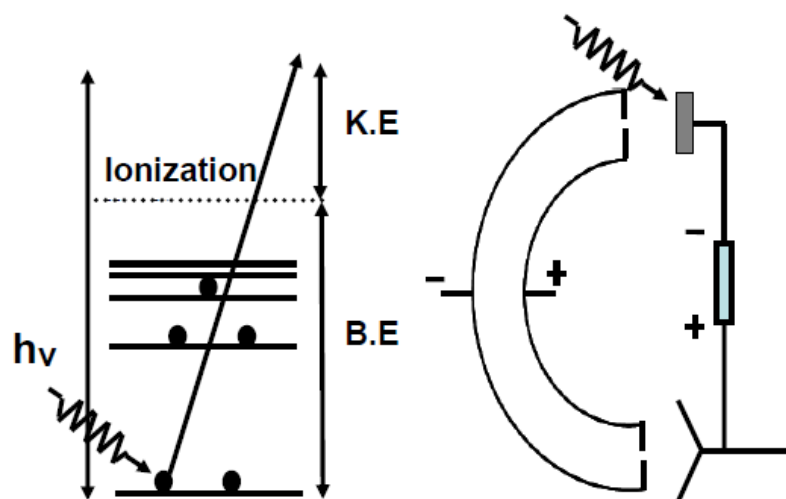


Figure 2.12: (A) Principle of Photo-electron spectroscopy, (B) Schematic of XPS^[24]

Monochromatic X-ray or UV radiation falls on the sample and ejected electrons pass between a pair of electrically charged hemispherical plates which act as an energy filter, allowing electrons of only a particular kinetic energy to pass through –

the pass energy, E_{pass} . The resulting electron current, measured by an electron multiplier, indicates the number of electrons ejected from the surface with that kinetic energy. E_{pass} can be systematically varied by changing the retarding voltage (VR) applied to the analyzer. XPS measurements of different samples were carried out on a VG MicroTech ESCA 3000 instrument at Center for Materials Characterizations (CMC), National Chemical Laboratory, Pune. The core level binding energies (BE) were corrected with the carbon binding energy of 285 eV.

2.II.10 BET Surface Area Measurement

The specific surface area of a material is measured by BET surface area analyzer. In this technique, gas molecules are made to physically adsorb on the solid surface of the specimen.^[25] In 1938, Stephen Brunauer, Paul Hugh Emmett, and Edward Teller published an article about the BET theory. The word “BET” consists of the first initials of their family names. The concept of the theory is an extension of the Langmuir theory, which is a theory for monolayer molecular adsorption, to multilayer adsorption with the following hypotheses: (a) gas molecules physically adsorb on a solid in layers infinitely; (b) there is no interaction between each adsorption layer; and (c) the Langmuir theory can be applied to each layer.

The resulting BET equation is expressed by the following equation

$$\frac{1}{v[(\frac{P_0}{P})-1]} = \frac{c-1}{v_m c} \left(\frac{P}{P_0}\right) + \frac{1}{v_m c} \quad 2.10$$

Where P and P_0 are the equilibrium and the saturation pressure of adsorbates at the temperature of adsorption, v is the adsorbed gas quantity (for example, in volume units), v_m is the monolayer adsorbed gas quantity and c is the BET constant, which is expressed by following equation.

$$c = \exp\left(\frac{E_1 - E_L}{RT}\right) \quad 2.11$$

E_1 is the heat of adsorption for the first layer, and E_L is that for the second and higher layers and is equal to the heat of liquefaction. Equation (2.10) is an adsorption isotherm and can be plotted as a straight line with $1 / v[(P_0 / P) - 1]$ on the y-axis and $\phi = P / P_0$ on the x-axis according to experimental results. This plot is called a BET

plot. The linear relationship of this equation is maintained only in the range of $0.05 < P / P_0 < 0.35$. The value of the slope (A) and the y-intercept (I) of the line are used to calculate the monolayer adsorbed gas quantity v_m and the BET constant c . The following equations can be used.

$$v_m = \frac{1}{A+I} \quad 2.12$$

$$c = 1 + \frac{A}{I} \quad 2.13$$

Total surface area S_{total} and a specific surface area (S) are evaluated by the following equations, where v_m is in units of volume which are also the units of the molar volume of the adsorbate gas, N is Avogadro's number, s is adsorption cross section of the adsorbing species, V is molar volume of adsorbate gas and a is mass of adsorbent (in g)

$$S_{BET,total} = \frac{v_m N s}{V} \quad 2.14$$

$$S_{BET,total} = \frac{S_{total}}{a} \quad 2.15$$

BET surface area measurements of different samples were carried out on a Quadrasorb-SI instrument at National Chemical Laboratory, Pune. This is a state-of-the-art, high-performance Surface Area Analyzer and Pore Size Analyzer with four independent analysis stations.

2.II.11 Superconducting Quantum Interferometry Device (SQUID)

SQUID is an extremely sensitive tool used to measure magnetic moment of the order of 10^{-6} emu. ^[26,27]. Such an immensely high sensitivity of the SQUID devices is associated with measuring changes in magnetic field related with one flux quantum. SQUID consists of two superconductors separated by thin insulating layers to form two parallel Josephson junctions. One of the discoveries associated with Josephson junctions was that flux is quantized in units.

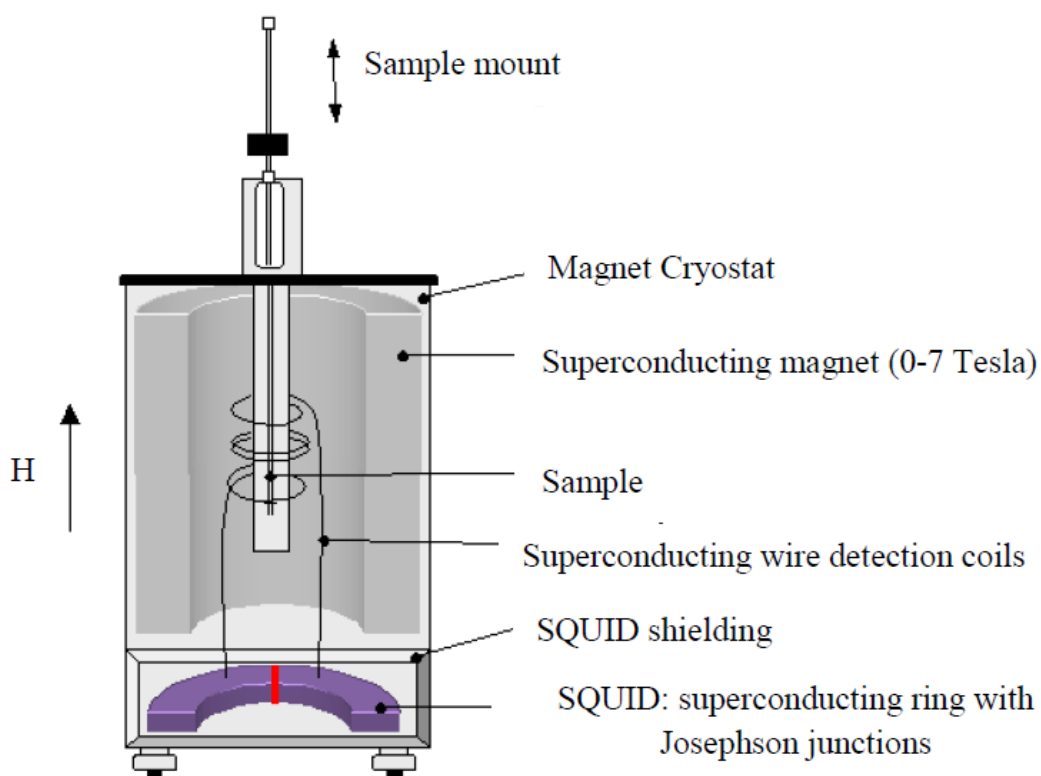


Figure 2.12: An illustration of SQUID Magnetometer

Figure 2.12 shows the schematic diagram or illustration of SQUID Magnetometer. In SQUID magnetometer the sample is placed in an applied magnetic field of 0-11 Tesla produced by a superconducting magnet. The sample is moved slowly through a set of detection coils coupled to the SQUID via superconducting wires. The output voltage detected by the SQUID magnetometer is proportional to the magnetic moment of the sample. The SQUID output voltage, when properly calibrated using a sample of known magnetic moment, can be used to provide accurate values for the magnetization of the sample.

In the present work magnetic property measurements of Magnetite-GO composite using SQUID has been done on instrument Quantum Design MPMS SQUID VSM at National Chemical Laboratory, Pune. The SQUID magnetometer has certain advantages over the VSM, such as it provides better sensitivity (of the order of 10^{-6} emu) in the magnetization measurement as compared to the VSM sensitivity (of the order of 10^{-4} emu). This is because SQUID magnetometer involves

superconducting Josephson junctions, which is very sensitive to any minute change in magnetic flux/voltage. For the operation of these Josephson junctions, they are maintained in liquid helium. Hence, at higher temperature ($> 300\text{K}$), the measurement is difficult as liquid helium starts boiling off. However, in VSM pick up coils do not require cooling for their operation. Therefore, VSM can be operated at higher temperature also.

2.II.12 Electrochemical Measurements

Cyclic voltammetry or CV is a type of potentiodynamic electrochemical measurement. In a cyclic voltammetry experiment the working electrode potential is ramped linearly versus time as in case of linear sweep voltammetry, however when cyclic voltammetry reaches a set potential, the working electrode's potential ramp is inverted. Thus potential scans are taken for a particular potential window in cyclic manner. The current at the working electrode is plotted versus the applied voltage to give the cyclic voltammogram trace.

In this case the voltage is swept between two values at a fixed rate, however now when the voltage reaches V_2 the scan is reversed and the voltage is swept back to V_1 . A typical cyclic voltammogram (**Figure 2.13**) recorded for a reversible single electrode transfer reaction is shown in below. In cyclic voltammetry, the electrode current versus applied potential is represented. The ramping is known as the experiment's scan rate (V/s). The potential is applied between the reference electrode and the working electrode and the current is measured between the working electrode and the counter electrode. These data are then plotted as current (i) vs. potential (E). As shown in **Figure 2.13**, the forward scan produces a current peak for any analytes that can be reduced (or oxidized depending on the initial scan direction) through the range of the potential scanned. The current will increase as the potential reaches the reduction potential of the analyte, but then falls off as the concentration of the analyte is depleted close to the electrode surface. If the redox couple is reversible then when the applied potential is reversed, it will reach the potential that will reoxidize the product formed in the first reduction reaction, and produce a current of reverse polarity from the forward scan. This oxidation peak will usually have a similar shape to the reduction peak. As a result, information about the redox potential and

electrochemical reaction rates of the compounds is obtained. Cyclic Voltammetry provides a wide range of information about the electrode and electrode/electrolyte interaction and the nature of the cyclic voltammogram depends upon the types of measurements for desired applications.

In this thesis work we have used cyclic voltammetry measurements for supercapacitor and battery applications. The charge (capacity) of each cycle is measured and the capacitance C_s , in farad (F), is calculated by the following equations. Both are plotted as a function of cycle number. This curve is called the capacity curve. In practice, charge is commonly called capacity. If capacity falls by a set value – 10 % or 20 % is usual and, the actual number of cycles indicates the cycle-life of the capacitor. In general, commercial capacitors can be cycled for hundreds of thousands of cycles.

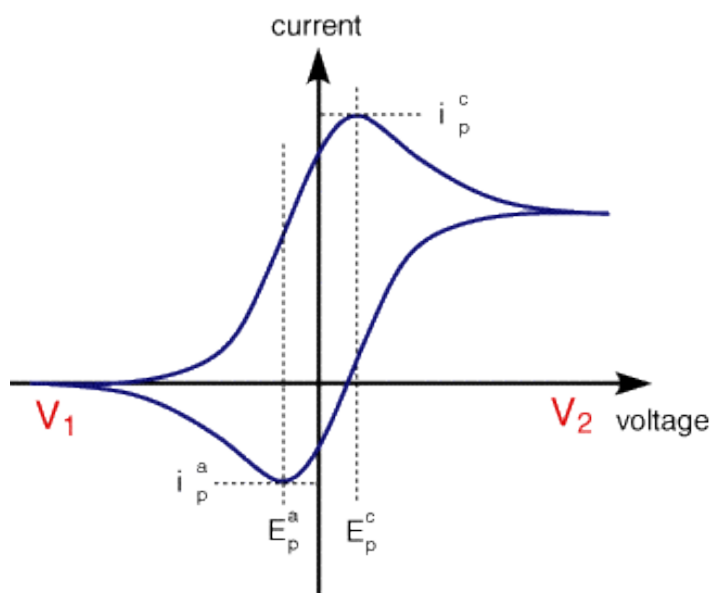


Figure 2.13: A typical cyclic voltammogram (<http://www.ceb.cam.ac.uk/pages/linear-sweep-and-cyclic-voltametry-the-principles.html>)

The slope of the curve (dv/dt) is constant and is defined by following equation.

$$C = Q/V \text{ or } Q = CV$$

Therefore,

$$dQ/dt = Cs dv/dt$$

$$\text{and } I = Cs dv/dt \quad \text{hence, } Cs = 2I \frac{dt/dv}{m} \quad 2.16$$

Where, V is the cell potential in volts (V), I is the cell current in amperes (A), and Q is the charge in coulombs (C) or ampere-seconds (As). The factor 2 comes in the last equation to account for 2 electrode system. The capacitance (C) should be divided by the mass loading of carbon in order to get specific capacitance.

2.III References

1. Gleiter, *Progress in Meter. Sci.* **1989**, 33, 323.
2. N. Wada, *Jap. JK. Appl. Phys.*, **1969**, 8, 551.
3. K. Tanaka, K. Ishizaki, and M. Uda, *J. Mater. Sci.*, **1987**, 22, 2192.
4. J. S. Haggerty, W. R. Cannon, and J. I. Steinfeld, "Laser Induced Chemical Process." Plenum Press, New York, **1981**.
5. J. Gopalakrishnan, *Chem Mater*, **1995**, 7, 1265.
6. L. G. Hubert-Pfalzgraf, S. Daniele, J.M. Decams, *J. Sol-Gel Sci. Technol.*, **1997**, 8, 49.
7. X. Wang, Z. Zhang, and S. Zhou, *Mater. Sci. Eng. B: Solid-State Mater. Adv. Technol.*, **2001**, B86, 29.
8. U. Schubert and N. Hüsing, *Synthesis of Inorganic Materials*, Wiley-VCH, **2000**, pp. 396.
9. C. T. Nguyena, D. P. Kim, *J. Mater. Chem.* **2011**, 21, 14226.
10. J. Yamashita, M. Shioya, T. Kikutani, T. Hashimoto, *Carbon*, **2001**, 39, 207.
11. A. Ahmadpour and D. D. Do, *Carbon*, **1997**, 35, 1723.
12. J. Laine and A. Calafat, *Factors Carbon*, 1991, **29**, 949.
13. N. Chandrasekharan and P. V. Kamat, J. Hu and G. Jones, *J. Phys. Chem. B*, **2000**, 104, 11103.
14. P. V. Kamat, *J. Phys. Chem. B*, **2002**, 106, 7729.
15. Wyckoff, R. W. G. *Crystal Structures*, 2nd ed.; Wiley: New York, **1964**.
16. R. Loudon, *Adv. Phys.* **2001**, 50, 813.
17. D. A. Long, *Raman Scattering*, McGraw Hill Book Company, New York, **1977**.

18. J. Duan, S. Yang, H. Liu, J. Gong, H. Huang, X. Zhao, R. Zhang, Y. J. Du, *Am. Chem. Soc.*, **2005**, 127, 6180.
19. Y. Ding, Z. L. Wang, *J. Phys. Chem. B.*, **2004**, 108, 12280.
20. G. Lawes, *Scanning electron microscopy and X-ray microanalysis: Analytical chemistry by open learning*, John Wiley & sons, **1987**.
21. C. N. Banwell, E. M. McCash, *A Book: Fundamentals of Molecular Spectroscopy, 4th Ed.*, Tata McGraw Hill Publishing Co. Ltd., **2002**.
22. J. Coates, *Interpretation of Infrared Spectra: A Practical Approach, Encyclopedia of Analytical Chemistry*, R.A. Meyers (Ed.), 10815, John Wiley & Sons Ltd, **2000**.
23. V. G. Bhide, *Indian Ref: Mössbauer Effect and Its Applications*, ed. by (Tata McGraw Hill, New Delhi, **1973**).
24. X. D. Wu, D. Dijkamp, S. B. Ogale, A. Inam, E. W. Chase, P. F. Miceli, C. C. Chang, J. M. Tarascon, T. Venkateshan *Appl. Phys. Lett.*, **1987**, 51, 861.
25. A. Adamson, A. Gast, *Physical Chemistry of Surfaces, 6th ed.*, Wiley, **1997**.
26. A. Barone *Principles and Applications of Superconducting Quantum Interference Devices*, ed. World Scientific Publishing, **1992**.
27. J. Clarke, *Scientific American* **1994**, 271, 36.

Chapter-3

From Dead Leaves to High Energy Density Supercapacitor

*In this work, functional microporous conducting carbon with high surface area of about $1230 \text{ m}^2 \text{ g}^{-1}$ is synthesized by a single step pyrolysis of plant dead leaves (dry waste, ground powder) without any activation and studied for supercapacitor application. Although the detailed study performed and presented here is on dead Neem leaves (*Azadirachta indica*), the synthesis method is generic and applicable to most forms of dead leaves. Indeed we have examined the case of dead Ashoka leaves as well. The comparison between the Neem and Ashoka leaves brings out the importance of the constitution and composition of the bio-source in the structural and electronic properties of carbon. We have also studied the cases of pyrolysis of green leaves and un-ground dead leaves against the ground dead leaves powder. The concurrent high conductivity and microporosity realized in the case of ground dead leaves powder materials are key to the high energy supercapacitor performance.*



Dead leaves to Supercapacitor

3.1 Introduction

Waste management is one of the most prevalent problems of big cities. Fortunately, through several environmental awareness programs communities have begun to separate dry and wet waste matter. Most such waste is a rich source of carbon but may contain other elements in different proportions depending on the source. In most of the municipal waste management centers, the waste from natural sources is directly burnt off. This produces ash and hazardous gaseous pollutants. There have been some initiatives to employ the ash in certain applications in the form of passive fillers. But other than this there has not been much effort on reusing or converting the natural waste to a significant application. With extensive ongoing research work around carbon-based opto/electronic/energy applications, if the natural waste and some of the man-made waste is harnessed towards electronically active functional forms of carbon, one could get a value-added product for diverse and growing carbon-based applications.

Carbon is the most naturally occurring abundant material exhibiting variety of molecular and structural forms such as graphite, diamond, nanotubes, graphene, fullerene, nano-diamonds, amorphous carbon, porous carbon etc. with various applications.^[1-6] Amongst these porous carbon and graphene have high surface area, chemical inertness, and synthetically tunable electrical, thermal and optical properties. These versatile properties of specific carbon based materials make them efficient to be used in supercapacitors, batteries,^[7,8] and as superabsorbents for gases and toxins.^[9]

Supercapacitors have been attracting significant research interest lately due to their wide range of applications in electrical vehicles, digital devices, pulsing techniques etc. due to their high durability, high power density and fast charging-discharging mechanism.^[10-12] Mostly activated carbon materials having high surface area (2000-3000 m²g⁻¹) are used as electrode materials in supercapacitor applications with specific capacitance around 250-350 Fg⁻¹.^[13-21] Clearly efforts aimed at enhancing these properties by suitably engineering of the synthesis of functional carbon while concurrently reducing costs is a desirable research endeavour.

Scientists have tried several interesting synthetic routes to obtain high quality carbon. These include carbonization of organic/polymeric precursors,^[22-24] chemical vapour deposition,^[25-31] excimer laser ablation of graphitic targets,^[32-34] sputtering / plasma based synthesis,^[35-36] arc discharge synthesis,^[37-38] chemical methods etc.^[39-40] More recently researchers have started utilizing organic waste materials for the synthesis of carbon for specific absorbant or charge storage applications.^[7-9, 41] Waste materials such as food, agricultural wastes, and even insects have already been utilized as a bio-source of carbon in graphene synthesis.^[42-48] Activated carbon has also been synthesized by pyrolyzing waste material with some chemical or physical additives as agents for activation. The purpose of such activation is to enhance the surface area and introduce porosity to make the materials functionally more effective. Physical activation mainly includes activation with steam, CO₂ etc. and chemical activation involves uses of chemicals such as NaOH, KOH, CaO, Ca(OH)₂, K₂CO₃, etc. which are known as porogens.^[13-21, 49-53]

In this work we demonstrate synthesis of high surface area microporous conducting carbon material by one step pyrolysis of plant dead leaves (abundant waste material) without any chemical or physical activation and have examined its properties for supercapacitor application.^[54] Although the detailed study performed and reported here is on dead Neem leaves (*Azadirachta indica*), the process is clearly generic and applicable to most forms of dead leaves. Indeed we have examined the case of dead Ashoka leaves as well. The comparison between the Neem and Ashoka leaves brings out the importance of the constitution and composition of the bio-source in the nature of carbon formed and its properties. We have also examined and compared the cases of pyrolysis of green leaves as well as un-ground dead leaves with that of ground dead leaves powder in full details. To the best of our knowledge there is only one report by Beguin et.al. in the literature wherein they have demonstrated synthesis of high surface area carbon from waste sea-weeds without any activation.⁵⁵ Using the functional carbon derived from dead plant leaves (CDDPL) as a charge storage material in a supercapacitor, we have achieved very promising results: a high specific capacitance (400 Fg⁻¹) and very high energy density 55 Wh kg⁻¹ at a current density of 0.5 Ag⁻¹. The areal capacitance value of the carbon derived from dead

(Neem) plant leaves (CDDPL) is also significantly high ($32 \mu\text{F cm}^{-2}$). Moreover, in an organic electrolyte the material shows a specific capacitance of 88 Fg^{-1} at a current density of 2 Ag^{-1} . These performance features can be attributed to the high specific surface area associated with the narrow micropore distribution as well as high electrical conductivity of the CDDPL material. This performance is clearly superior to that of most commercially available and synthetically obtained activated carbon forms that have been used in ultracapacitor charge storage networks.

Despite their high power density capability supercapacitors always struggle with the limitation of low energy density. To solve this problem hybrid capacitor designs - two different electrodes- have started to become more popular. Such hybrid capacitors have also been classified into three categories, namely the composite type, asymmetric type and battery type. Detail description of these types has been provided in chapter 1. In our work apart from EDLC type supercapacitor we have also used the dead leaves derived carbon as electrode material in battery type hybrid capacitor configuration. In Li ion hybrid electrochemical capacitor configuration with $\text{Li}_4\text{Ti}_5\text{O}_{12}$ capacity of $\sim 32 \text{ mAhg}^{-1}$ and a specific capacitance of 72 Fg^{-1} is obtained with the leaf derived carbon. This is comparable with the results obtained from the commercial activated carbon electrode materials. The details pertaining to these studies are presented and discussed in this chapter.

3.2 Experimental

3.2.1 Materials

Neem (*Azadirachta indica*) dead leaves were collected from National chemical laboratory campus (please see the photo in **Figure 3.1**). N-Methyl-2-pyrrolidone (NMP) was used from Rankem chemicals and PVP (Polyvinylpyrrolidone) was obtained from Aldrich Chemicals. Ashoka (*Saraca asoca*) leaves were also obtained locally.

3.2.2 Synthesis of functional carbon

The dead Neem leaves were collected in large quantity, thoroughly washed, cleaned and dried at 60°C in an oven. These dried leaves were crushed to get fine

powder which was stored in a completely dry atmosphere. For the synthesis of functional carbon 10g Neem leaf powder was heated in an alumina crucible at 600°C, 800°C or 1000°C for 5 hrs in different experiments in argon atmosphere at a heating rate of 10°C per min in a split tube furnace. **Figure 3.1** shows the process pathway used for the synthesis of carbon from dead leaf powder and subsequent supercapacitor measurements.



Figure 3.1: Schematic diagram for the synthesis of functional carbon from dead leaves and the supercapacitor based thereupon.

For the sake of comparison pyrolysis of dead leaves from another plant source namely Ashoka (*Saraca asoca*) was also performed at 1000°C for 5 hrs and the corresponding material was studied. In all cases the light green coloured Neem leaf powder was changed to black coloured carbon after heating. This carbon was then thoroughly washed and ground in a mortar pestle to get fine powders. This carbon was characterized by several techniques. The process discussed in this work is easily scalable to large amount for the synthesis of functional mesoporous conducting carbon. We also examined and compared the cases of pyrolysis of green leaves as well as un-ground dead leaves with that of ground dead leaves powder.

3.2.3 Electrochemical Measurements in 1M H₂SO₄

All the electrodes were prepared on glassy carbon. Two glassy carbon substrates having similar area were used for each measurement. The carbon material was loaded on the substrate following standard procedure protocol used for supercapacitor measurements. Thus, 80 wt % Neem leaf derived carbon (CDDPL) was mixed with 15 wt % conducting carbon (acetylene black) and 5wt% PVP binder. To the above mixture 2-3 drops of NMP (N-Methyl-2-pyrrolidone) were added and ground thoroughly to make viscous slurry. Then this slurry was coated on the glassy carbon substrate with 1 mg loading in 1 cm² area. After making the electrodes they were dried in vacuum for 24 hrs at 60°C for the measurements. Electrochemical cyclic voltammetry studies were performed in 1M H₂SO₄ solution between potential range 0-1V at various sweep rates.

3.2.4 Electrochemical Measurements with 1M LiPF₆ in EC: DEC

All the electrochemical measurements were conducted in two electrode coin-cell (CR2016) assembly. For the coin cell assembly, electrodes were made of 4 mg of leaf derived carbon, 2 mg of super-p (conducting carbon) and 1 mg of binder TAB-2. Supercapacitors were assembled with two symmetric carbon electrodes and separated by Whatman paper and filled with 1 M LiPF₆ in EC:DEC (by 1:1 wt.%, DAN VEC) electrolyte solution. Cyclic voltammetric (CV) studies were carried out using Solartron, 1470E and SI 1255B Impedance/gain-phase analyzer coupled with a potentiostat.

3.2.5 Electrochemical Impedance Spectroscopy Measurements

Electrochemical Impedance Spectroscopy measurements (EIS, Autolab PGSTAT 30 (Eco-Chemie)) were performed for symmetrical supercapacitor cell consisting of the dead Neem leaf derived carbon electrodes in both 1M H₂SO₄ (aqueous) and 1M LiPF₆ in EC: DEC (organic) electrolytes. The frequency range used for the study was from 10 kHz to 10 mHz in the presence of AC amplitude of 10 mV with no external DC applied voltage.

3.2.6 Electrochemical measurements for battery type hybrid supercapacitor

All the electrochemical measurements were carried out by the standard two electrodes CR 2016 coin cell assembly. The composite test electrodes were formulated with 80% active material, 10% of conducting carbon (Super-P), 10% of binder (teflonized acetylene black, TAB-2) with ethanol as a solvent and pressed over 200 mm² stainless steel mesh (Goodfellow, UK). For the single electrode performance (half-cells), insertion type 100 material Li₄Ti₅O₁₂, Neem leaf derived carbon and commercial AC were used as working electrode materials and metallic lithium served as both the counter and reference electrode. Micro-porous fibrous paper (Whatman, Cat. No. 1825-047, UK) was used as a separator and filled with 1M LiPF₆ in ethylene carbonate (EC) / dimethyl carbonate (DMC) (1:1 wt %, Selectipur LP 30, Merck KGaA, Germany) as electrolyte solution for both the half-cell and Li-Hybrid electrochemical capacitor assembly.

3.2.7 Characterization

The functional carbon products synthesized from dead leaves by the different protocols stated above were examined by X-ray powder diffraction using Philips X'Pert PRO diffractometer with nickel-filtered Cu K α radiation, Raman spectroscopy using LabRAM HR800 from JY Horiba and high-resolution transmission electron microscopy (IFEI, Tecnai F30, FEG with 300 kV). The surface area values of all the samples were determined by Brunauer Emmett Teller (BET) adsorption method (Quadratorb automatic volumetric instrument). Cyclic Voltametry measurements were performed by Auto Lab (model PGSTAT 30 ,eco-chemie).

3.3 Results & Discussions

Analysis of the composition of fresh Neem leaves (**Table 3.1**), reveals a 59.4% moisture content. In dry leaves the moisture content is far less and hence the primary constituents of dead Neem leaves are carbohydrates, fibers and protein. Carbohydrate has been established as an important source of functional carbon. ^[56-58] The fiber, which is mainly composed of cellulose, lignin and hemicelluloses, also contributes to carbon source. Besides these organic components, Neem leaves also

contain Ca and Mg in minute amounts. Interestingly Ca and Mg salts have already been independently used as porogens to create pores in the synthesis of activated carbon. Thus the natural presence of these minerals in dead Neem leaves should help create pores in the synthesized carbon without activation, as discussed later. **Figure 3.2a** shows XRD pattern of the carbon synthesized from Neem dead leaves at 1000°C. The two broad peaks around $2\theta \sim 23.3^\circ$ and 43.8° represent graphitic carbon, albeit with some disorder. The specific nature can be further elucidated by Raman spectroscopy. **Figure 3.2b** shows the Raman spectra for the same carbon material. The peaks present around 1320 cm^{-1} and 1590 cm^{-1} correspond to the characteristic D and G bands of carbon, respectively. The D (defect) band (1320 cm^{-1}) is due to the breathing mode of κ -point phonons of A_{1g} symmetry and the G (graphitic) band (1580 cm^{-1}) is assigned to the E_{2g} phonon of sp^2 carbon atoms.^[59-60] The high $I_D: I_G$ ratio (1.15) indicates presence of disorder in the carbon matrix.^[61]

Moisture	59.4%
Proteins	7.1%
Fat	1.0%
Fibre	6.2%
Carbohydrates	22.9%
Minerals	3.4%
Vitamin C	218 mg/100g
Glutamic acid	73.30 mg/100g

Table 3.1: Chemical composition of fresh Neem leaves

The HRTEM image in **Figure 3.2c** shows a highly porous network morphology which is revealed to be in the form of faceted nanometric pores in **Figure 3.2d**. The pore size of just 2 nm or less is reflected in **Figure 3.2e**. The onion-like n-layer graphitic character (measured d-spacing equal to 0.34 nm) is brought out in **Figure 3.2f**. This renders good conductivity.

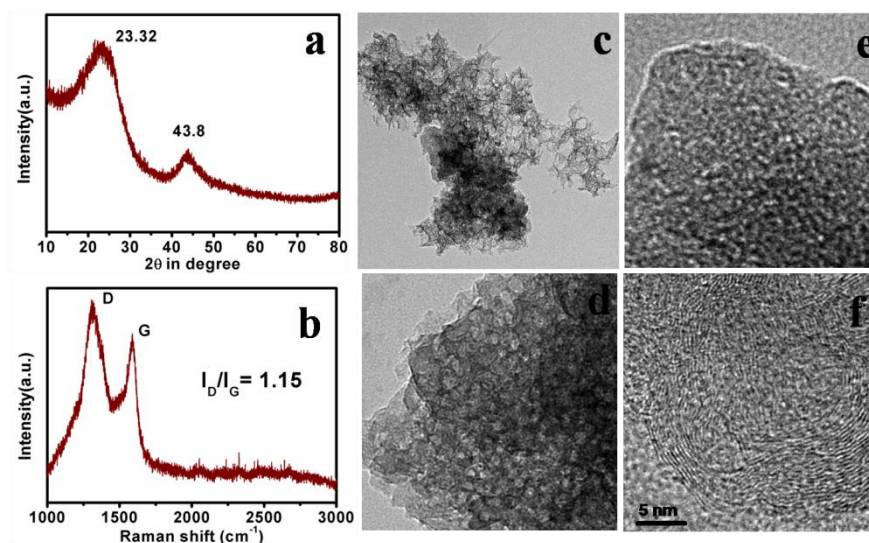


Figure 3.2: (a) XRD Spectra, (b) Raman Spectra, (c-f) HR-TEM images, of the carbon derived from dead plant leaves (CDDPL)

Figure 3.3a depicts the pore size distribution (PSD) for Neem leaf derived carbon (CDDPL material) as obtained by N₂ adsorption which shows a bimodal distribution of micropores and mesopores. Since nitrogen is known to undergo condensation process in micropores, [62] to obtain a more reliable pore size distribution (PSD) we also performed the gas adsorption-desorption experiments with CO₂ at 273K. The PSD thus obtained is plotted in **Figure 3.3b**. This figure clearly shows a bimodal distribution of 0.5 to 1 nm (5-10 Å) micropores along with a small proportion around 2 nm (20 Å) mesopores. The inset of **Figure 3.3a** shows BET nitrogen adsorption-desorption isotherm at 77K of the CDDPL material, while the inset of **Figure 3.3b** shows the isotherm for CO₂ adsorption case. The isotherm of **Figure 3.3a** corresponds to a hysteresis loop that is characteristic of a type IV isotherm. This hysteresis loop indicates capillary condensation which arises due to a different mechanisms of adsorption and desorption in micropores. The loop described above can be further categorized as H4 type (associated with narrow pore size distribution). Low pressure hysteresis is observed in the isotherm plot which is also due to presence of micropores in the system. The specific surface area measured in accordance with the standard BET method is 1230 m²g⁻¹.

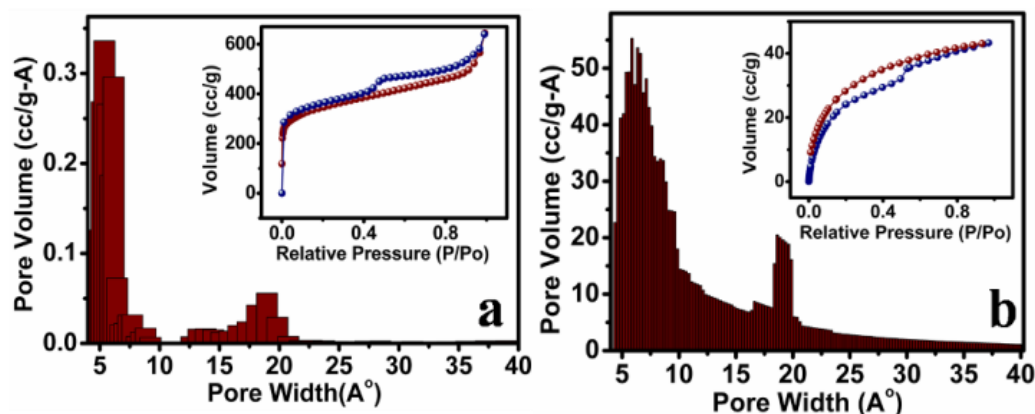


Figure 3.3: (a) Pore size distribution in N_2 for Neem leaf derived carbon, inset is the adsorption-desorption isotherm for N_2 ; (b) Pore size distribution in CO_2 for Neem leaf derived carbon, inset is the adsorption-desorption isotherm for CO_2

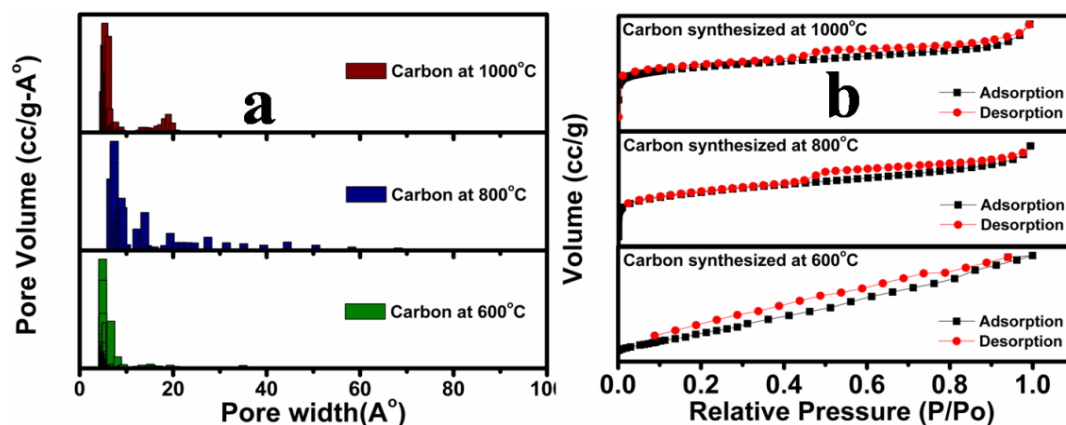


Figure 3.4: (a & b) Pore size distribution and N_2 adsorption isotherms of carbon pyrolyzed at different temperature (600°C, 800°C and 1000°C)

The surface area value thus realized without any activation or pre/post treatment is quite high as compared to other cases of synthetic carbon obtained by using activating agents such as KOH, K_2CO_3 etc. which specifically introduce pores for the enhancement of surface area. The high surface area compounded with a bimodal size distribution comprising of micropores and mesopores is useful from the standpoint of supercapacitor application. Micropores have high surface area to volume ratio and when present in significant amount play important role in the adsorption-desorption processes via diffusion. Mesopores contribute to the large surface but also provide high adsorbate accessibility by providing wider transport

channels to micropores.^[63]

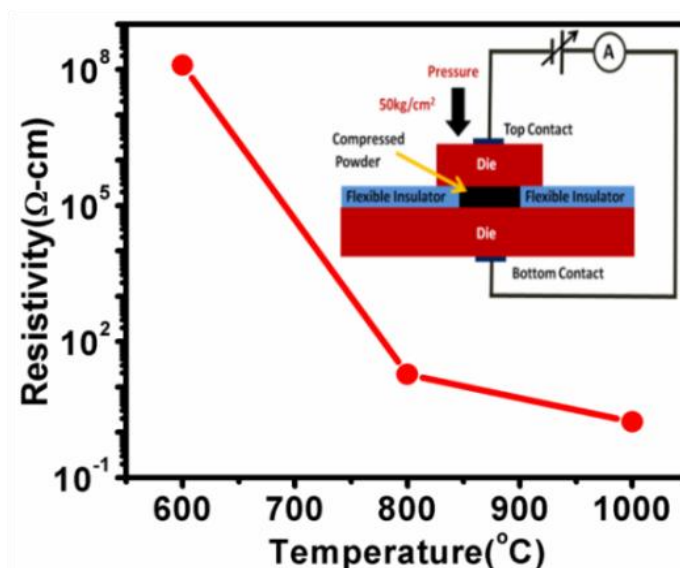


Figure 3.5: Resistivity of carbon materials synthesized at 600°C, 800°C and 1000°C; inset is the schematic diagram of conductivity measurements under pressure.

For comparison we also examined the surface area and pore distribution for the carbon pyrolyzed at other temperatures such as 600°C and 800°C. The pore distribution diagram and adsorption-desorption isotherms for all the three cases (600°C, 800°C and 1000°C) are provided in **Figure 3.4a and b**. In the case of the sample pyrolyzed at 800°C the surface area is significantly lower, down to 229 m²g⁻¹, whereas in the case of the sample pyrolyzed at 600°C the surface area is even lower, only 49 m²g⁻¹. In the 600°C sample mostly micropores are observed, whereas in the 800°C sample some mesopores appear but with a broad size distribution.

We also estimated the conductivity of carbon obtained by pyrolysis at 600°C, 800°C or 1000°C for 5h in flowing argon, because it is also an important parameter for supercapacitor application. Since it is very difficult to make a mechanically strong pellet out of porous carbon powder for conductivity measurements, all the conductivity measurements were carried out under an applied fixed and measured pressure (50 kg cm⁻²). The schematic diagram of the measurement process is depicted in the inset of **Figure 3.5**, where the powder is placed in a die and a known pressure is applied. The contact is

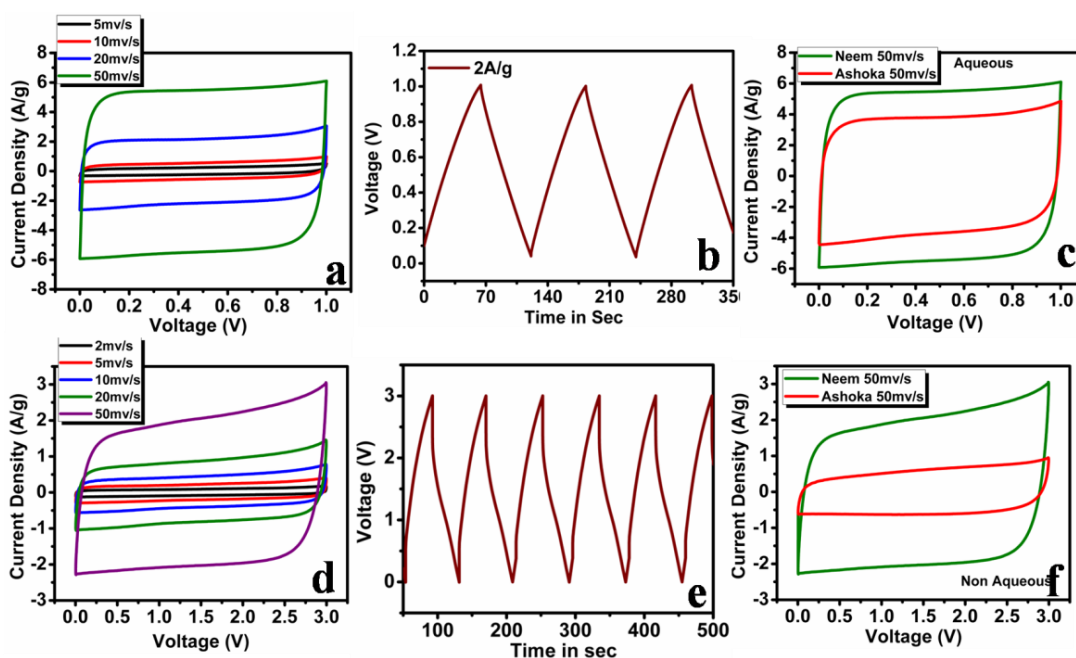


Figure 3.6 : (a-c) aqueous measurements and (d-f) is non aqueous measurements : (a & d) Cyclic Voltametry (CV) measurements of Neem leaf derived carbon at different scan rates in $1M H_2SO_4$ (aqueous) and $1M LiPF_6$ in EC:DEC (organic) respectively ; (b&e) Galvanostatic charge discharge curve of Neem leaf derived carbon at $2A g^{-1}$ in aqueous and organic respectively; (c&f) CV curve of Neem leaf derived carbon and Ashoka leaf derived carbon at $50 mvs^{-1}$ scan rate in aqueous and organic electrolyte respectively.

made from both the sides of the die, and the top and bottom parts of the die are separated by a flexible insulator to avoid contact. Under the known pressure the resistance is measured and the resistivity is calculated and shown in **Figure 3.5**. From the resistivity values it is observed that with increase in the maximum pyrolysis temperature the resistivity decreases rapidly. The resistivity values of the samples synthesized at $600^{\circ}C$, $800^{\circ}C$ and $1000^{\circ}C$ are found to be $\sim 1.25 \times 10^8 \Omega cm$, $\sim 19 \Omega cm$, and $\sim 1.7 \Omega cm$, respectively. Clearly, the carbon synthesized at $1000^{\circ}C$ is found to be highly conducting in nature.

Electrochemical measurements were performed to evaluate the performance of the material in the context of supercapacitor application in both aqueous and organic electrolyte media. The corresponding results are summarized in **Figure 3.6**. We observed that the electrochemical (supercapacitor) properties of the samples

pyrolyzed at 600°C and 800°C are much inferior to those of the sample pyrolysed at 1000°C (**Figure 3.7 and Table 3.2**).

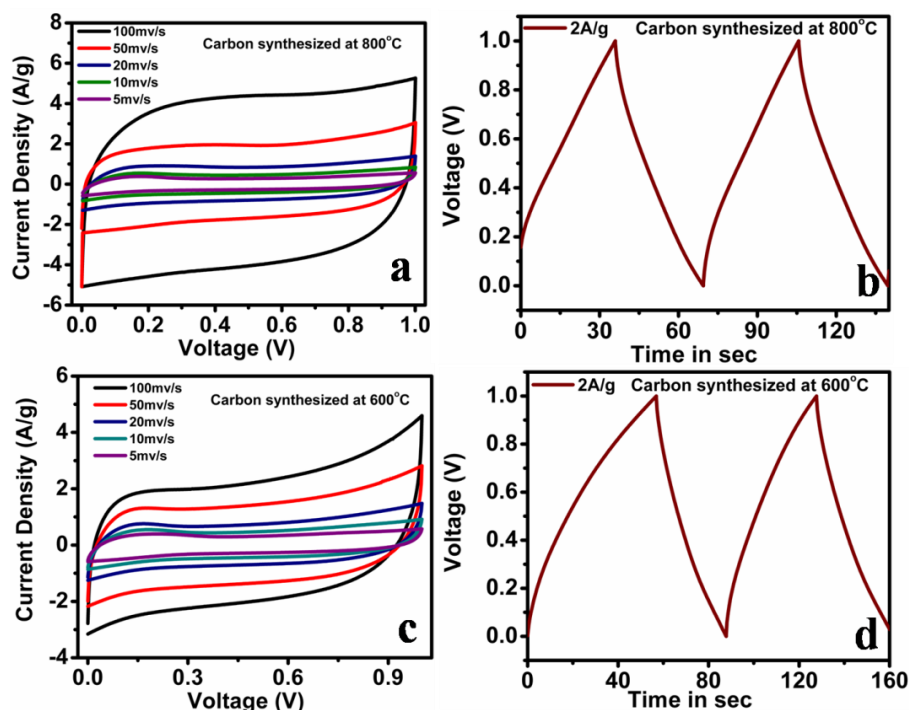


Figure 3.7: (a & b) Cyclic Voltammetry and charge discharge curves for Neem leaf derived carbon at 800°C; (c and d) Cyclic Voltammetry and charge discharge curves for Neem leaf derived carbon at 600°C

Therefore, in the following discussion we focus on carbon obtained by pyrolyzing dead leavaes at 1000°C. As shown in **Figure 3.6a**, a nearly perfect rectangular shaped loop is obtained for a sweep rate of 5, 10, 20, and 50 mVs⁻¹ without any redox peaks (oxidation or reduction). In the supercapacitor context such a rectangular shape represents a perfect electrical double layer formation (reversible adsorption and desorption of the ions) across the surface of the carbon, a testimony to the high specific surface area microporous character of the material. From the data shown in **Figure 3.6a**, it can be seen that the capacitive behaviour is maintained even at a very high scan rate. This performance at high scan rate establishes the high power capability of the microporous CDDPL material.

Pyrolysis Temperature (°C)	Specific Capacitance (Fg ⁻¹)	Specific Energy Density WhKg ⁻¹			Specific Power Density WKg ⁻¹		
		0.5Ag ⁻¹	1Ag ⁻¹	2Ag ⁻¹	0.5Ag ⁻¹	1Ag ⁻¹	2Ag ⁻¹
600	70	10	4	2.5	151	163	257
800	180	25	17	11	523	785	1191
1000	400	55	42	40	569	1191	2526

Table 3.2: Comparison of Specific capacitance, Energy density and power density of all the three carbon materials synthesized at 600°C, 800°C and 1000°C

For quantitative considerations, the specific capacitance is calculated from the galvanostatic charge discharge values by using the following equation 3.1:

$$C_s = \frac{2I \frac{dt}{dv}}{m} \quad 3.1$$

Where C_s is the specific capacitance (Fg⁻¹), I is current, m is the active mass and (dv/dt) is the slope obtained from the discharge curve. The typical charge-discharge plots at 2Ag⁻¹ current densities are shown in **Figure 3.6 b**. The specific capacitance values are calculated at different current densities ranging from 0.5 Ag⁻¹ to 10 Ag⁻¹, and are given in **Figure 3.8**. The highest specific capacitance value 400 Fg⁻¹ is obtained at a current density of 0.5 Ag⁻¹. As the current density increases the specific capacitance value decreases which is related to the limited diffusion of the active ions on the electrode surface because of fast charging. At high current density all the micropores are not accessible to the electrolyte, hence the relative capacitance is less as compared to the capacitance at low current density.

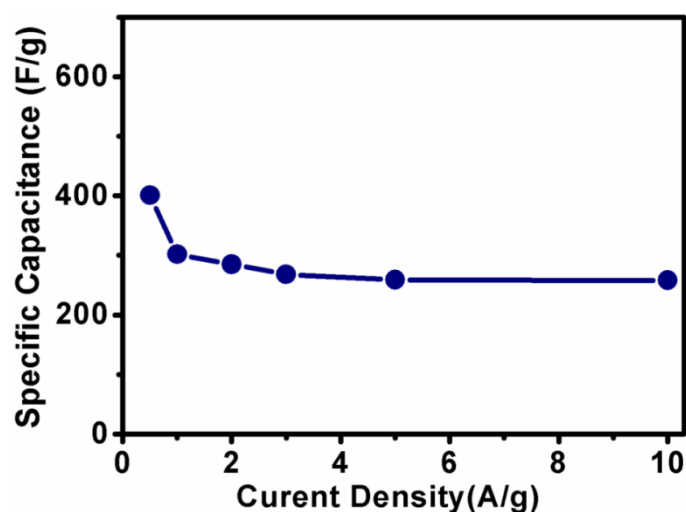


Figure 3.8: Plot of specific capacitance with different current densities which shows even at very high current density (10 Ag^{-1}) the specific capacitance is still high as 290 Fg^{-1} .

The areal capacitance of the CDDPL obtained at 1000°C has also been determined. Areal capacitance is very important in supercapacitor applications for small electronic devices. ^[64-65] Generally a low mass loading of active materials is used in supercapacitors for obtaining very high gravimetric capacitance. However as a consequence their areal capacitance values are suppressed ($5\text{-}12 \mu\text{Fcm}^{-2}$). ^[66-70] Interestingly though, the CDDPL material obtained in our study shows a significantly high value of areal capacitance ($32 \mu\text{Fcm}^{-2}$) as compared to other waste carbon based materials used for energy storage. For comparison purposes and to see the generic nature of the carbon forming process involving dead leaves, we also tested another dead-leaf source, namely Ashoka Leaves. Similar protocols were followed for the carbon synthesis.

The cyclic voltametry measurements for Ashoka leaf-derived carbon are shown in **Figure 3.6 c**. They also show a perfect rectangular shape suggesting that a double layer is being formed. From the galvanostatic charge discharge measurements (**Figure 3.9**) the specific capacitance comes out to be 250 Fg^{-1} at a current density of 0.5 Ag^{-1} . This is also quite good, although inferior to that of Neem leaf derived carbon.

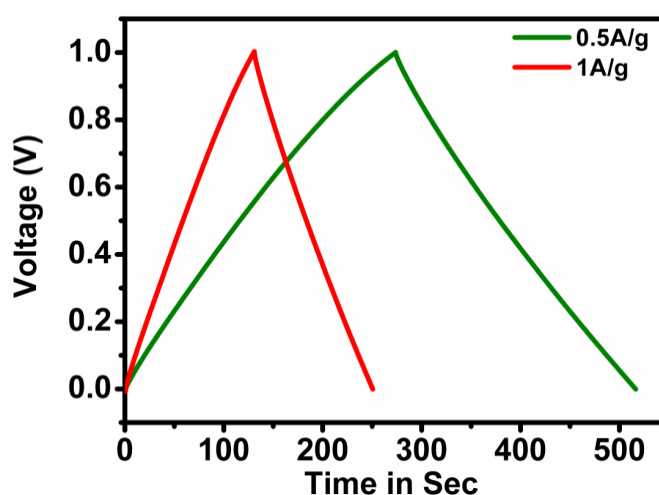


Figure 3.9: Charge Discharge curve of Ashoka leaf derived carbon at 1A/g^{-1} and 0.5A/g^{-1} with $1\text{M H}_2\text{SO}_4$

To compare the performance of both types of leaves we studied the morphology/constitution and composition of green leaf, dead leaf and dried leaf powder (obtained by grinding). **Figure 3.10** shows that in the case of Neem leaf the morphology changes slightly from that of green leaf (**Figure 3.10 a**) to dry leaf (**Figure 3.10 b**), but it changes drastically from dry-leaf to dry-leaf powder (**Figure 3.10 c**), the latter obtained by grinding of the dry leaves. Even in the capacitance performance, the green leaf derived carbon (195Fg^{-1}) and the dry leaf derived carbon without grinding (373Fg^{-1}), showed less specific capacitance than the ground dry leaf powder (401Fg^{-1}) which can be attributed to the lack of proper porosity.

The Cyclic Voltammetry curves of green leaf derived carbon and dry leaf derived carbon without grinding at a scan rate of 20mVs^{-1} are shown in **Figure 3.11a and b**, respectively. From **Figure 3.10c** it is clearly seen that there are large porous structures present which is due to the loss of some matter during the process of grinding. As the powder itself is porous, one can expect that after pyrolysis also it may generate a porous carbon matrix. As seen from SEM micrograph, these porous structures are absent in the case of Ashoka green leaf (**Figure 3.10d**), dry leaf (**Figure 3.10e**) and dry leaf powder (**Figure 3.10f**).

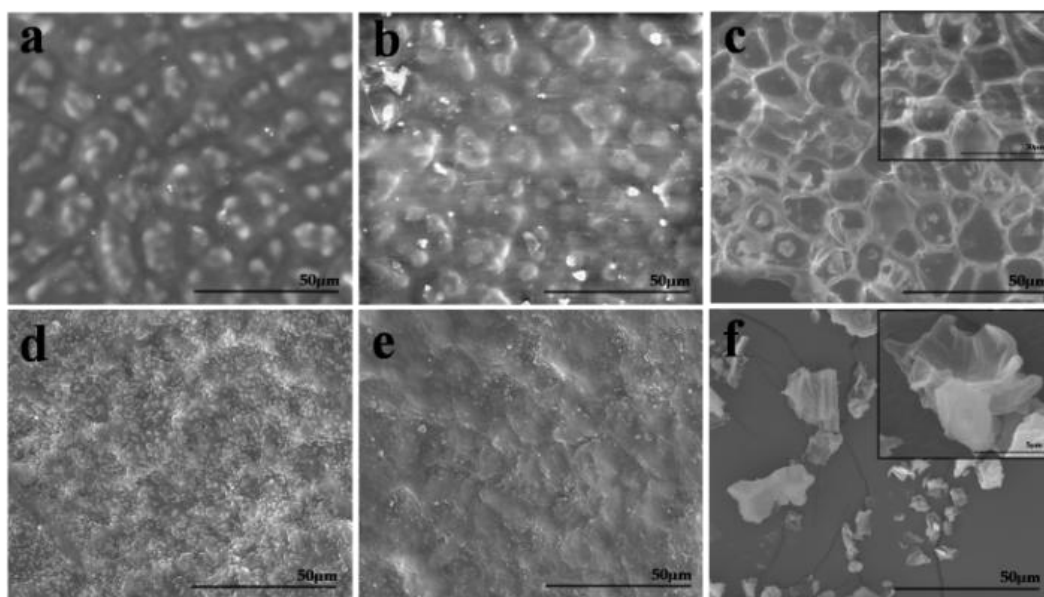


Figure 3.10 : SEM Images of (a)Neem Green Leaf (b)Neem Dry Leaf (c) Dry Neem leaf powder (d) Ashoka Green Leaf (e) Ashoka Dry Leaf (f) Dry Ashoka Leaf Powder

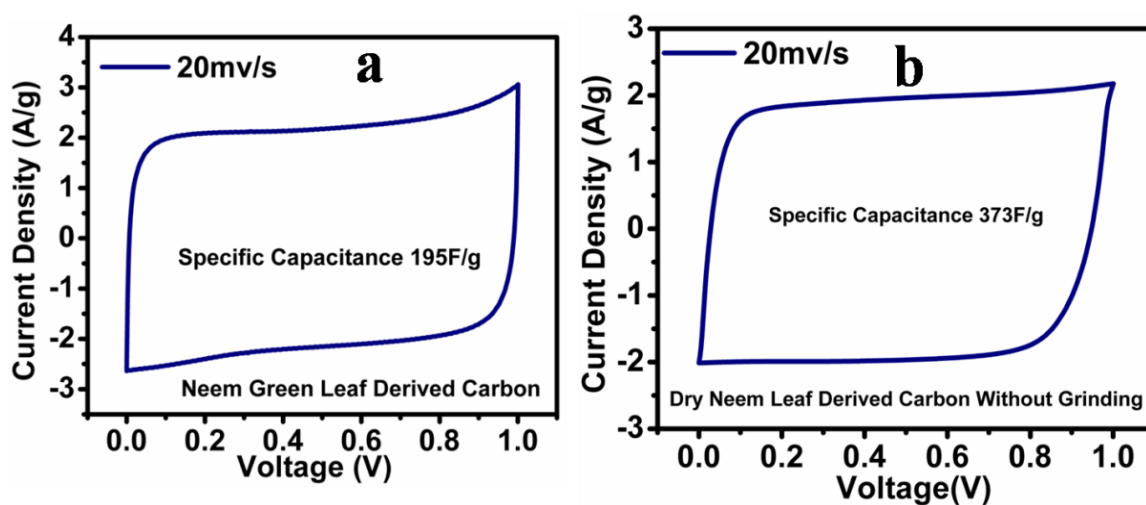


Figure 3.11 : a) CV curve for the carbon synthesized from fresh green leaves at a scan rate of 20 mVs^{-1} ; b) CV curve of Neem dry leaf without grinding at 20 mVs^{-1} in $1 \text{M H}_2\text{SO}_4$ at a scan rate of 20 mVs^{-1}

These constitutional difference affect the surface area and porosity of carbon derived from these leaves. The elemental mapping of Neem and Ashoka dry leaf is presented in **Figure 3.12 a and b** which show that in the case of Neem dry leaf the Ca (pink) content is comparatively much higher and well distributed than in the case

of Ashoka dry leaf. These results were also confirmed with the EDAX analysis shown in **Table 3.3**.

From the EDAX results, the Ca to C ratio for Neem leaves is clearly seen to be much higher in comparison to Ashoka leaves. The Ca content increases from green leaf to dry leaf and finally to dry leaf powder due to loss of some organic matter because of mechanical heat generated from the grinding process. Apart from Ca there is also a small percentage of Mg present. The stated Ca content is very useful in our case as Ca is known to be a good porogen.

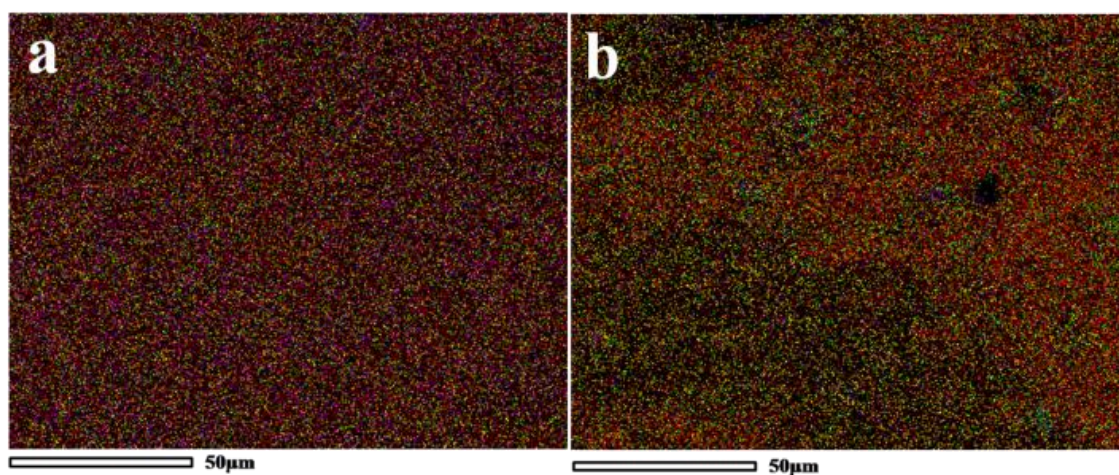


Figure 3.12: Elemental mapping of (a) Neem Leaf (b) Ashoka Dry leaf. Red- C, Green- O, Pink- Ca, Blue- Mg, Yellow- Al

There are many reports wherein researchers have mixed Ca salts in the samples for the creation of pores and to increase in the surface area.^[49-54] In case of leaf these minerals are well distributed in the leaf matrix as shown in the elemental mapping which helps in natural creation of pores, enhancing the surface area. As the Ca content is high in the case of Neem leaf, there are more well defined pores and larger surface area ($1230\text{m}^2\text{g}^{-1}$) in the corresponding carbon as compared to the Ashoka leaf derived carbon, which has a surface area of $705\text{m}^2\text{g}^{-1}$ **Figure 3.13**.

Element (wt%)	Neem Green Leaf	Neem Dry Leaf	Neem Dry Powder	Ashoka Green Leaf	Ashoka Dry Leaf	Ashoka Dry Powder
C	78.06	72.47	71.51	75.48	74.18	72.87
O	15.26	17.92	13.53	19.80	21.99	22.09
Ca	5.89	6.94	11.32	1.85	1.98	2.21
Mg	0.10	0.21	1.30	0.18	0.16	0.21
Ca/C Ratio	0.075	0.095	0.16	0.024	0.026	0.030

Table 3.3: EDAX analysis of Neem and Ashoka leaf derived carbon

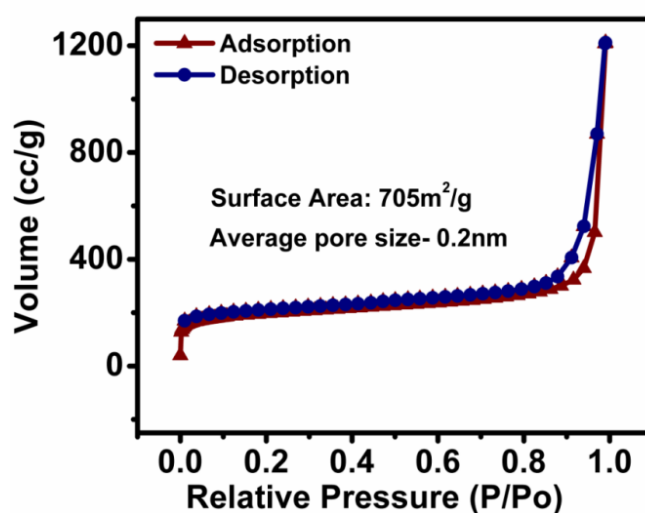


Figure 3.13: BET surface area measurements of Ashoka leaf derived carbon.

Table 3.4 compares different carbon materials synthesized from natural waste and their performance in supercapacitors. This table clearly shows that the carbon derived in our case without any activation or special treatment shows an excellent performance than other waste material derived carbon (Bamboo, waste coffee beans, sugarcane baggase etc.). The very high performance can be attributed to the the availability and wettability of the micropores whose dimensions are comparable to the dimensions of the solvated ions (cations or anions). To obtain a high performance supercapacitor it is important to understand the effect of surface area and pore size. Generally capacitance value increases with an increase in the BET surface area; but in some cases limitation in capacitance value is encountered even when the surface area is very high (more then $2000 \text{ m}^2\text{g}^{-1}$).^[13-21]

Materials	Activating agent	BET Surface Area (m^2g^{-1})	Maximum Capacitance (Fg^{-1})	Measurements Done at	Electrolyte	Ref. No.
Rice husk	NaOH	1886	210	$0.2\text{mA}\text{g}^{-1}$	3M KCl	15
Firwood	H_2O	1131	140	25mVs^{-1}	0.5M H_2SO_4	18
Pistachio Shell	KOH	1096	120	10mVs^{-1}	0.5M H_2SO_4	19
Firwood	KOH	1064	180	10mVs^{-1}	0.5M H_2SO_4	19
Bamboo	KOH	1251	260	1mAcm^{-2}	30wt% H_2SO_4	20
Banana Fibers	ZnCl_2	1097	74	$500\text{mA}\text{g}^{-1}$	1M Na_2SO_4	17
Corn Grains	KOH	3199	257	$1\text{mA}\text{g}^{-1}$	6M KOH	44
Waste coffee beans	ZnCl_2	1019	368	$50\text{mA}\text{g}^{-1}$	1M H_2SO_4	46
Waste News Paper	KOH	416	180	1mAcm^{-2}	6M KOH	16
Seaweeds	No activation	746	264	$200\text{mA}\text{g}^{-1}$	1M H_2SO_4	55
Sugar-cane bagasse	ZnCl_2	1788	300	$250\text{mA}\text{g}^{-1}$	1M H_2SO_4	45
Cassava peel waste	KOH	1352	264	-	0.5M H_2SO_4	47
Sunflower seed shell	KOH	2509	311	$250\text{mA}\text{g}^{-1}$	30wt% KOH	48
Argan seed shell	KOH/mel amine	2062	355	$125\text{mA}\text{g}^{-1}$	1M H_2SO_4	14
Neem Dead Leaves	No activation	1230	400	$500\text{mA}\text{g}^{-1}$	1M H_2SO_4	Our work

Table 3.4: Comparison of the properties of carbon materials synthesized from waste and their use in supercapacitor

The pore size therefore plays a more important role in determining the charge storage capacity. Thus by engineering the pores properly high capacitance value can be achieved even at low surface area. Micropores less than 2 nm are critical for charge storage, and it is also seen that the pore size up to 0.5 nm is suitable for aqueous (1M

H₂SO₄) based electrochemical supercapacitor. ^[71-74] In H₂SO₄ electrolyte, the sizes of the Hydrated SO₄²⁻, (H₂O)₁₂ (Hydration number calculated around 12.16) and H₃O⁺ are around 5.33Å and 4.2Å, respectively. ^[75-76] Thus, the pore size in the CDDPL exactly corresponds to that of hydrated ions. The solvent ions thus perfectly fit into the available porous carbon network without wastage of free space. Such water-tight accommodation of these ions in the porous carbon matrix results in a strong confinement of these ions in the small carbon pores. A strong confinement would consequently lead to a distorted solvated ionic shell causing a greater interaction between the carbon network (electrode) and the trapped charged ions of the electrolyte ^[71-72] which leads to increase in the value of the supercapacitance.

From the pore size distribution (**Figure 3.3**) it can be observed that, there are also some pores of around 2nm diameter. These bigger pores must clearly help in the transport of the ions from the surface to the bulk of the electrode so that the micropores can be accessed properly.

The energy density and power density are calculated by the following equations:

$$S_E = \frac{C_s(\Delta V)^2}{2} \quad 3.2$$

$$S_p = \frac{S_E}{t} \quad 3.3$$

Where S_E is the specific energy density, S_p is the specific power density, C_s is the specific capacitance of the active material (Fg⁻¹), t is the discharging time and ΔV is the potential window in 1M H₂SO₄ for charging and discharging.

The specific energy, power density, specific capacitance and aerial capacitance values for different current densities of our CDDPL material are presented in **Table 3.5**. It can be clearly noted that at 0.5 Ag⁻¹ our carbon synthesized at 1000°C shows very significant energy density value of 55 Wh Kg⁻¹. As the current density increases energy density gets suppressed. This is because at very high current density only some parts of the pores (surface mainly) are accessed by the electrolyte leading to very fast discharge, whereas at low current density all the pores including those near the surfaces and also in the bulk are accessed by the electrolyte and hence

discharges are slow. In our case, even at a very high current density 10 Ag^{-1} there is only a limited drop in the value of energy density (30.63 KW kg^{-1}).

The comparative specific energy and power density table is shown in **Table 3.6** where it can be clearly identified that the energy and power density of the carbon derived from Neem dead leaves is higher than that for other carbon materials synthesized from waste. Also it shows comparable energy and power density with graphene and graphene/CNT based composites.

Current Density (Ag^{-1})	0.5	1	2	3	5	10
Specific Capacitance (Fg^{-1})	401	302	285	268	259	258
Areal Capacitance (μFcm^{-2})	32.0	24.5	23.17	21.7	21.05	21.0
Power Density (WKg^{-1})	569	1191	2526	3620	6480	11685
Energy Density (WhKg^{-1})	55	42	40	37	36	35.8

Table 3.5: Calculated specific capacitance, areal capacitance, power densities and energy densities of CDDPL material at different current densities

The Ragone plot of **Figure 3.14** can be used for further analysis of the performance of our material. Usually increase in the power density compromises the energy density value.^[45,46,77-79] But in our case the CDDPL shows no significant decrease in the energy density. At current drain time of 10s the energy and power density values are found to be 35 Wh Kg^{-1} and 11685 W kg^{-1} , respectively, which are significantly higher than other aqueous based charge storage reports.^[77-81] These high values clearly demonstrate the stable performance of the carbon derived from dead plant leaves which is the result of the beneficial effects of the large number of tiny micropores present in the carbon matrix.

Materials	Medium	Max energy Density	Max Power Density	Ref. no.
Activated carbon from waste coffee beans	1M H ₂ SO ₄	20 WhKg ⁻¹	-	46
Carbon from sea weeds	1M H ₂ SO ₄	19.5 WhKg ⁻¹	-	55
Activated carbon from sugarcane bagasse	1M H ₂ SO ₄	10 WhKg ⁻¹	-	45
Binder free RGO-CNT film	1M H ₂ SO ₄	59.9 WhKg ⁻¹	250 WKg ⁻¹	75
Ultrathin graphene film	2M KCl	15.4 WhKg ⁻¹	55 WKg ⁻¹	76
Graphene-CNT	0.5M H ₂ SO ₄	21.74WhKg ⁻¹	78.29 kWKg ⁻¹	77
Carbon derived from dead leaves	1M H ₂ SO ₄	55.5 WhKg ⁻¹	10 kWKg ⁻¹	Our Work

Table 3.6: Comparison of energy density and power density of various carbon materials with dead leaf derived carbon

In case of aqueous medium the potential window is limited to about 1(V), hence the achievable energy density is also limited. Hence supercapacitor measurements in organic electrolyte are more important since the potential window can be extended to 3(V). We therefore tested the performance of the dead leaf derived carbon with an organic electrolyte 1M LiPF₆ in EC:DEC in a potential window of 0-3(V). **Figure 3.6 d-f** shows the CV and charge discharge data for both the Neem and the Ashoka leaf derived carbon. **Figure 3.6 d** shows the CV curves of Neem leaf derived carbon at various scan rates (2, 5, 10, 20, 50mvs⁻¹) in an organic electrolyte. It can be clearly seen that the curves show rectangular nature in all the scan rates. The specific capacitance of 88Fg⁻¹ is calculated from the charge discharge curve measured at a current density of 2Ag⁻¹ which is shown in **Figure 3.6 e**.

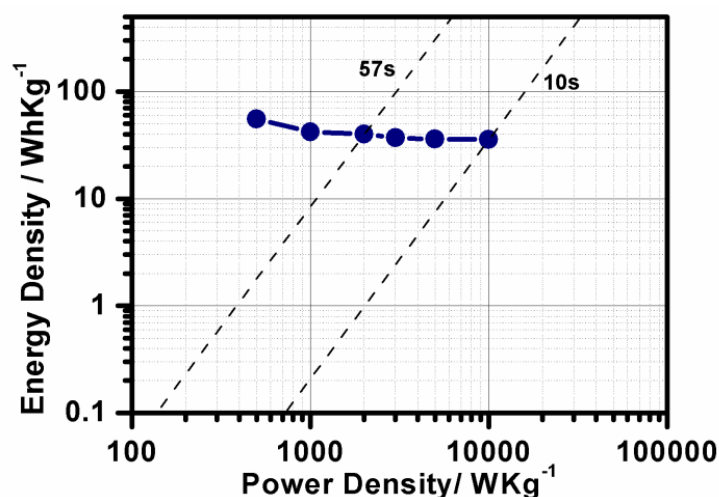


Figure 3.14: Ragone plot (plot of energy density vs power density)

Similar measurements were also done with Ashoka leaf derived carbon for the same current density (**Figure 3.15**), which gave a specific capacitance value of 21Fg^{-1} which is less as compared to Neem leaf carbon. This decrease in specific capacitance is due to the decrease in the surface area and porosity in case of Ashoka leaf derived carbon. The energy density for Neem leaf derived carbon in organic electrolyte is calculated to be 56WhKg^{-1} at 2Ag^{-1} from equation 2 which is higher (40% enhancement) than that the case of aqueous electrolyte, which is 40WhKg^{-1} at 2Ag^{-1} current density.

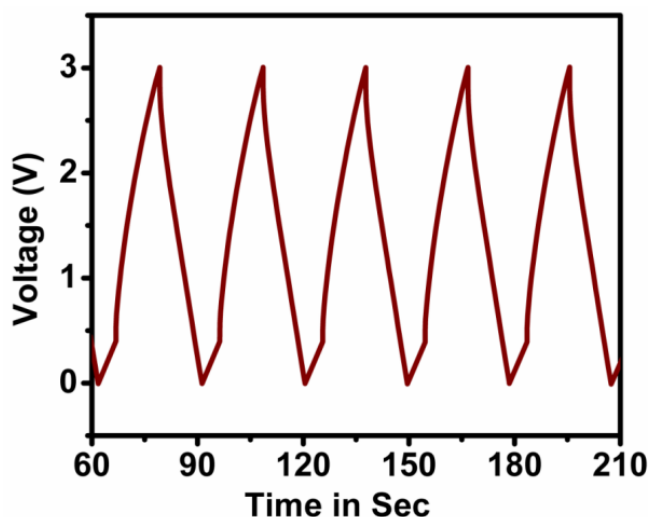


Figure 3.15: Charge discharge data of Ashoka leaf derived carbon at 2Ag^{-1} current density in organic electrolyte.

Figure 3.16 a shows the Nyquist plot for carbon in 1M H₂SO₄ in the frequency range from 10 kHz to 10 mHz. This figure clearly shows an almost vertical straight line parallel to the imaginary axis (Z'') at low frequency region showing nearly ideal capacitor behaviour. The data in the middle frequency region reflect the consequences of certain key factors such as porosity, thickness of the electrode etc. for the diffusion of the ions through the porous network of the electrode.^[82-83] These introduce an initial semicircle character into the straight line behaviour at high frequency range, which shifts the capacitor behaviour towards a lower frequency value on the real axis. Hence, on the whole the impedance spectrum for a supercapacitor can be divided into two parts consisting of low frequency and high frequency regions. The transition point of these two regions is known as the ‘Knee frequency’ below which the capacitance nature dominates.^[84]

The inset of **Figure 3.16a** shows the magnified high frequency region showing the semicircle. The fitted equivalent circuit consists of an equivalent series resistance (ESR) in series with a parallel combination of capacitor (C_{dl} , double layer capacitance) and resistor (R_F) in series with Warburg impedance element (W) corresponding to the electrolyte ion diffusion into porous network of carbon electrode material. The ESR shows the total contact resistance between the current collector-electrode material and ohmic resistance of the electrode-electrolyte interface.

In our case (with 1M H₂SO₄) ESR comes out to be 2.67 Ω showing a good conducting behaviour.^[85] Further effort is needed to reduce it by optimizing the device and contact properties. The Warburg impedance element has a small contribution indicating good access for the electrolyte ions into porous carbon material even at higher frequencies. The knee frequency in this case is 57 Hz below which the capacitive behaviour dominates. This is in good agreement with the knee frequency domain reported for the carbon based supercapacitors.^[86-87]

Figure 3.16 b gives the Bode phase plot which indicates that in the low frequency region the phase shift is $\sim 90^\circ$ (sharper slope) indicating primarily an almost full double layer charge storage phenomenon and near absence of faradic (redox) type charge storage phenomenon.^[88] A shallower slope accounts for more faradic (redox) type charge storage phenomenon.

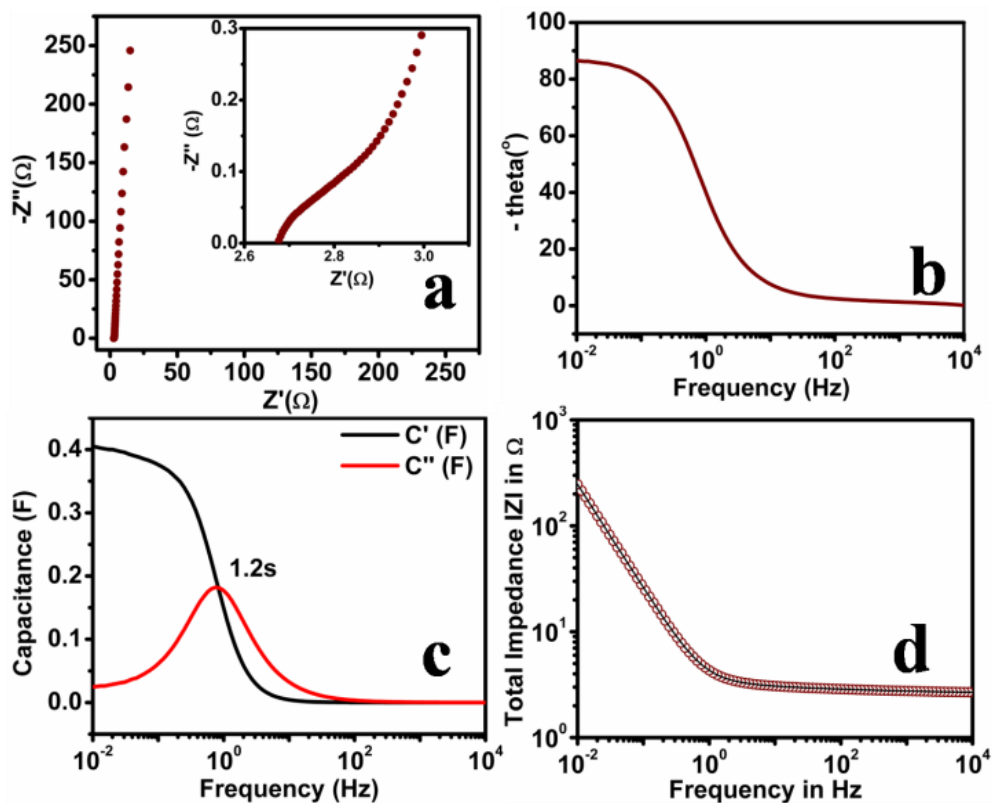


Figure 3.16: (a) Nyquist plot for carbon electrode in 1M H_2SO_4 , inset shows the magnified higher frequency region; (b) Plot of Bode phase angle with frequency; (c) Frequency dependant real and imaginary capacitance plot; (d) Plot of total impedance vs frequency

The plots of frequency dependant real (C') and imaginary (C'') components of capacitance are shown in **Figure 3.16 c**. In the low frequency region the capacitance (C') remains constant at ~ 0.4 F which is the saturated capacitance at low frequency. The capacitance value decreases sharply above 0.1 Hz and becomes constant above 10 Hz. At low frequency, electrolyte ions penetrate deep inside the pores of carbon material accessing more electrode surface thereby contributing to the high capacitance value. At higher frequencies electrolyte ions can only have access to the surface of carbon materials whereas the deeper pores are not accessed giving rise to a sharp decrease in the capacitance. The sharp peak in the graph of frequency dependant imaginary component of capacitance (C'') shows a maximum capacitance (C'') at a frequency f_0 which corresponds to relaxation time as $\tau_0 = 1/f_0$ which is ~ 1.2 s. This relaxation time signifies the minimum time needed to discharge all the energy from the device with an efficiency of $>50\%$.^[89] This low relaxation time (~ 1.2 s) also

indicates the maximum accessibility of the outer surface of Neem leaf derived carbon material to the electrolyte ions.

Figure 3.16 d shows the plot of total impedance (Z) vs frequency (Hz) for dead Neem leaf derived carbon. When the frequency is low during the potential applied, the electrolyte ions try to penetrate deeper into the electrode from the orifice to the bottom of the pores. Hence at low frequency the bottom of the pores will also contribute to the resistive and capacitive elements leading to higher impedance as shown in **Figure 3.16 d**. At high frequency the electrolyte ions are only able to penetrate near the orifice of the pores hence resistive and capacitive elements near the orifice alone can respond. The penetration depth increases with decrease in the frequency. A straight line is obtained at low frequency region which is due to the accumulation of ions at the bottom of the pores whereas in the middle frequency region a straight line is obtained due to the semi- infinite ion migration (dipoles) through various micropores. A horizontal line in the high frequency region signifies the dominance of electronic transport over this regime. ^[90-91]

The Nyquist plot for supercapacitor with carbon electrode in 1M LiPF₆ in EC:DEC is shown in **Figure 3.17 a**. The inset shows the magnified high frequency region. The low frequency region is similar to the case of aqueous electrolyte which shows purely capacitor behaviour. The major difference is however observed in the high frequency region, as shown in **Figure 3.17 b**, wherein a shift of the semicircle is seen towards higher value on the real axis, which is accounted for by the electrolyte viscosity which resists the penetration of electrolyte into the micropores at higher frequencies. The bigger semicircle also indicates the lower ionic conductivity of the electrolyte which in turn affects the electrolyte-electrode interface resistance. ^[82]

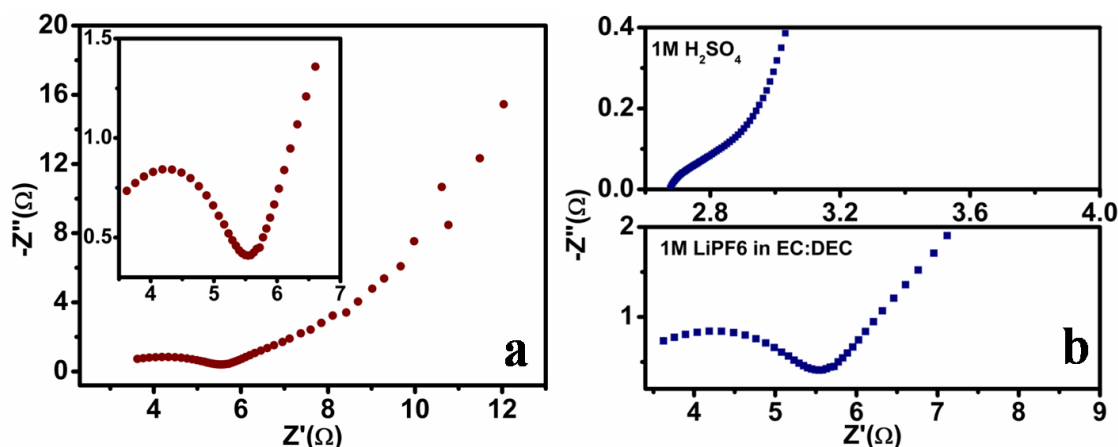


Figure 3.17: a) Nyquist plot for Neem leaf derived carbon carbon electrode in 1M LiPF₆ in EC: DEC (organic).inset shows magnified high frequency region; b) Comparison of Nyquist plot for carbon carbon electrode in 1M H₂SO₄ (aqueous) and 1M LiPF₆ in EC: DEC (organic) for Neem leaf derived carbon.

From electrochemical impedance spectroscopy measurements we can conclude that the carbon electrodes show nearly ideal capacitive behaviour with low ionic resistance inside the porous structure indicating the fast diffusion of electrolyte ions into the porous network. The phase angle $\sim 90^\circ$ shows the dominant contribution of double charge storage mechanism and nearly complete absence of any redox reaction making the carbon derived from dead Neem leaves a suitable material for supercapacitor application.

Along with EDLC type supercapacitor we have also studied the performance of Neem leaf derived carbon as electrode in hybrid supercapacitor. Although, EDLC delivers excellent power density, it has limitations of energy density beyond $\sim 10 \text{ Wh kg}^{-1}$.^[92] Hence, EDLC alone is incapable of powering hybrid electric vehicles and electric vehicles.^[93] On the other hand, Li-ion batteries (LIB) provides high energy density, but the desired power density is not sufficient to drive such vehicles.^[94-96] In this context it is very difficult for individual system to offer the desired energy and power density. The solution to this problem can be to integrate both EDLC and LIB in a single system to achieve both high energy and power density. This configuration is known as Li ion hybrid electrochemical capacitor. Generally this configuration consists of Li-insertion type electrode (battery component) coupled with high surface

area carbonaceous materials preferably activated carbon as counter electrode (supercapacitor component) in Li-ion conducting non-aqueous electrolytes.

Among various Li insertion type materials such as pre-lithiated graphite, $\text{Li}_4\text{Ti}_5\text{O}_{12}$ [92, 93], LiCrTiO_4 [97-98], LiFePO_4 [99] etc, spinel phase $\text{Li}_4\text{Ti}_5\text{O}_{12}$ is found to be appropriate materials due to its salient features such as no volume variation during Li-insertion/extraction (Zero strain host), appreciable theoretical capacity ($\sim 175 \text{ mAh g}^{-1}$) with high reversibility, thermodynamically flat operating potential ($\sim 1.55 \text{ V vs. Li}$), easy synthesise and eco-friendliness. [100] Among the carbonaceous materials, graphene, and porous carbons are found significant due to their high specific capacitance with good cycleability in EDLC configuration, high surface area ($\sim 2000 \text{ m}^2 \text{ g}^{-1}$), excellent electrical conductivity and good chemical and thermal stabilities. [101] In this work we have used the Neem dead leaves derived carbon as electrode material in Li ion hybrid configuration along with $\text{Li}_4\text{Ti}_5\text{O}_{12}$.

The capacitive behaviour of the Neem leaf derived carbon tested above the open circuit voltage (OCV) (*vs.* Li) is attributed to the reversible adsorption and desorption behaviour of anions present in the electrolyte (PF_6^-) and subsequent electric double layer formation across the electrode/electrolyte interface. [98, 102-105] Also, such single electrode performance is very crucial to balance the mass between the electrodes during the fabrication of Li-Hybrid electrochemical capacitor. Generally, in conventional symmetric supercapacitor the applied potential is equally distributed among the two electrodes. Whereas, in the asymmetric configuration, particularly Li-Hybrid electrochemical capacitor the two electrodes undergo different energy storage mechanisms hence the applied potential gets divided into specific capacitance of the individual electrodes.

This un-equal distribution leads to the partial utilization of the electro-active material, resulting in to suppression of energy density. [98, 105] Therefore the mass balance between the electrodes is necessary for the complete utilization of the active material and to achieve high energy density Li-Hybrid electrochemical capacitor. Therefore, half-cell was constructed with dead leaves derived carbon and tested from OCV to the decomposition potential of conventional carbonate based electrolyte (3-4.6 V *vs.* Li).

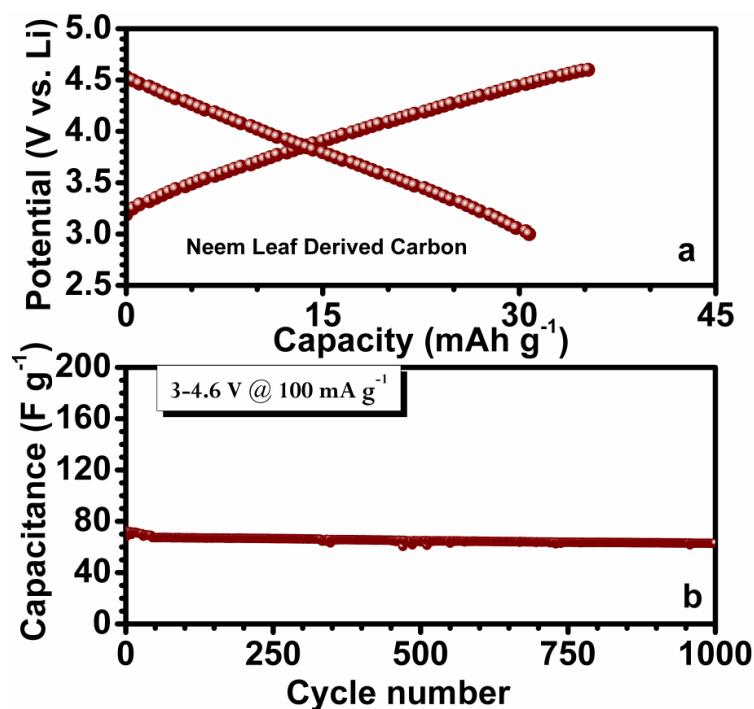


Figure 3.18: a) Typical galvanostatic charge-discharge curves of various carbonaceous materials in single electrode configuration between 3-4.6 V vs. Li at current density of 100 mA g^{-1} , in which metallic lithium acts as counter and reference electrode. (b) Plot of specific discharge capacitance vs. cycle number. The data points are collected after every 10 cycles.

Figure 3.18 a shows galvanostatic charge-discharge curves at a current density of 100 mA g^{-1} . The leaf derived carbon electrode shows linear variation of potential with respect to time. Such linear variation corresponds to the perfect reversible adsorption/desorption of PF_6^- anions. ^[98-103] The leaf derived carbon showed a reversible capacity of $\sim 32 \text{ mAh g}^{-1}$ which is comparable to the commercially used activated carbon.

The reversible capacity can be converted into the specific capacitances (CSP) by using the following equation proposed by Amatucci *et al.* ^[103]

$$C_s(\text{F/g}) = \frac{i(\text{A}) \times t(\text{s})}{3600 \times m(\text{g})} = \frac{\text{mAh/g (Observed Capacity)}}{3600/dV(\text{mV})} \quad 3.4$$

$$= \text{Observed Capacity}(\text{mAh/g}) \times 3600/dV(\text{mV})$$

Where, I is applied current, t is discharge time, m weight of the active material and dV is testing window of the aforementioned half-cell configuration (1600 mV).

However, the said relation is valid if the variation of voltage with respect to time is linear. By using this equation the specific capacitance was calculated to be 72Fg^{-1} for Neem leaf derived carbon in Li ion hybrid capacitor configuration. Plot of the specific discharge capacitance vs. cycle number is given in **Figure 3.18 b**, where it can be clearly seen that the electrode exhibit a very stable cycling performance except for a minor fading in the initial cycles. Capacitance fading in initial cycles is common for the case of non-aqueous electrolytes ^[93]. Even after 1000 cycles the fading in the specific capacitances is noticed to be very negligible.

Based on the electrochemical performance of the spinel phase $\text{Li}_4\text{Ti}_5\text{O}_{12}$ under the same current rate, the active material loading of anode ($\text{Li}_4\text{Ti}_5\text{O}_{12}$) to leaf derived carbon cathode was optimized into 1:5.26 for the fabrication of Li-Hybrid electrochemical capacitor. The cell was constructed using Neem leaf derived carbon as cathode and insertion type spinel phase $\text{Li}_4\text{Ti}_5\text{O}_{12}$ anode and cycled over 1-3 V testing range at various current densities under the optimized mass loadings described above. The results are shown in **Figure 3.19 a**.

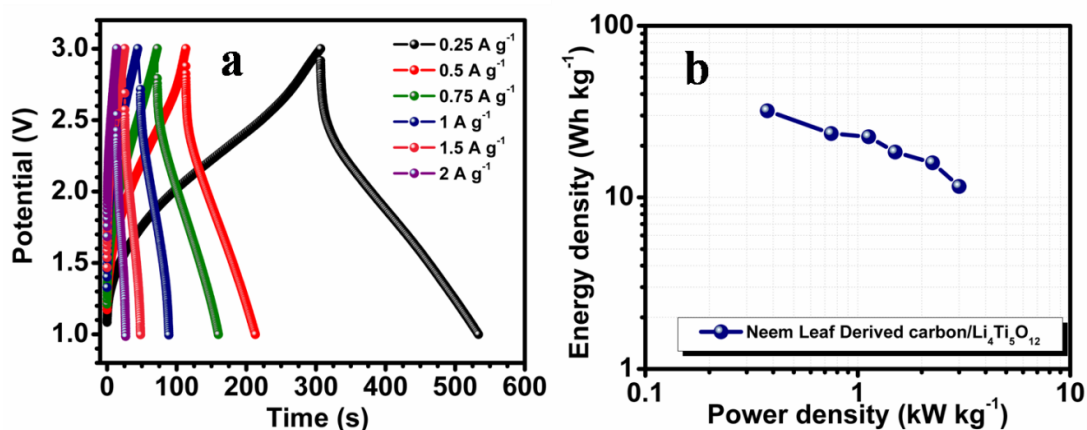


Figure 3.19: a) Galvanostatic charge-discharge profiles conducted between 1-3 V for Leaf derived carbon / $\text{Li}_4\text{Ti}_5\text{O}_{12}$ Li-Hybrid electrochemical capacitor; b) Ragone plot of Li-Hybrid electrochemical capacitor comprising of leaf derived carbon cathode.

The constructed hybrid cell showed minor ohmic drop ~ 3 V followed by monotonous discharge curve and a sudden drop of potential (~ 1.4 V onwards). This

monotonous discharge curve corresponds to the breaking of the electric double layer across the electrode/electrolyte interface and simultaneous extraction of Li from the spinel lattice. Specific energy (E_{SP}) and power densities (P_{SP}) of the Li-HEC are calculated using the following relation,

$$P_{sp} = \Delta E \times I / M \quad 3.5$$

$$\text{and } E_{sp} = P_{sp} \times t \quad 3.6$$

Where $\Delta E = (E_{\max} + E_{\min})/2$ and E_{\max} and E_{\min} are respectively the potential at beginning of discharge and at the end of discharge curves of galvanostatic cycle and M is the active mass loading of both electrodes (mg, anode + cathode).^[98,104,105-106] The specific energy density of $\sim 26 \text{ Wh kg}^{-1}$ was obtained for the Neem leaf derived carbon. **Figure 3.19 b** shows the Ragone plot constructed from the energy density and power density values calculated at different current densities. This Ragone plot shows high energy density and power density for the Neem leaf derived carbon electrode.

3.4 Conclusion

In summary high surface area microporous functional (conducting) carbon is synthesized from the dry waste of dead plant leaves (Neem and Ashoka) without any external activation and studied for supercapacitor application. The carbon synthesized at $1000 \text{ }^\circ\text{C}$ from Neem leaves exhibits a very high charge storage capacity with specific capacitance of 400 Fg^{-1} and energy density of 55 WhKg^{-1} in $1 \text{ M H}_2\text{SO}_4$. The capacitance is also tested with organic electrolyte (1 M LiPF_6 in EC:DEC) which shows a specific capacitance of 88 Fg^{-1} at a current density of 2 Ag^{-1} and with a energy density value of 56 WhKg^{-1} . The energy density is realized to be 40% higher in the case of organic electrolyte than the case of aqueous electrolyte at the same current density of 2 Ag^{-1} . This high supercapacitor performance can be attributed to a specific nature of microporosity combined with high surface area ($1230 \text{ m}^2 \text{ g}^{-1}$) which is due to the uniform distribution of the minerals present in the leaf. These minerals are known to be good porogen which create pores during the process of pyrolysis. The generic nature of the proposed process of dead leaves is confirmed by a similar study on another plant, namely Asoka. The corresponding carbon material shows a specific capacitance of 250 Fg^{-1} in aqueous and 21 Fg^{-1} in organic media. Both the leaf-types

show very good performance with Neem leaf exceeding the other. We show that the differences can be traced to the constitution and composition of the Bio-source. We have also studied the cases of pyrolysis of green leaves as well as un-ground dead leaves with that of ground dead leaves powder. In Li ion hybrid electrochemical capacitor configuration with $\text{Li}_4\text{Ti}_5\text{O}_{12}$ capacity of $\sim 32 \text{ mAhg}^{-1}$ and a specific capacitance of 72 Fg^{-1} is obtained. This is comparable with the commercial activated carbon electrode materials. This proves that carbon derived from Neem dead leaves is highly useful electrode material for supercapacitor applications.

3.5 References

1. G. Wang, L. Zhang and J. Zhang, *Chem. Soc. Rev.*, **2012**, 41, 797.
2. E. Frackowiaka and F. B'eguine, *Carbon*, **2001**, 39, 937.
3. L. Dai, D. W. Chang, J. B. Baek and W. Lu, *Small*, **2012**, 8, 1130.
4. X. Zhao, H. Tian, M. Zhu, K. Tian, J. J. Wang, F. Kang and R. A. Outlaw, *J. Power Sources*, **2009**, 194, 1208.
5. H. Pan, J. Li and Y. P. Feng, *Nanoscale Res. Lett.*, **2010**, 5, 654.
6. L. L. Zhang and X. S. Zhao, *Chem. Soc. Rev.*, **2009**, 38, 2520.
7. S. Flandrois and B. Simon, *Carbon*, **1999**, 37, 165.
8. A. G. Pandolfo and A. F. Hollenkamp, *J. Power Sources*, **2006**, 157, 11.
9. C. X. Guoab and C. M. Li, *Energy Environ. Sci.*, **2011**, 4, 4504.
10. S. Bose, T. Kuila, A. K. Mishra, R. Rajasekar, N. H. Kim and J. H. Lee, *J. Mater. Chem.*, **2012**, 22, 767.
11. B. W. Ricketts and C. Ton-That, *J. Power Sources*, **2000**, 89, 64.
12. M. Jayalakshmi and K. Balasubramanian, *Int. J. Electrochem. Sci.*, **2008**, 3, 1196.
13. X. zhou, L. Li, S. Dong, X. Chen, P. Han, H. Xu, J. Yao, C. Shang, Z. Liu and G. Cui, *J. Solid State Electrochem.*, **2012**, 16, 877.
14. A. Elmouwahidi, Z. Zapata-Benabithé, F. Carrasco-Mar'ín and C. Moreno-Castilla, *Bioresour. Technol.*, **2012**, 111, 185.
15. Y. Guo, J. Qi, Y. Jiang, S. Yang, Z. Wang and H. Xu, *Mater. Chem. Phys.*, **2003**, 80, 704.

16. D. Kalpanaa, S. H. Cho, S. B. Lee, Y. S. Lee, R. Misra and N. G. Renganathan, *J. Power Sources*, **2009**, 190, 587.
17. V. Subramanian, C. Luo, A. M. Stephan, K. S. Nahm, S. Thomas and B. Wei, *J. Phys. Chem. C*, **2007**, 111, 7527.
18. F. Wu, R. Tseng, C. Hu and C. Wang, *J. Power Sources*, **2004**, 138, 351.
19. F. Wu, R. Tseng, C. Hu and C. Wang, *J. Power Sources*, **2005**, 144, 302.
20. Y. Kim, B. Lee, H. Suezaki, T. Chino, Y. Abe, T. Yanagiura, K. Park and M. Endo, *Carbon*, **2006**, 44, 1581.
21. J. Yang, Y. Liu, X. Chen, Z. Hu and G. Zhao, *Acta Phys.–Chim. Sin.*, **2008**, 24, 13.
22. P. Jagdale, M. Sharon, G. Kalita, N. M. N. Maldar and M. Sharon, *Adv. Mater. Phys. Chem.*, **2012**, 2, 1.
23. A. Shaikjee and N. J. Coville, *Carbon*, **2012**, 50, 3376.
24. K. László, A. Bóta, L. G. Nagy and I. Cabasso, *Colloids Surf., A*, **1999**, 151, 311.
25. L. Qingwen, Y. Hao, C. Yan, Z. Jin and L. Zhongfan, *J. Mater. Chem.*, **2002**, 12, 1179.
26. G. Che, B. B. Lakshmi, C. R. Martin and E. R. Fisher, *Chem. Mater.*, **1998**, 10, 260.
27. M. Kumar and Y. Ando, *J. Nanosci. Nanotechnol.*, **2010**, 10, 3739.
28. L. Chow, D. Zhou, A. Hussain, S. Kleckley, K. Zollingera, A. Schultea and H. Wang, *Thin Solid Films*, **2000**, 368, 193.
29. A. Reina, X. Jia, J. Ho, D. Nezich, H. Son, V. Bulovic, M. S. Dresselhaus and J. Kong, *Nano Lett.*, **2009**, 9, 30.
30. X. Li, W. Cai, J. An, S. Kim, J. Nah, D. Yang, R. Piner, A. Velamakanni, I. Jung, E. Tutuc, S. K. Banerjee, L. Colombo and R. S. Ruoff, *Science*, **2009**, 324, 1312.
31. D. Wei, Y. Liu, Y. Wang, H. Zhang, L. Huang and G. Yu, *Nano Lett.*, **2009**, 9, 1752.
32. M. Tabbal, P. M´erel, M. Chaker, M. A. El Khakani, E. G. Herbert, B. N. Lucas and M. E. O'Hern, *J. Appl. Phys.*, **1999**, 85, 3860.
33. Y. Zhang, H. Gu and S. Iijima, *Appl. Phys. Lett.*, **1998**, 73, 3827.

34. X. Kong, Y. Huang and Y. Chen, *J. Mass Spectrom.*, **2012**, 47, 523.
35. F. Wen, N. Huang, H. Sun, J. Wang and Y. X. Leng, *Surf. Coat. Technol.*, **2004**, 186, 118.
36. S. Vizireanu, S. D. Stoica, C. Luculescu, L. C. Nistor, B. Mitu and G. Dinescu, *Plasma Sources Sci. Technol.*, **2010**, 19, 034016.
37. Y. Saito, K. Kawabata and M. Okuda, *J. Phys. Chem.*, **1995**, 99, 16076.
38. Z. Qin, Z. J. Li and B. C. Yang, *Mater. Lett.*, **2012**, 69, 55.
39. J. Lee, J. Kim and T. Hyeon, *Adv. Mater.*, **2006**, 18, 2073.
40. Y. Si and E. T. Samulski, *Nano Lett.*, **2008**, 8, 1679.
41. F. Lufrano and P. Staiti, *Int. J. Electrochem. Sci.*, **2010**, 5, 903.
42. G. Ruan, Z. Sun, Z. Peng and J. M. Tour, *ACS Nano*, **2011**, 9, 7601.
43. X. zhou, L. Li, S. Dong, X. Chen, P. Han, H. Xu, J. Yao, C. Shang, Z. Liu and G. Cui, *J. Solid State Electrochem.*, **2012**, 16, 877.
44. M. S. Balathanigaimani, W. Shim, M. Lee, C. Kim, J. Lee and H. Moon, *Electrochem. Commun.*, **2008**, 10, 868.
45. T. E. Rufford, D. Hulicova-Jurcakova, K. Khosla, Z. Zhu and G. Q. Lu, *J. Power Sources*, **2010**, 195, 912.
46. T. E. Rufford, D. Hulicova-Jurcakova, Z. Zhu and G. Q. Lu, *Electrochem. Commun.*, **2008**, 10, 1594.
47. A. E. Ismanto, S. Wang, F. E. Soetaredjo and S. Ismadji, *Bioresour. Technol.*, **2010**, 101, 3534.
48. X. Li, W. Xing, S. Zhuo, J. Zhou, F. Li, S. Qiao and G. Lu, *Bioresour. Technol.*, **2011**, 102, 1118.
49. F. Rodriguez-Reinoso and M. Molina-Sabio, *Carbon*, **1992**, 30, 1111.
50. J. A. Macia Agullo, B. C. Moore, D. Cazorla-Amoros and A. Linares-Solano, *Carbon*, **2004**, 42, 1367.
51. E. Raymundo-Pinero, P. Azais, T. Cacciaguerra, D. Cazorla- Amoros, A. Linares-Solano and F. Beguin, *Carbon*, **2005**, 43, 786.
52. J. E. Vargasa, L. G. Gutierrez and J. C. Moreno-Piraján, *J. Anal. Appl. Pyrolysis*, **2010**, 89, 307.
53. M. A. Lillo-Ródenas, D. Cazorla-Amorós and A. Linares- Solano, *Carbon*, **2003**, 41, 267.

54. M. Biswal, A. Banerjee, M. Deo and S. Ogale, *Energy Environ. Sci.*, **2013**, 6, 1249.
55. E. Raymundo-Pinero, M. Cadek and F. Beguin, *Adv. Funct. Mater.*, **2009**, 19, 1032.
56. A. T. Rodriguez, X. Li, J. Wang, W. A. Steen and H. Fan, *Adv. Funct. Mater.*, **2007**, 17, 2710.
57. D. Jagadeesan and M. Eswaramoorthy, *Chem.–Asian J.*, **2010**, 5, 232.
58. S. Kubo, R. Demir-Cakan, L. Zhao, R. J. White and M. Titirici, *ChemSusChem*, **2010**, 3, 188.
59. H. Kim, J. Cho, S. Jang and Y. Song, *Appl. Phys. Lett.*, **2011**, 98, 021104.
60. D. Mhamane, W. Ramadan, M. Fawzy, A. Rana, M. Dubey, C. Rode, B. Lefez, B. Hannoyerd and S. Ogale, *Green Chem.*, **2011**, 13, 1990.
61. N. Shimodaira and A. Masui, *J. Appl. Phys.*, **2002**, 92, 902.
62. V. Jiménez, A. Ramírez-Lucas, J. Antonio Díaz, P. Sánchez and A. Romero, *Environ. Sci. Technol.*, **2012**, 46, 7407–7414.
63. A. G. Pandolfo and A. F. Hollenkamp, *J. Power Sources*, **2006**, 157, 11–27.
64. G. Zheng, L. Hu, H. Wu, X. Xie and Y. Cui, *Energy Environ. Sci.*, **2011**, 4, 3368.
65. J. R. McDonough, J. W. Choi, Y. Yang, F. L. Mantia, Y. Zhang and Y. Cui, *Appl. Phys. Lett.*, **2009**, 95, 243109.
66. M. D. Stoller and R. S. Ruoff, *Energy Environ. Sci.*, **2010**, 3, 1294.
67. K. Jurewicz, C. Vix-Guterla, E. Frackowiak, S. Saadallaha, M. Reda, J. Parmentier, J. Patarin and F. Beguin, *J. Phys. Chem. Solids*, **2004**, 65, 287.
68. Y. Horng, Y. Lu, Y. Hsu, C. Chen, L. Chen and K. Chen, *J. Power Sources*, **2010**, 195, 4418.
69. S. R. C. Vivekchand, C. S. Rout, K. S. Subrahmanyam, A. Govindaraj and C. N. R. Rao, *J. Chem. Sci.*, **2008**, 120, 9.
70. R. H. Baughman, C. Cui, A. A. Zakhidov, Z. Iqbal, J. N. Barisci, G. M. Spinks, G. G. Wallace, A. Mazzoldi, D. D. Rossi, A. G. Rinzler, O. Jaschinski, S. Roth and M. Kertesz, *Science*, **1999**, 284, 1340.
71. D. Hulicova-Jurcakova, M. Seredych, G. Q. Lu, Teresa and J. Bandosz, *Adv. Funct. Mater.*, **2009**, 19, 438.

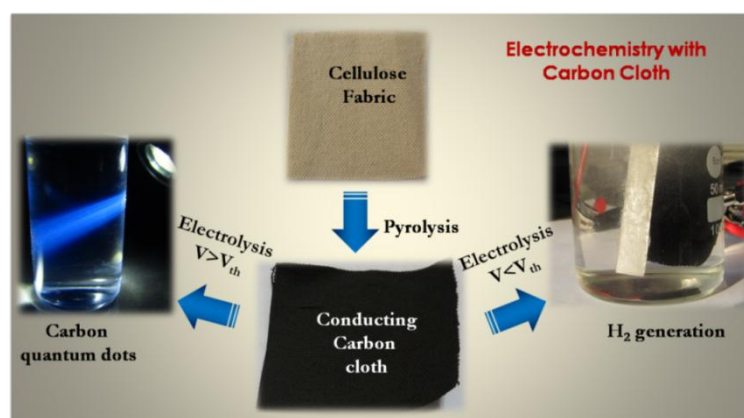
72. J. Chmiola, G. Yushin, Y. Gogotsi, C. Portet, P. Simon and P. L. Taberna, *Science*, **2006**, 313, 1760.
73. J. Chmiola, C. Largeot, P. Taberna, P. Simon and Y. Gogotsi, *Angew. Chem., Int. Ed.*, **2008**, 47, 3392.
74. C. Largeot, C. Portet, J. Chmiola, P. Taberna, Y. Gogotsi and P. Simon, *J. Am. Chem. Soc.*, **2008**, 130, 2730.
75. M. Endo, T. Maeda, T. Takeda, Y. J. Kim, K. Koshiba, H. Hara and M. S. Dresselhaus, *J. Electrochem. Soc.*, **2001**, 148, A910.
76. L. Eliad, G. Salitra, A. Soffer and D. Aurbach, *J. Phys. Chem. B*, **2001**, 105, 6880.
77. X. Zhao, C. Johnston and P. S. Grant, *J. Mater. Chem.*, **2009**, 19, 8755.
78. E. J. Ra, E. Raymundo-Pinero, Y. H. Lee and F. Beguin, *Carbon*, **2009**, 47, 2984.
79. S. Yang, K. Chang, H. Tien, Y. Lee, S. Li, Y. Wang, J. Wang, C. M. Ma and C. Hu, *J. Mater. Chem.*, **2011**, 21, 2374.
80. Z. Huang, B. Zhang, S. Oh, Q. Zheng, X. Lin, N. Yousefi and J. Kim, *J. Mater. Chem.*, **2012**, 22, 3591.
81. A. Yu, I. Roes, A. Davies and Z. Chen, *Appl. Phys. Lett.*, **2010**, 96, 253105.
82. P. L. Taberna, P. Simon and J. F. Fauvarque, *J. Electrochem. Soc.*, **2003**, 150, A292.
83. Q. Cheng, J. Tang, J. Ma, H. Zhang, N. Shinya and L. C. Qin, *Carbon*, **2011**, 49, 2917.
84. C. Du and N. Pan, *Nanotechnology*, **2006**, 17, 5314.
85. F. Lufrano and P. Staiti, *Int. J. Electrochem. Sci.*, **2010**, 5, 903.
86. L. Yuan, X. H. Lu, X. Xiao, T. Zhai, J. Dai, F. Zhang, B. Hu, X. Wang, L. Gong, J. Chen, C. Hu, Y. Tong, J. Zhou and Z. L. Wang, *ACS Nano*, **2012**, 6, 656.
87. C. Niu, E. K. Sichel, R. Hoch, D. Moy and H. Tennent, *Appl. Phys. Lett.*, **1997**, 70, 1480.
88. A. Ghosh and Y. Hee Lee, *ChemSusChem*, **2012**, 5, 480.
89. D. Pech, M. Brunet, H. Durou, P. Huang, V. Mochalin, Y. Gogotsi, P. L. Taberna and P. Simon, *Nat. Nanotechnol.*, **2010**, 5, 651.

90. S. Pyuna, C. Kima, S. Kima and J. Kim, *J. New Mater. Electrochem. Syst.*, **2002**, 5, 289.
91. J. Lee, J. Kima and S. Kim, *J. Power Sources*, **2006**, 160, 1495.
92. K. Naoi, P. Simon, *Electrochem. Soc. Interface*, **2008**, 17, 34.
93. K. Naoi, Y. Nagano, Hybrid Supercapacitors in Organic Medium, in: *Supercapacitors*, Wiley-VCH Verlag GmbH & Co. KGaA, **2013**, 239.
94. N. S. Choi, Z. Chen, S.A. Freunberger, X. Ji, Y.-K. Sun, K. Amine, G. Yushin, L.F. Nazar, J. Cho, P.G. Bruce, *Angew. Chem. Int. Ed.*, **2012**, 51, 9994.
95. E.J. Cairns, P. Albertus, *Annu. Rev. Chem. Biomol. Eng.*, **2010**, 1, 299.
96. V. Aravindan, J. Gnanaraj, Y.-S. Lee, S. Madhavi, *J. Mater. Chem. A*, **2013**, 1, 3518.
97. C.V. Rao, B. Rambabu, *Solid State Ionics*, **2010**, 181, 839.
98. V. Aravindan, W. Chuiling, S. Madhavi, *J. Mater. Chem.*, **2012**, 22, 16026.
99. X.-L. Wu, L.-Y. Jiang, F.-F. Cao, Y.-G. Guo, L.-J. Wan, *Adv. Mater.*, **2009**, 21, 2710.
100. Z. Yang, D. Choi, S. Kerisit, K.M. Rosso, D. Wang, J. Zhang, G. Graff, J. Liu, *J. Power Sources*, **2009**, 192, 588.
101. Y. Zhu, S. Murali, W. Cai, X. Li, J.W. Suk, J.R. Potts, R.S. Ruoff, *Adv. Mater.*, **2010**, 22, 3906.
102. I. Plitz, A. DuPasquier, F. Badway, J. Gural, N. Pereira, A. Gmitter, G.G. Amatucci, *Appl. Phys. A: Mater. Sci. Process.*, **2006**, 82, 615.
103. G. G. Amatucci, F. Badway, A. Du Pasquier, T. Zheng, *J. Electrochem. Soc.*, **2001**, 148, A930.
104. V. Aravindan, N. Shubha, W.C. Ling, S. Madhavi, *J. Mater. Chem. A*, **2013**, 1, 6145.
105. V. Aravindan, W. Chuiling, M.V. Reddy, G.V.S. Rao, B.V.R. Chowdari, S. Madhavi, *Phys Chem Chem Phys*, **2012**, 14, 5808.
106. V. Aravindan, M.V. Reddy, S. Madhavi, S.G. Mhaisalkar, G.V. Subba Rao, B.V.R. Chowdari, *J. Power Sources*, **2011**, 196, 8850.

Chapter-4

Water Electrolysis with a Conducting Carbon Cloth: Sub-Threshold Hydrogen Generation and Super-Threshold Carbon Quantum Dot Formation

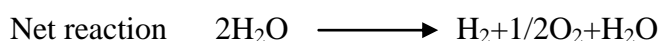
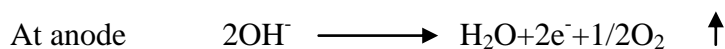
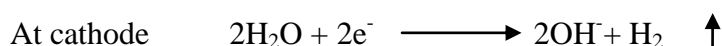
In this work we have demonstrated the efficient use of functional conducting carbon cloth anode (obtained by controlled pyrolysis of commercial cellulose cloth) in the alkaline electrolysis process which not only reduces the electrical energy need (and thereby the cost) because of sub-threshold hydrogen generation, but provides an interesting route for facile and large scale generation of carbon quantum dots. The sub-threshold hydrogen generation at 0.2V in two electrode system is due to the turbostratic nature of graphitic carbon in the cloth which provides plenty of defects sites for slow oxidation of carbon in 1M NaOH electrolyte. In two electrode system the quantity of hydrogen evolved was measured to be $24\text{mlcm}^{-2}\text{Hr}^{-1}$ for an applied voltage of 1V. Interestingly at super-threshold potential (driving voltage above 1.23V + overpotential) along with the high quantity of hydrogen oxidized carbon exfoliates from the cloth surface in the form of carbon quantum dots (5-7 nm). These show bright blue fluorescence under UV light. The mechanism of the sub-threshold hydrogen generation and super-threshold carbon quantum dot formation was investigated in details and the same is presented and discussed in this chapter.



4.1 Introduction

Carbon based materials have remained at the forefront of chemistry and materials science research due to their attractive chemical, electronic and catalytic properties. ^[1-4] The ubiquity and existence of carbon in different structural and functional forms (in bulk as well as nano) make them even richer in terms of the variety properties they support. Indeed, the electronic, thermal and optoelectronic behaviour of carbon nanotubes, graphene and graphene quantum dots have made this evident more than ever in recent times. ^[5-9] In the context of the current energy crisis and the intense research towards efficient, cost effective and clean energy generation and storage, such carbon based systems and their composites promise very interesting options. Studies of such low dimensional, low Z forms are also quite rich from the standpoint of fundamental science. In this chapter we present some interesting and novel strategy to employ a specific form of carbon material for hydrogen generation.

The potential of hydrogen gas as a fuel is unarguable; the energy density is one of the highest (120 Jg^{-1}) with water as the by-product of the combustion. Moreover, hydrogen can be produced from several different sources such as water, biomass, natural gas or coal. ^[10-13] Currently the most commonly used and fairly efficient method of hydrogen production is coal gasification and methane reforming reaction, both being energy intensive with undesirable environmental impacts. ^[10-11] Hydrogen generation from biomass is a sustainable method but is still far from being efficient. ^[11] Water electrolysis is one of the earliest known methods of producing highly pure gases of hydrogen and oxygen. The discovery of electrolytic water splitting was first observed in acidic water, however due to corrosion related concerns alkaline water electrolysis has become more common in water electrolysis technology. Other related methods developed in recent times are proton exchange membrane water electrolysis and steam electrolysis. In alkaline electrolysis, the half cell reactions are as follows:



As per the above reactions, hydrogen is evolved at the cathode and oxidation of OH⁻ ions at anode leads to the evolution of oxygen. Therefore the kinetics of this electrochemical reaction is highly dependent upon the type and configuration of anode and cathode. The rate of oxidation of OH⁻ ions to oxygen molecule at the anode surface is usually very poor and is the limiting factor in alkaline electrolysis process. The theoretical minimum potential required for this reaction to occur is 1.23V with respect to normal hydrogen electrode (NHE). In real electrolysis process due of several resistive factors at the interfaces of the electrode/electrolyte and electrode/conducting substrate an overpotential of 0.3 to 0.8V is required ^[14]. The overall efficiency of the electrolytic water splitting reaction depends upon the minimization of this overpotential, which depends on the selection of the electrode material with favourable microstructure, pore structure and electrocatalytic property (electrode to improve the reaction kinetics of the OH⁻ oxidation to oxygen molecule), an appropriate electrolyte. It also depends on the design of the electrolytic cell (distance between electrodes, sizes of electrodes etc). Amongst these the selection of electrode is the most crucial parameter. Platinum is known to be the most efficient electrode material for water reduction, followed by stainless steel, which is more commonly used in the industry. ^[15-17] Recently graphite and carbon nanotube based electrodes have been studied as potentially low cost and efficient anode materials. ^[18] Dubey *et al.* showed that the defects on the surface of multiwall carbon nanotube pellet play a key role in enhancing the current density of the electrode. ^[18] However since the amount of hydrogen produced is directly correlated to the current (or charge) being passed through the electrolytic cell, it really comes down to the threshold voltage (and overpotential) when one wants to operate the cell at lower wattage (or at higher efficiency). In this context in 1979 Farooque *et al.* had proposed a carbon assisted water electrolysis process in which coal slurry was used as the sacrificial agent in acidic water where CO₂ (instead of O₂) and H₂ evolved during the electrolysis. Since carbon oxidation to CO₂ thermodynamically requires less energy (threshold at 0.21V), this mechanism provided overall reduction in the overpotential for water splitting ^[19]. Seehra *et al.* further studied and optimized this process but the yield remained lower for the operating voltages below 1.23 V. ^[20]

In the present work we demonstrate that alkaline water electrolysis using a functional carbon cloth as anode shows an onset of hydrogen generation much below 1.23 V. Importantly, the porous structure with large quantity of defects and high conductivity of the functional cloth allow high current densities comparable to precious platinum. The turbostratic disorder in the structure of the cloth facilitates oxidation during the electrolysis process which starts off at as low a voltage as ~0.2 V. Although this process is also carbon-assisted water electrolysis, the extent of carbon oxidation is intrinsically controlled leading to oxygen evolution in contrast to CO₂ evolution as reported by Farooque *et al.* [19] and Seehra *et al.* [20] with the addition of carbon slurry. Most remarkably, when the operating voltage is beyond water decomposition, we observe that there is formation of copious quantity of carbon quantum dots (CQDs) emanating from the cloth anode in the electrolyte. We study the microstructural and electrochemical properties of this most interesting anode material in several details and present the mechanism underlying the sub-threshold hydrogen generation and super-threshold CQD formation.

4.2 Experimental

4.2.1 Materials

The cellulose fabric was obtained locally and used directly without any further treatments. NaOH and H₂SO₄ were purchased from Loba Chemicals and Rankem respectively. Pt foil used as cathode was purchased from Alfa Aesar.

4.2.2 Functional Carbon Cloth synthesis

The cellulose fabric was placed on an alumina plate and was subjected to pyrolysis at 1000° C for 4 Hr in a split tube furnace under continuous flow of argon gas. The heating rate was 10°C per min. After the reaction was over a black coloured conducting carbon cloth was obtained (**Scheme 4.1**). It was characterized by several techniques and was directly used as an anode in the water electrolysis process.

4.2.3 Characterization of the carbon cloth

The synthesized cloth material was characterized by x-ray diffraction using Philips X'Pert PRO diffractometer with nickel-filtered Cu K α radiation, Raman spectroscopy using Lab RAM HR800 from JY Horiba, high-resolution transmission electron microscopy using IFEI, Tecnai F30, with 300 KV FEG and field-emission

scanning electron microscopy (FESEM; Hitachi S-4200). The surface of cloth was examined by x-ray photoelectron spectroscopy (XPS) on a VG scientific ESCA-3000 spectrometer using non-monochromatized Mg K α radiation (1253.6 eV) at a pressure of about 1×10^{-9} Torr. All the electrochemistry measurements were done with Autolab PGSTAT30 (Eco-Chemie)

4.2.4 Electrochemical measurements for water electrolysis process

All the electrochemical experiments were performed in a closed glass cell made up of three separated chambers for anode (carbon cloth, graphite, platinum), cathode (platinum) and reference electrode (Saturated calomel electrode). All the three chambers were connected with glass frit for ion transport. All the measurements were performed with both the three and two electrode systems. The electrolyte used for the measurements were 1M NaOH and 3.7M H₂SO₄. For the electrolysis process 100 ml of electrolyte was poured in the glass assembly and the externally connected anode/cathode were placed into it. For all the three electrode system measurements saturated calomel reference electrode was used. External voltage of 0-2V was supplied through the potentiostat and the current was measured from by cyclic voltametry. Autolab PGSTAT 30-Eco-Chemie was used to sweep the voltage at a scanning rate of 10 mV s⁻¹.

4.2.5 Gas Analysis

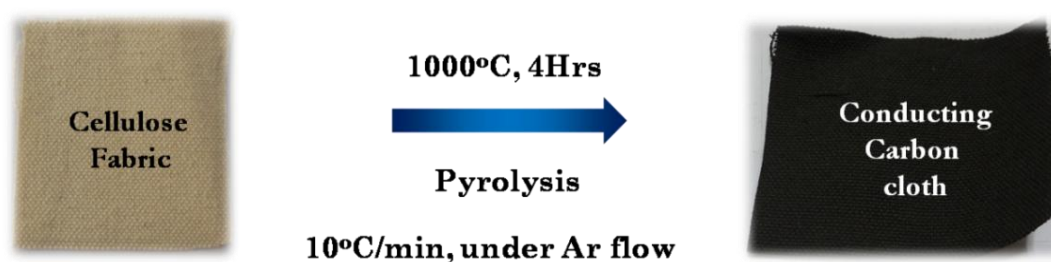
All the gases evolved at the anode and the cathode, were analyzed by Gas Chromatography (GC). A closed glass reaction cell with three electrode assembly, having provision for withdrawal of the gaseous samples at desired intervals, was employed in these experiments. Prior to each experiment, the reaction cell was purged with nitrogen for a few minutes. The evolved hydrogen was sampled with a 500 μ l syringe (Hamilton) and analyzed periodically by using the gas chromatograph (Agilent model-1020), equipped with a 9ft Mol-Sieve 5A column having argon as the carrier gas and a thermal conductivity detector maintained at 400 K. All the CO₂ detection experiments were performed with the porapak Q column.

4.2.6 Synthesis and Purification of carbon quantum dots

Carbon quantum dots (CQDs) were synthesized by using two electrode systems with the cloth as anode and Pt as cathode with 100 ml of 1M NaOH in a 250 ml glass beaker. A constant potential of 2V was applied for 1 Hr between the

electrodes. After 1 Hr a brown coloured solution was collected and diluted to 500 ml. The pH of the solution was neutralized to 7 by adding dilute HCl followed by the addition of ethanol drop by drop. To the above solution Mg_2SO_4 salt was added and stirred for 10 mins. This solution was then filtered and purified by using a dialysis membrane (3.5 kD). The purified CQD suspension was used for all the characterizations.

4.3 Results and Discussions



Scheme 4.1: Synthesis of carbon cloth from cellulose fabric

Figure 4.1a shows the XRD pattern for the pyrolyzed cloth which shows two prominent peaks at 2θ value of around 25 and 44 which correspond to the (002) and (101) planes of turbostratic carbon.^[21,22] The Raman spectrum of the cloth shown in **Figure 4.1b** also shows the D and G bands at 1300 cm^{-1} and 1590 cm^{-1} , respectively.

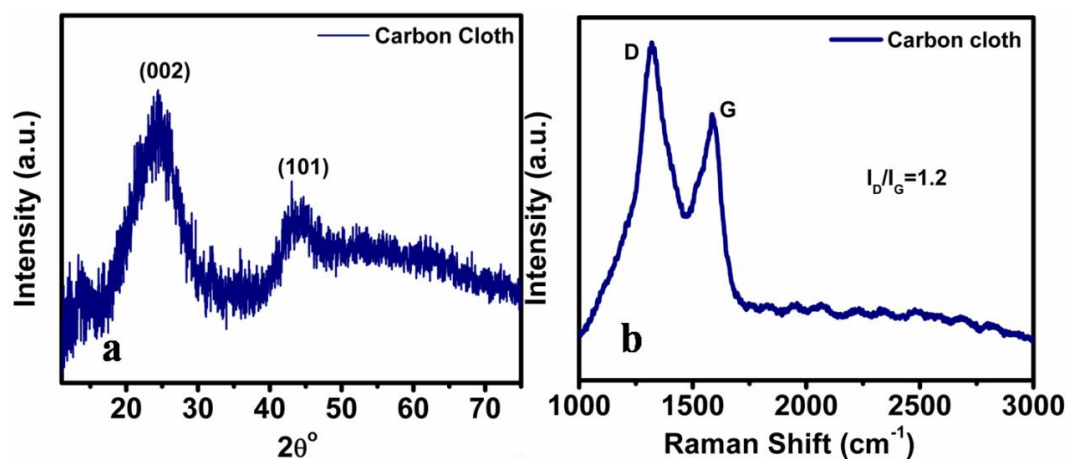


Figure 4.1: a) X-ray diffraction, b) Raman spectrum for the conducting carbon cloth

The G-band represents the presence of graphitic nature and D band corresponds to the defects presents in the system. From this figure it can be clearly observed that the

intensity of D band is higher than the G band with I_D/I_G ratio ~ 1.2 which represents high concentration of defects present in the cloth surface which is due to the imperfections in the turbostratic structure of the carbon cloth. [23]

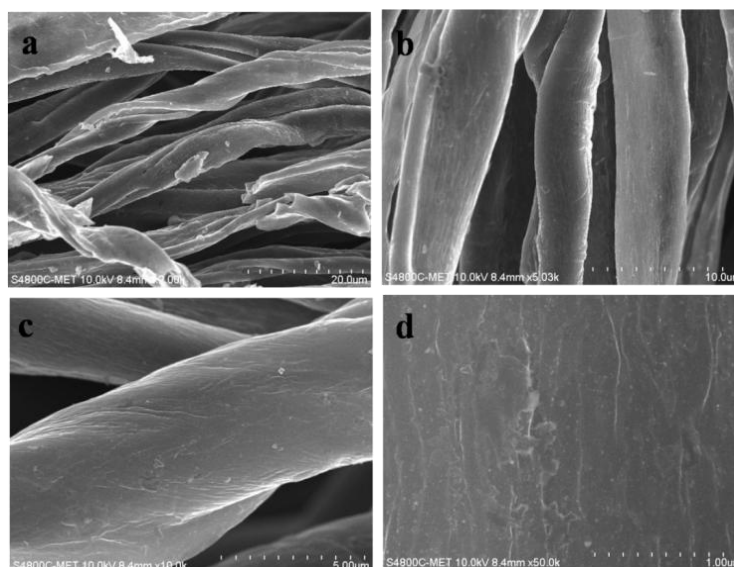


Figure 4.2: a-d) FESEM images of carbon cloth

The microstructure of the as-synthesized carbon cloth was studied with FESEM and the images are shown in **Figure 4.2a-d**. Expectedly, these images show fibre-like structures present in the carbon cloth with rough surfaces. The frequency dependant conductivity data for the material is shown in **Figure 4.3** which shows that the carbon cloth is highly conducting in nature.

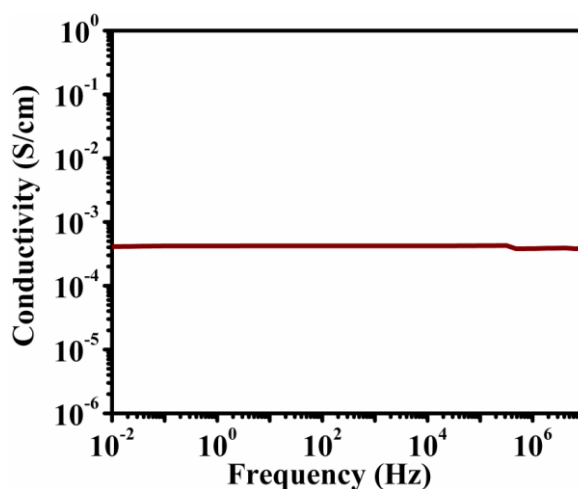


Figure 4.3: Frequency dependant conductivity data for carbon cloth

4.3.1 Sub-Threshold Hydrogen Generation

Figure 4.4 shows the I-V scan of the water electrolysis process using functional cloth as anode and Pt foil as cathode in 1M NaOH electrolyte in a three electrode system. For comparison, I-V scans of graphite-Pt and Pt-Pt combinations of anode-cathode are also presented. As seen from these plots, the functional cloth shows dramatically high current density as compared to both graphite and Pt anodes.

In order to truly monitor the onset potential of the oxidization of anode in the application context we also recorded the I-V data under two electrodes set up, which is shown in **Figure 4.5**. From this plot it can be clearly seen that the plots for graphite and Pt anode start to take off above only 1.5 V which is consistent with the reported operating potential for water splitting including the overpotential. However, remarkably, in case of functional cloth, the kick off is around 0.2 V which plateaus at around 1.5 V and then again takes off. We demonstrate that this sub-threshold hydrogen generation starts off due to oxidation (etherification) of the carbon on the surface of the turbostratic functional cloth.

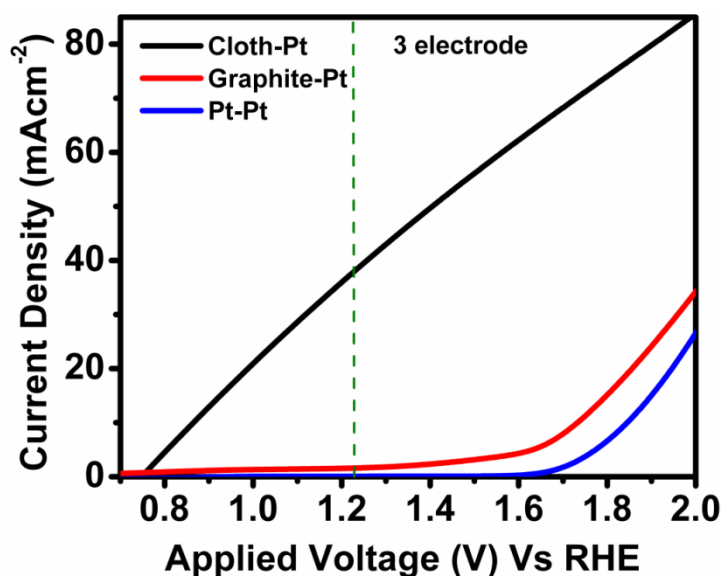


Figure 4.4: Cyclic Voltammetry curves for cloth-Pt, graphite-Pt and Pt-Pt cases in a three electrode system from -1V to 1V range.

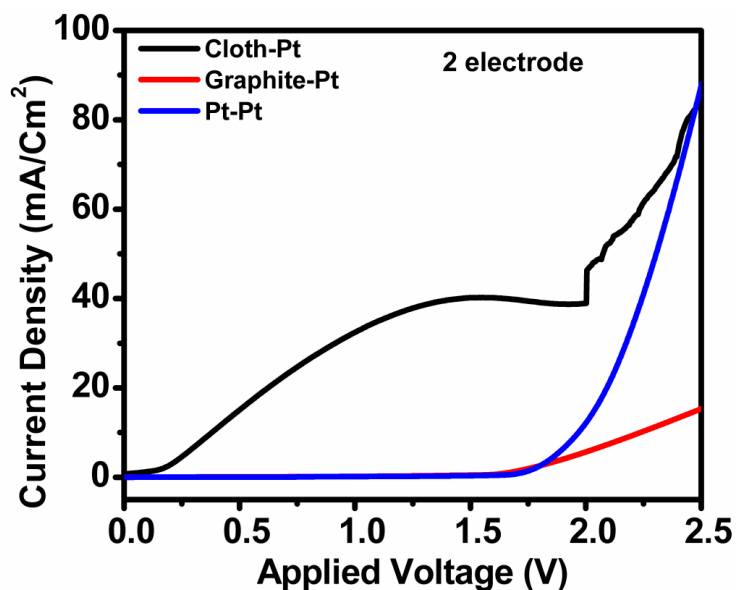


Figure 4.5: Cyclic Voltammetry curve for cloth-Pt, graphite-Pt and Pt-Pt cases in two electrode system from 0-2V.

A current density as high as 32 mA cm⁻² was observed in this region which is almost 3 orders of magnitude higher as compared to graphite and Pt as anode. Beyond 1.5 V there is an increase in the rate of hydrogen generation as seen in the change of slope in the I-V plot for the cloth, which is associated to the take-over of regular water electrolysis process similar to graphite and Pt anodes. This can also be more clearly

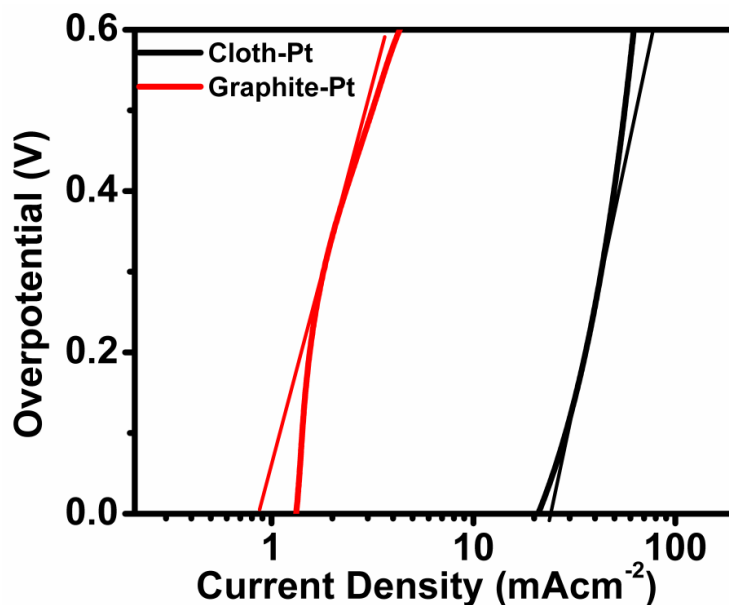


Figure 4.6: Tafel plot for cloth-Pt and graphite-Pt in three electrode system

understood from the Tafel plot shown in **figure 4.6** which represents the exchange current density calculated by drawing a tangent to the x-axis. From this graph it was observed that the exchange current density is the case of carbon cloth is higher (24 mAcm^{-2}) than the graphite and Pt as anodes. (1 mAcm^{-2} for graphite and 0.3 mAcm^{-2} for Pt).

The evolved hydrogen was measured using Gas Chromatography as presented in **figure 4.7**. In this plot the total amount of hydrogen evolved over one hour is presented when a constant voltage of 1V (sub-threshold) and 2V (super-threshold) is applied. The most important thing to note here is that at 1 V only cloth showed hydrogen evolution (24 ml/cm^2). Graphite and platinum did not show even a trace of hydrogen. At 2V there is an obvious increase in the yield for the case of cloth from 24 to 56 ml/cm^2 , which is much higher (> 5 times) than the amount of hydrogen evolved with graphite or platinum as anodes. The difference in hydrogen yield here is consistent with the differences in current densities measured via I-V scans. At all times the gas evolved at the anode was confirmed to be oxygen.

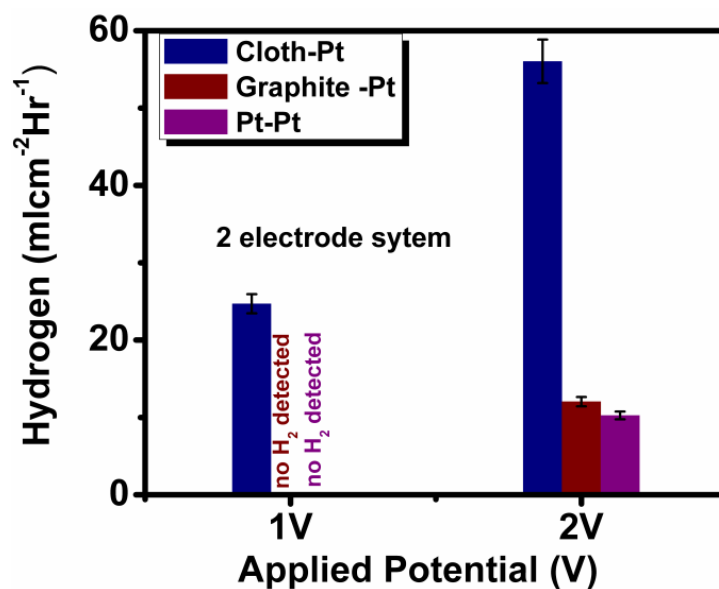


Figure 4.7: H_2 measured at 1V and 2V applied potential for cloth, graphite and Pt as anode

We propose that the primary reason for such a high rate of hydrogen evolution in the case of cloth as anode (even as compared to graphite) is due to the catalytically active surface defects present in the carbon cloth. As this cloth has been synthesized

at 1000°C, there is partial graphitization in the structure which gives rise to turbostratic (disordered) structure. Such a turbostratic cloth holds topologically distorted nanoscale graphene units and has more surface and edges available for the electrolysis, (and related catalytic) process. At the same time it can undergo oxidation more easily. In 1M NaOH as electrolyte there is a high concentration of OH⁻ ions. In a typical alkaline electrolysis process the OH⁻ ions get oxidized at the anode surface and form O₂ molecules. But in case of the turbostratic functional cloth, the OH⁻ ions can get adsorbed on the surface and can oxidize the carbon surface successively from C-OH to C=O to -COOH etc. under the applied potential. These oxidation reactions start at very low potentials, they are exothermic in nature and they cause irreversible changes on the surface of the cloth. ^[24-25] Thus the required energy for hydrogen

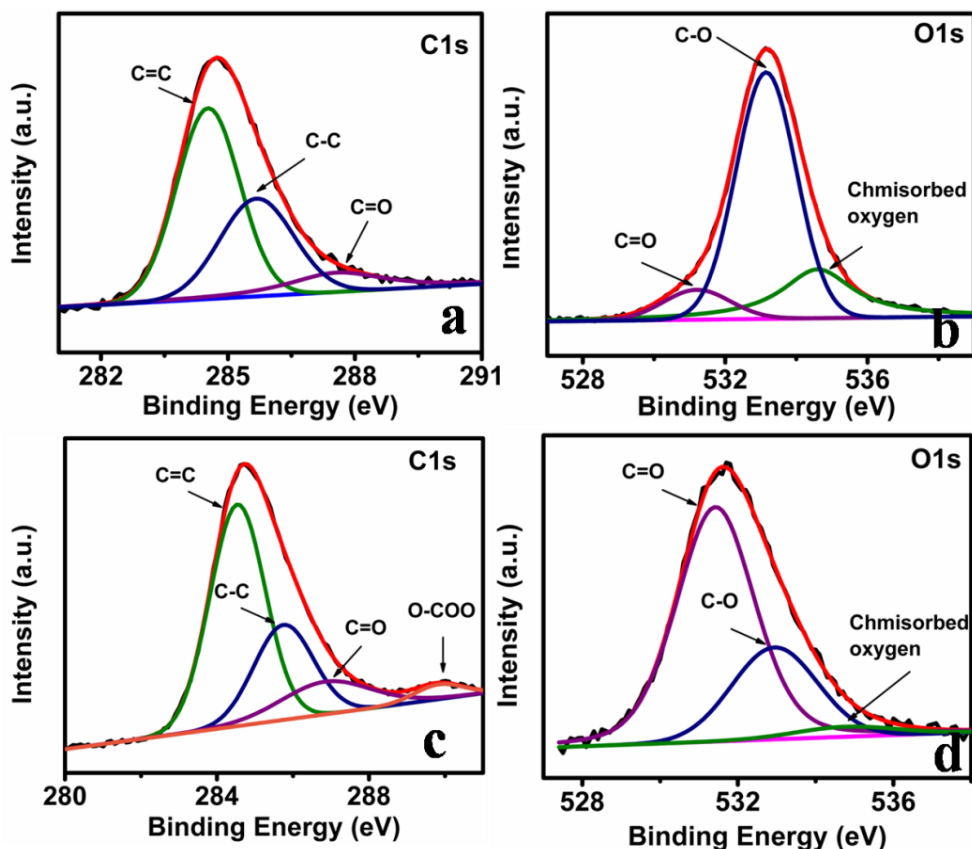


Figure 4.8: a) and b) C1s and O1s spectra of fresh cloth; c and d) C1s and O1s spectra of used cloth for electrolysis.

generation below the threshold voltage of 1.23V is taken from the oxidation of carbon surface. Therefore as the cloth itself participates in the electrolysis process the overall

efficiency of hydrogen generation is higher as compared to pure electrolytic water splitting.

Although this is also a carbon-assisted water electrolysis process, the distinct difference with respect to the previous slurry work^[19,20] is that herein instead of CO₂ evolution oxygen gas is getting evolved and concurrently the electrode is undergoing a chemical change (oxidation). To confirm this proposed mechanism, we investigated the functional cloth which had undergone the electrolysis process by x-ray photoelectron spectroscopy (XPS) and the data are shown in **Figure 4.8**.

The parts (a) and (c) in this figure show the C1s spectra of fresh conducting carbon cloth and electrochemically processed carbon cloth, respectively. In the case of the fresh cloth the C1s spectrum can be fitted with three major peaks which correspond to C=C (binding energy 284.6 eV), C-C (binding energy 285.67 eV) and C=O (binding energy 287.8 eV).^[26-32] This clarifies that the fresh cloth contains only a few percent oxygen containing groups on the surface. However the C1s spectrum of the electrochemically processed carbon cloth shows an additional peak at binding energy 289.7eV along with the three peaks corresponding to C=C, C-C and C=O. This peak corresponds to O-COO which is ester and carboxylic group. This proves that during the electrolysis process the surface of the cloth undergoes oxidation (hydroxyl to carboxyl to ester groups getting attached to the carbon on the surface). In line with this **Figure 4.8 b and d** depict the O1s spectra of the fresh cloth and the electrochemically processed cloth, respectively. In the case of fresh cloth the O1s spectrum consists of 3 peaks which belong to C-O (binding energy 533.1 eV), C=O (binding energy 531.26 eV) and chemisorbed oxygen (binding energy 534.6 eV).^[26-32] In the case of the electrochemically processed cloth the intensity of C=O peak is enhanced (highest intensity peak) as compared to the fresh cloth case. This is also due to the anodic oxidation observed during the electrolysis process.

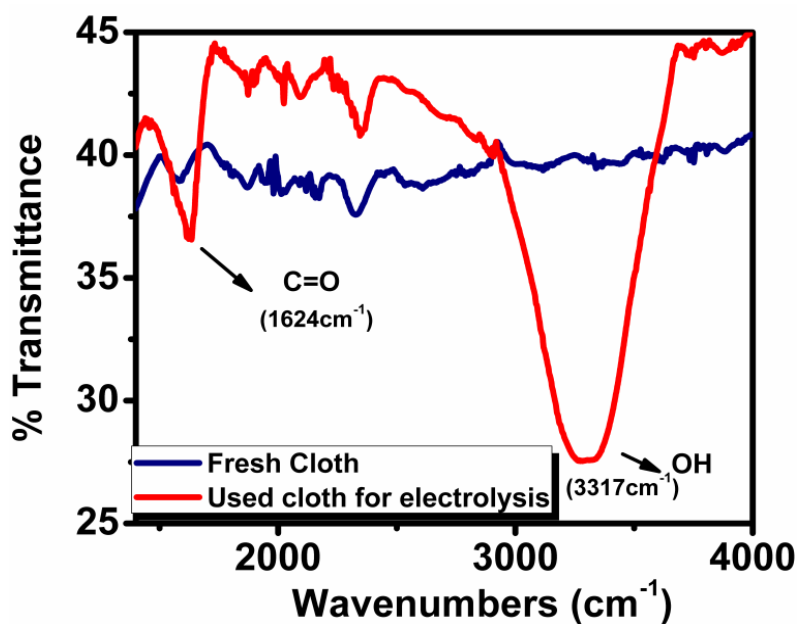


Figure 4.9: FTIR-ATR spectra of fresh cloth and used cloth after electrolysis

Figure 4.9 shows the FTIR spectra for the cases of fresh carbon cloth and electrochemically processed cloth from electrolysis in the attenuated total reflection (ATR) mode to further reveal the oxidation process during electrolysis. In the case of electronically processed cloth the peak appearing at $\sim 1640\text{ cm}^{-1}$ is associated with carbonyl or quinone groups present on the surface which is almost absent in case of the fresh cloth.^[33-34] The appearance of this peak clearly indicates the electrochemical oxidation of the surface of carbon cloth during electrolysis. Also the emergence of the giant broad peak at $\sim 3317\text{ cm}^{-1}$ due to the OH groups present on the carbon surface distinguishes the surface of the electrochemically processed carbon cloth from the fresh one indicating that the processed cloth has undergone stronger oxidation.

In line with the carbon assisted water electrolysis proposed by Farooque *et al.*^[19] and later studied in more details by Seehra *et al.*^[20], we studied the electrochemical performance of the functional conducting carbon cloth in an acidic medium. Since under acidic conditions the cloth surface is even more prone to oxidation, we observed that with 3.7M HNO₃ as electrolyte the cloth underwent complete oxidation and released CO₂ instead of O₂ at voltages lower than 1.23V. This is consistent with the observation for coal slurry in acidic water. But since the cloth

itself is conducting, it could act as both the electrode and at the same time a sacrificial component getting oxidized itself into CO_2 .

4.3.2 Super-Threshold Carbon Quantum Dot Formation

When a potential above 1.5V (1.23 + overpotential) is applied during the electrolysis with the functional conducting carbon cloth as an anode and Pt as a cathode, a very interesting observation was made. It was observed that the electrolyte solution slowly turned brown in colour. Interestingly, this was not observed when graphite was used as anode. When this solution was purified and characterized with HR-TEM and photoluminescence spectroscopy, it was observed that it contained carbon quantum dots. The HR-TEM images show well dispersed 5-7 nm particles as shown in **Figure 4.10 a-d**.

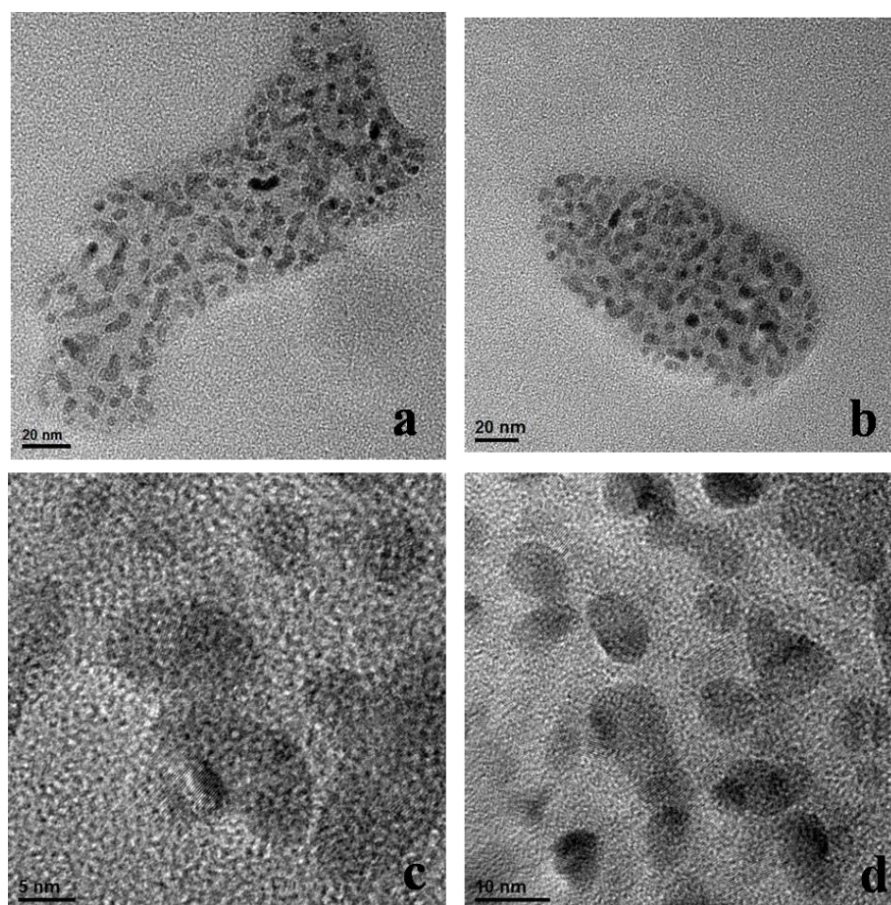


Figure 4.10: a-d) HRTEM images of carbon quantum dots generated from carbon cloth

Figure 4.11 represents the photoluminescence spectra of carbon quantum dots dispersed in water at different excitation wavelengths. The PL spectra show that the fluorescence emission of carbon quantum dots is excitation dependent which is commonly observed in the case of carbon and graphene quantum dots. ^[35-40] In case of carbon quantum dots the excitation-dependent PL behaviors is not only because of the presence of particles with different sizes but also distribution of different emissive sites on each carbon dot. The fluorescence peak shifted from 490 to 527nm when the excitation wavelength changed from 380 to 480 nm. Also the peak intensity was observed to decrease with increase in the excitation wavelength. The inset of this figure shows the bright blue colored emission of carbon quantum dots (CQDs) under UV light.

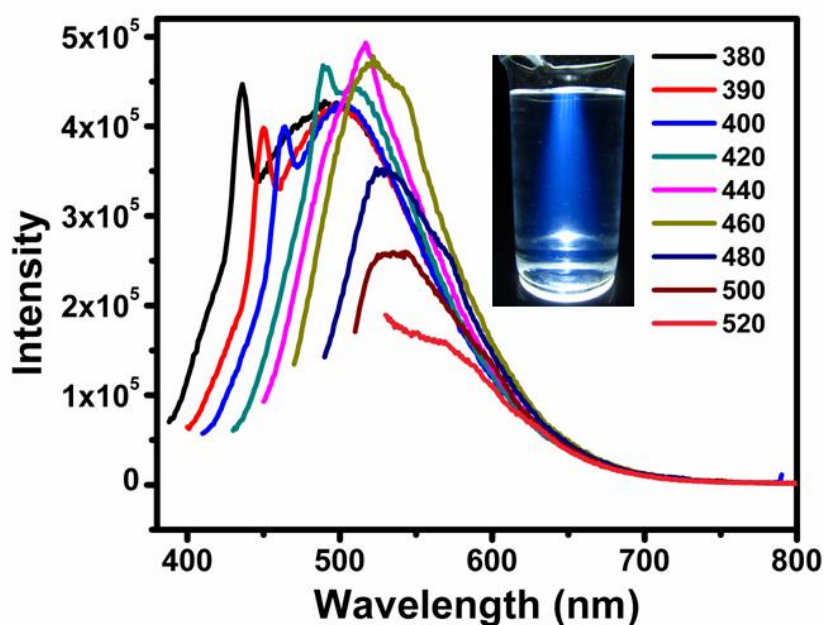


Figure 4.11: Photoluminescence spectra of carbon quantum dots dispersed in water; inset shows blue colour fluorescence of carbon quantum dots under UV light

Upon careful observation of the I-V data and onset of quantum dot formation, we realized that the sub-threshold hydrogen generation and super-threshold quantum dots formation processes are actually interlinked. The quantum dot formation process only starts when the hydrogen generation through water splitting takes over above 1.5 V. Hence again this quantum dot formation mechanism can be explained on the basis of anodic oxidation of the carbon cloth. Often in electrochemical processes of carbon

based electrodes it has been observed that the electrode itself undergoes reduction or oxidation and there are some reports of formation of graphene or carbon quantum dots using this approach. ^[41-43]

In our case, in line with the earlier discussion on oxidation of turbostratic cloth surface in alkaline electrolyte, at potentials up to 1.5V, the OH⁻ ion get bonded to the carbon surface and form C-OH along with the release of one electron. Subsequent oxidation continues forming -HC=O, -C=O, -COOH and also -O-COO- etc. with each step releasing corresponding number of electrons. However above a particular threshold voltage, the carbon turbostratic units themselves begin to get exfoliated from the surface forming carbon quantum dot. It should be pointed out that the standard protocol of chemical synthesis of graphene from graphitic powder does involve oxidative exfoliation followed by reduction of the product. Since in our case it starts off above ~1.5V, probably the release of oxygen gas molecules at anode can also help with internal mechanical stresses in the exfoliation of turbostratic carbon units from the surface. Although there have been several reports of electrochemical synthesis of graphene and carbon quantum dots, ^[41-43] as per our knowledge this is the most dilute condition in terms of electrolyte concentration, number of cyclic voltammetry cycles and applied voltage, where carbon quantum dot synthesis occurs.

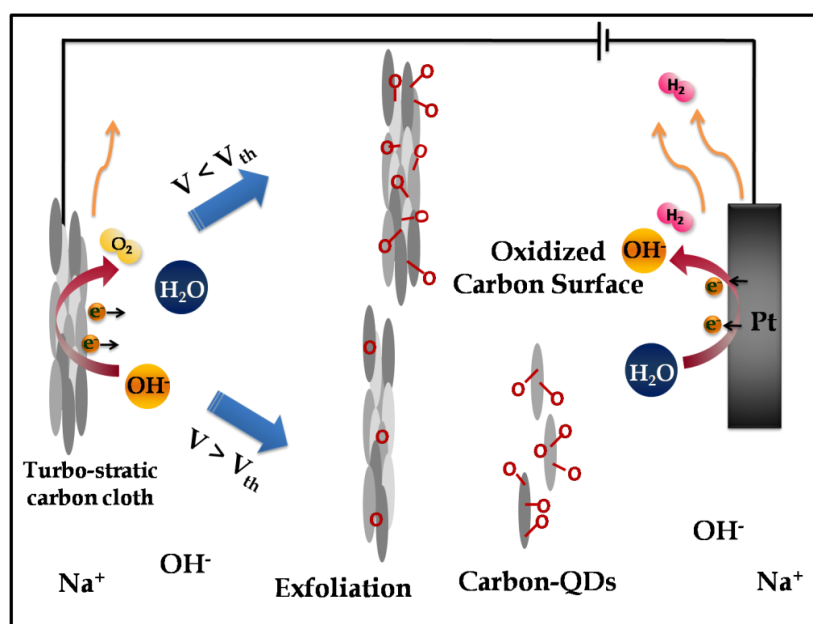


Figure 4.21: Schematic diagram for the possible mechanism of electrochemical reactions occurring at the carbon cloth surface

In summary, we briefly restate the overall proposed mechanism of sub-threshold hydrogen generation and super-threshold carbon quantum dot formation with the help of a schematic diagram which is shown in **Figure 4. 22**. As shown, when the applied potential is below 1.23V (plus the overpotential), the water molecules get dissociated into OH^- by taking electrons from the Pt surface. The OH^- ions then travel to the anode and oxidize the carbon surface by releasing electrons. This exothermic oxidation process proceeds slowly from C-OH to COOH during the subsequent electrochemical reactions by releasing energy. This energy leads to the onset of hydrogen evolution much below the threshold potential. When the applied potential is greater than 1.23V (plus the overpotential) further oxidation of the already oxidized carbon surface leads to the exfoliation of tiny turbostratic carbon units into the electrolyte solution. These units are identified to be highly water-dispersed carbon quantum dots (CQDs) with highly oxidized surface. We emphasize that the peculiar turbostratic graphitic nature of the conducting carbon cloth is central to the observed unique features of this experiment, which not only provides high conductivity to act as an electrode but also supplies many reactive sites for the reaction to occur at low potential. Graphite, graphene, CNT or other such carbon forms do not provide these special features.

4.4 Conclusion

In this report we demonstrate an immensely interesting electrochemical functionality of a conducting carbon cloth as electrode material. This functional cloth, which was obtained by simple one-step pyrolysis of an industrial cellulose cloth, when used as anode in an electrochemical cell, shows very high efficiency (much higher than Platinum as anode) for hydrogen generation. Most importantly, the hydrogen generation was observed to start much below 1.23V vs RHE (as low as 0.2 V). We show that this is made feasible because of the highly disordered-turbostratic structure and high conductivity of the functional cloth. Due to this, in alkaline electrolyte, the cloth undergoes irreversible oxidization and in effect allows sub-threshold hydrogen generation. Only above the threshold voltage oxygen is observed to be evolved. Another very interesting finding is that, above 1.5 V corresponding to rapid hydrogen evolution, the oxidized carbon cloth allows exfoliation of nanoscale

turbostratic carbon units from the surface due to its defective structure leading to its suspension in the electrolyte as carbon quantum dots (CQDs). No such CQD formation occurs at comparable or even higher voltages with graphite anode. We believe that this study opens up a great opportunity for further work and optimization of structure of carbon based materials for electrolysis application.

4.5 References

1. S. Tomita, T. Sakurai, H. Ohta, M. Fujii, and S. Hayashi, *J. Chem. Phys.*, **2001**, 114, 7477.
2. R. L. McCreery, *Chem. Rev.*, **2008**, 108, 2646.
3. T. W. Odom, J. Huang, P. Kim, and C. M. Lieber, *J. Phys. Chem. B*, **2000**, 104, 2794.
4. N. M. R. Peres, F. Guinea, and A. H. Castro Neto, *Phys. Rev. B*, **2006**, 73, 125411.
5. A. A. Balandin, *Nat. Mater.*, **2011**, 10, 569.
6. J. Nilsson, A. H. Castro Neto, F. Guinea, and N. M. R. Peres, *Phys. Rev. Lett.*, **2006**, 97, 266801.
7. E. Bekyarova, M. E. Itkis, N. Cabrera, B. Zhao, A. Yu, J. Gao, and R. C. Haddon, *J. Am. Chem. Soc.*, **2005**, 127, 5990.
8. S. Jhi, S. G. Louie, and M. L. Cohen, *Phys. Rev. Lett.*, **2000**, 85, 1710.
9. Z. Zhang, J. Zhang, N. Chena and L. Qu, *Energy Environ. Sci.*, **2012**, 5, 8869.
10. J.O'M. Bockris, *Int. J. Hydrogen Energy*, **2002**, 27, 731.
11. J. A. Turner, *Science*, **2004**, 305, 972.
12. W. Lubitz, B. Tumas, *Chem. Rev.*, **2007**, 107, 3900.
13. R. M. Navarro, M. A. Peña, and J. L. G. Fierro, *Chem. Rev.*, **2007**, 107, 3952.
14. K. Mazloomi, N. Sulaiman, H. Moayedi, *Int. J. Electrochem. Sci.*, **2012**, 7, 3314.
15. M. Carmo, D. L. Fritz, J. Mergel, D. Stolten, *Int. J. Hydrogen Energy*, **2013**, 38, 4901.
16. A. Nidola, *Int. J. Hydrogen Energy*, **1989**, 4, 367.
17. H. B. Suredini, J. L. Cerne, F. C. Crnkovic, S. A. S. Machado, L. A. Avaca, *Int. J. Hydrogen Energy*, **2000**, 25, 415.

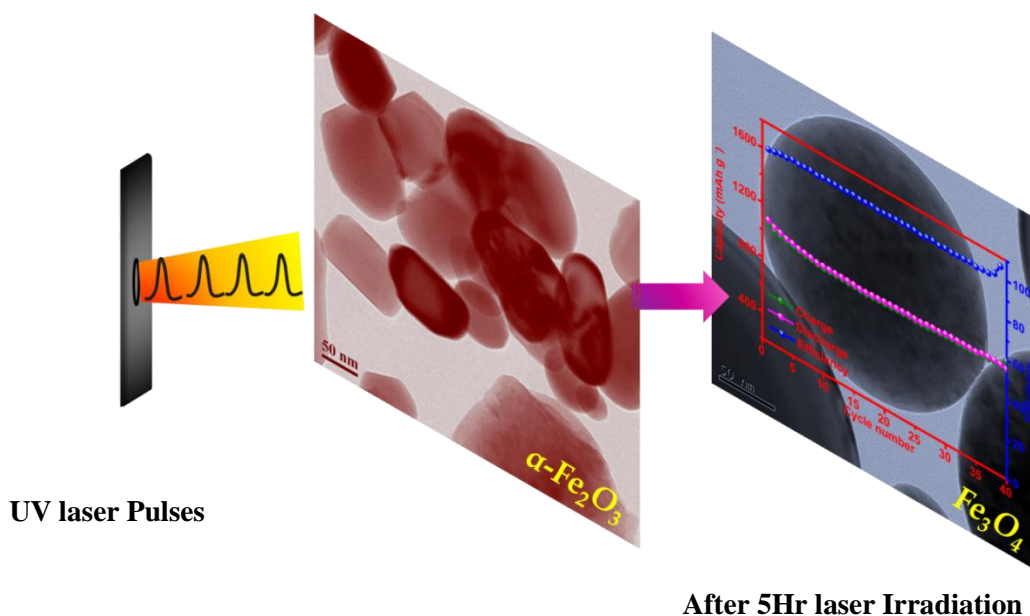
18. P. K. Dubey, A. S. K. Sinha, S. Talapatra, N. Koratkar, P. M. Ajayan, O. N. Srivastava, *Int. J. Hydrogen Energy*, **2010**, 35, 3945.
19. R. W. Coughlin and M. Farooque, *Nature*, **1979**, 279, 301.
20. M. S. Seehra, S. Ranganathan and A. Manivannan, *Appl. Phys. Lett.*, **2007**, 90, 044104.
21. Y. Wang, F. Su, C. D. Wood, J. Y. Lee, and X. S. Zhao, *Ind. Eng. Chem. Res.*, **2008**, 47, 2294.
22. L. Ci, B. Wei, C. Xua, J. Liang, D. Wu, S. Xie, W. Zhou, Y. Li, Z. Liu, D. Tang, *J. Cryst. Growth*, **2001**, 233, 823.
23. A. Eckmann, A. Felten, A. Mishchenko, L. Britnell, R. Krupke, K. S. Novoselov, and C. Casiraghi, *Nano Lett.*, **2012**, 12, 3925.
24. S. F. Waseem, S. D. Gardner, G. He, W. Jiang, U. Pittman Jr, *Journal of Material Science*, **1998**, 33, 3151.
25. Z. Shao, S. M. Haile, J. Ahn, P. D. Ronney, Z. Zhan & S. A. Barnett, *Nature*, **2005**, 435, 795.
26. C. Ozlowskain, P. M. A. Sherwood, *J. Chem. Soc., Faraday Trans.*, **1985**, 81, 2745.
27. T. I. T. Okpalugo, P. Papakonstantinou, H. Murphy, J. McLaughlin, N. M. D. Brown, *Carbon*, **2005**, 43, 153.
28. H. Fang, C. Liu, C. Liu, F. Li, M. Liu, and H. Cheng, *Chem. Mater.* **2004**, 16, 5744.
29. Z. R. Yue, W. Jiang, L. Wang, S.D. Gardner, C.U. Pittman Jr, *Carbon*, **1999**, 37, 1785.
30. H. Estrade-Szwarcckopf, *Carbon*, **2004**, 42, 1713.
31. G. Lee, J. Kim, J. Yoon, J. Bae, B. C. Shin, I. S. Kim, W. Oh, M. Ree, *Thin Solid Films*, **2008**, 516, 5781.
32. L. Liu, Y. Qin, Z. Guo, D. Zhu, *Carbon*, **2003**, 41, 331.
33. R. Yudianti, H. Onggo, Sudirman, Y. Saito, T. Iwata and J. Azuma, *The Open Materials Science Journal*, **2011**, 5, 242.
34. J. Gulyás, E. Földesa, A. Lázárc, B. Pukánszky, *Composites: Part A*, **2001**, 32, 353.

35. H. Li, X. He, Z. Kang, H. Huang, Y. Liu, J. Liu, S. Lian, C. H. A. Tsang, X. Yang, and S. Lee, *Angew. Chem. Int. Ed.*, **2010**, 49, 4430.
36. Y. Sun, B. Zhou, Y. Lin, W. Wang, K. A. S. Fernando, P. Pathak, M. J. Meziani, B. A. Harruff, X. Wang, H. Wang, P. G. Luo, H. Yang, M. E. Kose, B. Chen, L. M. Veca, and S. Xie, *J. Am. Chem. Soc.*, **2006**, 128, 7756.
37. H. Li, Z. Kang, Y. Liu and S. T. Lee, *J. Mater. Chem.*, **2012**, 22, 24230.
38. S. N. Baker and G. A. Baker, *Angew. Chem., Int. Ed.*, **2010**, 49, 6726.
39. H. Liu, T. Ye, and C. Mao, *Angew. Chem. Int. Ed.*, **2007**, 46, 6473.
40. P. G. Luo, S. Sahu, S. Yang, S. K. Sonkar, J. Wang, H. Wang, G. E. LeCroy, L. Cao and Y. Sun, *J. Mater. Chem. B*, **2013**, 1, 2116.
41. C. U. Pittman Jr, W. Jiang, Z. R. Yue, S. Gardner, L. Wang, H. Toghiani, C.A. Leon y Leon, *Carbon*, **1997**, 37, 1797.
42. J. Gulyása,b, E. Földesa, A. Lázárc, B. Pukánszky, *Composites: Part A*, **2001**, 32, 353.
43. K. W. Hathcock, J. C. Brumfield, C. A. Goss, Eugene A. Irene, and Royce W. Mumy, *Anal. Chem.*, **1995**, 67, 2201.

Chapter-5

Pulsed Laser Synthesis of Mesoscopic Fe_3O_4 Spheres for Use as Anode Material in High Performance Li ion Battery

This chapter focuses on the synthesis and study of spherical particles of magnetite (Fe_3O_4) as anode material in Li ion battery. About 200 nm sized magnetite particles are synthesized directly from bulk commercial $\alpha\text{-Fe}_2\text{O}_3$ powder by pulsed excimer (UV) laser irradiation technique in solution phase. The Fe_3O_4 particles show a capacity of 1100 mAhg^{-1} at a current density of 100 mA g^{-1} . The capacity is highly stable up to 40 cycles without any significant capacity fading. The coulombic efficiency of 97% is achieved with high stability and reversibility.



Direct Conversion of bulk $\alpha\text{-Fe}_2\text{O}_3$ to mesoscopic Fe_3O_4 spheres

5.1 Introduction

Lithium ion batteries have been widely used as power sources for portable electronics over the past several decades.^[1-4] Immense research has been carried out to reduce the cost and increase the efficiency of Li ion battery by designing and manipulating the anode and cathode materials. The efficiency of Li ion battery is limited because of the low theoretical capacity (372 mAhg⁻¹) of graphite anode.^[5,6] Hence it is unable to meet the ever growing energy demand of high energy and high power density for portable electronics. Therefore current research is focused on the synthesis of novel anode materials with promising properties for such high performance Li ion battery.

Apart from carbon materials various nanostructured transition metal oxides such as Fe₂O₃, Fe₃O₄, NiO, CoO, Co₃O₄, CuO etc. are being widely investigated as anode materials for Li ion battery because of their high capacity.^[7-11] These materials can replace conventional graphite anode because of their high theoretical capacity which ranges from 500 to 1200 mAhg⁻¹.^[12-16] However most of these metal oxides usually suffer from very high volume expansion/contraction, and severe particle aggregation associated with the Li ion insertion/extraction process. This results in large capacity fading and poor cycling stability, especially at high rates. Despite enormous research for the improvement of properties of anode materials reversible capacity, cyclability, and high-rate capability are still unresolved major issues and remain a great challenge for this field of Li ion battery.^[17-22]

Among various metal oxides, hematite (α -Fe₂O₃) and magnetite (Fe₃O₄) have been widely studied as the most promising electrode materials because of their high theoretical capacity (1004 mAhg⁻¹ for α -Fe₂O₃ and 924 mAhg⁻¹ for Fe₃O₄), eco-friendliness, and natural (earth) abundance.^[23-28]

The reactions of α -Fe₂O₃ and Fe₃O₄ with lithium can be written as follows.



When coupled with the higher intrinsic densities, iron oxides offer about six times higher volumetric capacity than graphite (5.17-5.24 gcm⁻³ Vs. 2.16 gcm⁻³ for

graphite) which is a major advantage for smaller battery packs.^[29-31] The performance of these iron oxides is also affected by their synthesis methods. Mostly these oxides are synthesized by sol-gel, hydrothermal, co-precipitation, soft and hard templating, microwave, electro-deposition and electrospinning techniques.^[32-39] The morphological control of these oxides materials is becoming increasingly important for high performance in Li ion battery design. Because of the Li intercalation process, the size and shape of these materials should be ideal to avoid distortion of the structure and capacity loss.

As stated above, Fe_3O_4 has proved to be a fairly efficient anode material for Li ion battery.^[40-45] There are many reports on the use of Fe_3O_4 nanoparticles as electrode material and these reports have also addressed various problems and limitations in this context. The major limitations of Fe_3O_4 as anode material are capacity fading due to the lack of stability and decrease in the columbic efficiency. A lot of studies have been reported on the synthesis of Fe_3O_4 but there is hardly any report on direct conversion of $\alpha\text{-Fe}_2\text{O}_3$ to Fe_3O_4 . As $\alpha\text{-Fe}_2\text{O}_3$ is the most stable phase amongst all the iron oxides, converting $\alpha\text{-Fe}_2\text{O}_3$ to Fe_3O_4 is a non-trivial process. There are literature reports on the synthesis of Fe_3O_4 from $\alpha\text{-Fe}_2\text{O}_3$ by high pressure high temperature reduction by passing reducing gases.^[46-47]

In this present work we have synthesized mesoscopic Fe_3O_4 by a novel and simple method involving exposure of $\alpha\text{-Fe}_2\text{O}_3$ bulk powder suspended in water to 20 ns Excimer laser pulses (UV, 248 nm) under constant stirring. In view of the nature of the results obtained, we term this as pulsed laser induced reactive micro-bubble synthesis (PLRMS) process. Pulsed UV laser treatment of suitably chosen chemical precursors is a very unique method for the synthesis of nanoparticles because of two reasons; first photo-dissociation of molecules caused by direct UV laser absorption and second, high temperature local heating (few thousand degrees, plasma formation) caused by energy dissipation leading to local high pressures as well.^[48-49] These dynamics effects render chemical changes in the molecules and precursors including decomposition and subsequent associations/reactions with the suspending media or ambient. Reactions can in fact be manipulated by adding some external reagents which can construct totally new compounds after the photo-thermal melting. After the

short time melting either photofusion or photo-fragmentation of particles has been observed which leads to bigger particles or smaller particles, respectively. ^[50-51] There are many reports on size reduction of gold and silver nanoparticles in colloidal solutions by pulsed laser photo-fragmentation. ^[50-52] Separately, size growth of gold nanoparticles is also reported using pulsed 532 nm laser light, wherein a maximum size of at most less than 100 nm was achieved due to the subsequent photo-fragmentation. ^[53-54] Thus, laser irradiation techniques have been primarily used to control the size of particles. The tremendous promise of this technique in terms of reactive synthesis however has remained considerably less explored.

In this work direct conversion of α -Fe₂O₃ to Fe₃O₄ has been observed with no intermediate product formation. We believe that the 20 ns UV (248 nm, $h\nu = 5\text{eV}$) laser pulses melt and vaporize the bulk α -Fe₂O₃ particles suspended in water / ammonia solution forming bubbles with local high pressure/superheated water and ammonia (vapour) resulting in the formation of reduced phase Fe₃O₄. The rounded spherical type morphology realized herein conforms to this picture very well. Various characterizations confirm the formation of the ferromagnetic magnetite phase. We tested these Fe₃O₄ particles as anode material for Li ion battery and found a high capacity of $\sim 1100 \text{ mAhg}^{-1}$. Interestingly the capacity of laser synthesized Fe₃O₄ particles is highly stable up to 40 cycles with 97% coulombic efficiency retention.

5.2 Experimental Section

5.2.1 Materials

Bulk α -Fe₂O₃ was purchased from Alfa aesar (99.99 %) and aqueous 30% NH₃ solution was obtained from Ranchem chemicals.

5.2.2 Synthesis of Fe₃O₄ particles from bulk α -Fe₂O₃

100 mg of bulk α -Fe₂O₃ powder was dispersed in 25 ml of water by using ultra-sonication in a probe sonicator for 30 mins. To the above solution 25 ml of 30% aqueous NH₃ solution was added and the entire solution was transferred to a 100 ml quartz beaker. This solution was then subjected to pulsed excimer laser (248 nm, pulse width 20 ns) irradiation at an energy density of $\sim 214 \text{ mJ/cm}^2$ and pulse repetition rate of 10 Hz for 5h under constant stirring. This solution was then washed

with D.I. water several times to remove excess ammonia and then dried in a vacuum oven at 60°C overnight. The dried powder was then used for anode material in Li ion battery. To observe the phase change during the progress of reaction samples were subjected to laser irradiation for different times and thoroughly characterized by various techniques (30mins, 1.5Hr, 3Hr, and 5Hr).

5.2.3 Characterizations

The synthesized α -Fe₂O₃ and Fe₃O₄ particles were characterized by X-ray powder diffraction using Philips X'Pert PRO diffractometer with nickel-filtered Cu K α radiation, Raman spectroscopy using Lab RAM HR800 from JY Horiba, high-resolution transmission electron microscopy using IFEI Tecnai F30 with 300 KV FEG and field-emission scanning electron microscopy (FESEM, Hitachi S-4200). The surfaces of α -Fe₂O₃ and Fe₃O₄ were examined by X-ray photoelectron spectroscopy on a VG scientific ESCA-3000 spectrometer using non mono-chromatized Mg K α radiation (1253.6 eV) at a pressure of about 1×10^{-9} Torr. All the electrochemistry measurements were done with Autolab PGSTAT30 (Eco-Chemie). Magnetism measurements were performed on SQUIDVSM magnetometer (Quantum Design). Mössbauer analysis was performed using ⁵⁷Co(Rh) γ -ray source and α -Fe foil as the standard for calibration. Diffuse reflectance spectra was recorded in JASCO V-570 spectrophotometer.

5.2.4 Electrochemical Measurements

All the Electrochemical measurements were carried out by using two electrode CR 2016 coin cell assemblies. Working electrode was prepared by making slurry of Fe₃O₄ with conducting carbon (Super-P) and binder (teflonized acetylene black, TAB-2) using ethanol as solvent and pressing it on a 200 mm² stainless steel mesh (Goodfellow, UK). Pure Li metal was used for counter electrode. A micro-porous paper (Whatman, Cat. No. 1825-047, UK) was used as a separator along with 1M LiPF₆ in ethylene carbonate (EC)/dimethyl carbonate (DMC) (1:1 wt %, Selectipur LP 30, Merck KGaA, Germany) as electrolyte solution. All this cell assembly process was carried out in a glove box to maintain inert atmosphere. The performance of the coin cell was then tested for several charge and discharge cycles.

5.3 Results and Discussions

Figure 5.1 a and b depict pictures of quartz beakers containing α - Fe_2O_3 solution before laser irradiation (dark red coloured solution) and the solution obtained after 5Hr laser irradiation under stirring (black coloured Fe_3O_4). After stopping the magnetic stirring all the particles get attracted quickly towards the magnetic needles as shown in **Figure 5.1 c**. One can also put a magnet on the side to pull the entire powder sideways. Given the non-magnetic character of α - Fe_2O_3 and ferromagnetism (FM) arising only from Fe_3O_4 , this result implies that either all α - Fe_2O_3 is converted into Fe_3O_4 or one has a composite of the two with strong contribution of the FM phase.



Figure 5.1: Conversion of bulk α - Fe_2O_3 to Fe_3O_4 after 5Hr laser irradiation; a) α - Fe_2O_3 in aqueous ammonia solution before laser irradiation; b) After 5 Hr laser irradiation showing formation of black colored Fe_3O_4 ; c) Magnetic Fe_3O_4 particles attracted to the magnetic needle after the stirring stopped

Figure 5.2 shows the x-ray diffraction (XRD) of bulk α - Fe_2O_3 and various samples obtained after pulsed laser irradiation for different times (30min, 1.5Hr, 3Hr and 5Hr). It can be observed from this figure that the XRD of bulk Fe_2O_3 shows pure phase of hematite whereas after 30mins of laser irradiation the peaks begin to get modified implying changes in the phase constitution. After about 1.5Hrs of laser irradiation new peaks of magnetite (Fe_3O_4) start appearing gradually indicating partial conversion of α - Fe_2O_3 to Fe_3O_4 whereas after 3Hr, intensity of the new peaks corresponding to the Fe_3O_4 phase start increasing significantly with a concurrent decrease in the intensity of α - Fe_2O_3 peaks. After 5Hrs of laser irradiation almost complete conversion of α - Fe_2O_3 to Fe_3O_4 is observed as the XRD shows magnetite

phase tiny percentage of hematite (small peaks in the XRD). In the case of bulk α - Fe_2O_3 the highest intensity peak was observed at 2θ value 33.1° which corresponds to the (104) plane(s) but after 5Hr irradiation the highest intensity peak observed is at 35.4 (311 plane) which belongs to magnetite phase (Fe_3O_4).

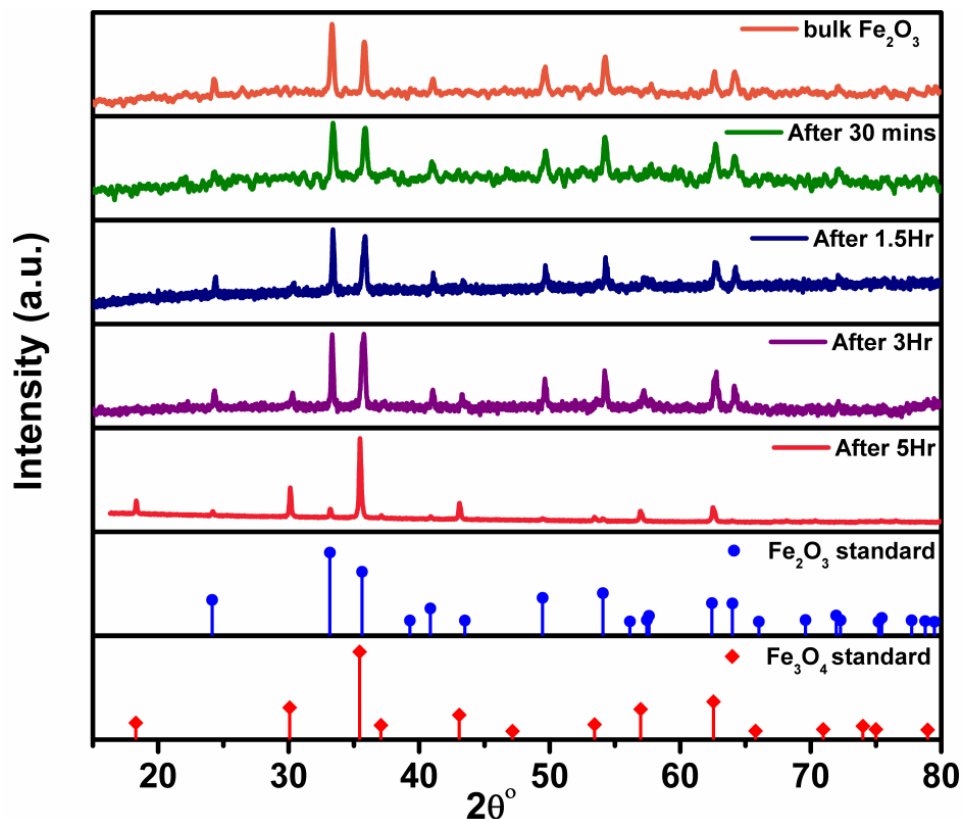


Figure 5.2: XRD spectra of laser synthesized powders at different time intervals: bulk α - Fe_2O_3 , after laser irradiation for 30 mins, 1.5 Hr, 3 Hr and 5 Hr along with standard spectra of α - Fe_2O_3 and Fe_3O_4 for comparison.

Figure 5.3 shows Raman spectra of the initial bulk α - Fe_2O_3 and the Fe_3O_4 powder formed after 5Hr laser irradiation. It is observed that along with Fe_3O_4 there are small signatures of α - Fe_2O_3 (shown by *) on the surface after 5Hr laser irradiation. The Raman spectra of bulk α - Fe_2O_3 show a number of peaks at 228cm^{-1} (A_{1g}) (s), 244cm^{-1} (E_g) (w), 292cm^{-1} (E_g) (s), 412cm^{-1} (E_g) (s), 499cm^{-1} (A_{1g}) (w), 612cm^{-1} (E_g) (m), 660cm^{-1} (Longitudinal optical, E_u), 1320cm^{-1} (s). These correspond to pure hematite phase. ^[55-56] In the case of 5Hr laser irradiated sample weak features are noted at 300 and 550cm^{-1} which are assigned as T_{1g} mode of vibration of magnetite whereas a strong peak is noted at 670cm^{-1} which belongs to the A_{1g} mode of

magnetite (Fe_3O_4). These results are in good agreement with the reported literature values and confirm the formation of Fe_3O_4 phase. [56, 57-60]

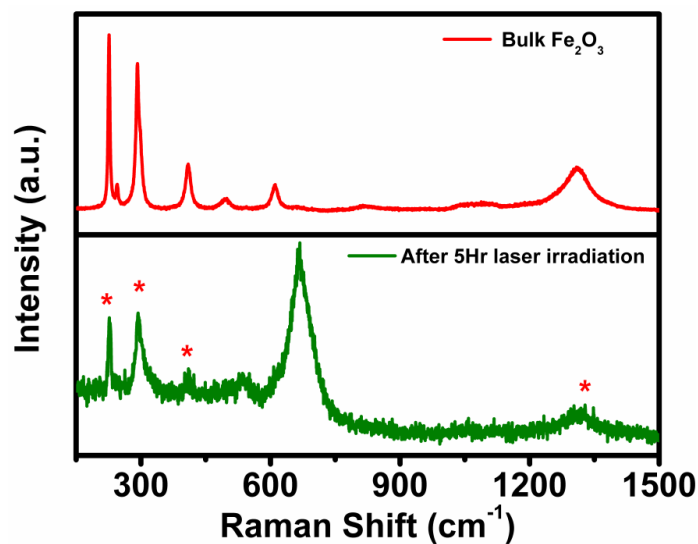


Figure 5.3: Raman spectra of $\alpha\text{-Fe}_2\text{O}_3$ and Fe_3O_4 synthesized after 5Hr laser irradiation.

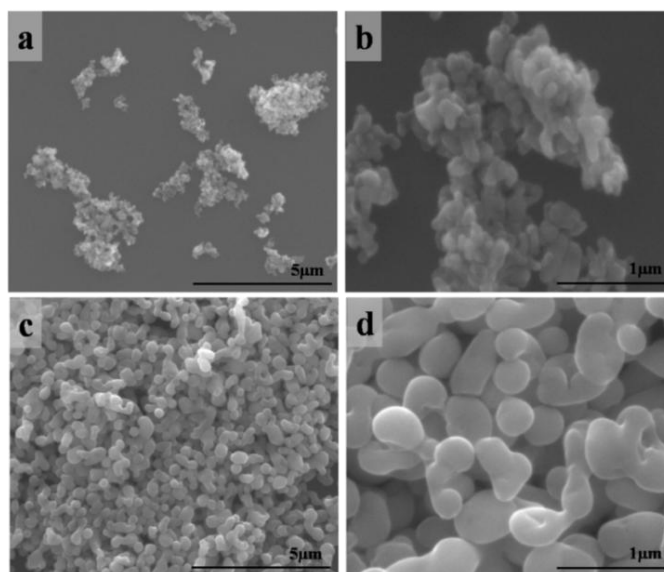


Figure 5.4: SEM images of bulk $\alpha\text{-Fe}_2\text{O}_3$ (a and b), and the material synthesized after 5Hr laser irradiation (c and d).

The morphological features of bulk $\alpha\text{-Fe}_2\text{O}_3$ and Fe_3O_4 powder formed after 5Hrs of pulsed laser treatment are reflected by the SEM images in **Figure 5.4**. These images show that in the case of bulk $\alpha\text{-Fe}_2\text{O}_3$ random distribution of particles is seen

with agglomeration. After 5Hr of laser irradiation these particles show a remarkable morphology evolution forming nearly spherical balls of 200-250 nm with defined features. The morphology of Fe_3O_4 particles formed was also studied by HRTEM imaging, the corresponding results represented in **Figure 5.5**. In **Figure 5.5 a-c** spherical balls of Fe_3O_4 with particle size around 200-250 nm are observed and the lattice fringes shown in **Figure 5.5 d** match very well with the spinel Fe_3O_4 phase with a d-spacing of 0.48 nm.

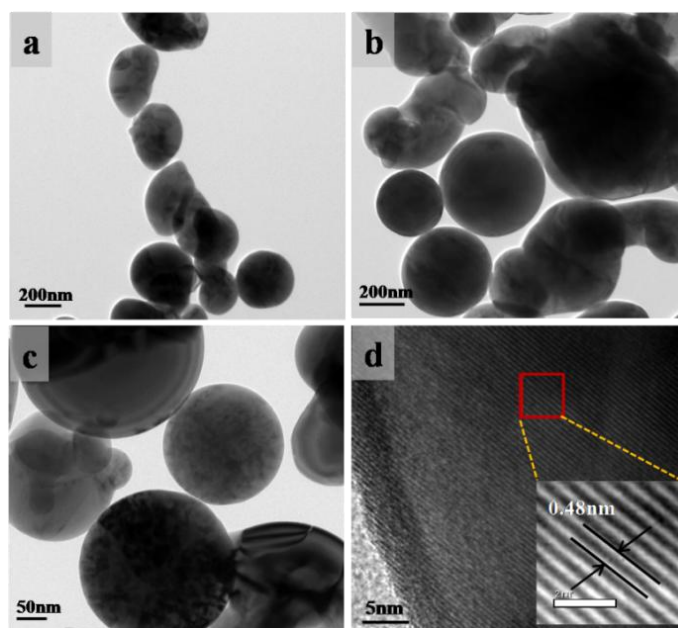


Figure 5.5: a-c) TEM images of Fe_3O_4 particles formed after laser irradiation on different scales, d) lattice fringes with d spacing of 0.48 nm corresponding to Fe_3O_4 .

The change of phase from $\alpha\text{-Fe}_2\text{O}_3$ to Fe_3O_4 was also been studied by Diffuse Reflectance Spectroscopy (DRS) and the data are shown in **Figure 5.6**. The dark red colour of pure Fe_2O_3 (hematite) can be explained by ligand-to-metal charge transfer (CT) transition ($\text{O}^{2-} \rightarrow {}^2t_{2g}(\text{Fe}^{3+})$), which leads to a strong absorption peak (565-575 nm) in the UV range and extending to the visible range. Apart from this the band related to ${}^6A_{1g} \rightarrow {}^4T_{2g}$ appears in the range 673-677nm. ^[61-62] All these bands are absent in the case of the Fe_3O_4 sample synthesized after 5Hr laser irradiation which is because of the strong absorption by black colour Fe_3O_4 .

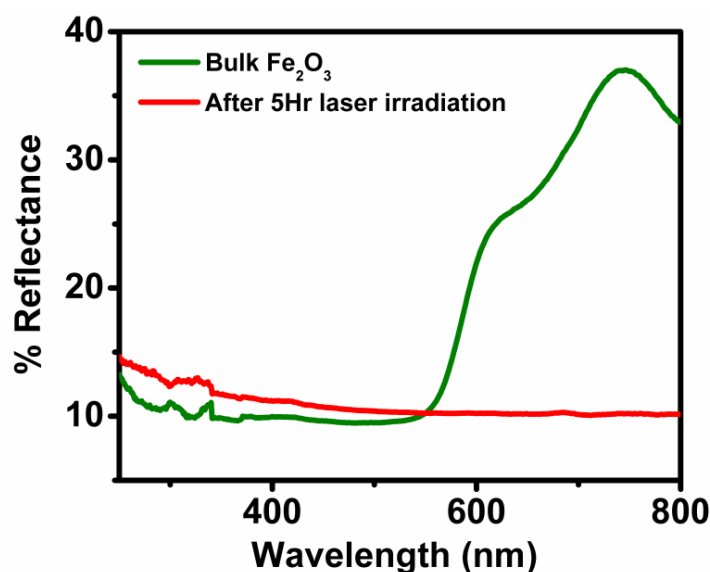


Figure 5.6: Diffuse reflectance spectra of bulk α - Fe_2O_3 and the material synthesized after 5Hr laser irradiation.

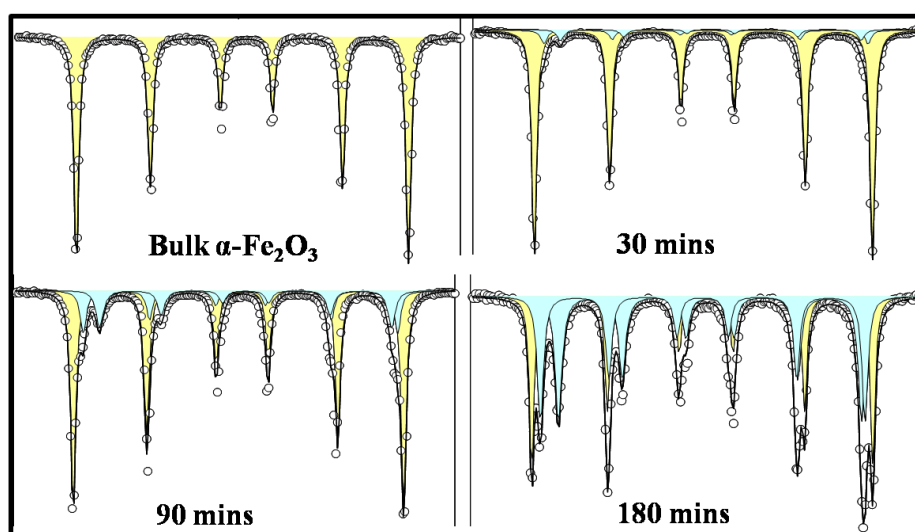


Figure 5.7: Mössbauer spectra for α - Fe_2O_3 after laser irradiation for different time intervals: 30min, 90min, 180min; showing gradual formation of Fe_3O_4 (blue colour) from α - Fe_2O_3 (yellow).

Mössbauer analysis is the most appropriate analysis for iron oxides. **Figure 5.7** depicts the Mössbauer spectra of bulk hematite and the samples obtained after pulsed laser irradiation for different times (30mins, 90mins and 180mins). These spectra show that in case of bulk hematite powder all the peaks match well with the α - Fe_2O_3 phase and in the other samples irradiated for different time intervals formation

of Fe_3O_4 phase can be clearly seen with increase in the Fe_3O_4 peak area and decrease in the Fe_2O_3 peak area. In the case of 5Hr laser irradiation the Mössbauer spectra shows magnetite phase along with a small percentage of hematite (**Figure 5.8a**). **Figure 5.8b** represents the percentage area of hematite and magnetite calculated from the Mössbauer spectra vs time, where it is clear that the percentage area of hematite decreases with time of laser irradiation along with a concurrent increase in the percentage area of the magnetite. After 5Hr laser irradiation 87% of magnetite is seen in the sample along with 13% of hematite.

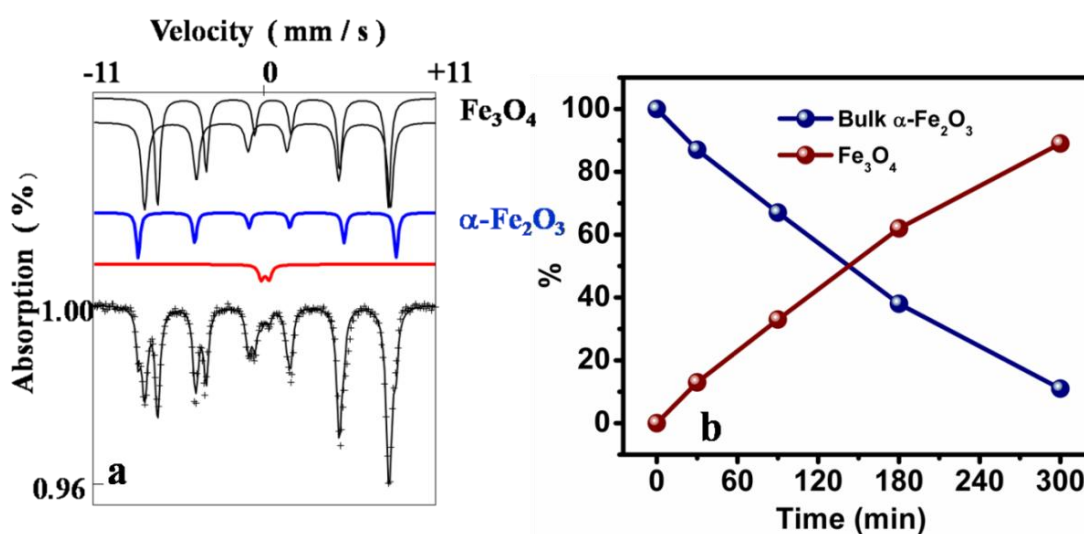


Figure 5.8: a) Mössbauer spectra of the material formed after 5Hr laser irradiation; b) Plot of area percentage Vs time for $\alpha\text{-Fe}_2\text{O}_3$, Fe_3O_4 for samples laser irradiated for different time durations as calculated from Mössbauer spectra.

After the laser irradiation, the entire black coloured powder is observed to be highly magnetic hence we also performed magnetization measurements using SQUID magnetometer. The M-H curves (**Figure 5.9**) for all the samples show that in the case of bulk $\alpha\text{-Fe}_2\text{O}_3$ no saturation magnetization observed, as expected in view of its antiferromagnetic nature whereas in the case of 5Hr laser irradiated sample a high saturation magnetization of 80 emu g^{-1} is observed. Given the known saturation magnetization of pure magnetite of 92 emu g^{-1} , this is consistent with the Mössbauer result that 87% of the sample is ferromagnetic. In all the other samples irradiated from 30 mins to 3Hr there is a progressive increase in the saturation magnetization indicating the gradual increase in the magnetic Fe_3O_4 component at the expense of

antiferromagnetic α - Fe_2O_3 powder. The nature of these curves shows ferromagnetic behaviour with coercivity of about 137 Oe (inset in the figure) representing typical behaviour of Fe_3O_4 . Clearly the particles formed are not superparamagnetic and this is consistent with the size of the particles as seen from the TEM/SEM results.

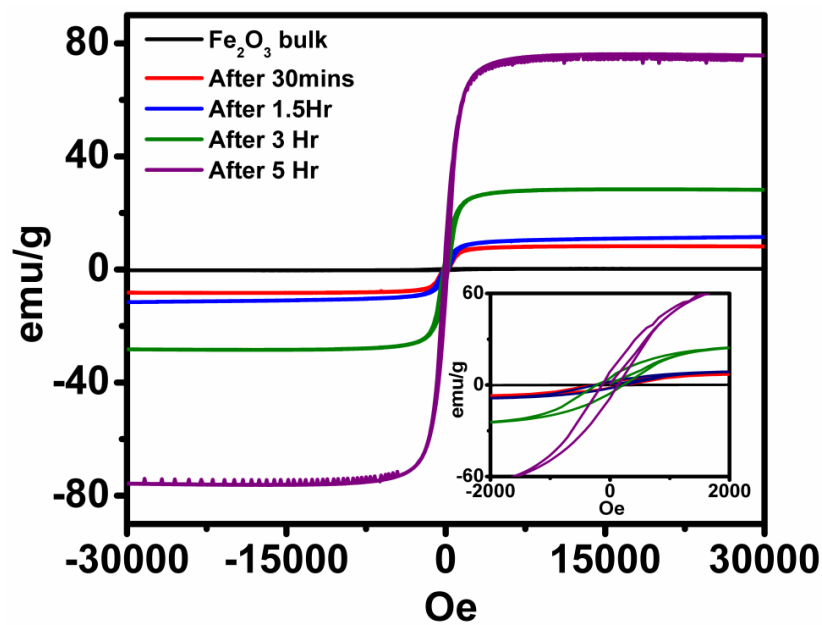
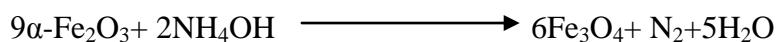


Figure 5.9: *M-H curves for bulk α - Fe_2O_3 , and the materials obtained after laser irradiation for 30 mins, 1.5 Hr, 3 Hr and 5 Hr ; inset is the magnified version to show coercivity.*

From the above characterizations it can be concluded that commercial bulk α - Fe_2O_3 powder gets slowly converted to magnetite (Fe_3O_4) with laser irradiation in the presence of NH_3 solution. The chemical reaction between α - Fe_2O_3 and aqueous NH_3 solution (NH_4OH) can be written as follows.



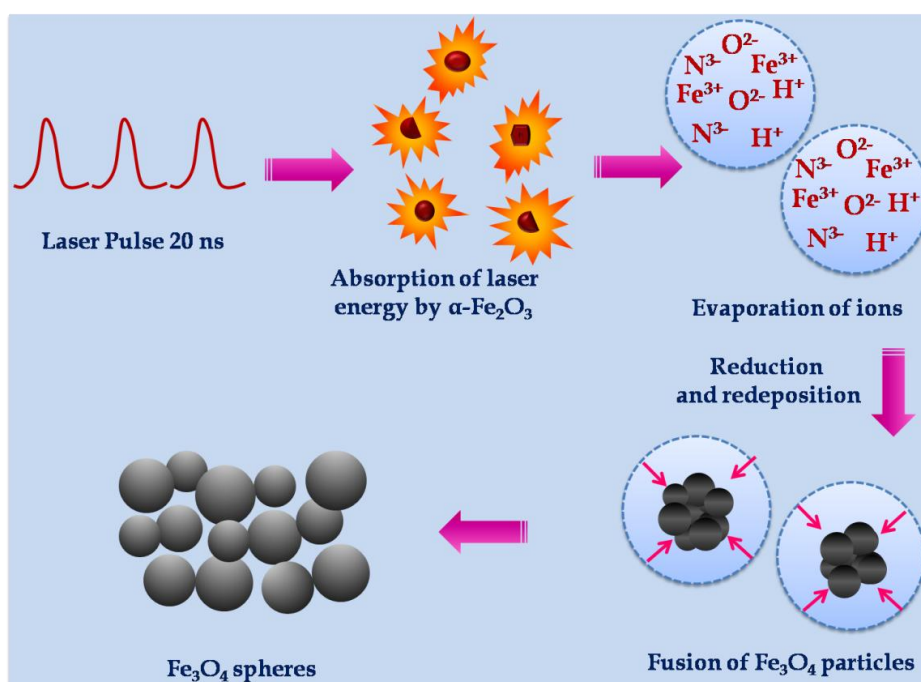


Figure 5.10: Possible mechanism pathway for the synthesis of Fe_3O_4 from bulk $\alpha\text{-Fe}_2\text{O}_3$

When solution suspended bulk $\alpha\text{-Fe}_2\text{O}_3$ powder is subjected to UV laser pulses, because of the high energy density of laser pulses (20 ns, 5 eV photons) photothermal melting and vaporization of $\alpha\text{-Fe}_2\text{O}_3$ particle surface layers can easily occur with very high local temperature (few thousand degrees). During this sequence of highly non-equilibrium events aqueous ammonium hydroxide can take out oxygen and form water and nitrogen molecules. This can result into the conversion of $\alpha\text{-Fe}_2\text{O}_3$ to Fe_3O_4 which would occur over duration of micro-milliseconds though relaxation of the excited micro-bubble zone through the laser pulse itself ceases in 20 ns. In solution based laser irradiation, photo thermal melting leads to two types of phenomena, photofission (photo fragmentation) or photofusion. If the melted state undergoes photo fission/fragmentation then the particle size will be smaller than the original whereas if photo fusion occurs then the particle size grows bigger than the original size. The size reduction takes place because of the vaporization of the particle. When the temperature of the particle rises to the boiling point, atoms and/or small particles are ejected through vaporization. This results in the reduction of the particle size. The amount of the ejected atoms and/or small particles depends on the absorbed laser energy. But in case of photofusion, the particle size grows to form

bigger particles. The size growth by photothermal melting process proceeds very slowly. There are many reports showing that particle aggregation before irradiation is an important factor for particle fusion.^[63-64] Because of Brownian motion of the particles in the solution, the particles attract each other and become aggregated because of weak repulsive force and attractive dipole-dipole interactions (hydrodynamic forces) leading to increase in the particle size.^[65] In this case the conversion of α -Fe₂O₃ to Fe₃O₄ occurs through photofusion process as the particle size grows bigger and becomes spherical in nature because of minimum surface energy. The possible mechanism for the formation of Fe₃O₄ is shown in **Figure 5.10**.

When solution dispersed α -Fe₂O₃ particles are subjected to pulsed UV laser irradiation the photon energy gets absorbed quickly and is then transmitted quite efficiently into the internal modes of the nanoparticles causing immense heating. If we assume in the first approximation that the incident energy is fully absorbed by the particle (absorption coefficient $\alpha=1$), for the case of an average spherical particle of 80 nm diameter the estimated absorbed energy per particle per pulse turns out to be $\sim 1.07 \times 10^{-11}$ J. Once again assuming that all of this energy is transformed into thermal energy the temperature rise of a single particle per pulse can be estimated to be $> 12000^\circ\text{C}$ (specific heat capacity of α -Fe₂O₃ taken to be to be 669 J/Kg^oC). Even if the incident energy is partially absorbed and/or there are losses of heat energy to the ambient via latent heat of vaporization, the crude estimate implies that the matter in the particle will evaporate very quickly and could also cause some ionization. Since the particle is suspended in solution the liquid layers in proximity will also evaporate rapidly causing cavitation or micro-bubble formation. This micro-bubble would then comprise of atoms, ions and radicals of the matter forming the nanoparticle as well as the liquid used for suspending the particles. Before the next 20 ns laser pulse strikes (for 10 Hz repetition frequency, this would be after 100 ms) rapid cooling of the hot micro-bubble would occur by dissipation of thermal energy to the ambient liquid and in the process the atoms, ions and radicals in the micro-bubble would react to form a compound. Continuation of the process over several hours can then transform and re-transform the whole material into another form and phase as observed. The phase would of course depend on the nature of the solution. For example, if it is simply water we get only α -Fe₂O₃ but with different size and shape. On the other hand in the

presence of ammonia solution, due to its reducing nature we can get spherical and larger Fe_3O_4 particles. The observed spherical shapes of the particles in the final product are a testimony to the presence of vapours in solution which can cause micro-bubbles for surface energy minimization. The increase in size of the particles implies fusion of material due to repeated exposure to successive laser pulses.

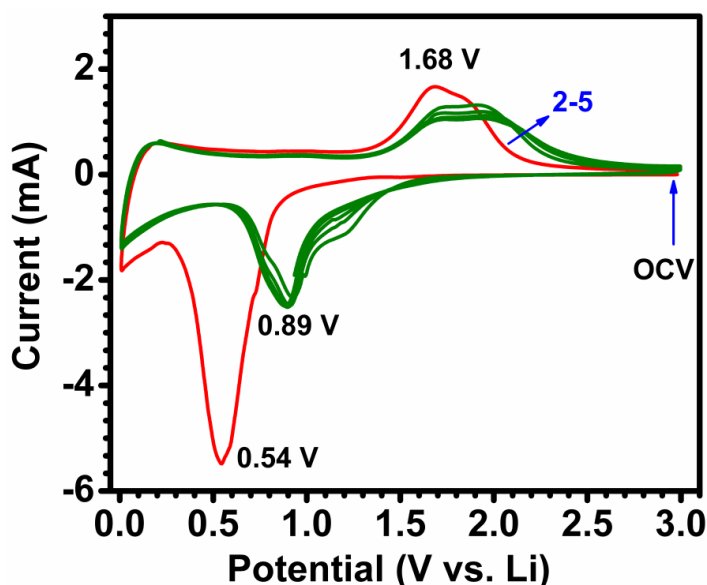
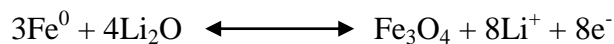
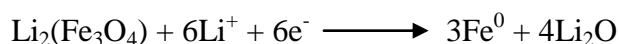
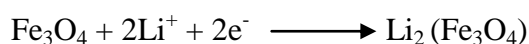


Figure 5.11: Cyclic Voltammogram of Li/ Fe_3O_4 half cell recorded between 0.005 and 3V at a scan rate of 0.1 mVs^{-1}

Since Fe_3O_4 is the most important transition metal oxide that has been widely studied as an anode material for Li ion battery (theoretical capacity 924 mAhg^{-1}), we examined the electrochemical properties of the pulsed laser synthesized Fe_3O_4 as anode material. Cyclic Voltammetry (CV) is the most convenient tool for studying the charge-discharge behaviour. CV measurements for laser-synthesized Fe_3O_4 mesoscopic spheres performed for Li/ Fe_3O_4 half cell at a scan rate of 0.1 mV s^{-1} between 0.005 and 3V vs Li are shown in **Figure 5.11**. Here metallic lithium acts as both the counter and reference electrode. During the first cathodic reaction one single peak appears at 0.54 V which corresponds to the reduction of Fe_3O_4 to Fe^0 which is due to the insertion of Li into the Fe_3O_4 lattice.⁴⁰ Similarly in the first anodic process two peaks are noted at 1.68 V and 1.84 V which correspond to gradual oxidation of Fe^0 to Fe^{2+} and then to Fe^{3+} to reform the magnetite phase.

The related electrochemical reactions are as given below:



The intensity of subsequent cathodic peaks decreases substantially because of the initial irreversible capacity loss. In the further cathodic and anodic cycles, there is not much change in the peak position and peak intensity which represents low polarization and high level reversible lithiation and delithiation process. [66-67]

Galvanostatic charge-discharge measurements were also performed in half-cell assembly (Li/Fe₃O₄) between 0.005 and 3V vs. Li at constant current density of 100 mA g⁻¹ and these data are shown in **Figure 5.12**. The initial specific discharge capacity was found to be 1723 mAh g⁻¹ whereas during the second cycle the discharge capacity decreased to 1100 mAh g⁻¹. Such capacity loss (irreversible capacity loss) is common for most of the transition metal oxides which is due to electrolyte

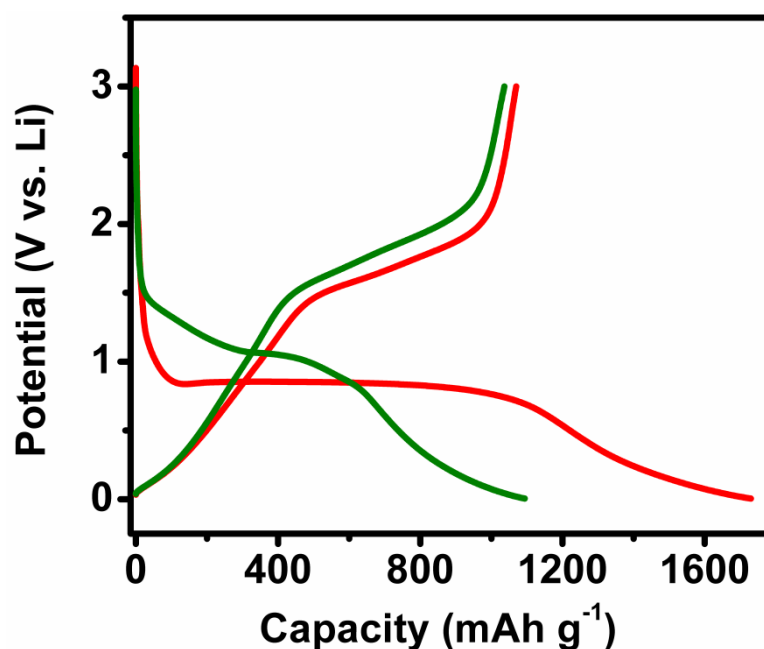


Figure 5.12: Typical galvanostatic charge-discharge curves of Li/Fe₃O₄ half-cell cycled between 0.005 and 3V vs. Li at constant current density of 100 mA g⁻¹ in ambient temperature conditions

decomposition and formation of solid electrolyte inter-phase layer (SEI).^[68] For the initial half cycle the discharge voltage drops down to 1.5 V and then gradually drops further to 0.9 V, then forming a small plateau between 0.8 V and 0.7 V. This plateau is clearly visible in the second cycle which is a typical characteristic of Fe₃O₄.

The rate performance of laser-synthesized Fe₃O₄ mesoscopic spheres is shown in **Figure 5.13** which has been performed for different current densities (100 mA g⁻¹, 250 mA g⁻¹, 500 mA g⁻¹, 1 Ag⁻¹ and 2 Ag⁻¹). A usual decrease in the specific capacity is observed with increase in the current density. The decrease in reversible capacity is mainly due to limited participation of active material (mainly the surface) in the reaction because of high current rate, whereas at a low current density all the surface as well as the bulk of the material can easily take part in the electrochemical reaction, thereby enhancing the total specific capacity. At a current density of 100 mA g⁻¹ the discharge capacity was found to be 1100 mAh g⁻¹ and it maintained at 530 mAh g⁻¹ even at a current density as high as 1 Ag⁻¹ which is greater than the theoretical capacity of graphite. After cycling at a high current density (2 Ag⁻¹) when the current was retained to 250 mA g⁻¹ the material shows almost the same reversible capacity as before which signifies its high rate capability and reversibility.

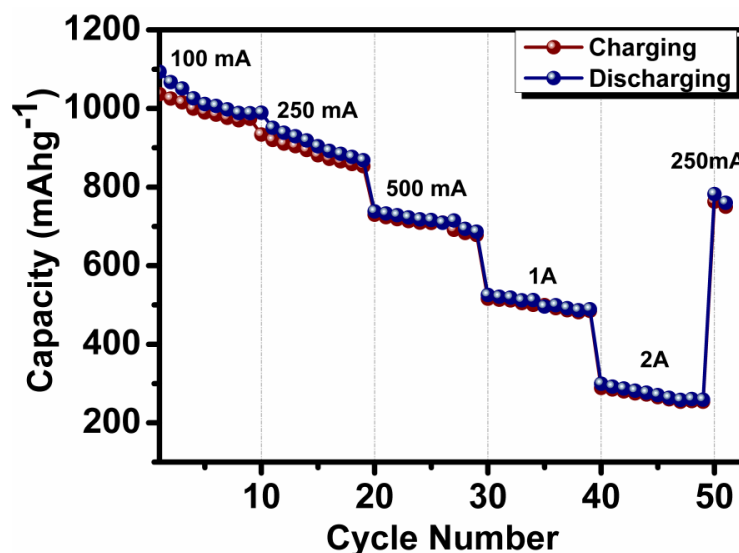


Figure 5.13: Plot of capacity vs. cycle number for Li/Fe₃O₄ half-cells cycled between 0.005 and 3V vs. Li at different current densities from 0.1 to 2 Ag⁻¹

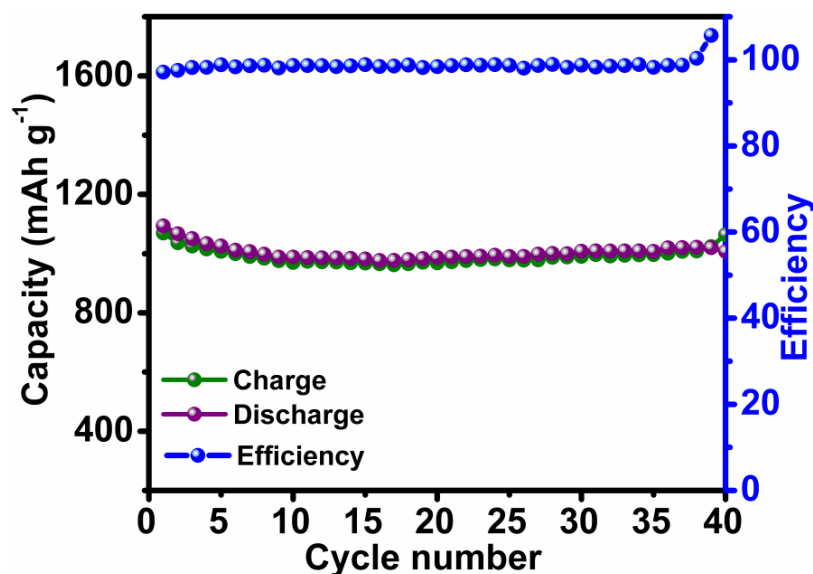


Figure 5.14: Cycling profiles of $\text{Li}/\text{Fe}_3\text{O}_4$ half-cells cycled between 0.005 and 3V vs. Li at constant current density of 100 mA g^{-1} with coulombic efficiency.

The cyclic stability of laser-synthesized Fe_3O_4 , performed at a current density of 100 mA g^{-1} show specific capacity of 1000 mAh g^{-1} which is stable up to 40 cycles without any capacity fading (**Figure 5.14**). This high stability is because of highly stable Fe_3O_4 structure which allows the reversible lithiation and delithiation. After 40 cycles the capacity of the material is $\sim 1000 \text{ mAh g}^{-1}$ which is even greater than the theoretical capacity of Fe_3O_4 which is mainly due to extra Li storage because of some faradic reactions taking place at the surfaces of Fe_3O_4 .^[69] The coulombic efficiency is also found to be very promising (97%) and maintained up to 40 cycles. Thus, the novel synthesis of Fe_3O_4 mesoscopic particles using pulsed excimer laser yields an excellent anode material for Li ion battery with high stability and high coulombic efficiency.

5.4 Conclusion

In conclusion highly spherical Fe_3O_4 particles having size of around $\sim 200 \text{ nm}$ are synthesized from bulk commercial $\alpha\text{-Fe}_2\text{O}_3$ powder by pulsed excimer (UV, 248 nm) laser irradiation of the suspended powder in ammonia (reducing) solution. The high energy laser pulses ($h\nu = 5 \text{ eV}$) create extremely high local temperature of $\sim 12000 \text{ }^\circ\text{C}$ by transient laser heating of particles which melt and evaporate forming a micro-bubble reaction zone. Dissipation of the energy occurs by micro-bubble

collapse through new bond formation and phase evolution. The presence of ammonia helps in the reduction of $\alpha\text{-Fe}_2\text{O}_3$ to Fe_3O_4 . Repeated laser pulses render growth of bigger particles. In the final product obtained after about 5 Hrs, 87% of Fe_3O_4 phase was found from the Mössbauer spectra, which is also consistent with the magnetization data. Importantly, the laser synthesized Fe_3O_4 particles show a high specific capacity of 1100 mAhg^{-1} at a current density of 100 mAg^{-1} . The rate performance measurements shows high rate capability with high reversibility where the specific capacity of 530 mAh^{-1} is observed even at a current density as high as 1 Ag^{-1} . This capacity value is found to be highly stable up to 40 cycles without any significant capacity fading. The coulombic efficiency of 97% is achieved with high stability and reversibility.

5.5 References

1. B. Scrosati, J. Garche, *J. Power Sources*, **2010**, 195, 2419.
2. B. Dunn, H. Kamath, J. Tarascon, *Science*, **2011**, 334, 928.
3. M. R. Palacín, *Chem. Soc. Rev.*, **2009**, 38, 2565.
4. B. Scrosati, J. Hassoun, and Y. Sun, *Energy Environ. Sci.*, **2011**, 4, 3287
5. H. Li, Z. Wang, L. Chen, and X. Huang, *Adv. Mater.* **2009**, 21, 4593
6. P. G. Bruce, B. Scrosati and J. Tarascon, *Angew. Chem. Int. Ed.* **2008**, 47, 2930.
7. C. M. Hayner, X. Zhao, and H. H. Kung, *Annu. Rev. Chem. Biomol. Eng.* **2012**, 3, 445.
8. C. Jiang, E. Hosono, and H. Zhou, *nanotoday*, **2006**, 1, 28.
9. L. Ji, Z. Lin, M. Alcoutlabi and X. Zhang, *Energy Environ. Sci.*, **2011**, 4, 2682.
10. D. Sheng Su and R. Schlögl, *ChemSusChem*, **2010**, 3, 136.
11. A. K. Shukla, and T. Prem Kumar, *Current Science*, **2008**, 94, 314.
12. M. Rosa Palacín, *Chem. Soc. Rev.*, **2009**, 38, 2565.
13. F. M. Courtel, H. Duncan, Y. Abu-Lebdeh and I. J. Davidson, *J. Mater. Chem.*, **2011**, 21, 10206.
14. B. Scrosati, *Electrochim. Acta*, **2000**, 45, 2461.

15. Z. Wu, W. Ren, L. Wen, L. Gao, J. Zhao, Z. Chen, G. Zhou, F. Li, and H. Cheng, *ACS nano*, **2010**, 4, 3187.
16. S. Paek, E. Yoo, and I. Honma, *Nano Lett.*, **2009**, 9, 72
17. J. M. Tarascon & M. Armand, *Nature*, **2001**, 414, 359.
18. J. Cabana, L. Monconduit, D. Larcher, and M. Rosa Palacín, *Adv. Mater.*, **2010**, 22, E170.
19. N. Choi, Z. Chen, S. A. Freunberger, X. Ji, Y. Sun, K. Amine, G. Yushin, L. F. Nazar, J. Cho, and P. G. Bruce, *Angew. Chem. Int. Ed.*, **2012**, 51, 9994.
20. J. B. Goodenough and Y. Kim, *Chem. Mater.* **2010**, 22, 587.
21. V. Etacheri, R. Marom, R. Elazari, G. Salitra and D. Aurbach, *Energy Environ. Sci.*, **2011**, 4, 3243.
22. A. Manthiram, *J. Phys. Chem. Lett.*, **2011**, 2, 176.
23. H. Xiao, Y. Xia, W. Zhang, H. Huang, Y. Gan and X. Tao, *J. Mater. Chem. A*, **2013**, 1, 2307.
24. A. Banerjee, V. Aravindan, S. Bhatnagar, D. Mhamane, S. Madhavi, S. Ogale, *Nano Energy*, **2013**, Article in press
25. S. Bai, S. Chen, X. Shen, G. Zhua and G. Wang, *RSC Advances*, **2012**, 2, 10977.
26. M. Zhang, D. Lei, X. Yin, L. Chen, Q. Li, Y. Wang and T. Wang, *J. Mater. Chem.*, **2010**, 20, 5538.
27. W. Zhang, X. Wu, J. Hu, Y. Guo, and L. Wan, *Adv. Funct. Mater.*, **2008**, 18, 3941.
28. Y. Wu, Y. Wei, J. Wang, K. Jiang, and S. Fan, *Nano Lett.* **2013**, 13, 818.
29. P. C. Wang, H. P. Ding, Tursun Bark, C.H. Chen, *Electrochim. Acta*, **2007**, 52, 6650.
30. T. Yoon, C. Chae, Y. Sun, X. Zhao, H. H. Kung and J. K. Lee, *J. Mater. Chem.*, **2011**, 21, 17325.
31. P. Wang, M. Gao, H. Pan, J. Zhang, C. Liang, J. Wang, P. Zhou, Y. Liu, *J. Power Sources*, **2013**, 239, 466.
32. C. Y. Haw, F. Mohamed, C. H. Chia, S. Radiman, S. Zakaria N.M. Huang, H. N. Lim, *Ceram. Int.*, **2010**, 36, 1417.

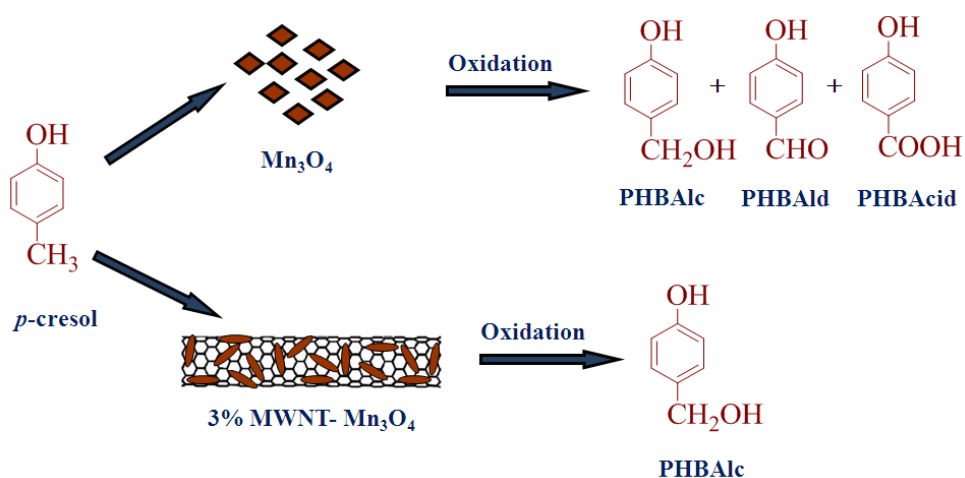
33. T. J. Daou, G. Pourroy, S. Bégin-Colin, J. M. Grenèche, C. Ulhaq-Bouillet, P. Legaré, P. Bernhardt, C. Leuvrey, and G. Rogez, *Chem. Mater.*, **2006**, 18, 4399.
34. S. Franger, P. Berthet, J. Berthon, *J Solid State Eletrochem*, **2004**, 8, 218.
35. J. Xu, H. Yang, W. Fu, K. Du, Y. Sui, J. Chen, Y. Zeng, M. Li, G. Zou, *J. Magn. Magn. Mater.*, **2007**, 309, 307.
36. K. Woo, H. J. Lee, J. Ahn, Y. S. Park, *Adv. Mater.*, **2003**, 15, 1761.
37. K. G. Chandrappa and T. V. Venkatesha, *Mater. Corros.*, **2012**, 63, 1.
38. Z. Ai, K. Deng, Q. Wan, L. Zhang, and S. Lee, *J. Phys. Chem. C*, **2010**, 114, 6237.
39. M. Zhang, D. Lei, X. Yin, L. Chen, Q. Li, Y. Wang and T. Wang, *J. Mater. Chem.*, **2010**, 20, 5538.
40. F. Xu, W. Kang, X. Wang, R. Liu, C. Zhao and Q. Shen, *CrystEngComm*, **2013**, 15, 4431.
41. Y. Chen, H. Xia, L. Lu, and J. Xue, *J. Mater. Chem.*, **2012**, 22, 5006.
42. Q. Zhang, Z. Shi, Y. Deng, J. Zheng, G. Liua, G. Chen, *J. Power Sources*, **2012**, 197, 305.
43. N. Zhao, S. Wu, C. He, Z. Wang, C. Shi, E. Liu, J. Li, *Carbon*, **2013**, 57, 130.
44. T. Muraliganth, A. V. Murugan and A. Manthiram, *Chem. Commun.*, **2009**, 7360.
45. C. He, S. Wu, N. Zhao, C. Shi, E. Liu, and J. Li, *ACS Nano*, **2013**, 7, 4459.
46. M.S. Valipour, *Transactions C: Chemistry and Chemical Engineering*, **2009**, 16, 108.
47. A. Mnrrnws, *Am. Mineral.*, **1976**, 61, 927.
48. F. Mafune, J. Kohno, Y. Takeda, and T. Kondow, *J. Phys. Chem. B*, **2003**, 107, 12589.
49. P. V. Kamat, M. Flumiani, and G. V. Hartland, *J. Phys. Chem. B*, **1998**, 102, 3123.
50. T. Tsuji, N. Watanabe, M. Tsuji, *Appl. Surf. Sci.*, **2003**, 211, 189.
51. A. Takami, H. Kurita, and S. Koda, *J. Phys. Chem. B*, **1999**, 103, 1226.
52. F. Mafun, *Chem. Phys. Lett.*, **2004**, 397, 133.

53. H. Fujiwara, S. Yanagida, and P. V. Kamat, *J. Phys. Chem. B*, **1999**, 103, 2589.
54. H. Kurita, A. Takami, and S. Koda, *Appl. Phys. Lett.*, **1998**, 72, 789.
55. D. L. A. de Faria, F. N. Lopes, *Vib. Spectrosc.*, **2007**, 45, 117.
56. A. M. Jubb and H. C. Allen, *ACS Appl. Mater. Interfaces*, **2010**, 2, 2804.
57. L. Slavov, M. V. Abrashev, T. Merodiiska, C. Gelev, R.E. Vandenberghe, I. Markova- Deneva, I. Nedkov, *J. Magn. Magn. Mater*, **2010**, 322, 1904.
58. N. Pinna, S. Grancharov, P. Beato, P. Bonville, M. Antonietti, and M. Niederberger, *Chem. Mater.*, **2005**, 17, 3044.
59. I. Chamritski, and G. Burns, *J. Phys. Chem. B*, **2005**, 109, 4965.
60. O. N. Shebanova and P. Lazor, *J. Raman Spectrosc.*, **2003**, 34, 845.
61. M. F. R. Fouda, M. B. ElKholly, S. A. Mostafa, A. I. Hussien, M. A. Wahba, M. F. El-Shahat, *Adv. Mat. Lett.*, **2013**, 4, 347.
62. K. Cheng, Y. P. He, Y. M. Miao, B. S. Zou, Y. G. Wang, T. H. Wang, X. T. Zhang, and Z. L. Du, *J. Phys. Chem. B*, **2006**, 110, 7259.
63. N. Chandrasekharan and P. V. Kamat, J. Hu and G. Jones, *J. Phys. Chem. B*, **2000**, 104, 11103.
64. P. V. Kamat, *J. Phys. Chem. B*, **2002**, 106, 7729.
65. R. Zamiri, A. Zakaria, M. S. Husin, Z. A. Wahab, F. K. Nazarpour, *Int. J. Nanomed*, **2011**, 6, 2221.
66. T. Zhu, J. S. Chen, and X. W. (David) Lou, *J. Phys. Chem. C*, **2011**, 115, 9814.
67. Y. He, L. Huang, J. Cai, X. Zheng, S. Sun, *Electrochim. Acta*, **2010**, 55, 1140.
68. H. Liu, G. Wang, J. Wang, D. Wexler, *Electrochem. Commun.*, **2008**, 10, 1879.
69. C. T. Cherian, J. Sundaramurthy, M. Kalaivani, P. Ragupathy, P. Suresh Kumar, V. Thavasi, M. V. Reddy, Chornng Haur Sow, S. G. Mhaisalkar, S. Ramakrishna and B. V. R. Chowdari, *J. Mater. Chem.*, **2012**, 22, 12198.

Chapter-6

Selectivity Tailoring in Liquid Phase Oxidation of *p*-cresol over MWNT-Mn₃O₄ Nanocomposite Catalysts

Highly selective multiwall carbon nanotube (MWNT)-Mn₃O₄ nanocomposite catalyst was designed for liquid phase oxidation of *p*-cresol, which gave highest selectivity of 90% to the first step oxidation product, namely, *p*-hydroxy benzyl alcohol. Mn₃O₄ nanoparticles and MWNT-Mn₃O₄ nanocomposites were synthesized by co-precipitation route using mixed precursors under controlled conditions. High-resolution transmission electron microscopy revealed the selective exposure of (101) and (001) planes of Mn₃O₄ nanoparticles in the MWNT-Mn₃O₄ composite. From the cyclic voltammetry study, lowering in oxidizing capacity of MWNT-Mn₃O₄ nanocomposite was confirmed which was due to incorporation of electron rich MWNT. Thus, selectivity tuning of the new material (MWNT-Mn₃O₄ nanocomposite) was found to be due to alteration in both the geometric as well as electronic properties. A plausible reaction pathway is proposed involving the predominant role of nucleophilic lattice oxygen (O²⁻) species due to exposure of particular crystal planes giving highest selectivity to *p*-hydroxy benzyl alcohol.



6.1 Introduction

Catalytic liquid phase oxidation of alkyl groups in substituted phenols is a core technology in fine chemicals and pharmaceutical industries.^[1-4] Therefore developing new materials by modifying their intrinsic properties has been a continuing effort for the last two decades.^[5-8] The major challenges in developing new catalysts are (i) stability of the metal function without leaching under oxidation conditions, (ii) maintaining activity in the presence of antioxidizing substrates like cresols, (iii) tailoring selectivity to the desired oxidation products, particularly to the first step oxidation product, and (iv) minimizing reaction time as well as the catalyst concentration. *p*-Cresol oxidation is an example of industrial oxidation process which involves stepwise oxidation to give a mixture of *p*-hydroxy benzyl alcohol, *p*-hydroxy benzaldehyde, and *p*-hydroxy benzoic acid depending upon the catalyst used and reaction conditions.^[5-7,9,10] Among these, both alcohol and aldehyde derivatives are important intermediates for the manufacture of vanillin (a widely used flavoring agent), trimethoxy benzaldehyde, various agrochemicals, and pharmaceuticals such as semisynthetic penicillin, amoxicillin, and the antiemetic drug trimethobenzamide.^[4,11,12] Efficient catalysts for oxidation reactions mainly involve oxides of transition metals having capability to form redox couples. In particular, Co-based catalysts systems and metals such as Cu, Mn supported on molecular sieves, carbon, resins and γ -Fe₂O₃ have been extensively studied for this oxidation reaction.^[13-15,16]

Among different types of catalysts, nanostructured catalysts have shown higher activity than their bulk counterparts which is observed in case of nanostructured Co₃O₄ catalysts,^[17] which could not only be due to the size reduction (high surface/volume ratio) alone but also due to the modified adsorption characteristics caused by geometric and electronic effects. Hence the present work was undertaken to further explore and understand the fundamental aspects of the nanostructured catalysts that govern their performance, especially their role in directing the selectivity pattern in a consecutive oxidation reaction. For this purpose, we synthesized nanostructured Mn₃O₄ and its composites with multiwalled carbon nanotube (MWNT) with different degrees of loading and investigated the correlation between its constitution, structural aspects, and the activity for oxidation of *p*-

cresol.^[18] Mn_3O_4 alone has been reported in the context of catalytic oxidation of methane, carbon monoxide,^[19] decomposition of NO and N_2O ,^[20-22] deoxygenation of nitrobenzene,^[23] while MWNT- Mn_3O_4 nanocomposite has been studied only in the context of supercapacitor and magnetism applications.^[24,25] To the best of our knowledge, ours is a first report of highly selective MWNT- Mn_3O_4 nanocomposite developed for selective liquid phase oxidation of *p*-cresol to intermediate *p*-hydroxy benzyl alcohol under mild conditions. The selective formation of intermediate *p*-hydroxy benzyl alcohol in a sequential oxidation of *p*-cresol could be attributed to the alterations in geometric as well as electronic characteristics of Mn_3O_4 by introducing electron rich rigid material like MWNT. The role of both these aspects has been studied in detail by high-resolution transmission electron microscopy (HR-TEM), X-ray Diffraction (XRD), X-ray photoelectron spectroscopy (XPS), Raman spectroscopy and cyclic voltametry (CV).

6.2 Experimental

6.2.1 Materials

Manganese acetate tetrahydrate, ethanol and xylene were obtained from Merck. Oleylamine was taken from Fluka. MWNT was purchased from Aldrich Chemicals. *p*-cresol was supplied by Loba Chemie, while sodium hydroxide was obtained from Merck. MWNT was purchased from Aldrich Chemicals. Analytical grade and HPLC grade methanol and *n*-propanol were obtained from Rankem.

6.2.2 Synthesis of Mn_3O_4 and MWNT- Mn_3O_4 nanocomposites

Nanostructured Mn_3O_4 was prepared using Manganese acetate, oleylamine, xylene and ethanol by co-precipitation method.^[26] In order to prepare 3% MWNT- Mn_3O_4 nanocomposite, commercially available MWNT was first functionalized with HNO_3 and H_2SO_4 in 1:3 ratios. In a typical procedure, 0.24 g of Manganese acetate and 0.0075 g of functionalized MWNT were properly dispersed in xylene at room temperature for 30 mins. To this, 4 ml of oleylamine was added and this mixture was then transferred to a round bottom flask, which was heated, from room temperature to 363 K under stirring. After the temperature reached 363 K, 1 ml H_2O was added and the stirring was continued at this temperature for 3 h. Then the mixture was cooled to room temperature, and highly dispersed 3% MWNT- Mn_3O_4 nanocomposites was

made to settle down by the addition of sufficient amount of ethanol. Then the solid material was isolated by centrifugation. The nanocomposite powder thus obtained was dried at 333 K for 3 h. The same procedure was followed for the synthesis of other MWNT-Mn₃O₄ composites with different degrees of loadings (Ratio of Mn₃O₄ to MWNT).

6.2.3 Characterization

The synthesized catalyst samples were characterized by X-ray powder diffraction using Philips X'Pert PRO diffractometer with nickel-filtered Cu K_α radiation, Raman spectroscopy using LabRAM HR800 from JY Horiba, high resolution transmission electron microscopy (HR-TEM) using IFEI, Tecnai F30, with 300 KV FEG and field-emission scanning electron microscopy (FESEM; Hitachi S-4200). The surfaces of the catalysts were examined by X-ray photoelectron spectroscopy (XPS) on a VG scientific ESCA-3000 spectrometer using non-monochromatized Mg K_α radiation (1253.6eV) at a pressure of about 1 x 10⁻⁹ Torr. The surface area values of all the samples were determined by BET adsorption method (Quadrasorb automatic volumetric instrument). The percentage metal oxide loading was obtained by the ICP (Inductive coupled plasma) analysis with Spectro 165 High Resolution ICP-OES Spectrometer (model no-ARCOSFHS12).

6.2.4 Catalytic activity

All the catalytic oxidation reactions were carried out in a 300 cm³ capacity high-pressure Hastelloy reactor supplied by Parr Instruments Co. U.S.A. The reactor was connected to an air reservoir held at a pressure higher than that of the reactor. A Hewlett-Packard model 1050 liquid chromatograph equipped with an ultraviolet detector was used for the analysis. HPLC analysis was performed on a 25 cm RP-18 column supplied by Hewlett-Packard. The products and reactants were detected using a UV detector at $\lambda_{\text{max}} = 223$ nm. 35% aqueous methanol was used as mobile phase at a column temperature of 308 K and a flow rate of 1 ml/min. Samples of 10 μL were injected into the column using an auto sampler HP 1100.

In a typical experiment, 3g of *p*-cresol, 4.5 g of NaOH and 70 cm³ of *n*-propanol were heated in a flask with a reflux condenser until the NaOH dissolved completely. This reaction mixture was charged to a 300 cm³ par autoclave. Then

0.02g catalyst was added, and the reaction mixture was heated to 373 K. After the desired temperature was attained, the reactor was pressurized with 6.5 bar nitrogen and 2.4 bar oxygen. Then the reaction was started by agitating at 900 rpm. When the pressure was absorbed, the reactor was again filled by oxygen. This was continued up to 2 h. The progress of the reaction was monitored by observing the pressure drop in the reservoir vessel as a function of time. After 2 h the reactor was cooled to room temperature and the unabsorbed nitrogen gas was vented out. Then the content of the reactor was discharged and the final volume was noted down. The final samples were analyzed in HPLC.

6.3 Results and Discussions

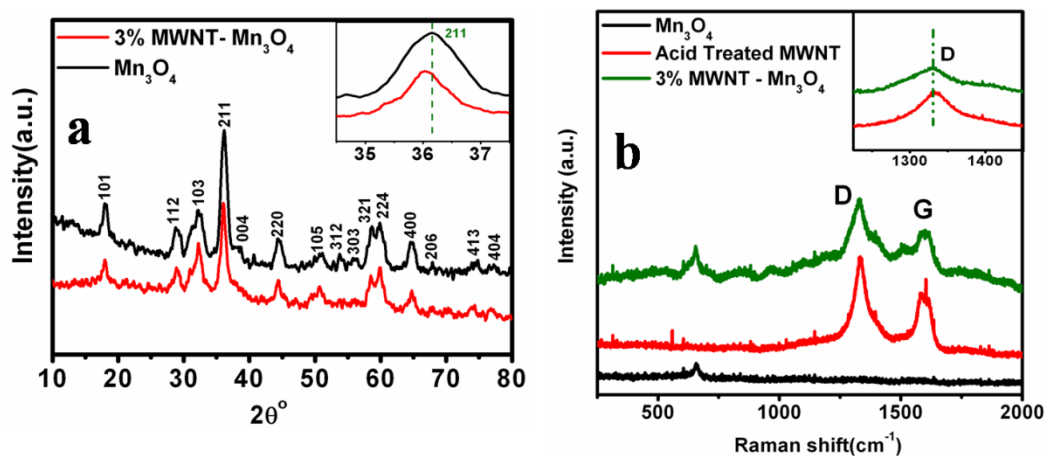


Figure 6.1: (a) XRD spectra of Mn_3O_4 and 3%MWNT- Mn_3O_4 ; inset shows shift of (211) peak towards lower 2θ due to addition of MWNT; (b) Raman spectra of Mn_3O_4 , acid treated MWNT, 3%MWNT- Mn_3O_4 ; inset shows broadening of D band.

As shown in **Figure 6.1a**, the XRD patterns of both Mn_3O_4 and 3% MWNT- Mn_3O_4 nanocomposites are identical with an intense peak at $2\theta = 36^\circ$ corresponding to (211) plane. The other peaks of lower intensity are also identical for both the samples and matches with those of tetragonal hausmannite phase (JCPDS card no. 24-0734). In both samples, no other peaks corresponding to any impurity phase(s) are seen, confirming that the product was tetragonal Mn_3O_4 . In order to distinguish Mn_3O_4 from γ - Mn_2O_3 which has similar structure and unit cell parameter as that of Mn_3O_4 ,^[27] our samples were also characterized by other techniques, which are discussed below. No signature of MWNT is observed in the XRD spectra of MWNT- Mn_3O_4 nanocomposite due to low concentration (only a few percent) of MWNT in the

composite. Also there is a considerable shift in the peaks of MWNT-Mn₃O₄ composites towards lower 2θ value as shown in the inset of **Figure 6.1a**. This shift in the peak is due to the strain involved during the formation of nano-composites. The Raman spectra for Mn₃O₄, MWNT, and MWNT-Mn₃O₄ nano-composite are shown in **Figure 6.1 b**. A single intense peak at 659 cm^{-1} confirms the highly pure phase of the synthesized Mn₃O₄.^[28] In the case of the MWNT sample, the two peaks are observed at 1328 cm^{-1} and 1579 cm^{-1} corresponding to D and G bands respectively, which match well with those reported in the literature.^[29] In the case of 3% MWNT-Mn₃O₄ nanocomposite sample, distinct peaks corresponding to MWNTs as well as Mn₃O₄ are observed. The interesting feature of the Raman spectra of MWNT-Mn₃O₄ nanocomposite is the broadening of the Mn₃O₄ and MWNT peaks as compared to the bare Mn₃O₄ nanoparticles and MWNT case. The broadening of D band of MWNT is shown in the inset of **Figure 6.1 b**. Such a broadening can occur because of two possibilities viz. (i) strain gradient originating from interface integration during the formation of MWNT-Mn₃O₄ composite, which involves anchoring of Mn₃O₄ on the molecular moiety like -COOH due to functionalization of MWNT and/or (ii) slightly broader particle size distribution which in the present case was in the range of 12-15 nm. This increase in particle size can also be correlated with the inset figure in XRD spectra which is shown in **Figure 6.1a**, where the peak is slightly broader in case of Mn₃O₄ than 3% MWNT-Mn₃O₄ nanocomposite. In addition, the nanosized nature of the material leads to a higher concentration of surface atoms and attendant phonon softening which can contribute to peak broadening. Such broadening is also reported in case of TiO₂-MWNT nanocomposite.^[30]

X-ray photoelectron spectroscopy is used to determine the surface oxidation states of all the species present in the bare Mn₃O₄ nanoparticles and various percentages of nanocomposites (**Figures 6.2a-f**). **Figure 6.2a and b** show the C1s XPS spectra of pristine MWNT and acid functionalized MWNT, respectively. Please note the different energy (x-axis) scales on the two figures. In the case of pristine MWNT the C1s peak can be resolved into two peaks which represent presence of two distinct chemical states of carbon on the surface of MWNT. The peak at the binding energy 284.6 eV corresponds to C-C carbon,^[31] and the peak at 286.1 is due to C-O carbon. Upon acid functionalization of MWNT, the C1s peak structure is seen to be

modified significantly. After deconvolution it exhibits four contributions for the best fit. The most resolved peak located at 284.6 eV is once again assigned to the C-C bonds, while the other three peaks having binding energies 285.4 eV, 286.9 eV and 290.1 eV correspond to carbon in the C-O, carbonyl (C=O) and carboxyl (-COOH) bonds, respectively.^[24, 32-33] Emergence of the new contributions clearly signifies introduction of polar oxygen groups into the surface of MWNT.

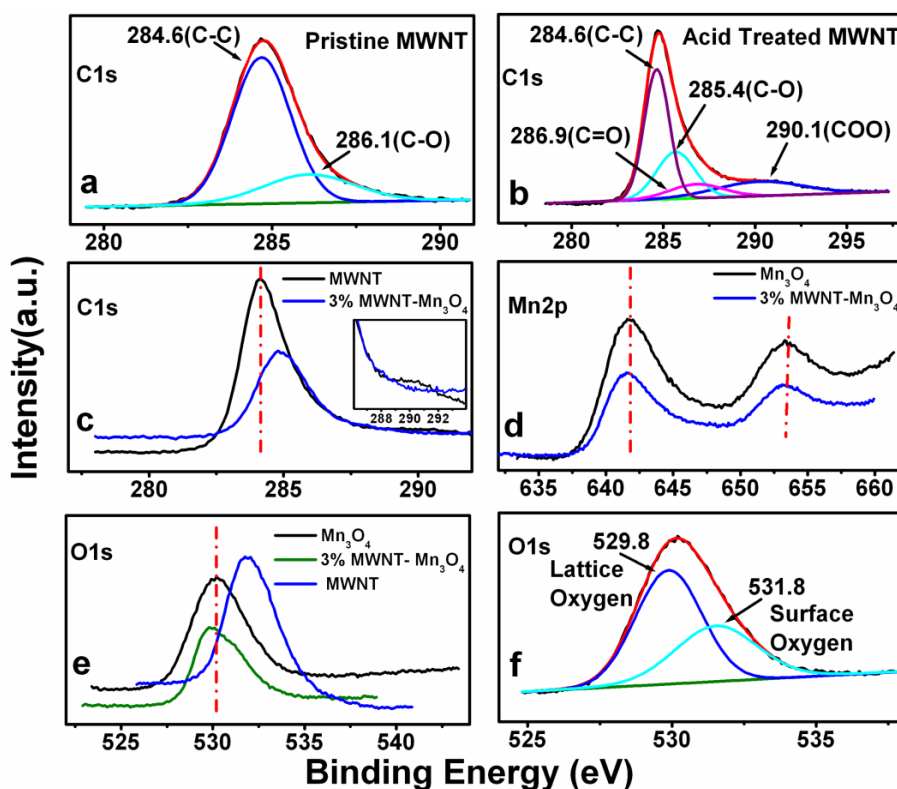


Figure 6.2 : XPS spectra of (a) C1s spectra of pristine MWNT, (b) C1s spectra of acid treated MWNT, (c) Comparison of C1s XPS spectra of MWNT, 3% MWNT-Mn₃O₄, (d) Comparison of Mn2p spectra for Mn₃O₄, 3% MWNT-Mn₃O₄, (e) Comparison of O1s XPS spectra Mn₃O₄, 3% MWNT-Mn₃O₄, MWNT, (f) O1s spectra of 3% MWNT-Mn₃O₄.

The C1s spectra of MWNT-Mn₃O₄ nanocomposite (3% case shown, others at low concentrations being nominally similar) and MWNT nanoparticles are compared in **Figure 6.2 c**, which reveal a significant shift towards the higher binding energy in the case of the nanocomposites. This shift can be attributed to the considerable strain imparted to the C-C bond configuration of MWNT and the related modification of the

electronic environment due to the anchoring of Mn_3O_4 nanoparticles on the surface of MWNT. The inset to **Figure 6.2c** is the enlarged view of the same spectra in the region of the binding energy from 285 eV to 295 eV. A distinct hump is clearly seen around 290 eV in the spectrum of MWNT which is due to the carboxylic group on the surface of MWNT. But this hump is absent in the case of the nanocomposite. This signifies the attachment of Mn_3O_4 to the carboxylic oxygen present on the surface of MWNT.

Figure 6.2d shows the comparison of the Mn2p XPS spectra for 3% MWNT- Mn_3O_4 nanocomposite and bare Mn_3O_4 nanoparticles. These two spectra are nearly similar having almost equal binding energy. The peak at a binding energy of 641.7 eV is due to Mn2p_{3/2} and the peak at 653.3 eV is assigned to Mn2p_{1/2}. These binding energy values match with the reported values for Mn_3O_4 .^[24,34-36]

The comparison of O1s spectra for MWNT, bare Mn_3O_4 , and 3% MWNT- Mn_3O_4 are shown in **Figure 6.2e**. Comparing all the O1s spectra, it can be seen that there is a shift in the case of the nanocomposites toward lower binding energy, which is again due to the strain involved during the formation of composites. The O1s peaks for the nanocomposites are more similar to the O1s peak of bare Mn_3O_4 , which is due to the uniform dispersion of Mn_3O_4 nanoparticles on the surface of MWNT with good surface coverage. The binding energy for O1s is shown in **Figure 6.2 f** for the case of 3% MWNT- Mn_3O_4 . After deconvolution, the peak shows two contributions. The peak at a binding energy of 529.8 eV is due to the lattice oxygen and the peak present at 531.8 eV can be attributed to either surface OH groups or other oxygen containing groups.^[34]

Figure 6.3 a shows HRTEM image of Mn_3O_4 , revealing highly faceted morphology with a nanoparticle size in the range of 8-10 nm (**Figure 6.3 a inset**). As shown in **Figure 6.3 b-f**, MWNT- Mn_3O_4 nanocomposite is again faceted type but with some degree of elongation along the MWNT length. This could be attributed to the anisotropic surface diffusion of adsorbed species and the differential role of axis vs curvature. These nanoparticles are seen to be uniformly dispersed on the MWNT surface with a size distribution of ~12-15 nm (**Figure 6.3c, d**). **Figure 6.3 e** is a

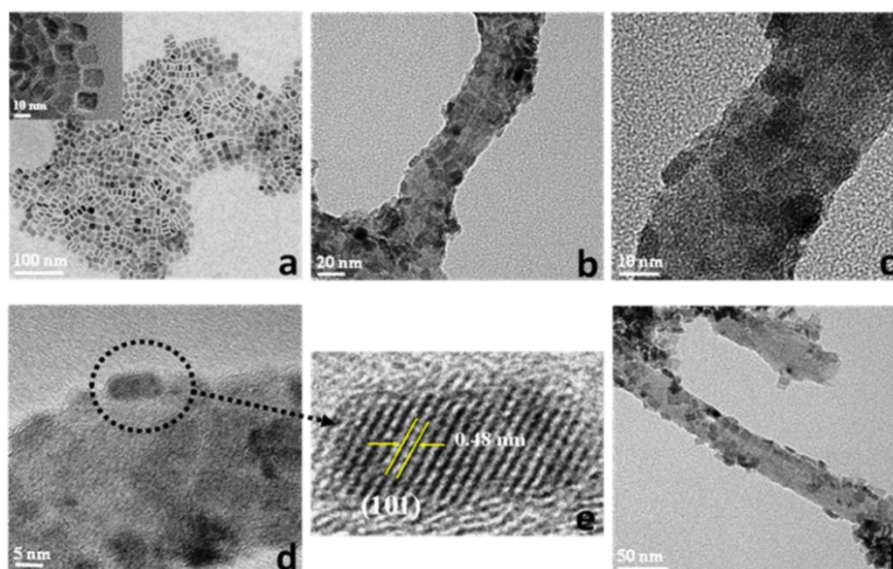


Figure 6.3: (a) HR-TEM image of Mn_3O_4 ; inset is a high magnification image showing 8-12 nm particles (b-f) HR-TEM image of 3% MWNT- Mn_3O_4 .

section of a Mn_3O_4 nanoparticle showing the axial growth in the direction of (101) with a lattice spacing of 0.48 nm and the other exposed side along the (001) plane. This was inferred from the inter-plane angle measured directly from the HR-TEM image. All these HRTEM images of MWNT- Mn_3O_4 composites indicate that most of the exposed sides of Mn_3O_4 nanoparticles are along two specific planes (101) and (001).

Sl. No.	Materials	BET Surface Area (m^2g^{-1})
1	Mn_3O_4	65.89
2	3% MWNT- Mn_3O_4	20.14
3	MWNT	15

Table 6.1: BET surface area measurements of Mn_3O_4 , MWNT, 3% MWNT- Mn_3O_4 .

Table 6.1 shows the surface area values for bare Mn_3O_4 and the MWNT- Mn_3O_4 nanocomposites. The surface area of the bare Mn_3O_4 nanoparticles was found to be $65.8 m^2g^{-1}$, which is seen to decrease substantially (to about $20 m^2g^{-1}$) in the case of the 3% MWNT- Mn_3O_4 nanocomposite. This decrease in the surface area of

nanocomposites could be due to the dispersion of Mn_3O_4 on a confined area of the MWNT matrix. This is also in accordance with the increase in particle size from 8-10 nm to 12-15 nm of bare Mn_3O_4 and MWNT- Mn_3O_4 nanocomposites, respectively. The surface area of only MWNT was found to be $15 \text{ m}^2\text{g}^{-1}$. In the nanocomposite, the Mn_3O_4 nanoparticles are anchored uniformly on the surface of MWNT, shielding some portion of the MWNT surface and dominating the m^2g^{-1} area estimate, albeit with somewhat enhanced size (12-15 nm).

The percent loading of metal oxide in the composites was studied by ICP analysis. The highest metal loading of 88% was observed for the case of 1% MWNT- Mn_3O_4 catalyst (**Figure 6.4**). The percent loading slightly decreased from 88 to 86 and 85% for 2 and 3% MWNT cases, respectively. Beyond 3% MWNT case, the metal oxide loading decreased continuously and significantly to 11% in the case of 10% MWNT, the maximum MWNT concentration examined in this work. The percent conversion and the selectivity patterns roughly follow similar trend as a function of nanocomposite composition, except for the 10% case. Also they bear an interesting nonmonotonic correlation, vis a vis, the metal oxide loading.

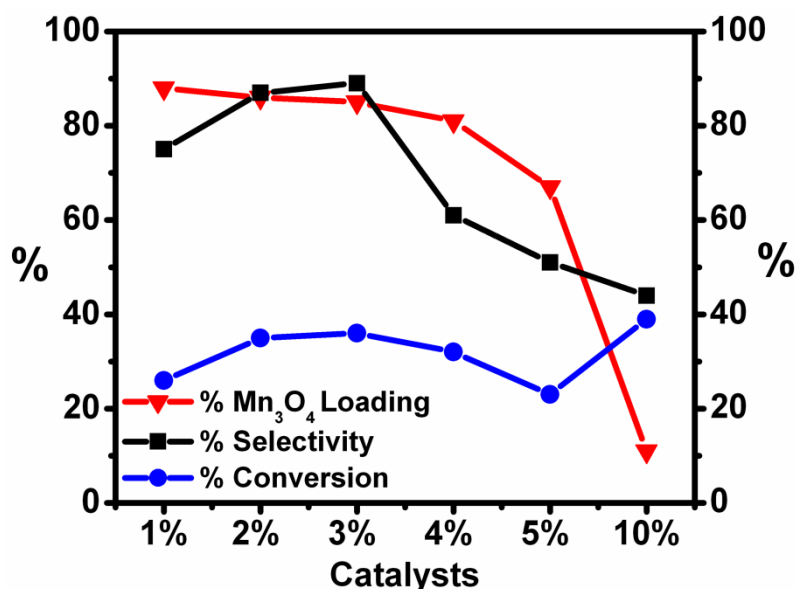


Figure 6.4: Percentage loading of Mn_3O_4 from ICP analysis in comparison with selectivity and conversion.

The percentage selectivity is seen to increase up to 90% in the case of 3% MWNT- Mn_3O_4 and then decreases. This could be explained by the relative degree of

heterogeneous and homogeneous nucleation of Mn_3O_4 nanoparticles. At low MWNT concentration (e.g., the 1% MWNT- Mn_3O_4 case), due to less concentration of MWNT it is possible that a fraction of Mn_3O_4 nanoparticles is formed by homogeneous nucleation and the same is not anchored on MWNT leading to higher performance. With increasing percent of MWNT to 2 and 3%, more Mn_3O_4 nanoparticles would form on the surface of MWNT and homogeneous nucleation contribution should decrease (**Figure 6.5**) leading to increasing conversion and selectivity. For further increase in MWNT percent (e.g., 4-10%), although all the nanoparticles would form on the MWNT surface, the exposed MWNT surface containing acid groups would get exposed more and more, leading to the formation of nonoxidation products. This would then decrease the selectivity considerably, as observed.

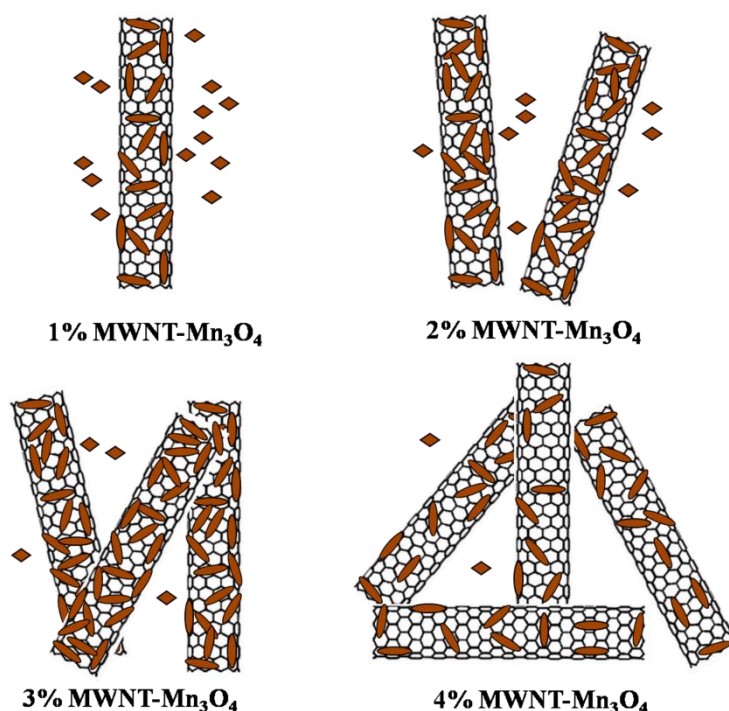


Figure 6.5: Possible homogeneous and heterogeneous nucleation of Mn_3O_4 nanoparticles in 1% to 4% MWNT- Mn_3O_4 nanocomposites.

The activity results of bare Mn_3O_4 and MWNT- Mn_3O_4 nanocomposites for the oxidation of *p*-cresol are discussed on the basis of conversion of *p*-cresol and selectivity to various products. The % conversion and selectivity were calculated by using equations (1) and (2) respectively as follows

$$\% \text{ Conversion} = \frac{C_i - C_f}{C_i} \times 100 \quad 6.1$$

$$\% \text{ Selectivity} = \frac{C_p}{C_x} \times 100 \quad 6.2$$

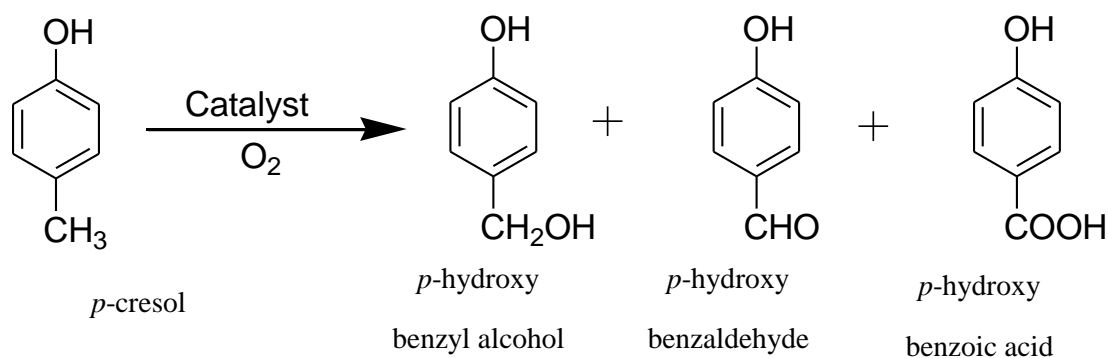
Where C_i = initial concentration of *p*-cresol

C_f = final concentration of *p*-cresol

C_p = concentration of product formed

C_x = concentration of *p*-cresol consumed

In order to study the product distribution, a few preliminary experiments of *p*-cresol oxidation were carried out using Mn_3O_4 and MWNT- Mn_3O_4 nanocomposites in *n*-propanol solvent under high-pressure conditions. The progress of the reaction was monitored by liquid phase analysis as a function of time. It was observed that the initial oxidation product was *p*-hydroxy benzyl alcohol that undergoes further oxidation to give *p*-hydroxy benzaldehyde and *p*-hydroxyl benzoic acid. Based on this the reaction pathway of *p*-cresol oxidation is shown in **Scheme 6.1**.



Scheme 6.1: *p*-cresol oxidation reaction

Results on catalyst screening for *p*-cresol oxidation are shown in **Figure 6.6**. Bare Mn_3O_4 shows 46% conversion of *p*-cresol and a selectivity of 43% toward *p*-hydroxy benzyl alcohol, the remaining constituents being *p*-hydroxy benzaldehyde and *p*-hydroxy benzoic acid. *p*-cresol conversion decreased to 26 and 35% in the case of 1 and 2% MWNT- Mn_3O_4 nanocomposites. In the case of 3% MWNT- Mn_3O_4 , the conversion remains almost same, that is, 36%. But conversion decreases in the case of

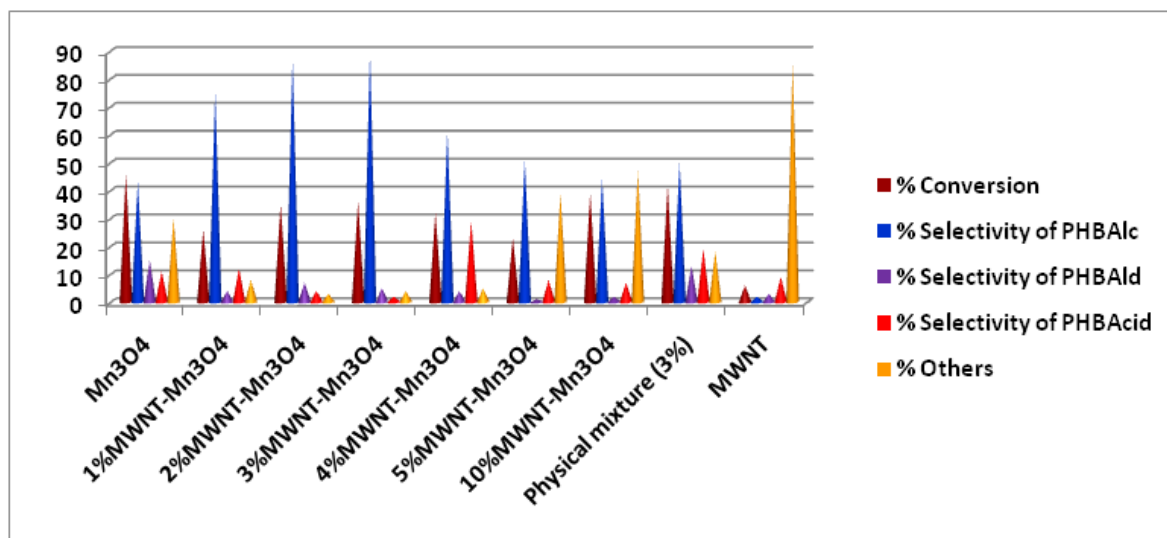


Figure 6.6: Activity Results of the catalysts (Reaction Conditions: Temperature 373 K: Pressure 7.9 bar: Agitation 900 rpm: Catalyst loading 20 mg)

4 and 5%, which was 32 and 23%, respectively. This decrease in *p*-cresol conversion for MWNT-Mn₃O₄ composite was not in the proportion to the decrease in surface area from 65 to 20m²g⁻¹ for the change in material from bare Mn₃O₄ to MWNT-Mn₃O₄ composite respectively. Nevertheless, the decrease in surface area was attributed to the dispersion of Mn₃O₄ on a confined area of MWNT that also might restrict the access of substrate molecules to the active sites on the surface of catalyst. This explanation is supported by a separate oxidation experiment carried out using a physical mixture of 3% MWNT and Mn₃O₄ in which 42% conversion of *p*-cresol was obtained which was very close to that obtained for bare Mn₃O₄. This experiment also showed that the selectivity of *p*-hydroxy benzyl alcohol is due to the composite formation only.

It is interesting to note a steep increase in the selectivity to an intermediate product, *p*-hydroxy benzyl alcohol up to 90% for both 2 and 3% MWNT-Mn₃O₄ composite catalysts as compared to 43% in the case of bare Mn₃O₄. *p*-Cresol oxidation over a variety of heterogeneous catalysts reported so far has shown mainly the formation of *p*-hydroxy benzaldehyde. Thus, the challenging task of obtaining the highest selectivity up to 90% toward first step oxidation product (*p*-hydroxy benzyl

alcohol) was achieved by 3% MWNT-Mn₃O₄ nanocomposites. The critical role of addition of MWNT on the selectivity pattern is discussed in detail below.

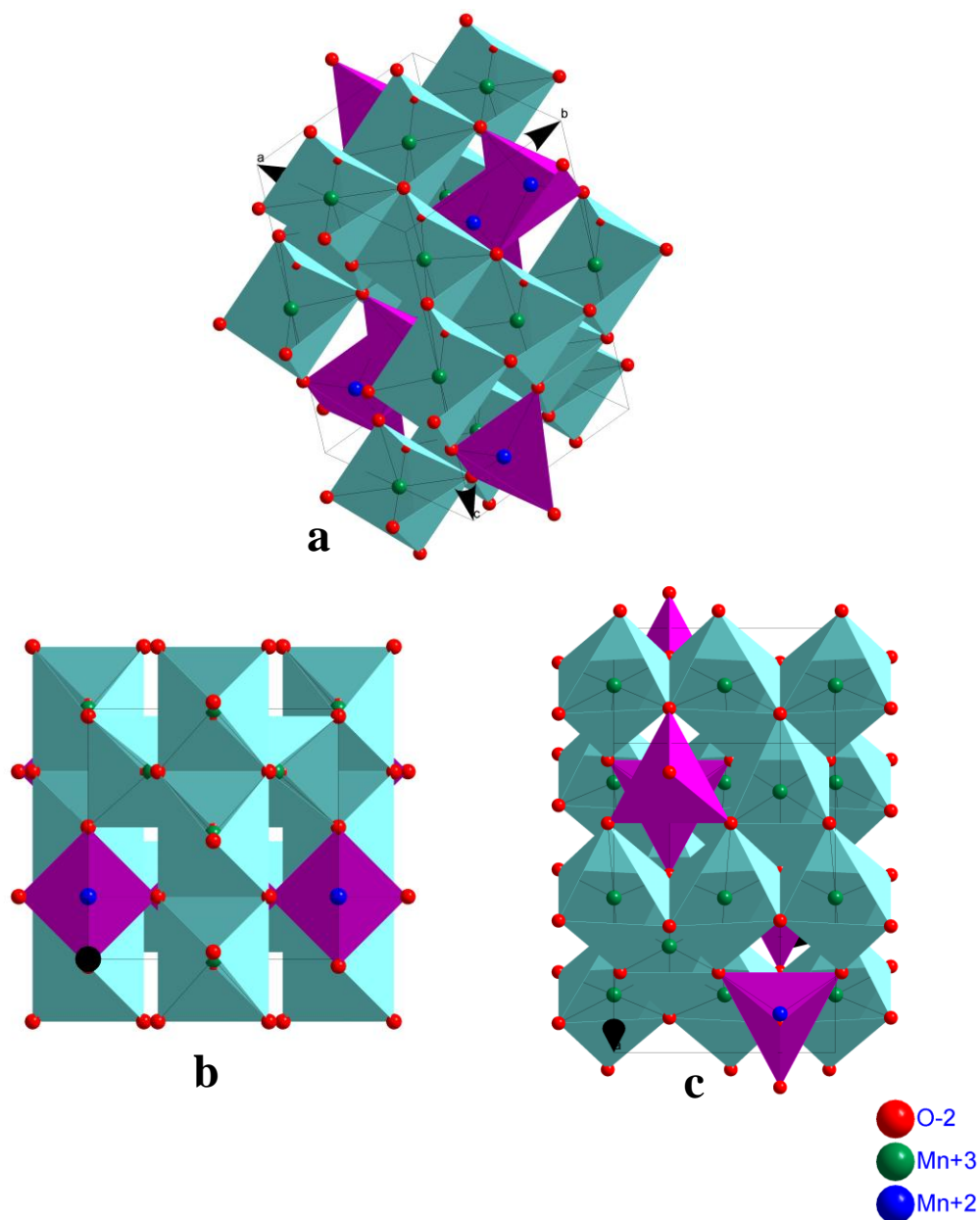


Figure 6.7: Crystal structure of (a) Normal spinel Mn₃O₄, (b) (001) plane of Mn₃O₄ spinel showing only Mn³⁺, (c) (101) plane of Mn₃O₄ showing both Mn²⁺ and Mn³⁺

In the case of the MWNT-Mn₃O₄ nanocomposites, selective exposure of two planes (101) and (001) of Mn₃O₄ was observed due to the structured support unlike

the case of bare Mn_3O_4 where several planes can be exposed to the substrate molecules. Such correlations between the exposure of selective planes and catalytic activity have been reported.^[37-38]

Figure 6.7a represents the crystal structure of Mn_3O_4 , which corresponds to a normal spinel structure with Mn^{2+} and Mn^{3+} in tetrahedral and octahedral sites, respectively. The selectively exposed planes (001) and (101) appear as shown in **Figure 6.7b,c**, respectively, which clearly indicate that the (001) plane contains only Mn^{3+} species and the (101) is composed of a mixture of Mn^{3+} and Mn^{2+} species. Between Mn^{3+} and Mn^{2+} species, Mn^{3+} is active for oxidation of *p*-cresol, because of its ability to be reduced to Mn^{2+} thus forming a redox couple (Mn^{3+} to Mn^{2+}). A plausible mechanistic pathway for *p*-cresol oxidation over MWNT- Mn_3O_4 composite is shown in **Figure 6.8**. This oxidation pathway is proposed considering the role of lattice oxygen as a primary oxidant in the oxidation process.^[23,39-41] As shown in **Figure 6.8**, the first step involves the adsorption of *p*-cresol molecule on the Mn^{3+} sites followed by C-H bond polarization.^[42] Formation of C-O bond takes place by the abstraction of one of the lattice oxygen associated with Mn^{3+} , which in turn gets reduced to Mn^{2+} as shown in the second step. The lattice oxygen vacancy created on the Mn^{3+} site is compensated by the neighboring Mn^{2+} atom. Concurrently, the electron produced at the Mn^{3+} center is transferred to the neighboring Mn^{2+} site. The molecular oxygen is adsorbed on the vacant Mn^{2+} site and it gets converted to lattice oxygen to replenish the oxygen loss.^[43] The last step involves desorption of *p*-hydroxy benzyl alcohol leading to the regeneration of catalyst, and another *p*-cresol molecule gets adsorbed and the cycle is repeated. Thus, Mn^{2+} and Mn^{3+} maintain a catalytic redox cycle for the conversion of molecular oxygen to lattice oxygen (O^{2-}) and hence the reoxidation of active centers (Mn^{3+}) takes place. Apart from the nucleophilic lattice oxygen species O^{2-} , some other reactive electrophilic oxygen species such as O^- and $\text{O}^{\cdot-}$ are also formed from the molecular oxygen.^[43] However, it is considered that the formation of nucleophilic lattice oxygen species on the surface are responsible for selective oxidation, while the electrophilic oxygen species are considered as strong oxidants leading to deep oxidation products. In the case of the MWNT- Mn_3O_4 nanocomposite, the formation of lattice oxygen species may be more favored than the formation of electrophilic oxygen species due to the selective

exposure of planes. This would lead to the oxidation of *p*-cresol primarily to *p*-hydroxy benzyl alcohol preventing the formation of subsequent oxidation products such as *p*-hydroxy benzaldehyde and *p*-hydroxy benzoic acid.

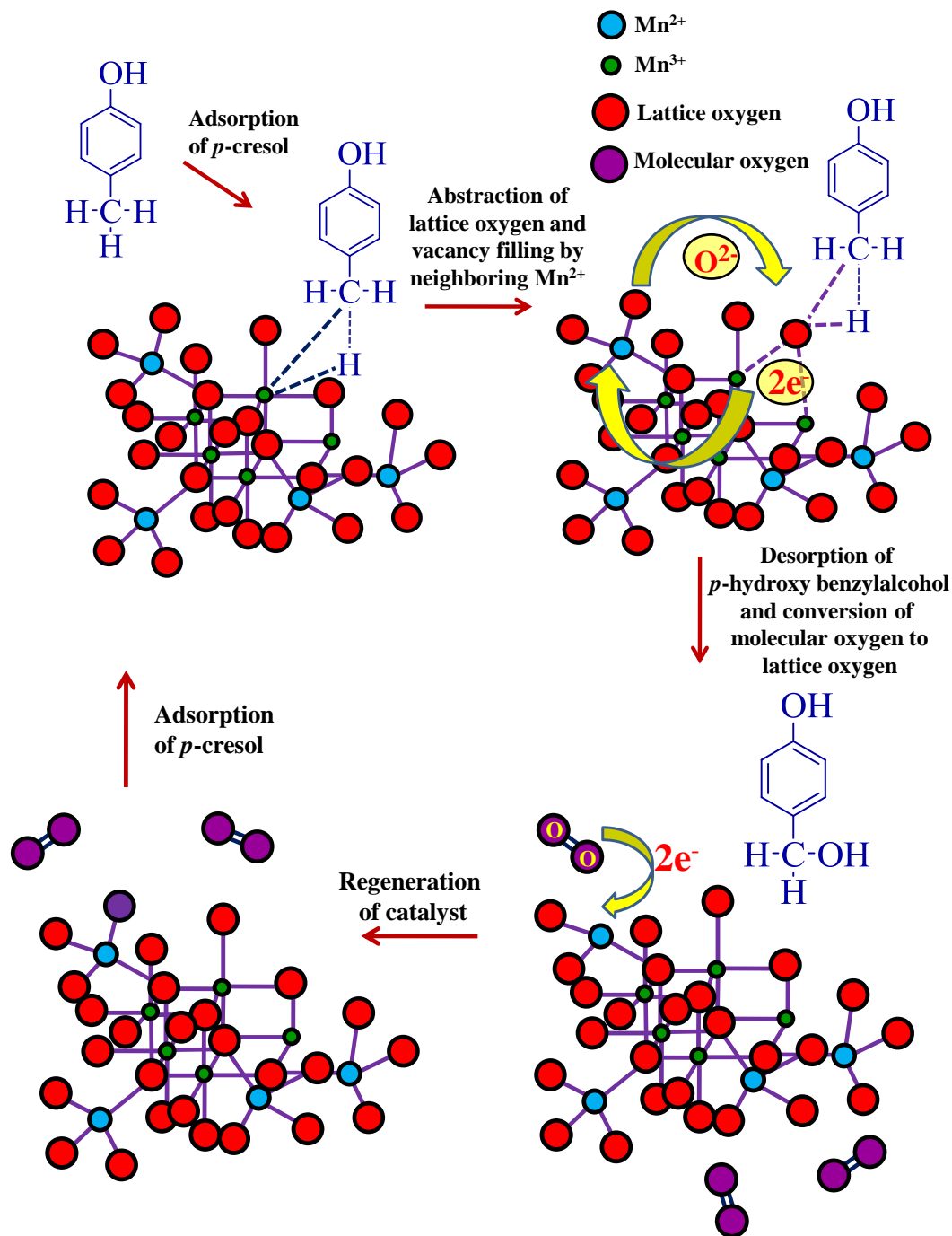


Figure 6.8: Possible mechanism pathway of oxidation of *p*-cresol to *p*-hydroxy benzyl alcohol.

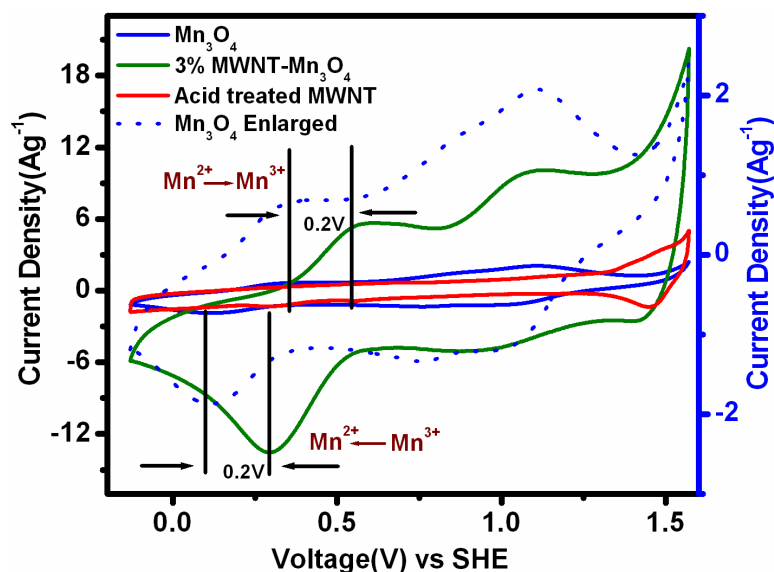


Figure 6.9: Cyclic Voltammetry measurements of acid treated MWNT, Mn_3O_4 and 3% MWNT- Mn_3O_4

The selective formation of intermediate *p*-hydroxy benzyl alcohol can be also explained by comparing redox potential profiles of various catalysts obtained by CV measurements. For this purpose, CV measurements were performed at a scan rate of 50 mV s^{-1} for the acid-treated MWNT, Mn_3O_4 nanoparticles, and 3% MWNT- Mn_3O_4 nanocomposite samples over the potential range of 1.6 to -0.2 V with standard hydrogen electrode (SHE) and 2M aqueous KCl solution. **Figure 6.9** shows the plots of current density versus potential for all the above cases. Since MWNT did not show any oxidation activity (**Figure 6.6**) as expected, no oxidation or reduction peaks were observed. However, Mn_3O_4 nanoparticles and 3% MWNT- Mn_3O_4 nanocomposite showed clearly the presence of oxidation and reduction peaks (blue and green respectively, **Figure 6.9**). In both cases, the first anodic peak in the low potential region could be assigned to the oxidation of Mn^{2+} to Mn^{3+} , while the second one to the oxidation of Mn^{3+} to Mn^{4+} . Similarly, the cathodic peak present at higher potential could be assigned to the reduction of Mn^{4+} to Mn^{3+} and the second one to the reduction of Mn^{3+} to Mn^{2+} . Comparison of the reduction peaks of Mn_3O_4 nanoparticles and 3% MWNT- Mn_3O_4 nanocomposite, showed a clear and substantial shift ($\sim 200 \text{ mV}$) toward higher potential values for 3% MWNT- Mn_3O_4 nanocomposite. Reduction peak indicates the oxygen reduction ability hence; higher

the potential value higher is the oxygen reduction ability, that is, lesser oxidizing ability. Thus lesser oxidizing ability of 3% MWNT-Mn₃O₄ composite than that of Mn₃O₄ is quiet evident from their CV profiles. Similar study has been reported in the case of iron nitride-doped carbon nanofibers.^[44] From this discussion, it can be inferred that Mn₃O₄ nanoparticles show higher oxidizing ability than that of MWNT-Mn₃O₄ nanocomposite, which results into deep oxidation giving a mixture of all the sequential oxidation products. Therefore, an electron rich system such as MWNT was deliberately introduced in the present composite to increase the electron density on Mn₃O₄ that restricts the oxidizing ability of the MWNT-Mn₃O₄ nanocomposite to achieve highest selectivity to *p*-hydroxy benzyl alcohol.

The selective formation of *p*-hydroxy benzyl alcohol (90%) could also be well correlated with the experimental observation that the moles of oxygen consumed for the *p*-cresol oxidation over MWNT-Mn₃O₄ nanocomposites are lower (0.026 mols) than those consumed over bare Mn₃O₄ (0.034 mols for 43% selectivity to alcohol and remaining aldehyde and acid) under identical conditions. With an increase in MWNT concentration from 4 to 10%, not only the selectivity to *p*-hydroxy benzyl alcohol is seen to decrease but also no other sequential oxidation product formation such as aldehyde and acid is noted. Instead other byproduct formation is observed. Similar product distribution was also observed for the case of only acid-treated MWNT where mainly other byproduct formation was observed without any significant conversion to well-defined sequential oxidation products. The decrease in selectivity in the case of 4, 5, and 10% MWNT nanocomposites can thus be attributed to the decrease in the percentage of Mn₃O₄ loading.

In order to study the stability of our catalysts, the recycling experiments were carried out in the following way: after the first oxidation run with the fresh 3% MWNT-Mn₃O₄ nanocomposite catalyst, it was filtered out and dried in an oven at 373 K for 3 h and was recharged to the reactor for the subsequent run. The procedure was followed for two subsequent oxidation experiments, and the results are shown in **Figure 6.10**. The catalyst was found to retain its activity even after second recycle.

Also no leached component of the catalyst was found in the solution under the reaction conditions which is confirmed by its characterization.

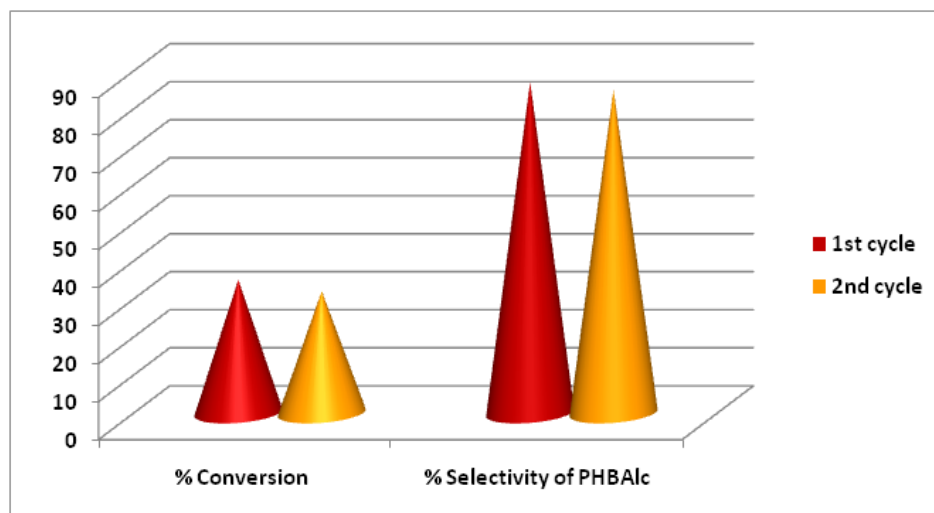


Figure 5.5: Catalyst recycling results of 3% MWNT- Mn_3O_4 .

6.4 Conclusion

The nanocomposites of Mn_3O_4 -MWNT (% MWNT between 0-10%) synthesized by co-precipitation route, show an excellent activity for liquid phase oxidation of *p*-cresol. It is clear from CV analysis that introduction of an electron rich system such as MWNT increases the electron density over Mn_3O_4 that could control the deep oxidation ability resulting in highest selectivity toward the first step oxidation product, namely *p*-hydroxy benzyl alcohol. Also HRTEM results reveal the exposure of particular crystal planes (101, 001) of Mn_3O_4 in the case of the nanocomposite that favor the formation of nucleophilic lattice oxygen (O^{2-}) species responsible for the highest selectivity of 90% to *p*-hydroxy benzyl alcohol. This is dramatically higher than that observed for the bare Mn_3O_4 nanoparticles (43%). The catalyst was recycled twice with retention of its activity. No leached components of the catalyst were found in solution under the reaction conditions of the present work.

6.5 References

1. M. Sittig, *Chemical Technology Review: Pharmaceutical Manufacturing Encyclopedia*, Noyes Data Corporation: Park Ridge, NJ, **1997**.
2. K. E. Clonts, R. A. McKetta, *Kirk-Othmer Encyclopedia of Chemical Technology*, 3rd ed.; Wiley-InterScience: New York, **1978**.
3. G. A. Burdock, *Encyclopedia of Food and Color Additives*; CRC Press: New York, **1997**.
4. S. Torii, H. Tanaka, T. Siroi, M. Akada, *J. Org. Chem.* **1979**, 44, 3305.
5. V. S. Kshirsagar, A. C. Garade, K. R. Patil, R. K. Jha, C. V. Rode, *Ind. Eng. Chem. Res.*, **2009**, 48, 9423.
6. C. V. Rode, M. V. Sonar, J. M. Nadgeri, R. V. Chaudhari, *Org. Proc. Res. Dev.*, **2004**, 8, 873.
7. C. Milone, R. Ingoglia, G. Neri, A. Pistone, S. Galvagno, *Appl. Catal. A*, **2001**, 211, 251.
8. S. N. Sharma, S. B. Chandalia, *J. Chem. Technol. Biotechnol.*, **1990**, 49, 141.
9. C. V. Rode, V. S. Kshirsagar, J. M. Nadgeri, K. R. Patil, *Ind. Eng. Chem. Res.*, **2007**, 46, 8413.
10. V. S. Kshirsagar, A. C. Garade, K. R. Patil, M. Shirai, C. V. Rode, *Top Catal.*, **2009**, 52, 784.
11. A. J. Poss, R. K. Belter, *J. Org. Chem.*, **1988**, 53, 1535.
12. D. V. Rao, F. A. Stuber, *Synthesis*, **1983**, 4, 308.
13. L. Yumin, L. Sheitian, Z. Kaizheng, Y. Xingkai, W. Yue, *Appl. Catal., A*, **1998**, 169, 127.
14. M. P. Peeters, M. Busio, P. Leijten, *Appl. Catal. A*, **1994**, 118, 51.
15. F. Wang, G. Yang, W. Zhang, W. Wu, J. Xu, *Chem. Commun.* **2003**, 1172.
16. A. C. Garade, M. Bharadwaj, S. V. Bhagwat, A. Athawale, C. V. Rode, *Catal. Commun.*, **2009**, 10, 485.
17. V. S. Kshirsagar, S. Vijayanand, H. S. Potdar, P. A. Joy, K. R. Patil, C. V. Rode, *Chem. Lett.*, **2008**, 37, 310.
18. M. Biswal, V. V. Dhas, V. R. Mate, A. Banerjee, P. Pachfule, K. L. Agrawal, S. B. Ogale, and C. V. Rode, *J. Phys. Chem. C*, **2011**, 115, 15440.
19. E. R. Stobhe, B. A. Boer, J. W. Geus, *Catal. Today*, **1999**, 47, 161.

20. T. Yamashita, A. Vannice, *J. Catal.*, **1996**, 163, 158.
21. H. W. Edwards, R. M. Harrison, *Environ. Sci. Technol.*, **1979**, 13, 673.
22. T. Yamashita, A. Vannice, *J. Catal.*, **1996**, 161, 254.
23. E. Grootendorst, Y. Verbeek, V. Ponce, *J. Catal.*, **1995**, 157, 706.
24. G. An, P. Yu, M. Xiao, Z. Liu, Z. Miao, K. Ding, L. Mao, *Nanotechnology*, **2008**, 19, 275709.
25. H. Zhang, N. Du, P. Wu, B. Chen, D. Yang, *Nanotechnology*, **2008**, 19, 315604.
26. T. Yu, J. Moon, J. Park, Y. I. Park, H. B. Na, B. H. Kim, I. C. Song, W. K. Moon, T. Hyeon, *Chem. Mater.*, **2009**, 21, 2272.
27. G. D. Mukherjee, S. N. Vaidya, C. Karunakaran, *Phase Transitions*, **2002**, 75, 349.
28. Y. Liu, Z. Liu, G. Wang, *Appl. Phys. A*, **2003**, 76, 1117.
29. E. F. Antunes, A. O. Lobo, E. J. Corat, V. J. Trava-Airoldi, A. A. Martin, C. Verissimo, *Carbon*, **2006**, 44, 2202.
30. S. Muduli, W. Lee, V. Dhas, S. Mujawar, M. Dubey, K. Vijayamohanan, S. H. Han, S. Ogale, *ACS Appl. Mater. Interfaces*, **2009**, 1, 2030.
31. G. W. Lee, J. Kim, J. Yoon, J. S. Bae, B. C. Shin, I. S. Kim, W. Oh, M. Ree, *Thin Solid Films*, **2008**, 516, 5781.
32. G. V. Ramana, B. Padya, R. N. Kumar, K. V. Prabhakar, P. K. Jain, *Indian J. Eng. Mater. S.*, **2010**, 17, 331.
33. S. W. Lee, B. S. Kim, S. Chen, Y. S. Horn, P. T. Hammond, *J. Am. Chem. Soc.*, **2009**, 131, 671.
34. S. K. Apte, S. D. Naik, R. S. Sonawane, B. B. Kale, N. Pavaskar, A. B. Mandale, B. K. Das, *Mater. Res. Bull.*, **2006**, 41, 647.
35. F. Jiao, A. Harrison, P. G. Bruce, *Angew. Chem.* **2007**, 119, 4020.
36. A. A. Audi, P. M. A. Sherwood, *Surf. Interface Anal.*, **2002**, 33, 274.
37. X. Xie, Y. Li, Z. Q. Liu, M. Haruta, W. Shen, *Nature*, **2009**, 458, 746.
38. L. Hu, Q. Peng, Y. Li, *J. Am. Chem. Soc.* **2008**, 130, 16136.
39. A. Bielanski, J. Haber, *Catal. Rev.-Sci. Eng.* **1979**, 19, 1.
40. V. D. Makwana, Y. C. Son, A. R. Howell, S. L. Suib, *J. Catal.*, **2002**, 210, 46.
41. F. Wang, J. Xu, S. Liao, *Chem. Commun.*, **2002**, 626.

42. V. D. Sokolovskii, *Catal. Rev.-Sci. Eng.* **1990**, 32, 1.
43. D. B. Dadyburjor, S. S. Jewur, E. Ruckenstein, *Catal. Rev.-Sci. Eng.* **1979**, 19, 293.
44. T. Palaniselvam, R. Kannan, S. Kurungot, *Chem. Commun.*, **2011**, 47, 2910.

Chapter-7

Summary and Future Scope

This chapter presents a summary of the work with concluding remarks for the research performed and reported in this thesis and then lays out the future scope pertaining to this work.

7.1 Summary of the thesis

A decade ago nanoscience was a curiosity-driven field focusing on diverse ways to synthesize nanoparticles and studies of their physical and chemical properties. With enhanced understanding and ability to manipulate and control nanosynthesis on a large scale, emphasis is now being laid upon novel applications of such systems emanating from their unique set of physical and chemical properties. Amongst the most investigated nanosystems are semiconductor quantum dots, noble metals and functional metal oxides. The work on metal oxides has witnessed considerable upsurge during the past few years with fields such as solar energy conversion, solar water splitting, photo-catalysis etc. acquiring centre stage. Another major development of the past decade has been the progress in the field of functional carbon materials, in particular, the low dimensional carbon systems such as fullerenes, CNTs, and graphene.

In the research work presented in this thesis we have attempted to bridge these two separately developing, interesting and key disciplines of science (namely, metal oxide nanomaterials and functional carbon) to explore newer application domains in the field of energy and environment. One of the main features of our efforts is the development of facile yet novel synthesis routes for functional carbon as well as specific transition metal oxides and explorations of their applications-driven fruitful integration. The current research work deals with various methods developed to obtain various forms of functional (high surface area and/or high conductivity) carbons and carbon-transition metal oxide nanocomposites, and their thorough characterizations using a wide variety of techniques. Apart from the novel synthesis methods the major part of this thesis is devoted to the discussion of various applications of current interest based on the new nanocomposites synthesized in this work. These applications cover important current areas such as energy storage, water splitting for hydrogen generation, catalysis, water purification etc.

The summary of the work done is as follows:

1. High surface area functional microporous conducting carbon materials are synthesized easily by pyrolysis of plant dead leaves such as Neem and Ashoka (dry waste, ground powder) without any activation and are studied for

supercapacitor application. The comparison between the Neem and Ashoka leaves shows the importance of the constitution and composition of the bio-source in the nature of carbon formed and its properties. The synthesized functional carbon exhibits a very high specific capacitance of 400 Fg^{-1} and energy density of 55 Wh kg^{-1} at a current density of 0.5 Ag^{-1} in aqueous $1\text{M H}_2\text{SO}_4$. Both the high conductivity and the microporosity realized in the carbeneous materials are key to the high energy supercapacitor application. In an organic electrolyte the material shows a specific capacitance of 88 Fg^{-1} at a current density of 2 Ag^{-1} . In Li ion hybrid electrochemical capacitor configuration with $\text{Li}_4\text{Ti}_5\text{O}_{12}$ a capacity value of 32 mAhg^{-1} and a specific capacitance of 72 Fg^{-1} are realized which are comparable to the case of commercially used activated carbon system. Clearly, the Neem derived carbon is highly useful electrode material for supercapacitor applications.

2. Highly conducting functional conducting cloth is synthesized by pyrolysis of cellulose fabric. It is examined as an anode electrode in the alkaline electrolysis process for water splitting and hydrogen generation. The efficiency of carbon cloth as anode is compared with other conventionally used anode materials such as graphite and platinum. It is observed that in the case of the carbon cloth anode sub-threshold ($\ll 1.23\text{V}$) hydrogen generation occurs which reduces the demand on overall electrical energy for the water splitting process. The sub-threshold hydrogen generation at 0.2V in the two electrode system is attributed to the turbostratic nature (nanoscale graphene-like units disorderly stacked together) of the carbon cloth obtained by relatively low temperature graphitization. Such turbostratic carbon provides plenty of defects sites for slow oxidation in 1M NaOH electrolyte. Interestingly at super-threshold potential, along with the high quantity of hydrogen generation because of high potential, the oxidized carbon begins to get exfoliated from the cloth surface in the form of carbon quantum dots ($6\text{-}8 \text{ nm}$) which show bright blue fluorescence under UV light. The mechanism of the sub-threshold hydrogen generation and super-threshold carbon quantum dot formation are investigated and discussed.

3. Spherical mesoscale morphology of Fe_3O_4 particles having size of around ~ 200 nm is realized from commercial bulk $\alpha\text{-Fe}_2\text{O}_3$ powder by pulsed excimer (UV, 248 nm) laser irradiation of the suspended powder in ammonia (reducing) solution. The high energy laser pulses ($h\nu = 5$ eV) create an extremely high local temperature of $\sim 12000^\circ\text{C}$ at the suspended particle site by transient laser heating of particles and it allows the particles to melt and evaporate forming a micro-bubble reaction zone. The presence of ammonia helps in the reduction of $\alpha\text{-Fe}_2\text{O}_3$ to Fe_3O_4 . The laser synthesized Fe_3O_4 particles show a high specific capacity of 1100 mAhg^{-1} at a current density of 100 mA g^{-1} . The rate performance measurements show high rate capability with high reversibility where the specific capacity of 530 mAh^{-1} is observed even at a current density as high as 1 Ag^{-1} . This capacity value is found to be highly stable up to 40 cycles without any significant capacity fading. The coulombic efficiency of 97% is achieved with high stability and reversibility.
4. MWNT- Mn_3O_4 nano-composite catalyst is synthesized by co-precipitation method and verified for liquid phase oxidation of *p*-cresol, which gives the highest selectivity of 90% to the first step oxidation product, *p*-hydroxy benzyl alcohol. Introduction of an electron rich system such as MWNT increases the electron density over Mn_3O_4 which controls the deep oxidation ability resulting in highest selectivity towards the first step oxidation product i.e. *p*-hydroxy benzyl alcohol. A plausible reaction pathway is proposed involving predominant role of nucleophilic lattice oxygen (O^{2-}) species due to exposure of particular crystal planes giving highest selectivity to *p*-hydroxy benzyl alcohol.

7.2 Scope for future work

Today in the 21st century, despite vast research being done by the enlightened scientific community around the world, no practically viable and sustainable solutions have emerged for the energy crisis faced by the world. The crisis emanates from the careless and indiscriminate use of conventional fuels which cause great and almost irreparable harm to our environment. Hence an enhanced attention to renewable forms

of energy is the need of the day. However these desirable forms of energy also face dual challenges of efficient energy conversion and high density (energy and power) storage

In resolving some of these challenges two aspects have to be taken care of. One is that the materials used should overcome the cost and efficiency challenges and second there should be efficient energy storage devices capable of long term stability. Keeping these aspects in mind, a few possible points pertaining to the possible future work based on the outcome of current thesis work are as follows:

1. As electrolysis of water is a highly efficient process for the energy conversion from electrical to chemical energy, the manipulation of electrode materials in terms of cost and efficiency is important for efficient hydrogen generation. Since we have already successfully demonstrated the use of carbon materials as electrode in alkaline electrolysis process with high efficiency on the laboratory scale, the manipulation and engineering of these materials for elevating them to the technology level is the next logical step of our research.
2. By engineering various forms of carbon materials with photoactive molecules the cost of the electrolysis process can be further minimized by replacing a part of electrical energy with solar power, resulting in the increase in the efficiency of the whole process.
3. Apart from energy conversion, focus should also be placed on energy storage devices such as battery and supercapacitors. To achieve both promising energy density for long term use and power density for burst of energy we need to design the device which can store high energy and can deliver that energy when required efficiently for long time. Integration of battery and supercapacitor concepts in a single device can fulfil these criteria. Hence designing of these types of hybrid devices by manipulating the properties of both the electric double layer type material such as functional carbon and battery type material such as metal oxides is essential to harness the benefits of both these materials.

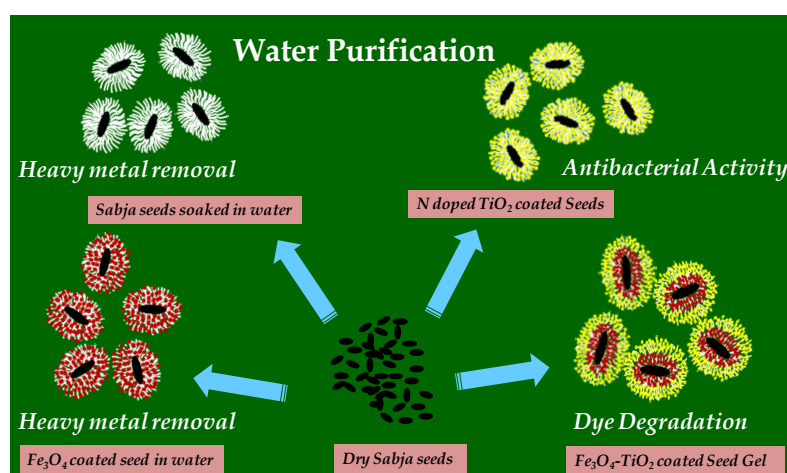
4. As high energy density is a limitation in the case of a supercapacitor and high power density in the case of battery, we need to new ideas in terms of materials and architectures to overcome these limitations. Hence efforts are needed to design suitable electrode materials for both these cases to achieve and optimize the desired material properties such as porosity (micro and meso pores), high surface area, high conductivity etc. These factors need to be optimized together not in individually because the performance of the material depends on all these parameters together.
5. Electrode materials such as carbon aerogels and their nanocomposites can be engineered and used for supercapacitor applications. One challenge is to make such speciality carbons with inexpensive precursors and processing methodologies.
6. Along with the electrode materials electrolytes also play a crucial role in the performance of supercapacitor. The effect of several electrolytes such as polymer gel electrolytes, organic and aqueous electrolytes on the supercapacitor performance can be studied and optimized to improve the performance.
7. In the case of Li ion battery there are several challenges to be addressed. One of the major challenges is the reaction of the cathode material with the electrolyte in the case of the high-voltage layered, spinel and olivine cathodes. To overcome this problem surface modification of cathode material is necessary.
8. Another disadvantage in the case of Li ion battery is the huge volume with the high-capacity alloy anodes which affects the capacity and cyclic stability. Use of nano-engineered active-inactive composites could improve the volume expansion and offer better cycle life.
9. Design and development of high-voltage electrolytes with a wide electrochemical window such as 0-5.3 V vs Li/Li⁺ which would be compatible

with both the cathode and the anode will have considerable positive impact on the field of Li ion battery.

Appendix

Nanoparticle-loaded multifunctional natural seed gel-bits for efficient water purification

*In this work we demonstrate the use of natural seed based hydrogel bits as robust, recoverable and recyclable support for multipurpose water purification application. We show that the inexpensive and easily available natural seeds Sabja (*Ocimum basilicum*), which can absorb water to about 30 times their weight can be easily loaded with nanoparticles of functional metal oxides such as visible light photocatalyst N-doped TiO_2 or magnetite (Fe_3O_4) for effective multiple water purification objectives such as efficient photocatalytic degradation of toxins or bacteria, heavy metal ion (As^{3+} , Cr^{6+} , Pb^{2+} , Cd^{2+}) removal or simple particulate filtering. Indeed, innovative nanoparticle loading strategy can be used to load organic and inorganic materials concurrently, sequentially or simultaneously on the gel bits while they swell in the process of water absorption. Interestingly the gel bits maintain their individual identity without agglomeration or fusing, and given their swollen size of about few millimetres they can be easily separated out by simple cloth or millimetre scale filtering. This alleviates the difficulties associated with separating nanoparticles dispersed in the media directly for photocatalytic or other purification purposes. With magnetic nanoparticle co-loading they can also be separated out by magnetic field, which can be beneficial in situations wherein filtering may not be an easy option.*



A.1 Introduction

Amongst the top ten challenges facing the world today, water is clearly a major one that needs urgent attention. Availability of pure drinking water that is free of toxins, heavy metal ions and bio-organisms is a critical need of the large population in the developing countries. Importantly the solutions that have to be sought must necessarily be inexpensive.

Water pollution can occur due to several reasons and these causes contribute different pollutant types to the water system. With the rapidly growing industrial sector, water gets polluted routinely by the industrial waste products which are then directly drained to the water resources. Such waste is mainly composed of organic pollutants and heavy metal ions which make the drinking water non-potable. Metal pollution has severe harmful effects on biological systems. The main culprits in this respect, especially for human health, are arsenic, cadmium, mercury and lead ions and they adversely and seriously affect different biological functions of the human body.^[1-7] Apart from these heavy metals organic pollutants such as dyes are also toxic for environments and humans, and are known to affect the central nervous system.

Various approaches are being pursued to address and eliminate water pollution. These involve development of methods for water remediation such as chemical precipitation, ion exchange, resins, cementation, microbial reduction, electro dialysis and with several adsorbents like sunflower stalks, maize cob and husk, activated carbon etc.^[8-17] But these methods require several process steps for purification and separation of adsorbents from water. Bioremediation is also of considerable current interest for the removal of heavy metal wastes from water. Amongst the newer studies of interest in this respect nanotechnology is gaining considerable ground in view of the unique properties possessed by nanoparticles emanating from quantum effects and large surface to volume ratio. Importantly, these properties can be greatly tuned by controlling the nanoparticle size, shape and surface functionalization. Although these attributes allow great flexibility in engineering the functionality of the resultant materials for particular application goals such as water purification, the engagement of the nanosystem with a resource such as water brings in additional questions pertaining to nano-hazards, in the context of portability or use in agriculture. This is

because removal of dispensed nanomaterials in the water system for purposes of purification after their use is a non-trivial matter. Therefore, on one hand emphasis has to be laid on biocompatibility of nanocatalysts, and on the other, ways are needed to support the nanocatalysts on robust and recoverable hosts/matrices.

In this work we present a simple yet novel way to collectively address several of these problems based on mostly mechanistic concepts built around the natural seed system *Ocimum basilicum* (Indian name *Sabja*).^[18] Basil is a member of genus *Osmium*. It is available worldwide and is mostly found in the tropical region of Asia, Africa and central and south America.^[19] Basil is cultivated in Iran and is used as Pharmaceutical plant in high quantity. It is a well known source of flavouring principle and is also used in medicines to treat ulcer and diarrhoea.^[20] Basil seeds are also used in beverages in many parts of the Asia and Iran. There are many reports where it has been used for extraction of essential oil and gum.^[21,22] People have also used basil seeds for the synthesis of nanoparticles.^[23] When the seed is soaked in water, the swells into a gelatinous mass outside with an inside hard black core due to the presence of a polysaccharide layer.^[24] We demonstrate that these natural seeds which quickly form gel-bits by absorbing water to an extent of almost 30 times of their weight through swelling provide a facile, interactive, versatile, robust, and recoverable support system for nanocatalysts. We specifically demonstrate the diverse applicability and versatility of the concept for water purification for a) degradation of organic dyes (Methylene blue) by UV and visible light induced photocatalytic decomposition accomplished by loading of TiO₂ or N doped TiO₂ nanoparticles,^[25-29] respectively, b) efficient removal of heavy metal ions by adsorption by Fe₃O₄ nanoparticles (known for heavy ion removal)^[30-34] loaded on seed gel-bits, and c) elimination of bacterial pollution (*E coli*) by photocatalysis. There is one report where these seeds have been used for Cr removal from water,^[35] but to our knowledge there are no reports on nanoparticles loaded seeds used for water purification. We have also shown that concurrent loading of Fe₃O₄ (inside region of swollen seed) and TiO₂ (outside region) can be easily implemented for performing multiple functions including magnetic recovery after the process completion. While on a small scale even simple filtering through a wire mesh is possible in view of the few mm size of the swollen seeds, on a large scale a magnet is clearly more useful for recovery.

Finally we have also demonstrated the use of the seed mass as particle size separator using dynamic light scattering studies. It can be easily seen that the concepts discussed here can be applied to other technological or agricultural applications wherein nano or micro- particulate catalysts are needed to be held in a soft yet robust and easily recoverable support. Importantly, the seeds are easily available in large quantities at extremely low cost.

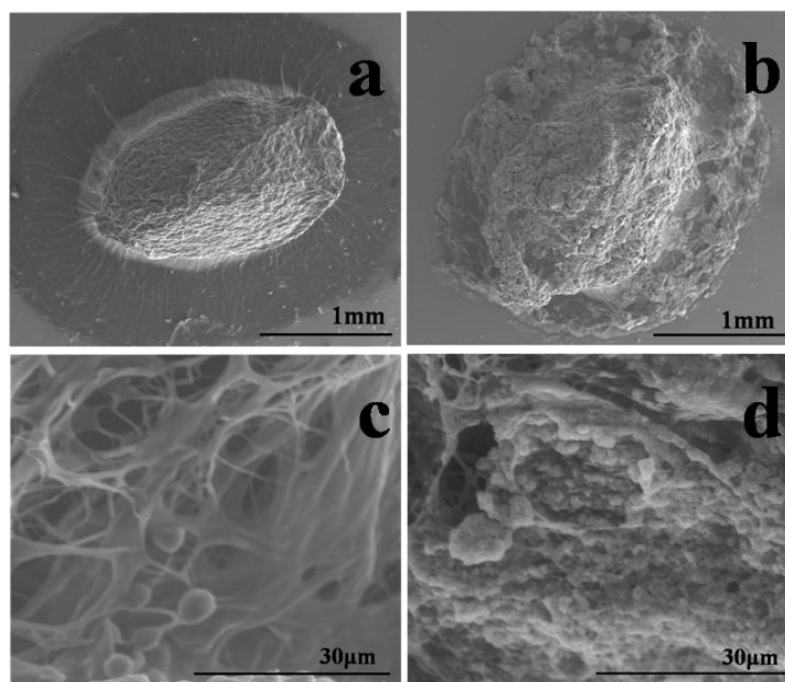


Figure A.1: SEM images of Sabja (*Ocimum basilicum*) seed after swelling in water and Fe_3O_4 coated seed; a and b) SEM images taken by drying the swollen bare seed and Fe_3O_4 coated seed respectively. C and d) SEM images taken for bare swollen seed and Fe_3O_4 coated seed in presence of water respectively (not dried).

The natural seeds named *Ocimum basilicum* swell significantly in the presence of water and concurrently absorb a high content of functional nanomaterials and/or molecules dispersed or dissolved in water due to their highly mesoporous internal constitution evolving in the swelling process. **Figure A.1a and b** show the SEM images of bare swollen seed and Fe_3O_4 coated seed on the same scale after drying. The latter clearly shows substantial and dense loading of Fe_3O_4 nanoparticles incorporated in the seed gel. Due to full collapse upon drying the particles are aggregated. **Figure A.1c and d** show the SEM images of both Sabja seed and Fe_3O_4

coated seed but without full drying of water and these reveal the empty and filled porous structures in the gel. The Environmental SEM images of the unloaded and Fe_3O_4 loaded seeds in the presence of water (without even partial drying) are given in **Figure A.2a-d**. Basically these data bring out that copious amounts of nanoparticles can be loaded into the internal microporous cavities of the gel during its swelling.

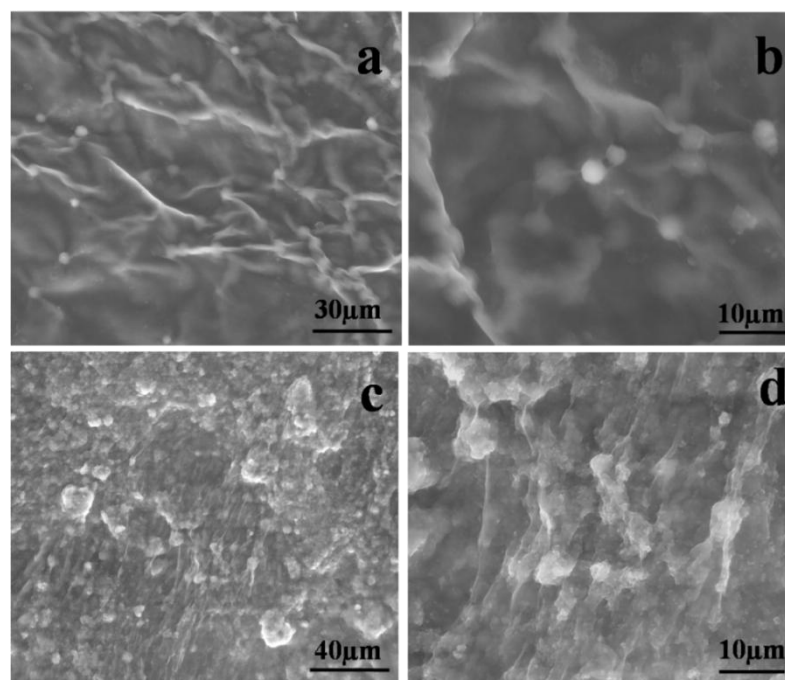


Figure A.2: Environmental SEM images of (a and b) water soaked Sabja seed; (c and d) Fe_3O_4 loaded Sabja seed in presence of water.

A.2 Experimental

A.2.1 Synthesis of Fe_3O_4 nanoparticles

8-10 nm Fe_3O_4 nanoparticles were synthesized by polyol method. 3g of Iron (III) acetyl acetonate was dissolved in 100 ml of triethylene glycol (TG). Then this solution was heated in an oil bath along with a condenser fitted to it with continuous stirring. Initially the temperature was increased slowly to 280°C in 2Hr and after reaching 280°C , it was allowed to remain stable at this temperature for 30 mins. After the reaction was complete the solution was allowed to cool to room temperature and the product was recovered by several time centrifugations with ethanol. Then the product was dried and characterized thoroughly by several techniques.

A.2.2 Synthesis of TiO₂ and N: TiO₂ nanoparticles

TiO₂ nanoparticles were synthesized by sol-gel technique. 5 ml Titanium Isopropoxide solution was added to 30 ml of ethanol in a round bottom flask. Then in another beaker hydrolysis mixture of 8 ml of ethanol, 2 ml of water and 2-3 drops of HNO₃ were mixed thoroughly and added drop-wise to the above mixture. This sol was then poured into a petri-dish. After some time the sol got slowly converted into a gel. This gel was then dried and crushed to make fine powder which was subjected to annealing treatment at 300°C for 2 Hrs to get TiO₂ nanoparticles. To obtain Nitrogen doped TiO₂ nanoparticles for which the optical absorption is shifted to the visible region allowing visible light (or solar) photocatalysis, the same protocol as above was followed but with addition of an appropriate amount of NH₂OH.HCl in the hydrolysis mixture. It was added drop wise and slowly with stirring. This xerogel is also clear and transparent, but is yellow in colour, which after crushing and calcination at 400°C for 2 hrs gives mildly yellow coloured powder.

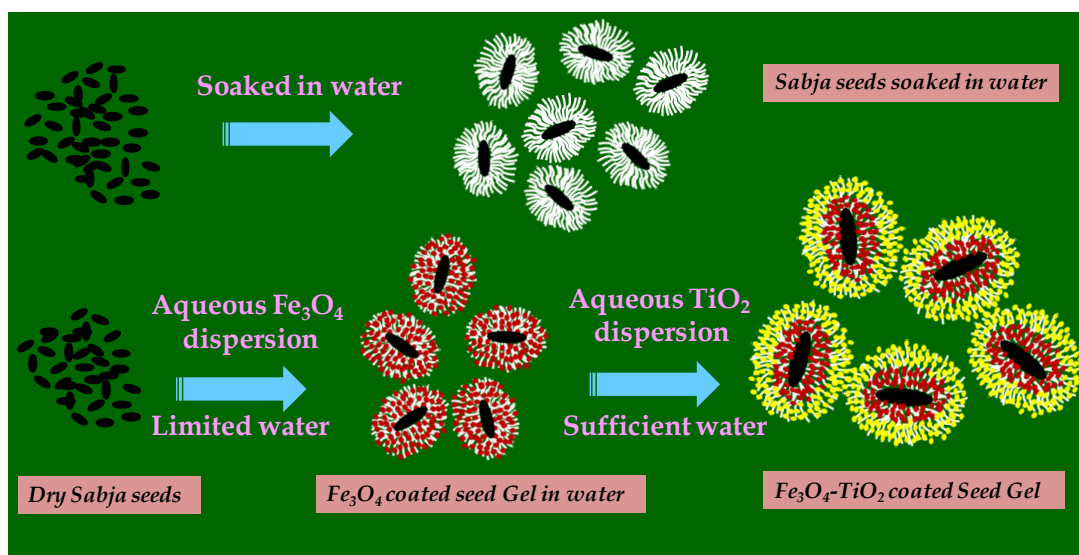
A.2.3 Separate loading of Fe₃O₄, TiO₂ or N: TiO₂ into the swelling natural seeds

For the loading of individual nanoparticles such as Fe₃O₄, TiO₂, N: TiO₂, a specific quantity (50 mg) of nanoparticles was dispersed in 100 ml of water. The above solution was sonicated for 15 mins for uniform dispersion of the nanoparticles. To this dispersion 500 mg of sabja seeds were added, stirred well and allowed to swell for 30 mins. After complete swelling of the seeds in the presence of nanoparticles the rest of the solution was decanted and the seeds loaded with nanoparticles were washed thoroughly to remove the free nanoparticles.

A.2.4 Sequential Coating of Fe₃O₄ -TiO₂ into the swelling natural seeds

In an interesting case, we also performed sequential loading of Fe₃O₄ and TiO₂ (or N doped TiO₂) nanoparticles. For this purpose, during the loading of Fe₃O₄ nanoparticle less quantity of water was used so as not to allow full swelling of the seeds. These partially swollen Fe₃O₄ coated seeds were then added to TiO₂ or N:TiO₂ nanoparticle solution for core shell type of seed loading. In this experiment 50 mg of Fe₃O₄ nanoparticles were well dispersed in 20 ml of water by sonication. Then 500 mg of natural seeds were added to this dispersion and stirred to get uniform loading of Fe₃O₄ on the swelling seed gel. Once the seeds were coated uniformly with Fe₃O₄,

they were washed several times to get rid of the rest of the solution containing Fe_3O_4 . In another beaker 50 mg of TiO_2 (or N: TiO_2) nanoparticles were dispersed thoroughly and the above seeds (already partially loaded with Fe_3O_4) were added to the suspension containing TiO_2 (or N: TiO_2). These seeds were allowed to stir for 30 mins for achieving uniform coating of titania nanoparticles. Then this suspension was washed again and finally the dual-loaded seeds were dispersed in 50 ml of water. The seeds loaded with Fe_3O_4 and TiO_2 (or N: TiO_2) were magnetic, as expected, and could be easily separated from the solution by a magnet. The schematic of the process is shown in **Scheme A.1**.



Scheme A.1: Coating of nanoparticle on Sabja seed gel bits

A.2.5 Photocatalysis experiments

All the photocatalysis experiments were carried out with 10^{-5} M methylene blue dye, this dye being used as a representative case. 300mg of Fe_3O_4 - TiO_2 coated seeds was added to 100 ml of 10^{-5} M methylene blue solution in 200 ml quartz beaker. This beaker was then kept under UV lamp (400 watts, light intensity at catalyst-dispersed liquid surface adjusted to $\sim 6\text{mW}/\text{cm}^2$) with constant stirring. UV-Vis spectra were measured for each sample at time intervals of 30 mins. For Fe_3O_4 /N-doped TiO_2 coated seeds, visible light photocatalysis was carried out by the similar procedure but with a visible light lamp (70 watts, light intensity at catalyst-dispersed liquid surface adjusted to $\sim 6\text{mW}/\text{cm}^2$). The power densities of the UV and Visible sources and

lamp geometry/placements (distances etc.) were adjusted to give comparable power densities at the liquid surface with dispersed catalyst. Degradation of methylene blue was studied again with UV/Vis spectra.

A.2.6 Photocatalytic treatment of E-Coli (Antimicrobial assay)

The antimicrobial activity of N-doped TiO₂ decorated seeds (*Ocimum Bascilicum*) in the presence of white light was tested on a gram negative organism, *Escherichia coli* (ATCC 10536, gram negative rods). White light was used as a light source (6mW/cm²). Agar plate method was used to study the bactericidal activity of the particles. Preinoculum of E.coli was inoculated in 10 ml of Luria Bertani medium and incubated at 37°C for overnight at 200 rpm. The culture obtained (10⁸ cfu/ml) was serially diluted to 10⁴ cfu/ml. Two tubes containing 0.85% saline were inoculated with 10⁴cfu/ml. One of the tubes was added with N doped-TiO₂ decorated seeds and both the tubes were kept on incubation at 37°C at 200 rpm for 8 hrs in the presence of white light which was kept at a distance of 15cm from the sample. Aliquots of 50 µl were taken from each of the tubes at regular interval of time (0, 2, 4, 8 hrs) and plated on agar plate. These plates were then incubated at 37 °C for 24 hrs. The colonies were then counted and the percentage of bacterial cell survival was calculated.

A.2.7 Heavy metal removal from water: Non competitive and competitive adsorption

Each of the heavy metal ion types was used separately with unloaded seeds and Fe₃O₄-loaded seeds for non-competitive adsorption study implying absence of any other ions in the medium. A specific amount As₂O₃, K₂Cr₂O₇, PbCl₂ and CdCl₂ was dissolved separately in 1L of water to make 1 ppm, 5ppm, 20 ppm, 30 ppm and 50 ppm solutions, and the pH of the solutions was maintained to be 2 by adding few drops of 0.5M HNO₃. A few ml solutions of the initial samples were taken out before adding the seeds to know the initial concentration of these ions. Identical concentrations of different solutions were ensured by using a single stock and 1 g amount of either unloaded seeds or Fe₃O₄ loaded seeds was added to it, separately. These solutions were allowed to stir for different time interval (15mins, 30mins, 45mins, 60mins, 90mins, 120mins) to study the rate of adsorption. After the specified time intervals samples were taken out and heavy metal ion concentration was

determined by inductively coupled plasma optical emission spectroscopy (ICP-OES) analysis in both the initial and final samples. For competitive adsorption study all the heavy metal ions were used simultaneously.

A.3 Results and Discussions

Figure A.3a shows the original *Ocimum basilicum* black seeds which swell fairly quickly (10-15 mins) when soaked in water (**Figure A.3b**). The weight gain by the seed is almost a factor of 30. After complete swelling these seeds have buoyancy in water (since the content is mostly water) which enables them to disperse and move

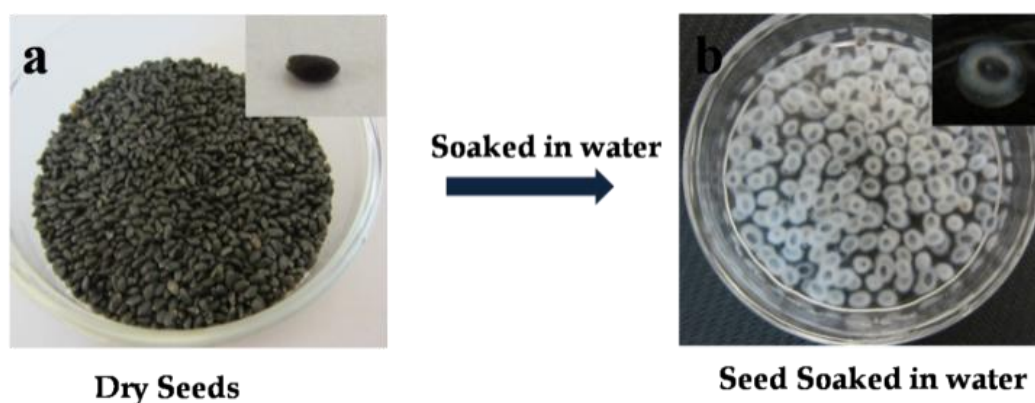


Figure A.3: Picture of Sabja (*Ocimum basilicum*) seeds and seeds soaked in water

around easily. Interestingly these swollen seeds maintain their identity in water and do not fuse; hence they can be termed as gel-bits. Due to their high absorbing power for water and natural gel-mesoporosity these seeds can take in any organic/polymeric molecules or inorganic particulates that may be dispersed or dissolved in water allowing facile molecular or nano (or micro) particle loading on the seeds during the course of their swelling.

We first discuss the results of the experiments of UV (or visible) light photocatalysis on sequentially Fe_3O_4 and TiO_2 (N: TiO_2) loaded seeds. In these experiments 10^{-5}M methylene blue (MB) dye solution was stirred with the nanoparticle loaded seeds under UV (or visible) light illumination and the degradation of the dye was examined. **Figure A.4** shows the picture of fresh Fe_3O_4 loaded seeds and the same after 5 cycles which still appear robust and fresh. The results of UV photocatalytic dye degradation of methylene blue with fresh Fe_3O_4 - TiO_2 coated seeds

are shown in **Figure A.5a and b**, which clearly reveal a rapid decrease in the intensity of the methylene blue peak ($\sim 661\text{nm}$). Almost 96% MB dye degradation is observed in 4 Hr. The same experimental procedure was repeated for 5 cycles and the stability of activity of the loaded seeds was studied. It was observed that after 5 cycles there is a progressive decrease (from 96% Degradation to 81% degradation) in the percent dye degradation as shown in **Figure A.5b**. Photocatalysis with $\text{Fe}_3\text{O}_4/\text{TiO}_2$ coated seeds shows only 9% dye degradation without UV light, as expected due to the higher band gap of TiO_2 (3.2 eV). The performance of $\text{Fe}_3\text{O}_4/\text{TiO}_2$ coated seeds was also tested after one month. It was observed that even after one month the nanoparticle loaded seeds show 72% degradation of MB dye in 4 Hr. Hence these seeds can be clearly used as stable and recoverable photocatalysis media. Presence of Fe_3O_4 in the core of the swollen seeds allowed us to recover the seeds after completion of photocatalysis by a magnet, and the same could be used again after washing thoroughly for the next cycle of the MB dye degradation experiment. Another interesting aspect that was noted was the absence of any growth of tiny leaves on the seeds loaded with nanoparticles. Such growth was seen on seeds exposed to light for weeks but was apparently suppressed in the case of nanoparticle loaded seeds. This interesting matter is being investigated further.

As seen from **Figure A.5c**, in the case of $\text{Fe}_3\text{O}_4/\text{N}:\text{TiO}_2$ sequentially loaded seeds, when the seeds dispersed MB solution is exposed to visible light, 98% degradation of MB dye is realized in 4Hrs. It was observed that even after 5 cycles (**Figure A.5d**) the percentage dye degradation of 83 % could be obtained in 4 hrs. Hence even after 5th cycle the coated seeds maintained good visible light photocatalytic activity. After 5th cycles the seeds were washed thoroughly and kept for one month. The coated seeds maintained their activity and stability which showed 60% of dye degradation in 4 hrs. It is clear that these nanoparticle loaded seeds can be used several times for the degradation of organic pollutants from water suggesting its cost effectiveness and stability.

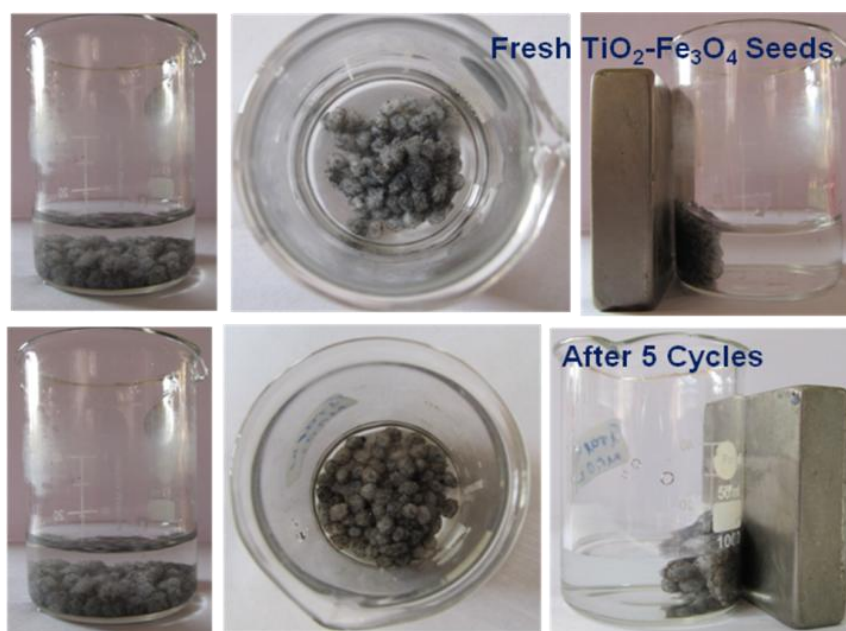


Figure A. 4: Picture of Fe_3O_4 – TiO_2 coated seeds before photo catalysis experiments and seeds after 5 cycles of experiments.

We also tested the antibacterial properties of N doped TiO_2 loaded seeds in the presence of visible light source (Please see the experimental section for the details of the procedure). The choice of N: TiO_2 system was made because it is known to exhibit visible light induced antibacterial activity.^[36-38] Results shown in **Figure A.6** bring out that the activity is directly proportional to the illumination time, as expected. After illumination time of only 2hrs, there was almost 50% reduction of the number of colonies and after 8 hrs only 5 out of 300 colonies were viable. Thus the N: TiO_2 nanoparticles adsorbed on seeds are highly effective in photo-catalytically killing the bacterial cells. The most important advantage of the studied process is that the seeds can be easily filtered out by a simple cloth or mesh filter, and reused several times. If one were to use N: TiO_2 nanoparticles as such for dispersion in water media for purification purposes the recovery of nanoparticles is a big problem, as is well known.

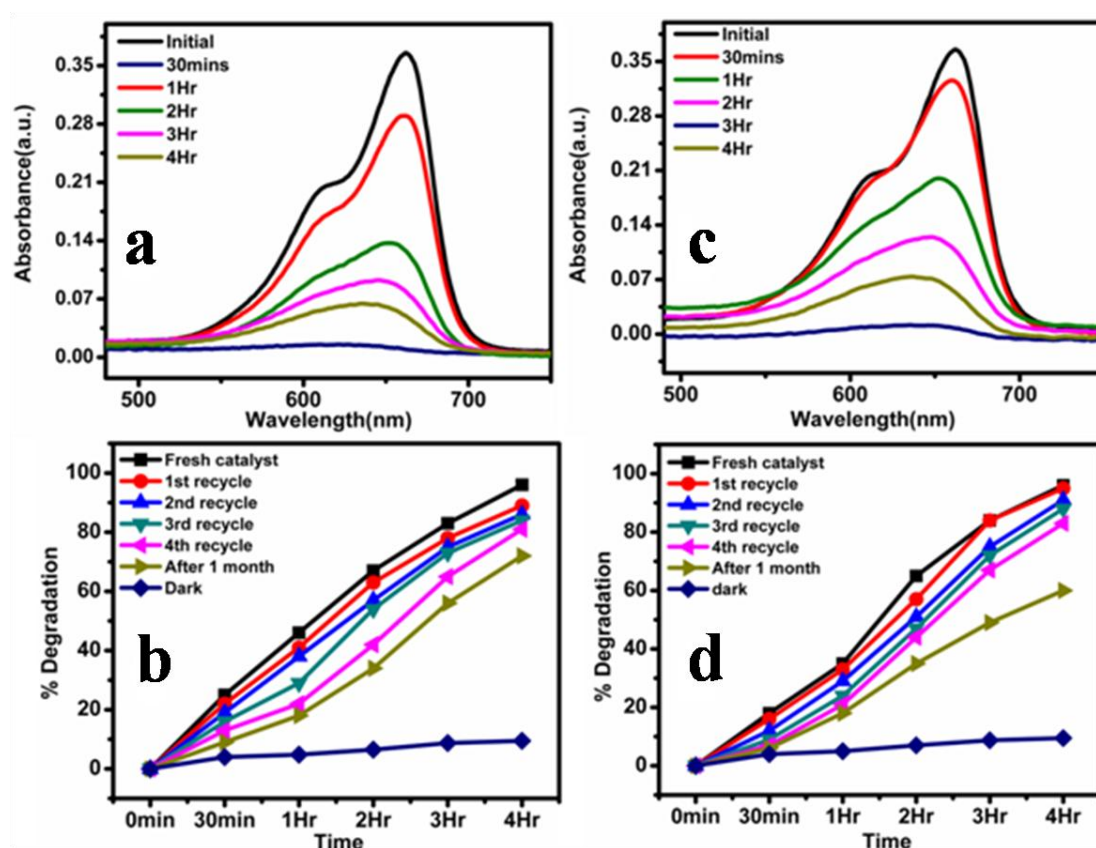


Figure A.5: a & c) UV light photocatalysis and percentage degradation of methylene blue with TiO_2 coated seeds; b & d) Visible light photocatalysis and percentage degradation of methylene blue with N doped TiO_2 coated seeds

As stated earlier, we also tested the efficacy of Fe_3O_4 nanoparticle loaded seeds for removal of various heavy metals such as Arsenic (As^{3+}), Chromium (Cr^{6+}), cadmium (Cd^{2+}) and lead (Pb^{2+}) which are threats for biological systems. ^[1-7, 39] **Table A.1** shows the comparison in the % removal of different heavy metal ions (5ppm) with both bare seeds and Fe_3O_4 loaded seeds in non-competitive adsorption experiments, wherein the heavy metal ions were taken separately. It was observed that bare seeds without Fe_3O_4 coating also show removal of heavy metal ions (As^{3+} -53%, Cr^{6+} - 69%, Pb^{2+} - 44%, Cd^{2+} – 32%), but the Fe_3O_4 loaded seeds show almost 90-100% removal of all heavy metal ions, which is significantly higher than the bare seeds. Hence loading the seeds with nanoparticles yields much superior performance in the removal of heavy metal ions.

Figures A.7 a-d show the heavy metal ion concentration dependence of the % removal for Fe₃O₄ loaded seed gel-bits for different time intervals. In the case of As, Cr and Cd, the Fe₃O₄ loaded seeds show excellent removal capacity by removing almost 60% of heavy metal ions even at the highest concentration of 50 ppm examined. However, in the case of Pb ions the removal efficiency is somewhat lower (50%) for the 50 ppm high concentration case. At lower concentrations (1 and 5ppm) Fe₃O₄ loaded seed gel-bits give highest removal capacity (~90%) in the case of As, Cr and Cd ions and slightly lower removal capacity (~78%) for Pb ions.

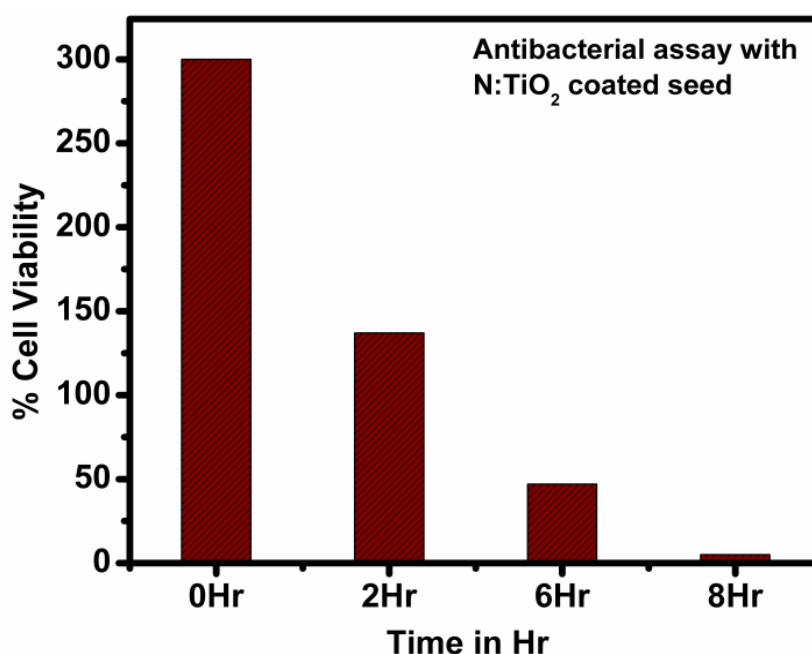


Figure A.6: Antimicrobial assay with N doped TiO₂ coated seed in presence of visible light

To study the competitive adsorption of As, Cr, Cd and Pb all the heavy metal ions were mixed in equal proportions to make the 50 ppm solution. **Figure A.8a** and **b** show the percentage removal of As, Cr, Cd and Pb from 50ppm solutions with unloaded seed gel-bits and Fe₃O₄ loaded seed gel-bits. **Figure A.8a** shows that in the case of unloaded seeds the removal capacity for As and Cr in 2 Hrs is high (up to 50%) whereas for Pb and Cd ions it shows 30-40% removal. However, as shown in

Sl.No.	Metals (5ppm)	% Removal	
		Sabja	Fe ₃ O ₄ –Sabja
1	As ³⁺	53.32	99
2	Cr ⁶⁺	69.40	97
4	Pb ²⁺	44.11	92
5	Cd ²⁺	32.35	84

Table A.1: Comparison of percentage removal of different heavy metals with bare Sabja seeds and Fe₃O₄ coated seeds.

Figure A.8b when Fe₃O₄ loaded seeds are employed, the removal capacity increases to 90% for As, 80% for Cr, 70% for Cd and 53% for Pb. Indeed, Fe₃O₄ is known to be a good adsorbent for heavy metal ions. Combining the high swelling ability of the seeds and good adsorption character of Fe₃O₄ leads to enhanced removal capacity.

Once adsorption experiments were done we recycled the natural seeds and nanoparticle-loaded seeds. The release of heavy metal ions was achieved by putting all the seeds in ethanol wherein the seeds got squeezed and all the heavy metals were released. Then the squeezed seeds were again put in water to swell and could be reused for another cycle for heavy metal adsorption.

It is now important to estimate the loss of loaded nanoparticles into solution for successive cycles of processing so as to establish the robustness of the catalysis support. Towards this end two measurements were performed, namely the inductively coupled plasma Optical Emission Spectroscopy (ICP-OES) studies to find out the Fe and Ti concentration in solution after each processing cycle (and thereby the effective weight of the number of nanoparticles lost) and gravimetric measurements reflecting the gradual loss of weight of the loaded seeds. The latter measurements are a bit tricky since the weight of water in seeds is a factor which could fluctuate. Hence the ICP-OES experiment was done with the same large number of seeds that were used in the

actual photo-catalysis experiments and statistics of several measurements was used to present the data. The trends are thus found to be quite systematic in both the cases.

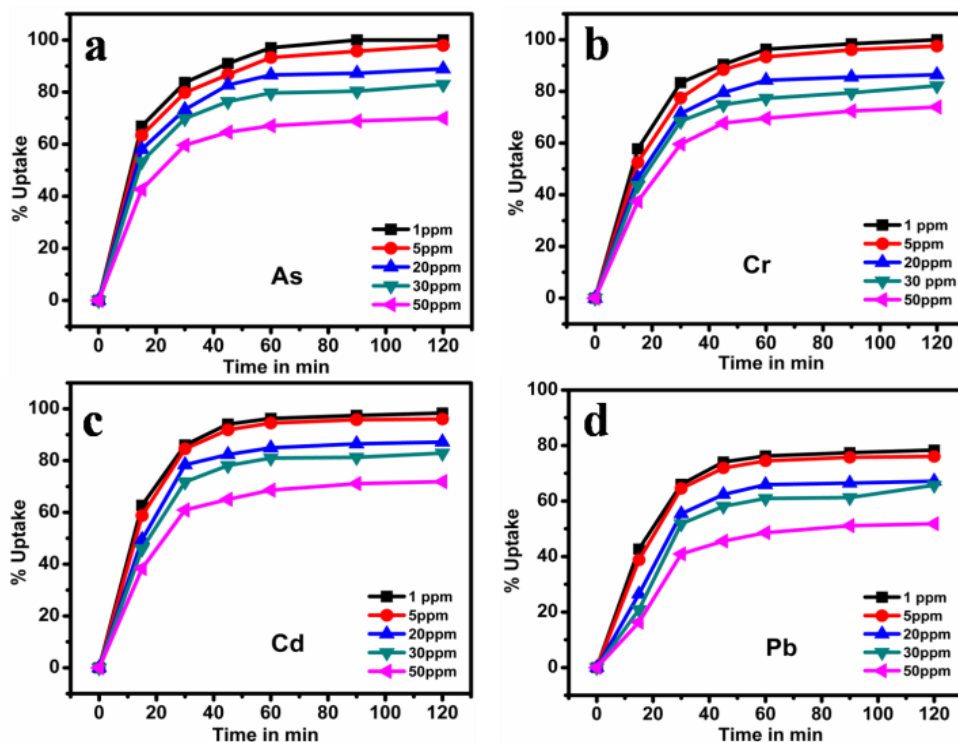


Figure A.7: a, b, c, d) % removal of As, Cr, Cd and Pb with Fe_3O_4 Sabja at different time interval and concentrations in non competitive adsorption.

In these experiments, 50 mg of Fe_3O_4 NPs powder was dispersed thoroughly in 20 ml of water for 30 mins by ultra-sonication. To this 500 mg (~ 184 seeds) of dry seeds were added and the solution was stirred well in limited quantity of water for the coating of Fe_3O_4 NPs onto the seeds, allowing limited swelling as for the photocatalysis experiments. Such Fe_3O_4 NP coated seeds were washed once to remove loosely bound Fe_3O_4 . In another beaker 50 mg of TiO_2 nanoparticle powder was dispersed uniformly in 50 ml of water and to this dispersion the Fe_3O_4 NPs coated seeds were added and stirred well for the shell-coating of TiO_2 NPs on Fe_3O_4 NPs core. These seeds were allowed to swell completely with sufficient water. After complete swelling this Fe_3O_4 - TiO_2 coated seeds were washed once with water to remove the loosely bound nanoparticles.

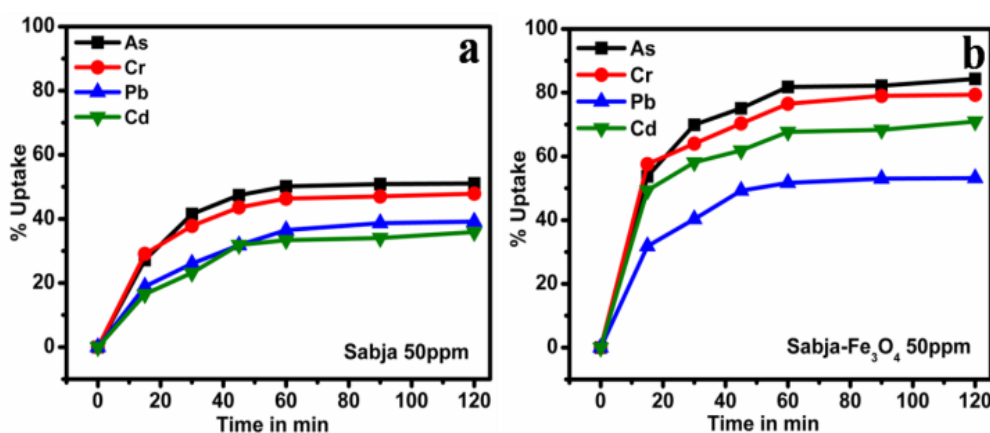


Figure A.8: a and b show removal of As, Cr, Pb and Cd from water with only Sabja and Fe₃O₄ coated Sabja respectively in competitive adsorption

The dual-loaded seeds were re-dispersed in 100 ml of water and stirred for 30 mins. After 30 mins the seeds were taken out by simple filtration and the rest of the solution was named sample 1. The procedure was repeated 5 times and solution samples were collected. The TiO₂ and Fe₃O₄ quantities in these solutions were determined by ICP analysis. For the ICP measurements 5 ml of each of these samples was dissolved in 10 ml of HF and H₂SO₄ mixture (1:1 ratio). The solutions were kept for 12 Hr for complete digestion of nanoparticles (Fe₃O₄ and TiO₂). Thereafter they were diluted to 100 ml and filtered. The metal concentration was determined by ICP spectroscopy in these solutions from which metal oxide amount was calculated. Apart from these studies, to estimate the total weight of nanoparticles loaded on each seed, 5 individual dual-loaded seeds were separately dissolved in HF and H₂SO₄ mixture (1:1 ratio) and subjected to digestion of nanoparticles. Then the solution was diluted for ICP analysis. The ICP-OES data are shown in **Table A.2**. Here the cycle no. represents the stirring cycle after which the weight was recorded.

For gravimetric studies similar basic procedure was followed for the coating of Fe₃O₄ and TiO₂ onto seeds (~10 seeds). After the coating these seeds were washed and weighed on a microbalance. Then these seeds were again re-dispersed in 100 ml of water and allowed to stir for 30mins. After stirring the seeds were filtered out and washed. The weight of these seeds was again noted down. Similar procedure was followed for 5 times and each time weight change was noted down to see the total loss

of nanoparticles weight during the stirring. Similarly 3 sets of experiments were done having 10 seeds and the results were shown in **Table A.3**.

ICP measurements						
Cycle no.	1 st	2 nd	3 rd	4 th	5 th	Total Loss
TiO ₂ (mg)	6	4	1	0.5	0.2	11.4
Fe ₃ O ₄ (mg)	3	1	0.3	0.05	0.004	4.354

Table A.2: ICP Analysis of various samples for TiO₂ and Fe₃O₄ quantity

Cycle no.	Initial	1 st	2 nd	3 rd	4 th	5 th
Weight (mg)	433	426	421	417	415	414
Loss (mg)		7	5	4	2	1
Weight in mg	422	436	431	428	427	426
Loss (mg)		6	5	3	1	1
Weight in mg	432	419	418	415	413	
Loss (mg)		9	4	1	3	2

Table A.3: Gravimetric Measurements of TiO₂ -Fe₃O₄ loaded seeds

From the ICP analysis the total nanoparticle loading per seed was found to be about 0.41 mg, while that from gravimetric analysis was found to be about 0.55 mg. This adequately corresponds to about 50 mg of Fe₃O₄ NPs and 50 mg of TiO₂ nanoparticles used for loading on about 185 seeds. From the ICP data shown in the **Table A.2**, it is seen that the loss of nanoparticles is about 10% for TiO₂ and 5% for Fe₃O₄ in the very first cycle and it goes down rapidly in the subsequent cycles. The initial loss may be attributed to still remaining loosely bound particles. In fact after the first couple of cycles the loss is really negligible suggesting that the catalyst support is quite robust. As expected, Fe₃O₄ being in the core, the loss of these nanoparticles is even less than that of the TiO₂ nanoparticles forming the outer shell. The gravimetric measurement data shown in the **Table A.3** are also fairly consistent

with this picture, although the error in the estimate is somewhat larger due to the reasons explained earlier. On the whole, both these measurements show that nanoparticle loading followed by adequate initial washing to remove loosely bound nanoparticles can render a fairly robust catalytic system for repeated use.

A.4 Conclusion

In summary use of natural seed based hydrogel bits as robust, recoverable and recyclable support for nanoparticulate catalytic media is demonstrated for multipurpose water purification application. Thus, *Ocimum basilicum* seeds, which absorb water to about 30 times their weight, loaded with nanoparticles of visible light photo-catalyst N-doped TiO₂ and/or magnetite (Fe₃O₄) are shown to be highly effective for photocatalytic degradation of toxins or bacteria, and for removal of heavy metal ions (As³⁺, Cr⁶⁺, Pb²⁺, Cd²⁺). Interestingly the gel bits maintain their individual identity without agglomeration or fusing, and given their swollen size of about few millimetres they can be easily separated out by simple cloth or millimetre scale filtering. This alleviates the difficulties associated with separating nanoparticles dispersed in the media directly for photocatalytic or other purification purposes. With magnetic nanoparticle co-loading they can also be separated out by magnetic field, which can be beneficial in situations wherein filtering may not be an easy option.

A.5 References

1. E. Sumesh, M. S. Bootharaju and A. T. Pradeep, *J. Hazard. Mater.*, **2011**, 189, 450.
2. Y. Wu, J. Zhang, Y. Tong and X. Xu, *J. Hazard. Mater.*, **2009**, 172, 1640.
3. J. T. Mayo, C. Yavuz, S. Yean, L. Cong, H. Shipley, W. Yu, J. Falkner, A. Kan, M. Tomson and V. L. Colvin, *Sci. Technol. Adv. Mater.*, **2007**, 8, 71.
4. M. Bissen and F. H. Frimmel, *Acta Hydrochim. Hydrobiol.*, **2003**, 31, 97.
5. H. Guo, D. Stüben and Z. Berner, *Sci. Total Environ.*, **2007**, 377, 142.
6. D. Mohan, K. P. Singh and V. K. Singh, *J. Hazard. Mater.*, **2006**, B135, 280.
7. I. Ojea-Jimenez, X. Lopez, J. Arbiol and V. Puntes, *ACS Nano*, **2012**, 6, 2253.

8. M. Kobya, E. Demirbas, E. Senturk and M. Ince, *Bioresour.Technol.*, **2005**, 96, 1518.
9. J. Wang and C. Chen, *Biotechnol. Adv.*, **2006**, 24, 427.
10. L. E. Eary and D. Ral, *Environ. Sci. Technol.*, **1988**, 22, 972.
11. J. C. Igwe, D. N. Ogunewe and A. A. Abia, *Afr. J. Biotechnol.*, **2005**, 4, 1113.
12. J. M. Chen and O. J. Hao, *Crit. Rev. Environ. Sci. Technol.*, **1998**, 28, 219.
13. Ü. B. Ögütveren, S. Koparal and E. Özel, *J. Environ. Sci. Health*, **1997**, A32, 749.
14. D. W. Blowes, C. J. Ptacek and J. L. Jambor, *Environ. Sci.Technol.*, **1997**, 31, 3348.
15. S. Babel and T. A. Kurniawan, *J. Hazard. Mater.*, **2003**, B97, 219.
16. S. A. Nosier, *Chem. Biochem. Eng. Q.*, **2003**, 17, 219.
17. S. H. Lin, S. L. Lai and H. G. Leu, *J. Hazard. Mater.*, **2000**, B76, 139.
18. M. Biswal, K. Bhardwaj, P. K. Singh, P. Singh, P. Yadav, A. Prabhune, C. Rode and S. Ogale, *RSC Adv.*, **2013**, 3, 2288.
19. A. Paton, M. R. Harley and M. M. Harley, in Basil, ed. R.Hiltumen and Y. Holm, Harwood Academic Publishers, The Netherlands, **1999**, 1.
20. F. Naghibi, M. Mosaddegh, S. M. Motamed and A. Ghorbani, *Iran. J. Pharm. Res.*, **2005**, 2, 63.
21. S. M. A. Razavi, S. Ali Mortazavi, L. Matia-Merino, S. H. Hosseini-Parvar, A. Motamedzadegan and E. Khanipour, *Int. J. Food Sci. Technol.*, **2009**, 44, 1755.
22. J. Fang, Y. Leu, T. Hwang and H. Cheng, *Biol. Pharm. Bull.*, **2004**, 27, 1819..
23. N. Ahmad, S. Sharma, M. K. Alam, V. N. Singh, S. F. Shamsi and B. R. Mehta, *Colloids Surf. B*, **2010**, 81, 81.
24. J. Azoma and M. Sakamoto, *Trends Glycosci. Glycotechnol.*, **2003**, 15, 1.
25. C. Burda, Y. Lou, X. Chen, A. C. S. Samia, J. Stout and J. L. Gole, *Nano Lett.*, **2003**, 3, 1049.
26. M. Liu, L. Piao, W. Lu, S. Ju, L. Zhao, C. Zhou, H. Li and W. Wang, *Nanoscale*, **2010**, 2, 1115.
27. Y. Tang, P. Wee, Y. Lai, X. Wang, D. Gong, P. D. Kanhere, T. Lim, Z. Dong and Z. Chen, *J. Phys. Chem. C*, **2012**, 116, 2772.

28. T. C. Jagadale, S. P. Takale, R. S. Sonawane, H. M. Joshi, S. I. Patil, B. B. Kale and S. B. Ogale, *J. Phys. Chem. C*, **2008**, 112, 14595.
29. S. G. Kumar and L. G. Devi, *J. Phys. Chem. A*, **2011**, 115, 13211.
30. Q. He, Z. Zhang, J. Xiong, Y. Xiong and H. Xiao, *Opt. Mater.*, **2008**, 31, 380.
31. S. Xuan, W. Jiang, X. Gong, Y. Hu and Z. Chen, *J. Phys. Chem. C*, **2009**, 113, 553.
32. K. F. Yao, Z. Peng, Z. H. Liao and J. J. Chen, *J. Nanosci. Nanotechnol.*, **2009**, 9, 1458.
33. L. Zhong, J. Hu, H. Liang, A. Cao, W. Song and L. Wan, *Adv. Mater.*, **2006**, 18, 2426.
34. L. Wang, J. Li, Q. Jianga and L. Zhao, *Dalton Trans.*, **2012**, 41, 4544.
35. J. S. Melo and S. F. D'Souza, *Bioresour. Technol.*, **2004**, 92, 151.
36. R. He, Y. Wei and W. Cao, *J. Nanosci. Nanotechnol.*, **2009**, 9, 1094.
37. A. F. Howard, B. D. Iram and S. Varghese, *Appl. Microbiol. Biotechnol.*, **2011**, 90, 1847.
38. Y. Yuan, J. Ding, J. Xu, J. Deng and J. Guo, *J. Nanosci. Nanotechnol.*, **2010**, 10, 4868.
39. J. Peng, Y. Song, P. Yuan, X. Cui and G. Qiu, *J. Hazard. Mater.*, **2009**, 161, 633.

List of Publications and Patents

Publications

1. **Mandakini Biswal**, Vivek V. Dhas, Vivek R. Mate, Abhik Banerjee, Pradip Pachfule, Kanika L. Agrawal, Satishchandra B. Ogale, and Chandrashekhar V. Rode, Selectivity Tailoring in Liquid Phase Oxidation Over MWNT-Mn₃O₄ Nanocomposite Catalysts, **J. Phys. Chem. C**, 2011, 115, 15440–15448.
2. **Mandakini Biswal**, Kirti Bhardwaj, Pradeep K. Singh, Pooja Singh, Prasad Yadav, Asmita Prabhune, Chandrashekhar Rode and Satishchandra Ogale, Nanoparticle-loaded multifunctional natural seed gel-bits for efficient water purification, **RSC Adv.**, 2013, 3, 2288-2295.
3. **Mandakini Biswal**, Abhik Banerjee, Meenal Deo and Satishchandra Ogale, From Dead Leaves to High Energy Supercapacitor, **Energy Environ. Sci.**, 2013, 6, 1249-1259.
4. **Mandakini Biswal**, Anil Suryawanshi, Vishal Thakare, Samuel Jouen, Beatrice Hannover, Aravindan Vanchiaapan, Madhavi Sriniasan, and Satishchandra Ogale, Mesoscopic Fe₃O₄ spheres for high performance Li ion battery anode: A new pulsed laser induced reactive micro-bubble synthesis process, **under revision in Journal of Material Chemistry A**.
5. **Mandakini Biswal**, Sarika Padhke, Aparna Vaidya, and Satishchandra Ogale, Water Electrolysis with a Conducting Carbon Cloth: Sub-Threshold Hydrogen Generation and Super-Threshold Carbon Quantum Dot Formation, **Under review in Chem Sus Chem**.
6. Anil Suryawanshi, **Mandakini Biswal**, Dattakumar Mhamane, Prasad Yadav, Abhik Banerjee, Shankar Patil, Vanchiappan Aravindan, Srinivasan Madhavi and Satishchandra Ogale, A comparative evaluation of differently synthesized

high surface area carbons for Li-ion hybrid electrochemical supercapacitor application, **submitted to Carbon.**

Patents

1. Conducting Carbon Cloth : Sub-Threshold Hydrogen Generation, Super-Threshold Carbon Quantum Dot Formation And Counter Electrode in Dye Sensitized Solar Cells, **Mandakini Biswal**; Sarika Aditya Kelkar; Mukta Chandrakant Tathavedkar; Shruti Anil Agarkar; Satishchandra Balkrishna Ogale; **Provisional application filed on 7/23/2013.**
2. Electronically Conducting Carbon And Carbon-Based Composites And Nanocomposites By Pyrolysis of Dead Leaves, **Mandakini Biswal**; Abhik Banerjee; Satishchandra Balkrishna Ogale, **Complete specification filed on 2/8/2013.**
3. Nanoparticle-loaded multifunctional natural seed gel bits for efficient water purification, **Mandakini Biswal**, Satishchandra Ogale, **under processing at IPG.**